

Developing a Probe for Real-Time Monitoring of Reagent Injections

by

David R. Stevenson

A thesis
presented to the University of Waterloo
in fulfillment of the
thesis requirement for the degree of
Master of Applied Science
in
Civil Engineering

Waterloo, Ontario, Canada, 2013

© David R. Stevenson 2013

Author's Declaration

I hereby declare that I am the sole author of this thesis. This is a true copy of this thesis, including any final required revisions, as accepted by my examiners.

I understand that this thesis may be made electronically available to the public.

David Stevenson

Abstract

Reagent injections designed to provide *in situ* mass destruction of soil and groundwater contaminants are commonly prone to failure due to inadequate distribution of the injected reagent. Reagent injections, in particular *in situ* chemical oxidation (ISCO) injections, require contact between the treatment reagent and targeted contaminant to allow for mass destruction in source zones and plumes. Subsurface heterogeneities that exist at all spatial scales prevent remediation specialists from accurate prediction of reagent distribution in the subsurface, even when significant site characterization and hydraulic testing has previously taken place.

A prototype probe system was developed to provide real-time monitoring of the distribution of injected reagents. This thesis focused on laboratory testing of the system to verify that the design was capable of indicating the presence of an injected reagent in the field. Temperature and two-wire dipole resistance sensors were developed with low-cost materials to provide feedback on the electrical conductivity (EC) signatures produced by typical reagents mixed as salt solutions. Sensors were attached to sections of PVC conduit and wired to a data acquisition system to control measurements and store data.

The temperature sensor was found to accurately respond to temperature changes in comparison to a commercial datalogger. Measured temperature differences between the constructed sensor and commercial datalogger were relatively constant, indicating that the constructed sensor could be calibrated to measurements from a commercial logger.

Static cell experiments were conducted in beakers with varying concentration sodium chloride (NaCl), potassium permanganate (KMnO₄) and sodium persulfate (Na₂S₂O₈) solutions to determine dipole resistance sensor response to variations in EC. Different fixed resistors were wired with the dipole sensor circuit to determine the impact on sensor readings. Results indicated a nonlinear correlation between two-wire dipole resistance sensor response and increasing EC. Each constructed dipole sensor behaved uniquely. Raw sensor response was calibrated to EC by accounting for the influence of the fixed resistor. Data was fit to a second-order polynomial with form $y = aEC^2 + bEC + c$, with r^2 ranging from 0.92-1.00 for experiments with 4-6 measurement points. Calibrations were accurate within the range of EC for each static

cell experiment; trends extrapolated beyond the measurement range were subject to significant error. The choice of fixed resistor did not appear to alter the accuracy of probe calibrations.

Flow cell experiments were designed to analyze dipole resistance sensor response to continuous changes in EC. EC breakthrough curves (BTCs) were produced by injecting NaCl tracer solutions into the flow cell. Initial flow cell experiments conducted in an open water system showed agreement between dipole sensor measurement and handheld EC measurements on the rising limb of BTCs and divergence between the two datasets on the falling limb of BTCs. To resolve these issues, a more sophisticated tank with a porous medium was built and tested to compare sensor response from a prototype probe and a commercial EC datalogger. EC BTCs were measured under two scenarios: (1) conditions with deionized water (DI) circulating through the tank as the background solution, and (2) conditions with a simulated groundwater solution with elevated EC circulating through the tank as the background solution. BTCs produced agreement between EC recorded by the commercial logger and dipole resistance measurements for both the rising and falling limbs of BTCs. Results indicated the dipole resistance sensor was not capable of resolving fine changes in EC that occurred during breakthrough. A calibration of all *in situ* measurements from the experiments with porous medium confirmed the simulated groundwater experiments were subject to significantly less variability than the deionized water experiments. The calibration applied to the simulated groundwater measurements produced BTCs that matched very closely with those recorded by the commercial logger.

Two field trials were also conducted during ISCO injections at contaminated sites where probes were installed in existing monitoring wells. The field trials did not successfully correlate dipole resistance sensor measurements with oxidant concentration. Observations from the second trial indicated the dipole sensor measurements correlated with EC of water samples.

This work has provided a theoretical representation of two-wire dipole resistance sensor response to EC and has verified expected results through laboratory experiments. It has analyzed the influence of temperature and choice of fixed resistors on two-wire dipole resistance sensor readings, has extensively tested sensor response to EC during static cell and BTC experiments, and has displayed the prototype probe is capable of indicating the presence of injected reagents that have an EC signature. Further research avenues include pilot-scale testing in the field and developing a design for use with a direct-push rig.

Acknowledgements

I would like to thank my thesis advisor Neil Thomson for giving me the opportunity to complete this degree and also for providing flexibility with regards to working arrangements. In addition to having the chance to work on a very interesting project, the experience of studying at Waterloo has provided me with many opportunities through the knowledge I have gained and the people I have met, and I will always be grateful for that. Thanks to Bruce Tunnicliffe and Rick MacGregor for their interest in this project and willingness to support research; I hope the end result of this work will benefit you as it has benefited me.

The technical staff at Waterloo play an important role in graduate research and I owe many people thanks for their contributions to this project. In particular, Terry Ridgway was instrumental in helping me in the initial design phases, while Mark Sobon, Mark Merlau, Paul Johnson, and Bob Ingleton all provided valuable assistance during laboratory and field experiments. I am also grateful for members of the Soil and Groundwater Research Group at Waterloo, in particular Tyler Gale, Mahsa Shayan, Angela McIsaac, and Michelle Cho for their assistance with field work.

Above all, I would like to thank my loving wife Krista and the rest of my extended family for their continued support and enthusiasm for all things I have ever undertaken during my life.

This research was funded by an NSERC Industrial Postgraduate scholarship in partnership with Vertex Environmental Inc., an NSERC Discovery grant awarded to Dr. Neil Thomson, and the American Petroleum Institute (API). I am also grateful for the in-kind support provided by WESA and SNC-Lavalin.

Dedication

for Krista

Table of Contents

Author's Declaration.....	ii
Abstract.....	iii
Acknowledgements.....	v
Dedication.....	vi
Table of Contents.....	vii
List of Figures.....	x
List of Figures (Continued).....	xi
List of Figures (Continued).....	xii
Appendix Figures.....	xiii
List of Tables.....	xiv
Appendix Tables.....	xiv
List of Abbreviations.....	xv
Chapter 1: Introduction.....	1
1.1 General Introduction.....	1
1.1.1 Previous work monitoring reagent injections.....	3
1.1.2 Advantages of <i>in situ</i> monitoring.....	3
1.2 Objectives.....	5
1.2.1 Research focus.....	5
1.3 Background.....	5
1.3.1 Parameters of interest.....	5
1.3.2 Conceptual model of electrical conductivity breakthrough.....	6
1.3.3 Electrical conductivity theory.....	7
1.3.3.1 Ionic mobility.....	10
1.3.3.2 Total dissolved solids.....	11
1.3.3.3 Ionic strength.....	11
1.3.4 Factors affecting <i>in situ</i> measurements.....	12
1.3.5 Examples of dipole resistance sensors used in environmental monitoring.....	13
1.4 Thesis Overview.....	14
Chapter 2: Probe Design.....	18
2.1 Design Constraints and Considerations.....	18
2.2 Material Selection.....	19
2.3 Prototype Sensor Designs.....	20
2.3.1 Temperature sensor construction.....	20
2.3.2 Dipole resistance sensor construction.....	21
2.3.3 Probes for field installations.....	22
2.4 Data Collection.....	22
Chapter 3: Laboratory Probe Tests.....	31
3.1 Overview.....	31
3.2 Temperature Tests.....	32
3.3 Dipole Resistance Sensor Experiments.....	33
3.3.1 Static cell.....	33
3.3.1.1 Static cell with DI.....	33
3.3.1.2 Static cell with NaCl.....	34
3.3.1.3 Static cell with NaCl: Sensor response over time.....	34

3.3.1.4	Static cell with NaCl: Sensor response to change in EC	35
3.3.1.5	Probe calibrations for static cell with NaCl.....	37
3.3.1.6	Influence of fixed resistor, R_f	38
3.3.1.7	Static cell with oxidants.....	40
3.3.2	Flow cell experiments	41
3.3.2.1	Tank construction	41
3.3.2.2	Recirculating DI	42
3.3.2.3	Breakthrough experiments.....	43
3.3.2.3.1	Calibration error in handheld meter.....	45
3.3.2.3.2	Tracer injection at inlet.....	45
3.3.2.3.3	Copper wire detectors.....	46
3.3.2.3.4	Collection of ions on probe detectors	47
3.3.2.3.5	Initial flow cell experiments with porous media	48
3.3.2.3.6	Conclusions of BTC analysis	48
3.4	Conclusions	49
Chapter 4:	High Resolution Laboratory Experiments.....	71
4.1	Introduction	71
4.2	Materials and Methods	71
4.2.1	Probe construction.....	71
4.2.2	Sandbox and monitoring equipment	72
4.2.3	Electrical conductivity breakthrough tests	74
4.3	Results and Discussion	75
4.3.1	Deionized water breakthrough tests	76
4.3.2	Simulated groundwater breakthrough tests	78
4.3.3	Influence of temperature	81
4.3.4	Arrival times of EC_m and X_m	83
4.3.5	Repeatability of measurements	85
4.3.6	Probe calibrations for NeST experiments	86
4.3.7	Considerations when scaling technology to field setting	89
4.3.7.1	Ionic concentration	89
4.3.7.2	Soil characteristics.....	89
4.4	Conclusions	91
Chapter 5:	Field Trials	111
5.1	Overview	111
5.2	Field trial 1: Fergus, Ontario	111
5.3	Field trial 2: Southern Ontario.....	113
5.4	Conclusions	114
Chapter 6:	Conclusions.....	125
6.1	Review of Research Goals.....	125
6.2	Temperature Sensor Performance.....	125
6.3	Dipole Resistance Sensor Performance	126
6.4	Limitations of Designed System.....	126
6.5	Contributions	127
6.6	Future Work.....	127
6.6.1	Pilot scale field testing	127
6.6.2	Direct-push design	128
References	130

Appendices

Appendix A: Supplementary Information for Chapter 1	135
A1: Summary of Pros and Cons Related to Potential Measurement Parameters.....	135
Appendix B: Supplementary Information for Chapter 2.....	137
B1: Material Degradation with Persulfate.....	137
Appendix C: Supplementary Information for Chapter 3.....	145
C1: Initial Flow Cell Experiments.....	145
Appendix D: Supplementary Information for Chapter 4	151
D1: NeSTs Construction.....	151
D2: Silica Sand Specifications.....	154
D3: CTD-Diver Specifications	155
D4: Deionized water BTCs.....	156
D5: Simulated Groundwater BTCs.....	169
D6: Probe Calibration for Handheld Meter and CTD-Diver	182
D7: EC Temperature Corrections	184

List of Figures

Figure 1.1: Conceptual model of probe installation.....	16
Figure 1.2: EC ₂₅ against ionic strength (From Lind, 1970, p.D275).....	17
Figure 2.1: Temperature sensor constructed from BetaTherm 10K3A1 thermistor, heat shrink, and Plasti Dip rubber compound.	26
Figure 2.2: Example of constructed two-wire dipole resistance probe.....	27
Figure 2.3: Field probe schematic. Temperature sensor shown was inserted in rubber stopper, which was force fit into the drilled hole. Other designs used temperature sensor fit directly in PVC. Sensors sealed with marine epoxy (LePage, Model 10-00397) and silicone (GE Model SE2184 24C).....	28
Figure 2.4: Wiring Diagram for resistance sensors.....	29
Figure 2.5: Expected relationship between dipole sensor reading (X) and probe conductance (mS) for various fixed resistors. Probe conductance is calculated as the inverse of resistance measured at the dipole sensor ($1/R_s$). For a dipole resistance sensor, R_s is related to EC through a second-order relationship.	30
Figure 3.1: Comparison of constructed temperature sensor to Schlumberger Mini-Diver reference, sensors submerged in DI water.....	56
Figure 3.2: Influence of temperature on dipole resistance sensor readings in DI static cell.....	57
Figure 3.3: Dipole resistance sensor response to static cell EC solutions. Each 1000 mL beaker contained 400 mL solution volume. Temperature only shown for Beaker 1; temperature records for other beaker were nearly identical. Initial temperatures for Beakers 1-5 ranged between 17.3-18.1 °C.	58
Figure 3.4: Location of thermistors of open water tests and example of different sizes and orientations of resistance sensors	59
Figure 3.5: Static cell NaCl experiments with varied EC arranged by probe. Experiments A-D shown.....	60
Figure 3.6: Static cell NaCl experiments with varied EC arranged by experiment. Experiments A-D shown.	61
Figure 3.7: EC calibrations to static cell data where Probe Conductance is calculated as $1/R_s$. Second order polynomial fit is in form $ax^2 + bx + c$. 24.9 kΩ fixed resistor (R_f) used for all data shown. For Probes 4-7, only fit for 4C is shown.....	62
Figure 3.8: Example of influence of different resistors, NaCl beaker experiments E and F	63
Figure 3.9: EC calibrations to static cell experiments with varied fixed resistors, R_f . Probe Conductance is calculated as $1/R_s$. Second order polynomial fit for Experiments E and F is in form $ax^2 + bx + c$	64
Figure 3.10: Static cell with sodium persulfate arranged by probe. Experiments G-H shown.....	65
Figure 3.11: Static cell with sodium persulfate arranged by experiment. Top panel shows experiment G, bottom panel shows experiment H.	66
Figure 3.12: Static cell with potassium permanganate. Experiment I shown.	67
Figure 3.13: Close-up of flow system used for initial flow cell experiments.....	68
Figure 3.14: Experimental results for recirculation of DI water collected during initial flow cell experiments	69
Figure 3.15: Example of BTC results from initial flow cell experiments, BTC-A shown	70
Figure 4.1: Schematic of flow through NeST system driven by peristaltic pump. Diagram shows case for water recirculated from outlet reservoir back to upstream reservoir. BTC experiments pumped water from outlet reservoir to waste. Adapted from (Bowen, 2010, p.18).....	98

List of Figures (Continued)

Figure 4.2: CTD-Diver bundled with dipole resistance sensor and thermistor for NeST breakthrough experiments. Sampling tube was not used during BTC experiments.	99
Figure 4.3: Example of BTCs measured during DI BTC experiments. BTC11 shown in top panels, BTC18 shown in bottom panels. Hollow blue points indicate records collected by the CTD-Diver, solid red shows data collected by the dipole resistance sensor. The panels on the right show the raw CTD-Diver (mS/cm) and dipole sensor (X) data. Panels on the left show data normalized to the peak value measured by each probe.	100
Figure 4.4: Example of dipole resistance sensor response to BTCs with irregular shapes. BTC10 shown in top panels, BTC15 shown in bottom panels. Hollow blue points indicate records collected by the CTD-Diver, solid red shows data collected by the dipole resistance sensor. The panels on the right show the raw CTD-Diver (mS/cm) and dipole sensor (X) data. Panels on the left show data normalized to the peak value measured by each probe. The raw CTD-Diver data shows examples where EC breakthrough did not follow a symmetrical curve.	101
Figure 4.5: Example of BTCs measured during simulated groundwater experiments. BTC43 shown in top panels, BTC49 shown in bottom panels. Hollow blue points indicate records collected by the CTD-Diver, solid red shows data collected by the dipole resistance sensor. The panels on the right show the raw CTD-Diver (mS/cm) and dipole sensor (X) data. Panels on the left show data normalized to the peak value measured by each probe.	102
Figure 4.6: Influence of temperature correction on CTD-Diver measurements for BTC 9. The hollow blue points show the raw CTD-Diver measurements, which were collected using as values referenced to 25 °C. The solid red points show the CTD-Diver data referenced to the <i>in situ</i> measurement temperature.	103
Figure 4.7: Example of error introduced by changing temperature during breakthrough.	104
Figure 4.8: Calibrated NeST data. Top panel shows dipole sensor peak, X_m , against CTD-Diver peak, EC_m . Probe conductance is calculated as inverse of sensor resistance (R_s). Second order polynomial fit is in form $ax^2 + bx + c$, where $x = EC_m$ and $y =$ probe conductance.	105
Figure 4.9: All NeST BTC data shifted according to gap between each peak. Probe conductance is calculated as inverse of sensor resistance (R_s). Second order polynomial fit is in form $ax^2 + bx + c$, where $x =$ CTD-Diver readings and $y =$ probe conductance. Each fit was produced by manually selecting 14 points from each data series that represented average sensor response.	106
Figure 4.10: Example of BTCs measured during DI experiments. BTC11 shown in top panels, BTC18 shown in bottom panels. Hollow blue points indicate records collected by the CTD-Diver, solid red shows data collected by the dipole resistance sensor. The panels on the left show the raw CTD-Diver (mS/cm) and dipole sensor (X) data. Panels on the right show the data calibrated to the fit from Figure 4.9.	107
Figure 4.11: Example of irregularly shaped BTCs measured during DI experiments. BTC10 shown in top panels, BTC15 shown in bottom panels. Hollow blue points indicate records collected by the CTD-Diver, solid red shows data collected by the dipole resistance sensor. The panels on the left show the raw CTD-Diver (mS/cm) and dipole sensor (X) data. Panels on the right show the data calibrated to the fit from Figure 4.9.	108

List of Figures (Continued)

Figure 4.12: Example of BTCs measured during simulated groundwater experiments. BTC43 shown in top panels, BTC49 shown in bottom panels. Hollow blue points indicate records collected by the CTD-Diver, solid red shows data collected by the dipole resistance sensor. The panels on the left show the raw CTD-Diver (mS/cm) and dipole sensor (X) data. Panels on the right show the data calibrated to the fit from Figure 4.9.....	109
Figure 4.13: Effect of ionic concentration on EC, taken from (Klein and Santamarina, 2003). EC peaks correspond to concentrations of ~6 mol/L (350 g/L) NaCl, 3 mol/L CaCl ₂ (333 g/L), 4.5 mol/L NaOH (180 g/L).....	110
Figure 5.1: Field Trial 1, Fergus, ON, Site Plan	116
Figure 5.2: Persulfate BTCs from Field Trial 1, taken from Greer et al.,(2011). The y-axis of each plot shows persulfate concentration in g/L.	117
Figure 5.3: Persulfate vs. EC for all Fergus samples (Greer et al., 2011).....	118
Figure 5.4: Persulfate vs. pH for all Fergus samples (Greer et al., 2011).....	119
Figure 5.5: Correlation of Persulfate with EC, RW8.....	120
Figure 5.6: Particulate material collected on detector surfaces.....	121
Figure 5.7: Field trial 2 site plan (adapted from Holtze, 2011).....	122
Figure 5.8: Schematic of probe installed at Field Site 2	123
Figure 5.9: Field trial 2, probes installed at MW-4, MW-107, and MW-202.....	124

Appendix Figures

Figure B1: Material tests with persulfate, visual results for samples 1 and 2.....	138
Figure B2: Material tests with persulfate, visual results for samples 3 and 4.....	139
Figure B3: Material tests with persulfate, visual results for samples 5 and 6.....	140
Figure B4: Material tests with persulfate, visual results for samples 7 and 8.....	141
Figure B5: Material tests with persulfate, visual results for samples 9 and 10.....	142
Figure B6: Material tests with persulfate, visual results for samples 11 and 12.....	143
Figure B7: Material tests with persulfate, visual results for sample 13.....	144
Figure C1: BTC-A to BTC-E collected during initial flow cell experiments. Dipole resistance measurements shown on left axis of left and right panels. EC measurements corresponding to the same tank location as dipole measurements shown on right axis of left and right panels. Start of injection defined as time when feed solution at inlet tube switched to NaCl.	148
Figure C2: Example of tailing BTC (Labaky, 2004, p.118)	149
Figure C3: Removal of noise caused by alternating current power source (Campbell Scientific, 2011a, p.55).....	150
Figure D1: 9 holes (1.25 cm diameter) drilled in upstream end of main reservoir	152
Figure D2: Approximately 400 1/16 inch holes drilled in downstream end of main reservoir	152
Figure D3: Nitex® screen.....	153
Figure D4: Completed NeST system used for BTC experiments described in Chapter 4	153
Figure D5: Grain size analysis for Barco Silica Sand #49*	154
Figure D6: BTC 16, 12, and 26.....	156
Figure D7: BTC 32, 33, and 14.....	157
Figure D8: BTC 13, 7, and 18.....	158
Figure D9: BTC 9, 11, and 35.....	159
Figure D10: BTC 34, 15, and 6.....	160
Figure D11: BTC 36, 19, and 20.....	161
Figure D12: BTC 10, 27, and 8.....	162
Figure D13: BTC 31, 25, and 28.....	163
Figure D14: BTC 22, 29, and 1.....	164
Figure D15: BTC 23, 30, and 5.....	165
Figure D16: BTC 17, 24, and 21.....	166
Figure D17: BTC 3, 37, and 2.....	167
Figure D18: BTC 4.....	168
Figure D19: BTC 72, 73, and 76.....	169
Figure D20: BTC 75, 74, and 69.....	170
Figure D21: BTC 70, 71, and 68.....	171
Figure D22: BTC 61, 62, and 57.....	172
Figure D23: BTC 59, 60, and 56.....	173
Figure D24: BTC 63, 65, and 58.....	174
Figure D25: BTC 64, 55, and 67.....	175
Figure D26: BTC 66, 48, and 53.....	176
Figure D27: BTC 54, 52, and 47.....	177
Figure D28: BTC 46, 51, and 39.....	178
Figure D29: BTC 44, 42, and 50.....	179
Figure D30: BTC 41, 40, and 45.....	180
Figure D31: BTC 43, and 49.....	181

List of Tables

Table 2.1: Materials exposed to persulfate and examined for degradation. H = 2% persulfate solution added to sample, L = 1% persulfate solution added.	25
Table 3.1: Sensor construction details for static cell experiments A-I	51
Table 3.2: Static cell experiment details	52
Table 3.3: Second order polynomial fit to static cell probe experiments in form $y = aEC^2 + bEC + c$ where a, b, and c are constants.	53
Table 3.4: Sensor construction details for BTC experiments BTC-A – BTC-E	54
Table 3.5: Details of select open water BTC experiments.....	55
Table 4.1: Simulated groundwater ionic concentrations in comparison to other potable water. Solution Type A was used for BTC39-44, Solution Type B used for BTC45-76.....	93
Table 4.2: Summary of data collected during NeST BTC experiments.....	94
Table 4.3: Summary statistics comparing variability in CTD-Diver peaks, EC_m	97
Table 5.1: Probe construction details for field trials	115

Appendix Tables

Table C1: Controlled variables in open water BTC experiments	147
Table C2: Variability in handheld conductivity measurements during open water BTC experiments....	147
Table D1: Properties of silica sand in NeST*	154
Table D2: Product specifications for CTD-Diver (Schlumberger Water Services, 2010, p.12).....	155
Table D3: Summary of CTD-Diver accuracy. Tests A and C used the specific conductivity setting where measurements are referenced to 25°C while Test B used the conductivity setting where measurement are not corrected. Summary statistics for Test B were calculated after the EC values were converted to EC_{25} using Eq.(5).	183
Table D4: Example of percent difference calculation for BTC9. Summary statistics were calculated using each measurement for BTC9 and subsequent spreadsheet calculations described in Appendix D7.....	185

List of Abbreviations

μ	ionic strength
$\frac{d}{A}$	cell constant
A	cross-sectional area of electrode plates
BTC	electrical conductivity breakthrough curve
d	distance between electrode plates
DI	deionized water
EC	electrical conductivity (mS/cm)
EC_{25}	electrical conductivity (mS/cm) of a solution measured at 25 °C
$EC_{electrolyte}$	electrical conductivity (mS/cm) of a static cell electrolyte solution
EC_{bulk}	electrical conductivity (mS/cm) measured <i>in situ</i> in contact with porous medium and porewater
EC_m	peak measured at CTD-Diver during BTC (mS/cm)
EC_{ref}	electrical conductivity (mS/cm) at reference temperature, typically 25 °C
EC_s	potassium chloride standard of known electrical conductivity (mS/cm)
EC_T	electrical conductivity (mS/cm) at measurement temperature
F	formation factor
$NaCl$	sodium chloride
$NeSTs$	nested storage tank system
R	resistance according to Ohm's Law (Ω)
R_f	fixed resistor (Ω)
R_s	resistance measured at dipole sensor (Ω)
$Sim\ GW$	simulated groundwater
S_a	specific surface area
TDS	total dissolved solids (mg/L)
X	two-wire dipole resistance sensor measurement (unitless)
X_m	peak measured at two-wire dipole resistance sensor during BTC (unitless)

Chapter 1: Introduction

1.1 GENERAL INTRODUCTION

Groundwater contamination sources are varied and include current and past agricultural and industrial activities. In situations that involve point-sources, the contaminants are typically distributed between source zones and plumes. When toxic substances are present, the resulting subsurface contamination may exceed regulatory standards prompting the need for clean-up of both the source zone and mobile dissolved phase plume.

For deeper sources, removal of contaminants through excavation proves to be impractical due to high costs (Davis, 1997) which necessitates an *in situ* treatment approach. This is particularly important if non-aqueous phase liquids (NAPLs) are present. In the 1980's and early 1990's, groundwater pump and treat was used almost universally as a clean-up technology to remove mass from the source zone and to contain the dissolved phase plume. While pump and treat has been shown to work well for plume containment, it is very ineffective for mass removal from source zones. The limitations of pump and treat prompted the development and testing of other mass extraction technologies such as soil vapor extraction and *in situ* air sparging that were deemed to be more cost effective (Mackay and Cherry, 1989; Krembs et al., 2010).

An alternative to mass extraction technologies are those that provide *in situ* mass destruction. The objective of an *in situ* mass destruction technology is to create reaction conditions where contaminants are immobilized or degraded into non-toxic end products when they are contacted or intercepted. A commonly used method to create the required reactive zone is to distribute reagents in the subsurface by a gravity-fed or pressurized injection. Both microbial and chemical reactions can be used to treat a wide range of organic, inorganic, and metallic contaminants. For efficient and effective treatment, the selected reagents must be delivered into the *in situ* reactive zone and the resulting biogeochemistry must be close to optimal for the desired reaction(s) to occur.

The injection and distribution of treatment reagents is a challenging task due in part to the uncertain subsurface geological and contaminant characteristics, and the role of heterogeneities that exists at all spatial scales. Hydraulic conductivity is perhaps the most critical property since

this will impact the ease at which a reagent can be delivered. Groundwater flow characteristics can affect reactive zones by controlling the rate at which the reagent will spread and mix with the groundwater. Failure to properly deliver the reagent and provide acceptable reactive zones is the major cause of failure for many types of treatment technologies. For *in situ* chemical oxidation (ISCO) in particular, inadequate distribution of oxidants caused by low permeability zones, heterogeneity, and oxidant consumption by aquifer materials and/or DNAPLs has resulted in poor remediation performance (Siegrist et al. (eds), 2011, p.21).

To mitigate failures caused by poor reagent distribution, recent trends have shown consultants and researchers investing more time, effort, and money on monitoring programs before, during, and after injection events (Cavé et al., 2007; Halihan et al., 2011; Harte et al., 2012). This research effort is focused on the development of cost-effective field methods to aid in our understanding of reagent delivery capabilities at actual contaminated sites. Specifically, the aim is to develop a suite of instruments which can be used to provide feedback on remediation progress and effectiveness during *in situ* treatment.

Monitoring the subsurface distribution of injected reagents is a difficult task because the acquisition of high resolution data, both spatially and temporally, often results in unacceptably high costs. Although multi-level wells have been shown to provide accurate vertical discretization at heterogeneous sites (Einarson, 2006, p.5), scientists and engineers often resort to sampling programs planned around existing screened wells at a site. A significant risk to this approach is apparent reagent delivery; a reagent may be assumed to be delivered over the entire vertical length of a well screen when in reality the reagent concentration mixed in a well is from an isolated location. Monitoring screened wells for reagent breakthrough can lead to diminished remediation performance or even failure when hydraulic fracturing and short-circuiting during pressurized injections lead to preferential flow paths intersecting with monitoring well screens (Suthersan et al., 2011).

In addition to considering well-type, remediation specialists must decide on an optimal combination of field and laboratory analyses to track injected reagents. Several types of commercial field kits are available for directly determining the presence of chemical oxidants or providing surrogate parameters such as pH, dissolved oxygen, alkalinity, iron, sulfate, chloride, manganese, potassium, sodium, etc. as a visual indication of concentration. In addition, water

samples are regularly tested for parameters such as pH, electrical conductivity (EC), temperature, oxidation-reduction potential (ORP), and dissolved oxygen using handheld field meters (Palaia et al., 2011, p.491). Field mass spectrophotometers are another instrument available to practitioners for providing close to real-time data during injection events (Halihan et al., 2012). Although traditional laboratory sampling approaches are always expected to be a staple of monitoring programs at contaminated sites, continually improving field measurement techniques provide operational economies that can be exploited by project managers. As a result, multiple efforts are currently pushing to develop technologies which can enhance monitoring capabilities while lowering costs (Cavé et al., 2007; Halihan et al., 2011; Harte et al., 2012, etc.).

1.1.1 Previous work monitoring reagent injections

Various geophysical methods have been employed to monitor reagent injections at contaminated sites. Nyquist et al. (1999) used surface direct current (DC) resistivity to monitor a permanganate injection recirculated between two horizontal wells, while Halihan et al. (2011) used electrical resistivity imaging (ERI) to monitor a pilot-scale ISCO sodium permanganate injection-extraction procedure with vertical wells. Harte et al. (2012) used borehole DC resistivity and surface electromagnetic (EM) methods to monitor the distribution and transport of a full-scale sodium permanganate injection at a site previously treated by ISCO. In addition, Lane et al. (2006) monitored the injection of vegetable oil emulsion (VOE) as a carbon substrate using a combination of cross-hole radar to track the reagent and conventional geophysical tools to characterize the site. These studies showed various degrees of success in mapping the distribution of injected reagents when background surveys were compared to surveys conducted at various intervals after the injections.

1.1.2 Advantages of *in situ* monitoring

In contrast to geophysical methods, this research is focused on monitoring approaches that can be used to provide feedback on the distribution of reagents in real-time, or close to real-time. Real-time data collection can allow remediation specialists to optimize injection programs on the fly, rather than waiting until an injection is complete before undertaking a geophysical survey. *In situ* monitoring devices have an advantage over the methods described above because they can provide continuous data without requiring extensive site visits and labour, which is typically the

largest component of monitoring costs (Palaia et al., 2011, p.497). In cases where an injected reagent has an electrically conductive signature, EC measurements can be used to monitor reagent distribution. *In situ* EC measurements directly measure changes in pore water EC, which can be used to infer the presence of an injected reagent. This can result in significant cost-savings if devices can be deployed efficiently without damaging probes. A trade-off when comparing geophysical methods to direct *in situ* approaches is measurement resolution; geophysical measurements can provide high-resolution data spatially, but are limited temporally by the number of site visits that are made. Conversely, *in situ* measurements can provide continuous temporal measurements, but are limited to the locations where measurement devices are installed. As a result, the benefits of *in situ* measurements are maximized when monitoring devices can record data at multiple depths and can also be installed in several locations surrounding injection points.

When considering ISCO remediation programs, a significant problem associated with monitoring oxidants *in situ* is the high oxidation potential of the reagent. Although several commercial transducers and probes currently available can monitor the chemical and physical signatures of ISCO injections, there is substantial risk that monitoring equipment may be damaged when it comes in contact with an oxidant. Due to the high cost of these probes and transducers, the benefits that real-time monitoring data can provide during an ISCO event are often overlooked.

Early efforts to develop a probe for *in situ* monitoring of oxidant injections are described by Cavé et al. (2007) where simple EC and ORP sensors attached to a polyvinylchloride (PVC) conduit were installed *in situ* by jetting. The study found a strong correlation between sensor response and the presence of permanganate injected into a sand aquifer during an experimental field test confined to a sheet pile box. In particular, the EC sensors not only responded to the presence of oxidant, they also showed a linear relationship between sensor response and potassium permanganate (KMnO₄) concentration.

These results indicate promise for deploying simple EC probes to monitor full-scale reagent injections, although detailed analysis of how these sensors respond to changes in the factors that influence EC is not currently available.

1.2 OBJECTIVES

1.2.1 Research focus

This research is focused on the development and testing of a suite of instruments that can be used to characterize reagent delivery progress and enhance the efficacy of *in situ* treatment systems. Existing characterization approaches are often time consuming and costly, and often provide data that is spatially and temporally limited. As a result, this work is focused on providing near real-time field data describing reagent delivery and subsequent transport to allow remediation programs to be optimized. Real-time feedback has the potential to decrease both treatment time and operational costs for remediation programs while providing a greater degree of understanding about reagent delivery at sites and whether or not acceptable reactive zones can be expected. The information can be used to prevent over-design of *in situ* treatment systems or temper treatment expectations.

The end goal of this project is to design a probe device that can be strategically installed as an array within and surrounding an *in situ* treatment zone as shown in Figure 1.1. Each device would be installed with a suitable direct-push method (vibrating hammer or Geoprobe) depending on the required depth. The device would be equipped with a variety of monitoring sensors designed to collect appropriate data for the chemical reagent investigated. A key goal of this research effort is to design a system that is both robust and inexpensive. To facilitate ease of use and rapid assessment, the spatial distribution of devices should provide information that can be used to vertically discretize reagent distribution over large areas. This effort has focused on designs that are suitable for use during ISCO, but could also be used with other reagents.

1.3 BACKGROUND

1.3.1 Parameters of interest

Sensors which directly measure reagent chemicals or byproducts have not been studied in this research. A brief literature search confirmed few to no commercial sensors have been developed that directly measure reagents injected for remediation. If available, it is unlikely commercial sensors would meet project goals of low-cost, robustness, and potential for installation with a

direct-push system. In addition, a sensor specific to a reagent component or byproduct could limit the design to a single reagent. This research is focused on a system which would be robust enough to monitor several types of reagents and has concentrated on measurement parameters that indicate the presence of an injected reagent, but do not directly measure a specified chemical compound. This approach allows more generalized sensors to be used or constructed which significantly reduces overall costs.

There are several surrogate physical and chemical parameters which can provide valuable information about the presence and concentration of an injected reagent without directly measuring the reagent itself. Parameters such as EC, temperature, ORP, and pH provide various degrees of information specific to a reagent.

Temperature and EC were selected as parameters of focus for this research. These parameters were chosen because sensors that were low cost and small enough for a drill rod design could easily be constructed. Reagents such as chemical oxidants are often packaged as dry salts that dissociate when mixed in solution. The resulting reagent solutions have a high ionic concentration signature that can be detected by an EC measurement. EC measurements are dependent on measurement temperature, making the inclusion of a temperature sensor a logical addition. Details describing the sensor selection process and why specific parameters were excluded from prototype designs can be referenced in Appendix A1.

1.3.2 Conceptual model of electrical conductivity breakthrough

A conceptual model of sensor response during and after a reagent injection can be developed for the probe arrangement shown in Figure 1.1, assuming each measurement point contains an EC and temperature sensor. For a single monitoring point, breakthrough of reagent concentration is expected if the probe is installed within the injection zone of influence. The monitoring point will reach a breakthrough of reagent concentration at some time during or after the injection; if ambient groundwater flow conditions exist, reagent concentration at the monitoring point will then decrease.

For the scenario of an ISCO injection, the conceptual model can be extended to consider EC breakthrough because oxidants are typically mixed as salt solutions that have elevated EC. A

baseline EC reading at a monitoring point should increase to a maximum value, which would correspond to the maximum concentration of oxidant, and then return to background levels after the injected slug has passed. This conceptual model ignores natural characteristics of hydrogeologic media and physical and chemical impacts of chemical oxidation. Natural gradients at a location may be too low to move an injected slug away from a monitoring point, reaction by-products may form that block pore spaces and alter transport of oxidant, and previously immobile pore spaces containing high conductivity solutes may become mobilized, altering EC readings. In addition, reactions between contaminants, oxidants, and natural groundwater constituents have the potential to alter observed EC.

Although the conceptual model ignores some complex factors, it is understood that monitoring locations in the zone of influence surrounding an ISCO injection point generally experience an increase in EC. If groundwater at the monitoring point is mobile and/or *in situ* conditions cause reactions which use charged ions to produce stable compounds, the EC increase would be followed by a decrease in EC at a time after the oxidant injection.

1.3.3 Electrical conductivity theory

Electrical conductance describes the ability of a material to allow electric current to flow through it and is inversely related to the medium's resistance to transmitting current. Electrical conductance and resistance are related to the electric current travelling through a medium and the electrical potential applied to create the current by Ohm's Law:

$$R = \frac{V}{I} = \frac{1}{L} \quad (1)$$

where R is resistance in ohms, I is electric current in amps, V is electric potential in volts, and L is electrical conductance in microsiemens (Miller et al., 1988 ,p.1; McCleskey, 2010, p.4).

Electrical current can flow through solid materials such as metals, or through ionic solutions. Electrical conductance through metals is a result of electrons which can move freely between atoms, travelling through the lattice structure of the metal when an electric current is applied. Ionic conductance does not depend on the transport of electrons, but is a measure of the movement of charged ions travelling through water (McCleskey, 2010, p.3). Pure water

conducts a negligible amount of electrical current due to dissolved CO₂ from equilibrium with the atmosphere and the slight dissociation of water molecules (Robinson and Stokes, 1965, p.3). This allows calculations of conductance for electrolyte solutions to only consider dissolved ionic species and neglect the contribution from dissociated water. Water quality investigations are typically only concerned with ionic conductance, which is also the focus of this thesis.

Specific conductance (L_{sp}), preferentially called “conductivity” or “electrical conductivity” in practice today (APHA et al., 2012, p.2-52) and denoted as EC in this thesis, describes the flux of current travelling through a unit cross-section of a medium. In practice, the conductivity of an ionic solution can be measured using alternating current (AC) and a Wheatstone bridge or a conductance meter and probe (McCleskey, 2010, p.4). EC is described by the following relationship:

$$L_{sp} = EC = \left(\frac{d}{A}\right)L \quad (2)$$

where d is the distance between electrode plates, A is the cross-sectional area of the plates, and L is ionic conductance (Millero, 2001, p.101). Conductivity is reported in units of Siemens/length, where length is typically cm and Siemen is the reciprocal of ohm. Conductance is typically reported with units ohm^{-1} . Before Siemens were adopted as an official SI unit in 1972, the reciprocal of ohms was typically reported as mho (CPGM, 1972).

A conductivity probe measures conductance of a solution and then relates it to EC . Spacing and cross-sectional area of the probe electrodes are not considered individually, and the ratio (d/A) is defined as the cell constant (C). For calibration of a conductivity probe in the laboratory, the cell constant is determined using a standard potassium chloride (KCl) solution of known conductivity (EC_s). Standard solutions are measured over a range of concentrations with electrodes that have been precisely constructed and therefore have known values for d and A . When a conductivity probe is calibrated in the laboratory, the electrical conductance of the standard (L_s) is measured. EC_s is already known, allowing the cell constant to be calculated as shown in Eq. 3:

$$C = \frac{EC_s}{L_s} \quad (3)$$

where C typically has units cm^{-1} (Robinson and Stokes, 1965, p.95; APHA et al., 2012, p.2-52). The calculated cell constant allows the unknown electrical conductivity of a solution, EC_u , to be reported based on the conductance measured for the unknown solution, L_u (APHA et al., 2012, p.2-52):

$$EC_u = CL_u \quad (4)$$

Experimental results are typically reported using EC rather than electrical conductance because EC considers the contribution of the measurement device cell constant when measuring the electrical properties of ionic flux through a unit area. This allows standardized comparison of measurements made with different devices. Conductance measurements alone do not isolate the influence of the cell constant which prevents direct comparison between experimental results from different probes.

Several properties influence EC. Solution temperature, combined with the type of ions present, total concentration, mobility, and valence contribute to measured values (APHA, 2012, p.2-52). For natural waters, temperature is known to influence EC in a nonlinear relationship that is described by Millero (2001, p.303). Although many models exist, for temperatures between 3 and 47°C, this relation is commonly approximated linearly:

$$EC_T = EC_{ref}[1 + a(T - 25)] \quad (5)$$

where EC_t is the electrical conductivity (mS/cm) at temperature t (°C), EC_{ref} is the electrical conductivity at a reference temperature, typically 25 °C, and a (°C⁻¹) is a temperature compensation factor that is specific to the reference temperature (Sorensen and Glass, 1987; Hayashi, 2004; Ma et al., 2011). The literature cites multiple values for the temperature compensation factor, a , ranging from 0.0187 – 0.025, although a value of 0.0191 is commonly used (Hayashi, 2004). This value is close to the rule of thumb used in many groundwater studies where EC is assumed to change 2% per degree Celsius difference from 25°C (Robinson and Stokes, 1965, p.87).

1.3.3.1 Ionic mobility

As mentioned above, EC is a function of solution temperature as well as the type and concentration of ions in solution. This is because EC describes the movement of ions through water. Ionic mobility (u) describes the ability of an ion to move through solution. This motion is restricted according to the drag force caused by fluid viscosity and the size of the ionic particle. The mobility of an ion under an electric field of unit strength is described as:

$$u = \frac{v}{E} \quad (6)$$

where v is a constant drift velocity, and E is a unit electric field (Robinson and Stokes, 1965, p.42; Millero, 2001, p.93). The drift velocity is a terminal velocity that the ion reaches when viscous drag force from the solution is equal to the force created by the electric field. This allows Stoke's law for ionic solutes to be applied, resulting in:

$$u = \frac{1}{6\pi\eta r} \quad (7)$$

where η is solution viscosity, and r is particle radius (Robinson and Stokes, 1965, p.43; Millero, 2001, p.107). Under normal conditions, which excepts cases of high intensity or high frequency electric fields, the acceleration of the ion particle is close to instantaneous, so Newton's law that force is the product of mass and acceleration does not need to be considered to describe the movement of the ion (Robinson and Stokes, 1965, p.42). The ions travel at a constant velocity, which is a function of the particle radius and solution viscosity. The particle velocity is proportional to the electric field applied, which allows Ohm's law from Eq. (1) to be used to describe resistance to the flow of current (Robinson and Stokes, 1965, p.42). Therefore, ionic mobility describes the validity for developing the conductance term in Eq. (1), where conductance is the inverse of electrical resistance, because velocity is ultimately a function of particle radius. Eq. (7) also shows particle mass does not affect ionic movement caused by an applied electric field, explaining why conductivity is independent of this parameter.

1.3.3.2 Total dissolved solids

Total dissolved solids (TDS) in groundwater is related to EC because dissolved constituents typically carry an ionic charge. As a result, groundwater is an electrolyte solution with measurable EC (Freeze and Cherry, 1979, p.84). As reported by Davis and DeWeist (1966, p.98), the major ions Na^+ , Mg^{2+} , Ca^{2+} , Cl^- , HCO_3^- , and SO_4^{2-} typically account for greater than 90% of TDS for natural waters. This allows for a linear relationship between the two parameters:

$$TDS = k_e EC \quad (8)$$

where TDS is expressed in mg/L, EC is $\mu\text{S}/\text{cm}$, and k_e is a linear conversion factor ranging from 0.54 to 0.96 (Hem, 1970, p.67).

1.3.3.3 Ionic strength

Ionic strength is a measure of ion interactions in solution and describes the intensity of the electric field in the liquid (Snoeyink and Jenkins, 1980, p.75). For dilute solutions, ions behave independent of each other. As concentration increases, ion-ion interactions also increase which causes the activity of ions to decrease (Tchobanoglous and Schroeder, 1987, p.51). Ionic strength of a solution, a term first introduced by Lewis and Randall (1921), can be determined according to:

$$\mu = \frac{1}{2} \sum_i C_i \times z_i^2 \quad (9)$$

where C_i is molarity (mol/L), and z_i is the charge of ionic species (Snoeyink and Jenkins, 1980, p.75; Tchobanoglous and Schroeder, 1987, p.51). For non-ideal solutions, where the sum of the volumes of individual components does not equal the total volume of the mixed solution, ionic strength can be calculated by using mass per kg of water, rather than molar concentration:

$$\mu = \frac{1}{2} \sum_i m_i \times z_i^2 \quad (10)$$

where m_i is molality (mol/kg) (Freeze and Cherry, 1979, p.90). Because EC describes the ability of a solution to conduct an electric current, while ionic strength is a measure of the intensity of

the electric field acting on a solution, EC and ionic strength are naturally interrelated. Lind showed a linear relationship existed between EC_{25} and ionic strength for pure salt solutions, as shown in Figure 1.2 (1970). Figure 1.2 indicates the following relationship for solutions composed from a single compound:

$$EC_{25} = m \mu + constant \quad (11)$$

where μ is ionic strength, EC_{25} is electrical conductivity at 25 °C in $\mu\text{S}/\text{cm}$, m is the slope of the line, and the constant describes the y-intercept for each curve (Lind, 1970). In addition to the relationships produced by Lind, ionic strength is commonly related to EC for natural waters that contain many different dissolved constituents:

$$\mu \cong 1.6 \times 10^{-5} \times EC_{25} \quad (12)$$

where EC_{25} is electrical conductivity at 25 °C in $\mu\text{S}/\text{cm}$ (Snoeyink and Jenkins, 1980, p.76; Tchobanoglous and Schroeder, 1987, p.91). The relationship between ionic strength and EC also indicates that ionic strength is related to TDS. Combining Eqs. (8) and (12) gives:

$$\mu = \frac{1.6 \times 10^{-5} TDS}{k_e} \quad (13)$$

As mentioned in section 1.3.3.2, Hem found k_e for natural waters to range between 0.54 and 0.96, although values above 0.75 were typically found to be cases with high sulfate concentrations (1970, p.67). Commercial conductance/TDS meters commonly use a conversion factor of 0.64, based on data reported by Langelier (1936), resulting in:

$$\mu = 2.5 \times 10^{-5} \times TDS \quad (14)$$

1.3.4 Factors affecting *in situ* measurements

Soil properties are known to influence *in situ* EC measurements and therefore need to be considered for the probe system described in this thesis. For a sensor installed in direct contact with soil grains, pore fluid EC and temperature provide a component of the overall EC measurement, while soil characteristics account for the rest of the recorded value. Soil properties

known to influence *in situ* EC measurements include porosity, water content, soil structure, particle shape and orientation, particle-size distribution, cation exchange capacity, and wettability (Friedman, 2005).

Surface conduction of a soil has been shown to significantly contribute to EC measurements for soils with high specific surface area, S_a , when the pore fluid has low ionic conductivity. The component of the overall measurement caused by specific surface area of the soil increases as soil porosity decreases (Klein and Santamarina, 2003).

1.3.5 Examples of dipole resistance sensors used in environmental monitoring

Dipole resistance sensors have been used in several water resources applications. Studies have highlighted the benefits of high resolution EC profiling for lithologic characterization (Sellwood et al., 2005) determination of groundwater velocity at the centimetre scale (Labaky et al., 2009; Devlin et al., 2012), monitoring *in situ* moisture content (Gawande et al., 2003), and monitoring the distribution of injected oxidants (Cavé et al., 2007).

The most well-known direct-push electrical conductivity instruments are the Direct Image conductivity logging tools produced by Geoprobe (<http://geoprobe.com>). These instruments feature both dipole and four-electrode resistance sensors that are calibrated to report EC. Although Geoprobe has developed several different commercial instruments, early design discussions by Christy et al. (1994) still describe the fundamental characteristics that are true for modern Geoprobe instruments and any other type of dipole or four-electrode sensors used to measure *in situ* EC. Four-electrode sensors have two main advantages over a dipole system; conductance measured by the sensor correlates linearly with EC compared to a polynomial or power relationship for the dipole system, and four-electrode systems measure a volume that can penetrate several centimeters into soil whereas dipole systems provide a direct-contact measurement (Christy et al., 1994). The first consideration is not a significant concern because a trend line can be fit to calibration data to provide an accurate prediction of EC, rather than using the linear cell constant fit used for four-electrode sensor calibration. However, direct contact measurements are a limitation for dipole sensors that are used *in situ*; because the sensor is only providing a contact measurement, there is a risk geologic media could obstruct the device and prevent it from providing a representative measurement of pore water EC.

Limitations of the dipole system in comparison to the four-wire system did not outweigh other design factors considered for this project. A dipole design is smaller than the four-wire set-up, requiring half the amount of wires and electrode contacts. This is a significant consideration for designs using direct-push drill rods; standard Geoprobe rods have a 3.175 cm outside diameter but only a 1.50 cm inside diameter at the threaded ends (measurement made by author).

Although Geoprobe devices have a proven track record of producing dipole devices for direct-push probes, these designs are significantly different from those used here. Geoprobe devices use a single circular contact for their devices, while this research has focused on designs using two wires. The Point Velocity Probe (PVP), first designed for a direct-push drill rod by Labaky et al. (2007) and then further refined as a design with PVC pipe by Devlin et al. (2009), uses dipole detectors very similar to the two-wire designs described here. PVPs provide a measurement of groundwater velocity by injecting a small volume of sodium chloride tracer through a port in the probe and then measuring an EC breakthrough curve at the dipole sensor. PVP measurements are used to calculate groundwater velocity based on the shape and timing of breakthrough curves and geometry of the probe. The success of PVPs accurately measuring groundwater velocity at the centimeter scale suggests this type of two-wire dipole sensor design should be capable of accurately measuring changing concentrations of electrically conductive reagents.

1.4 THESIS OVERVIEW

This study focused on laboratory testing of low-cost dipole resistance sensors that can be used for *in situ* monitoring of injected reagents, including chemical oxidants, and is meant to provide a more detailed understanding of how the probes respond to changes in pore water EC.

This thesis consists of six chapters plus references and related appendices. This first chapter introduces the topic of reagent injections at contaminated sites and discusses how enhanced monitoring during these events is required to deal with subsurface heterogeneity. It proposes research goals for this thesis to develop the early stages of a probe system capable of monitoring reagent injections *in situ*. Temperature and electrical conductivity are identified as parameters of focus. Relevant background information and theory related to *in situ* electrical conductivity measurements is included.

Chapter 2 describes the design process for a prototype probe. Design constraints and desirable probe characteristics are discussed. Construction methods, wiring diagrams, and datalogger programming are included.

Chapter 3 covers early laboratory tests to verify the effectiveness of the prototype probe design. It describes static cell and flow cell experiments analyzing temperature and dipole resistance sensor responses under various conditions. The chapter ends by identifying issues related to accurately measuring electrical conductivity breakthrough curves.

Chapter 4 summarizes a set of laboratory experiments designed to resolve the breakthrough curve issues encountered in the previous chapter. Analysis of data and sensor response characteristics are discussed.

Chapter 5 gives an overview of two separate field installations of prototype probes in existing wells during ISCO events.

Chapter 6 concludes this work by summarizing lessons learned, the current state of probe development, and potential future research.

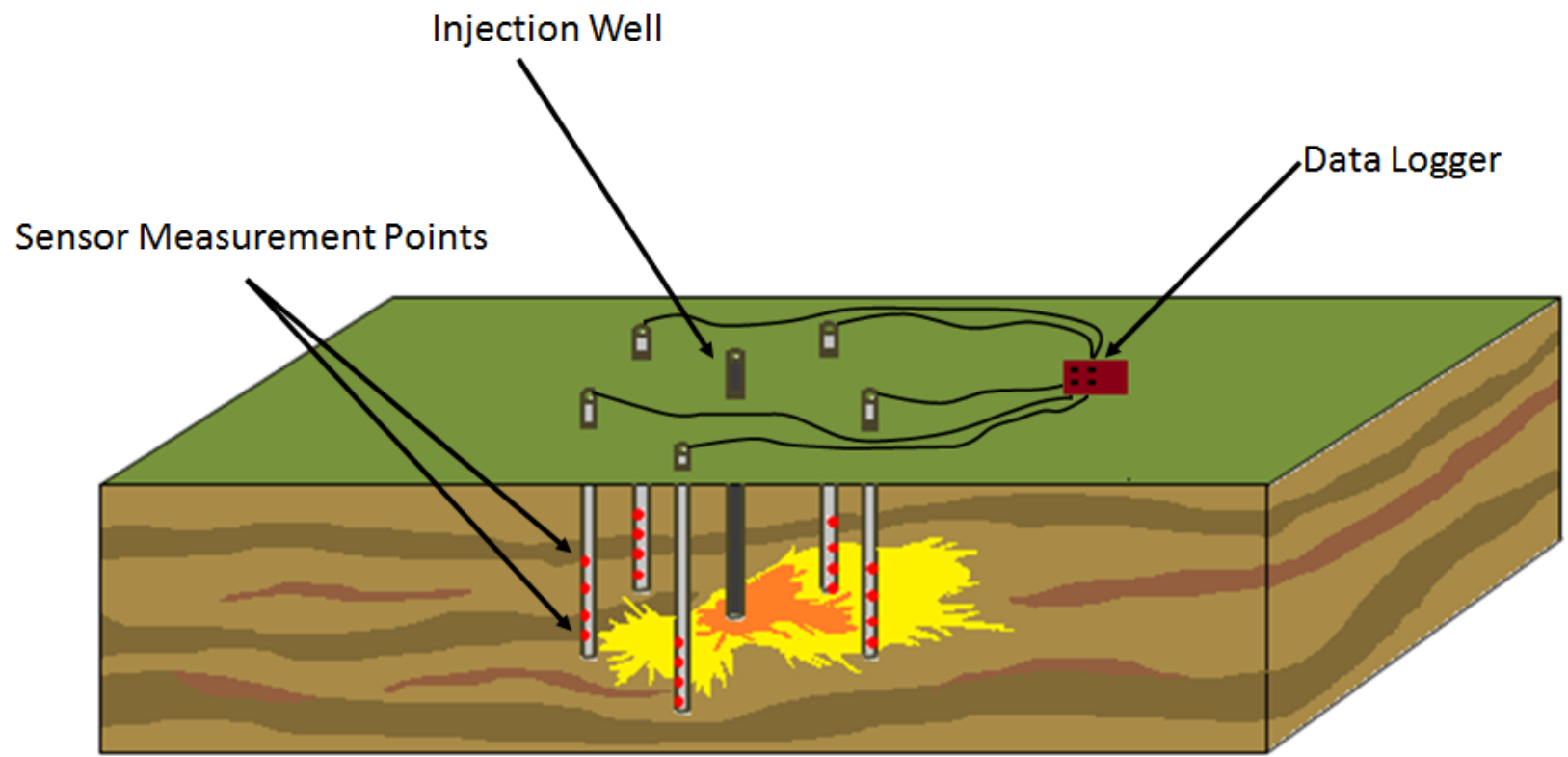


Figure 1.1: Conceptual model of probe installation

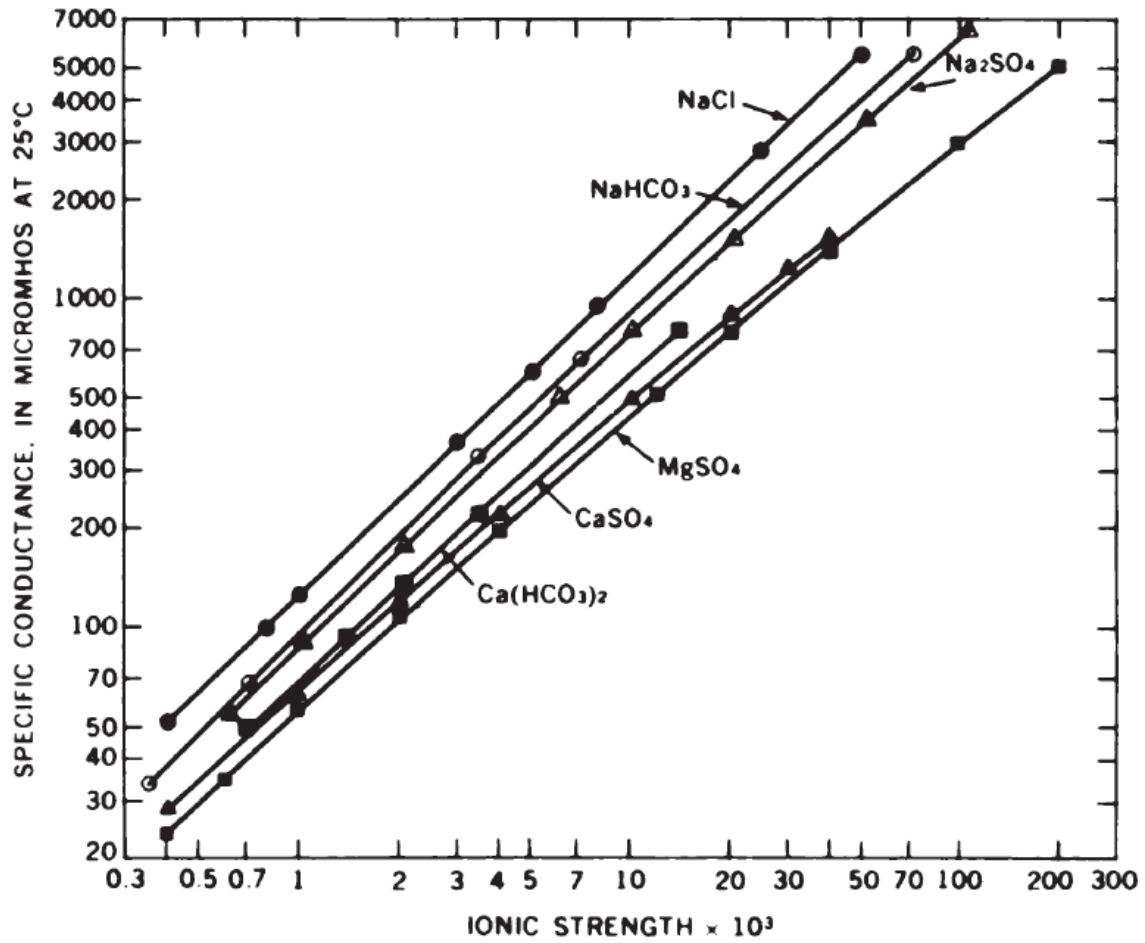


Figure 1.2: EC_{25} against ionic strength (From Lind, 1970, p.D275)

Chapter 2: Probe Design

2.1 DESIGN CONSTRAINTS AND CONSIDERATIONS

The oxidation potential of chemicals commonly used for ISCO necessitates that the developed monitoring devices used during injection events are resistant to degradation. The required degree of oxidation resistance is related to the material cost, required maintenance, and the quality of data generated. Sacrificing a piece of equipment to material degradation after a number of uses may be economical if the device is low-cost and provides information which aids in optimization of a remediation program. Cost considerations should include whether normal usage would require a device to be regularly refurbished and/or calibrated, and the amount of parts and labour required to perform maintenance. The above costs are generally related to the robustness and durability of the design. A second major design constraint related to cost is the installation method and associated equipment and labour.

Determining the presence of injected reagents, specifically chemical oxidants, does not necessarily require a value of oxidant concentration to be produced. Designs that meet research objectives range from systems that can simply indicate the presence of an oxidant, to systems that can produce a reliable oxidant concentration. Measurement uncertainty also needs to be considered. This research is focused on developing a system which can simply indicate the presence of an oxidant *in situ* using high-resolution time-series data which show differences before, during, and after an injection. This approach allows for less sophisticated sensors to be implemented thereby reducing probe costs.

Materials used for a probe system need to be capable of providing stable measurements in the presence of oxidants at injection concentrations. Ideal construction materials are those which are low cost and do not degrade in the presence of chemical oxidants.

Implementation of the probe monitoring system includes: equipment installation; monitoring before, during, and after the injection event(s); removal of equipment, and data collection, analysis and interpretation. Time saved during any of these stages reduces the overall costs of the monitoring program. Therefore, the focus is on designs where probes can be installed in existing wells or with the use of direct-push technology. For the case of direct-push

implementation, a cost is associated with using a direct-push rig to install and remove probes. Additionally, a direct push monitoring system may reduce the number of monitoring wells that need to be installed. In some cases, sites with unconsolidated media and shallow target treatment zones may allow for installation with jackhammers, preventing the need for a direct push rig.

Probe design was planned to take place in two stages:

1. PVC prototype with sensors attached to conduit. Field installations take place using existing monitoring wells or by jetting.
2. Direct-push design with sensors attached to drill rod. Field installations would take place with direct push rig or jackhammer.

The first design stage is the focus of this research effort and is meant to confirm a prototype is capable of adequately monitoring the presence of an injected reagent *in situ*. The work in this thesis has focused on testing sensor response under various conditions to verify scientific theory related to the temperature sensors and dipole resistance sensors. During this stage, consideration was given to direct push implementation and therefore, research focused on prototypes and sensors which would potentially be compatible with a drill rod.

The second design stage is largely related to construction methods and will tackle the practical challenge of using the scientific knowledge learned in the first stage to create a robust probe design suitable for industrial use. This design stage is beyond the scope of this thesis.

2.2 MATERIAL SELECTION

A basic test of how persulfate affects different materials was conducted to aid in selection of construction materials for prototype probes. The test was meant to provide a basic indication of how different materials respond to harsh environments, hence persulfate was the only reagent tested. Several materials, described in Table 2.1 were selected, cut into pieces, and placed in glass containers. The containers were then filled with 2% (20 g/L persulfate) or 1% (10 g/L persulfate) concentration sodium persulfate solutions. Material degradation was visually monitored for a period of three weeks. Tests were not conducted to determine if material properties such as tensile strength, brittleness, etc. changed. Samples were stored in a dark place to avoid photodegradation of the oxidant.

A summary of the visual monitoring results is provided in Table 2.1, further details can be referenced in Appendix B1. Several of the tested materials commonly used to construct groundwater monitoring devices such as aircraft cable, syringe tubing, polyisoprene, PVC, grade 304 stainless steel, marine epoxy and silicone did not show signs of physical degradation when exposed to 2% or 1% persulfate solutions. The most significant material degradation was observed for the copper conductor wires. The test results indicated that copper wires exposed to significant persulfate concentrations will degrade, and therefore may not be an ideal choice for field probes. Results suggested aircraft cable may be a better choice than copper wire for the exposed conductor section of a two-wire dipole resistance sensor. It was also observed the compound Ox-Gard Anti-oxidant Compound (Gardner Bender Model OX-100B) reduced degradation of copper wire caused by persulfate but was not able to fully prevent damage.

2.3 PROTOTYPE SENSOR DESIGNS

2.3.1 Temperature sensor construction

Campbell Scientific glass bead BetaTherm 10K3A1 thermistors were purchased from Campbell Scientific Canada at a cost of CAN \$15 each. The temperature sensors were prepared by clipping the wire leads of the thermistor to shorten them by approximately 2 cm and then soldering the ends to copper wire. Heat shrink (Plastronics Model PLF-100-1/16) was used to protect the bare wire. The glass bead end was dipped in Performix Plasti Dip rubber compound (Model 11601-06-C) to create a water proof seal. Figure 2.1 shows an example of a completed temperature sensor.

The probe was designed with the temperature sensor embedded in sidewall of a PVC conduit. After the temperature sensor was constructed, a hole with similar diameter as the bead end of the temperature sensor was drilled in the sidewall of a section of PVC. The temperature sensor was fit snug in the drilled hole and then sealed with marine epoxy (Marine epoxy (LePage, Model 10-00397)). However, many of the laboratory experiments were conducted with temperature sensors strapped to the outside of the PVC conduit, rather than installed in the sidewall (see Figure 3.4). This was done to reduce time required for experimental testing as the process of embedding and sealing a temperature sensor in the PVC conduit was time consuming. The expected difference

in response between temperature sensors embedded and sealed in PVC compared to those strapped to the outside is the embedded sensors would be a slightly slower response time because of the layer of epoxy used for the seal.

2.3.2 Dipole resistance sensor construction

Two-wire dipole resistance sensors were constructed using PVC pipe and copper lead wires. Typically, 18 gauge copper lead wires were used, although tests were also conducted with different gauge wires ranging from 14 to 22. Prototype probes were constructed with a variety of PVC pipe sizes, detector wire lengths, and orientations. Detectors were created using copper wire and stainless steel cable. Each detector was pulled through two holes drilled in the PVC sections to create a length of exposed detector for each wire. For most cases, a groove was filed between the two holes to allow the detector wires to lay nearly flush with the PVC surface. The copper wire leads were run through the inside of the PVC and out of the top so that they could be connected to the datalogger. Marine epoxy (LePage, Model 10-00397) was used to seal the holes where detector wires were exposed to the outside. The PVC bottom of each sensor was capped and sealed with silicone (GE Model SE2184 24C) or marine epoxy (LePage, Model 10-00397). An example of a constructed dipole sensor is shown in Figure 2.2.

Initial prototype designs used copper wire detectors. Although copper wire is not resistant to chemical oxidants, it was sufficient for preliminary laboratory tests using sodium chloride which were conducted to verify that the dipole sensors were capable of measuring solutions with varying EC. The copper wire detector design was created by simply stripping the end section of a lead wire (typically 2 – 3 cm), pulling it through the inside of the PVC section, and then tucking the detector end back into the PVC through the second drilled hole. The size of each detector was dictated by the spacing of the drilled holes. Detector wire lengths were clipped to prevent excess stripped wire lying open inside the PVC conduit.

Stainless steel cable was used in more advanced prototype designs to provide protection from chemical oxidation and corrosive environments. Short sections (<10 cm) of cable were cut to be used as detectors. The cable was attached to the copper leads using electrical wire crimp connectors. After the detectors were pulled through the inside of the PVC sections, excess wire

was trimmed. The flexibility of the stainless steel cable as well as challenges for soldering made working with stainless steel detectors more time consuming than construction using just copper.

Laboratory experiments were conducted with multiple probes, many of which had different detector geometry. The length, spacing, and orientation of detector wires were varied during probe construction to determine if changes in detector geometry would significantly alter measurement results. Detector lengths were varied between 1 and 2.5 cm, while detector spacing was varied between 0.3 and 2.5 cm. All detector geometries tested appeared to be capable of providing precise measurements. In general, it was found the smaller detector geometry of 0.3 cm spacing and 1 cm length appeared to provide the most reliable results, as there were some instances where larger detectors (e.g., 2.5 cm length, 2.5 cm spacing) did not appear to be as responsive. The effect of changing sensor geometry was investigated during initial experimentation and is not analyzed in detail in this thesis.

2.3.3 Probes for field installations

Field installations were designed with the same construction methods described above, with additional features. Field probes were constructed with a longer PVC section to allow sensors to be positioned below the water table to a depth inside monitoring wells aligning with the screened interval. Marine epoxy (LePage, Model 10-00397) was used to seal capped ends rather than silicone. Polyethylene sampling tubes were attached to the outside of the PVC conduit with zip ties to allow water sampling at the same location as sensors. The downhole ends of the sampling tubes were wrapped with Nitex screen held in place by steel wire to filter coarse particulate from samples and prevent clogging of the tube. Stainless steel cable was fastened to the top of the probes to allow them to be hung at specified depth within monitoring wells. Electrical cables for the field probes were also significantly longer to allow an above-ground connection with the datalogger. An example is shown in Figure 2.3.

2.4 DATA COLLECTION

A data acquisition system (Campbell Scientific, CR1000x) was used to communicate with the sensors and store sensor responses. This system is capable of programming several types of sensors as well as reversing signal polarity to avoid potential voltage offsets due to sensor

construction and wiring of dipole detectors. LoggerNet software (Campbell Scientific, 2011a, p.31) which allows the user to program the datalogger and collect recorded data was installed on a laptop computer (Dell Inspiron® 1420, Intel® T5450 1.67 GHz processor, 2 GB RAM).

The BetaTherm 10K3A1 thermistors used to construct the temperature sensors were the same as those used with Campbell Scientific's T109 temperature probes (Campbell Scientific, 2011b, p.1). A 24.9K Ω precision resistor, similar to the one used in the T109 temperature probe, was also used for temperature measurements. The CR1000x has several Campbell Scientific sensors and probes programmed into the logger memory which can be selected using CRBasic. This allowed the constructed temperature sensor to be programmed in CRBasic as a T109 sensor that provides output in $^{\circ}\text{C}$.

Two-wire half bridge measurements were used to measure resistance of the liquid and porous medium contacting the detector wires of each probe. These measurements relate a returned single-ended voltage to the excitation voltage as given by:

$$X = \frac{V_1}{V_x} \quad (15)$$

where V_x is the excitation voltage, V_1 is the single-ended voltage returned to the sensor, and X is unitless measurement value (CR100x User Manual, 2011, p.66). Each measurement was programmed to filter 60 Hz noise and to reverse measurement polarity to cancel any voltage offsets which could potentially influence records. Collected data was stored in ASCII tables. The ratio between excitation voltage and sensor return voltage is related to a fixed resistor, R_f , that completes the electrical circuit, and a variable resistor, R_s , which is the sensor resistance. The fixed resistor was wired between the single-ended voltage port, V_1 , and a ground. Multiple sizes of fixed resistors were tested during the experimental phase (eg: 22 Ω , 46.9 Ω , 218.2 Ω , 24.9k Ω , etc.). Preliminary testing showed a half bridge circuit produced significantly less measurement noise in comparison to single-ended voltage measurements (data not shown).

When the dipole resistance sensor is immersed in liquid, the sensor resistance, R_s , is a measurement of the electrical resistance of the fluid between the two detector wires. Figure 2.4 depicts the wiring diagram for each dipole sensor. The relationship between the measurement (X), sensor resistance (R_s), and the fixed resistor (R_f) produces:

$$X = \frac{V_1}{V_x} = \frac{R_f}{R_s + R_f} \quad (16)$$

Working with the wiring approach in Figure 2.4 and Eq. (16) is logical when collecting EC measurements because conductance is the inverse of resistance (Millero, 2001, p.101). When a sensor is wired as shown in Figure 2.4, an increase in EC results in a higher measurement value for X because R_s decreases.

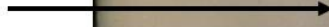
The wiring diagram shown in Figure 2.4 and the resulting relationship from Eq. (16) create an expected relationship between sensor reading (X) and probe conductance, where probe conductance is the inverse of resistance measured by the sensor (R_s). Figure 2.5 was developed from Eq. (16) and shows how X is related to probe conductance based on the choice of fixed resistor (R_f). The figure can be used to determine an appropriate R_f to wire with a dipole sensor. As mentioned in section 1.3.5, probe conductance for a dipole resistance sensor is proportional to EC based on a nonlinear fit. If the user knows the expected range of values for their EC measurements, and has already determined polynomial calibrations for different fixed resistors, an appropriate R_f can be selected so that sensor measurements do not fall on the asymptotic ends of the sensor-conductance curves in Figure 2.5. It should be noted that a noticeable reduction in measurement resolution was not observed for results in this thesis when measurements were collected close to the asymptotic ends of the theoretical curves in Figure 2.5. However, experiments were not designed to assess changes in measurement resolution and accuracy over the measurement range ($X = 0-1$).

Table 2.1: Materials exposed to persulfate and examined for degradation. H = 2% persulfate solution added to sample, L = 1% persulfate solution added.

Sample*	Description	Observed Results
1	Aircraft cable, galvanized, 1\16 x 7x7	No change for H or L
2	Aircraft cable (1), coated with Ox-Gard	No change for H or L
3	Copper conductor wire	Liquid turned blue. H: wire degraded, only small wire strands left in vial. L: wire partially degraded, some wire strands on bottom of vial.
4	Copper conductor wire, Ox-Gard	Liquid turned blue. H: wire broken in half, some small strands on bottom of vial. L: some degradation, wire strands on bottom of vial.
5	Plastic syringe tubing	No change for H or L
6	Polyisoprene non-latex condom (small piece)	H and L: Initial expansion of material, some edges splitting slightly
7	Polyisoprene non-latex condom (large piece)	H and L: Initial expansion of material, some edges splitting slightly
8	Iron nail with hardened marine epoxy on end	H and L: Significant degradation and rusting of nail, epoxy in tact
9	Schedule 40 PVC	No change for H or L
10	Schedule 80 PVC	No change for H or L
11	Grade 304 stainless steel	No change for H or L
12	Grade 304 stainless steel, coated with Ox-gard	No change for H or L
13	Nail with hardened silicone on end	Significant degradation and rusting of nail for both H and L, silicone appeared to stay in tact.

*Samples 1-8,13: 25 mL vials with teflon septa used; Samples 9-12: 250 mL jars with plastic caps

Heat shrink covering
connection between
thermistor wires and
copper wire



Rubber compound to
seal glass bead

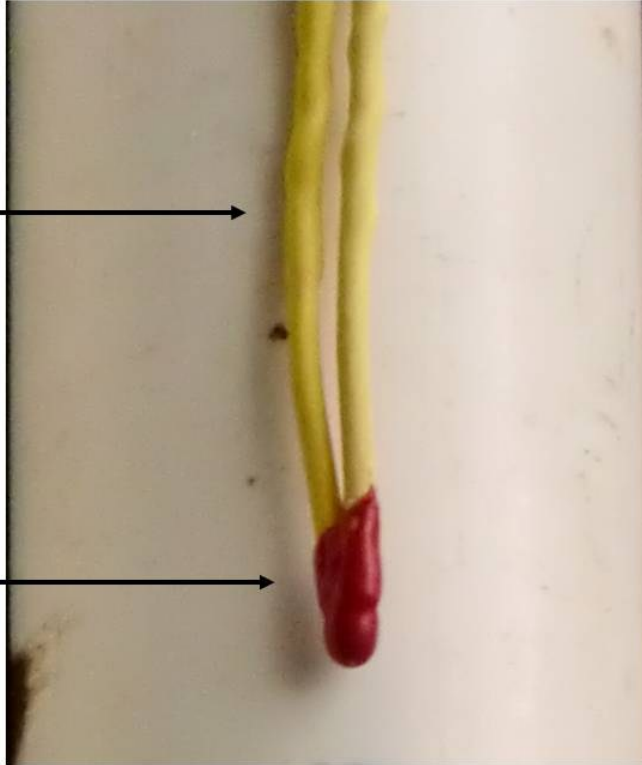


Figure 2.1: Temperature sensor constructed from BetaTherm 10K3A1 thermistor, heat shrink, and Plasti Dip rubber compound.

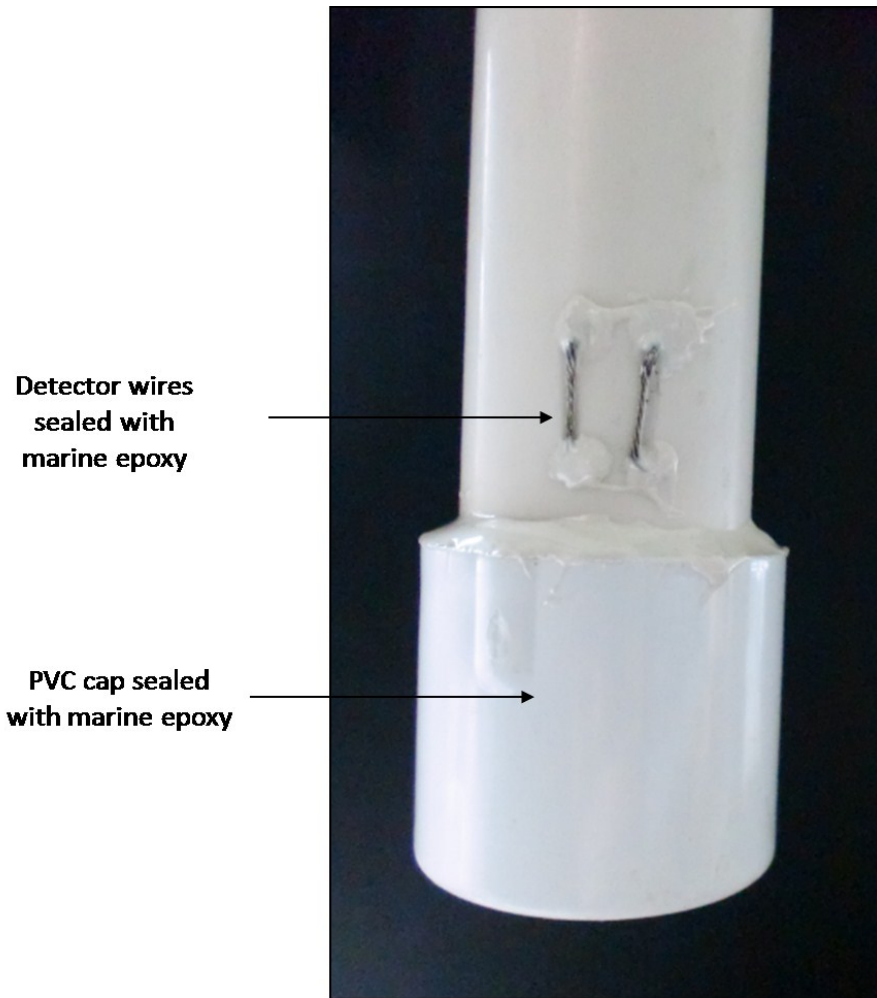


Figure 2.2: Example of constructed two-wire dipole resistance probe



Figure 2.3: Field probe schematic. Temperature sensor shown was inserted in rubber stopper, which was force fit into the drilled hole. Other designs used temperature sensor fit directly in PVC. Sensors sealed with marine epoxy (LePage, Model 10-00397) and silicone (GE Model SE2184 24C).

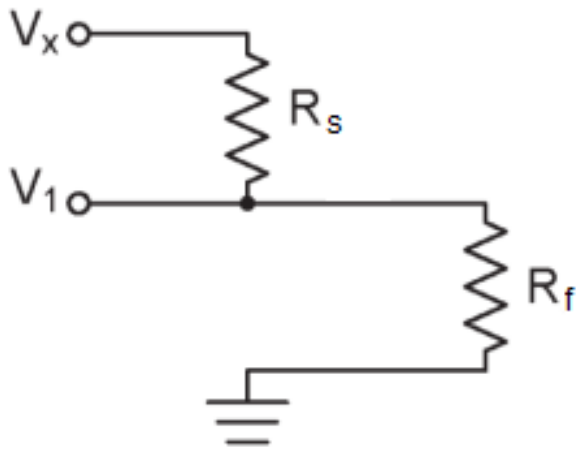


Figure 2.4: Wiring Diagram for resistance sensors.

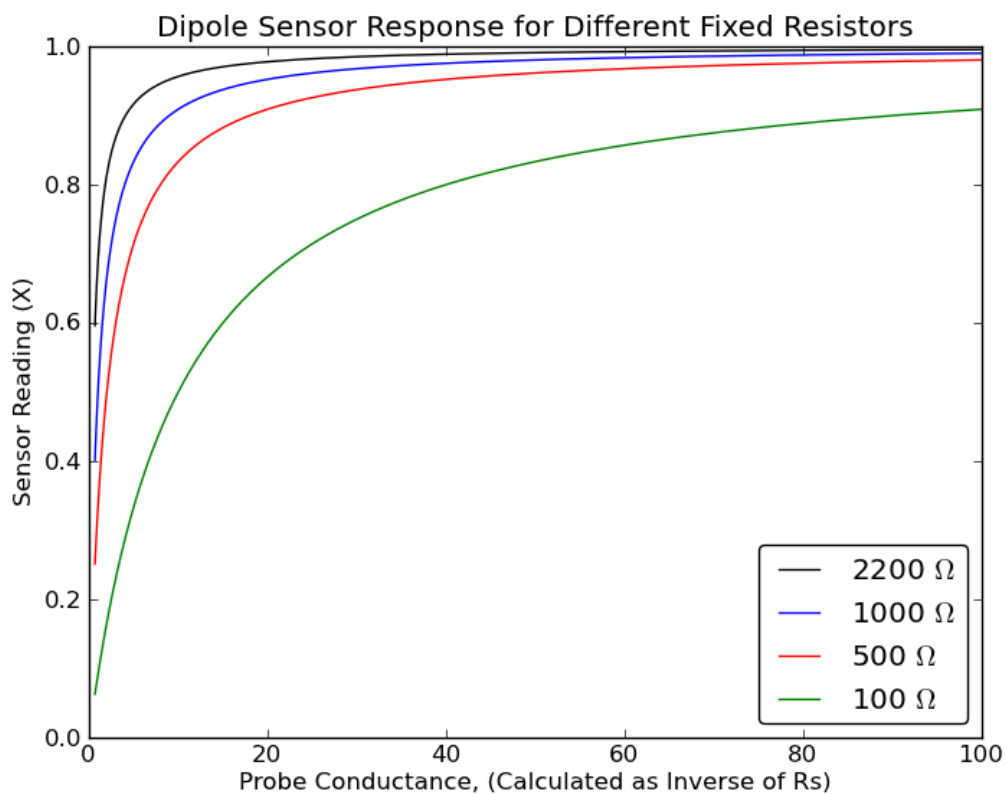


Figure 2.5: Expected relationship between dipole sensor reading (X) and probe conductance (mS) for various fixed resistors. Probe conductance is calculated as the inverse of resistance measured at the dipole sensor ($1/R_s$). For a dipole resistance sensor, R_s is related to EC through a second-order relationship.

Chapter 3: Laboratory Probe Tests

3.1 OVERVIEW

Laboratory experiments are a common component of environmental research and design because they allow tests to be conducted under controlled conditions. For hydrogeological investigations such as subsurface characterization, solute transport, or remediation design, various types of laboratory analysis are capable of providing empirical data needed to understand physical and chemical processes which may occur in the field. Batch tests, soil columns, flow cells, and sandbox tests are common laboratory approaches applied to provide information about physical transport properties of groundwater constituents, characteristics of aqueous, dissolved, and sorbed phase contaminants, and information about the interaction between contaminants, groundwater, porous media, and remediation technologies.

Laboratory tests were designed to determine if the prototype sensor system described in Chapter 2 could be programmed to record measurements, and provide data which could indicate the presence of reagents in the subsurface with enough resolution and accuracy to understand relative changes in reagent concentration. Hence tests were designed to determine the monitoring capabilities of the developed temperature and dipole resistance sensors. The two main goals of the laboratory tests were:

1. Determine if temperature fluctuations could be monitored
2. Determine capabilities of dipole resistance sensors
 - a. Quantify how measurements respond to changes in temperature
 - b. Determine if EC can be considered to be a relevant representation of reagent concentration, specifically oxidant concentration
 - c. Quantify how measurements respond to changes in EC

To achieve these goals, several static cell and flow cell tests were conducted. Three sets of static cell experiments were conducted with (1) DI water, (2) sodium chloride solutions, and (3) chemical oxidant solutions mixed in beakers. Static cell experiments tested both the temperature

sensor (section 3.2) and two wire dipole resistance sensor (section 3.3.1). This chapter also describes flow cell tests conducted with an open-water tank (section 3.3.2). Experiments in this chapter were performed under conditions that varied parameters such as salt concentration, flow rate, temperature, size of fixed resistors, and time. The results from the static cell and flow cell experiments in this chapter led to further laboratory testing with a more refined flow system which is discussed in Chapter 4.

3.2 TEMPERATURE TESTS

To confirm that the constructed thermistors were capable of recording temperature and temperature changes accurately, static cell tests were conducted by suspending sensors in beakers filled with DI. A controlled experiment was conducted with replicate beakers, each with 1000 mL of DI water, over a 24 hour period. Schlumberger Mini-Divers, model DI501, were hung in each beaker. A thermistor constructed according to the methods described in Chapter 2 was strapped to each Mini-Diver leaving the bead end exposed close to the Mini-Diver sensor port. Temperature records fluctuated during the test due to the diurnal heating cycle from the furnace system in the laboratory building. Data collected by the constructed temperature sensor was compared to temperature recorded by the Mini-Diver. Product specifications state the Mini-Diver does not require calibration (Schlumberger, 2012a, p.31); it was assumed the transducer was suitable to be used as a temperature standard for comparison with the constructed thermistors.

Figure 3.1 shows a relatively consistent difference of 0.18 °C between the Mini-Diver and thermistor in Replicate 1, with temperature difference between the two measurements ranging from 0.14 – 0.22 °C. Replicate 2 was slightly less consistent, with an average difference of 0.13 °C, and range between 0.09 - 0.2 °C. When a simple calibration is applied to the constructed temperature sensor data by shifting records for each replicate by the average differences of 0.18 and 0.13 °C, respectively, differences between the new datasets and Mini-Diver loggers is less than the reported Mini-Diver accuracy of +/- 0.2 °C for all measurements (Schlumberger, 2012a, p.13). These results demonstrate that the constructed thermistors are capable of accurately measuring changes in temperature and that minor calibration may be required to shift records to match a temperature reference.

3.3 DIPOLE RESISTANCE SENSOR EXPERIMENTS

3.3.1 Static cell

3.3.1.1 Static cell with DI

The response of dipole sensors to DI water was tested with a measured volume of water and probes placed in the beaker. In some cases, thermistors were attached to the outside of the PVC probes, directly above the resistance detectors to monitor temperature changes. An example of an experiment conducted over a 10 day period with 1000 mL beakers, 500 mL of DI, and 24.9k ohm resistors is shown in Figure 3.2. Sensor construction details for all static cell experiments are listed in Table 3.1. Figure 3.2 shows the two different dipole sensors behave similarly, but sensor response at each probe is unique. Sensor readings fluctuated as the solution temperature changed with diurnal changes in the laboratory temperature. In addition, there is an upward trend in the dipole measurements that correlate with increasing temperature. From the period of February 19 onward, temperature does not increase and dipole measurements are more stable. However, due to the fluctuations in temperature and the increase in solution temperature over time, the experiment from Figure 3.2 does not conclusively show whether upward drift in dipole resistance measurements is present. It is possible the changes in dipole measurements are a product of both increasing temperature and upward drift.

Changing temperature should not be expected to produce a linear effect on dipole measurements. Although Eq. (5) shows EC response to temperature is a linear relationship, dipole resistance measurements do not respond linearly to EC, explaining why Figure 3.2 does not show a consistent dipole response for a unit change in temperature. However, as shown in Figure 2.5, sensor value (X) has a decaying relationship with a unit change in probe conductance. As sensor value increases, any potential upward drift in measurements is masked when showing sensor value on a linear axis.

An important point to consider when analyzing Figure 3.2 is the scale of sensor values shown. Dipole measurements (X) can range between 0-1; the values recorded during experiments with DI are at the low end of this range because EC is minimal. Figure 2.5 shows a small change in

EC at this range produces a relatively large change in measurement value (X). Consequently, any fluctuations or drift in dipole measurements observed in Figure 3.2 represent little change in EC. As a result, potential upward drift in Figure 3.2 would only introduce minimal error into dipole sensor measurements (X) used to represent EC.

Dipole measurements in Figure 3.2 were collected to three significant digits after the decimal and are provided for illustration purposes; later experiments included more significant digits after the decimal which increased measurement resolution. Water volume in beakers was not found to influence measurements when dipole sensors were completely submerged.

3.3.1.2 Static cell with NaCl

Probes were placed in static cells with varying NaCl concentration to observe dipole sensor responses to changing EC. Initial experiments placed probes in a single beaker and monitored sensor response over time, while later experiments moved probes between beakers with varying NaCl concentration to analyze sensor response to changes in EC.

3.3.1.3 Static cell with NaCl: Sensor response over time

The experiment shown in Figure 3.3 consisted of five different dipole resistance probes, constructed according to details in Table 3.1 and wired with 24.9 k Ω fixed resistors, placed in five separate solutions of NaCl (BDH, BDH0286-500G). EC of each solution was measured with a handheld meter (Thermo Orion; model 1219000 with 013010MD conductivity probe). Temperature sensors, constructed according to the methods described in Chapter 2, were strapped to the outside of the PVC probes, directly above the dipole sensor, similar to what is shown in Figure 3.4. For the duration of the experiment, the dipole resistance detectors and the temperature sensors were submerged in the NaCl solution.

Figure 3.3 indicates that the resistance sensors record significantly different values when EC of the measurement solution is elevated. Measured values for each probe increased as EC of the solution increased, although Probe 3 and Probe 4 show nearly identical measurement value (X) for static solutions of 7.06 and 8.97 mS/cm, respectively. Although sensor response to each solution was unique to each sensor, Figure 3.3 shows that, in general, when resistance sensors

are constructed similarly, higher EC results in higher measurement value, regardless of the sensor.

Figure 3.3 also indicates the influence of measurement solution EC on resistance readings was greater than the influence of changing temperature. A temperature change of 1°C over the duration of the experiment did not affect measurements in comparison to the magnitude of changes caused by EC differences at the mS/cm scale.

3.3.1.4 Static cell with NaCl: Sensor response to change in EC

Data from experiments such as those shown in Figures 3.2 and 3.3 confirmed the dipole resistance sensors were capable of measuring aqueous solutions and were sensitive to temperature and EC. Further static cell experiments were conducted with NaCl solutions to determine sensor response to changes in EC. Similar to previous experiments, solutions with varying EC were prepared with laboratory grade NaCl (BDH, BDH0286-500G) and were measured with a handheld meter (Thermo Orion; model 1219000 with 013010MD conductivity probe). Probe construction details for all static cell experiments are described in Table 3.1.

Probes were placed in a beaker, left to stabilize and record measurements for at least 15 minutes, and then moved to a successive beaker with different EC. Probes moved to a beaker with lower NaCl concentration than the previous beaker were rinsed with DI water to mitigate altering EC of the beaker. Static cell experiments with varied EC are summarized in Table 3.2.

Results for Experiments A-D, where all probes were wired with 24.9 kΩ fixed resistors, are shown in Figures 3.5 and 3.6. Figure 3.5 shows data collected by each probe produced a similar response to changes in EC. Probes 4-7 showed very close replication of measurements for Experiments C and D. There was some divergence between Experiments A and B for Probes 1 and 2 which is illustrated in the top two panels of Figure 3.5.

The contrast between Experiments A and B shown in Figures 3.5 and 3.6 point to several sources of experimental error which could account for the differences between measurements. Differences in calibration of the handheld EC meter between experiments could introduce error, although it is unlikely this could account for such a large difference. Temperature was not monitored during the static cell experiments with varying EC and it is possible that the NaCl

solutions for Experiments A and B were different temperatures. However, static cell solutions were typically in the range of 20 °C for all experiments. Based on the rule of thumb that EC changes 2% per degree difference from 25 °C (Robinson and Stokes, 1965, p.87), even if the NaCl solutions for Experiments A and B had a 5 °C temperature difference, it would only account for a 10% shift in EC. Shifting any of the curves for Probes 1 and 2 laterally by a 10% change in EC does not provide a match between Experiments A and B.

A plausible explanation is there was some type of physical damage to the probes which caused sensor response to be altered. It is possible the copper wire detectors corroded between Experiments A and B, which took place 11 days apart. In the time between experiments, Probes 1 and 2 were used for other experiments with high concentration NaCl solutions. It is possible that this extended period of exposure affected the detector surface, causing a change in measurement properties of the sensor. The magnitude of probe response to EC is less for Experiment B. It would be expected that corrosion or rust on detector wires would increase the resistance measured by the sensor (ie: causing a reduction in measurement value, X) because the amount of current that would travel between the detectors would be reduced.

Corrosion or degradation of the detector wires is not the only possible explanation for altered detector response. Because the probes were left to log data over an extended period of time, it is possible salt precipitated on or around the detector wires and altered the response for each detector. The reverse excitation setting used with the datalogger program should avoid this type of sensor polarization issue, but it is not unreasonable to suggest that salt precipitation had an effect on recorded data.

Whether detector corrosion, precipitation of salt on/surrounding detector wires, or a combination of both were to influence measurements made by a probe, it would seem unlikely that multiple probes were affected in the exact same way. Whatever caused the differences in measurements between Experiments A and B did not alter the trends observed during each test. Figure 3.6 shows that the data collected during Experiment A was very similar for Probes 1 and 2; Experiment B showed the same agreement for Probes 1 and 2; and Experiments C and D showed the same trends for Probes 4-7 during each respective experiment. If something were to physically change the detector wires and alter their response to an aqueous solution, it would be expected that the degree of damage or change for each probe detector would be somewhat

unique. The results in Figure 3.6, where all probes in a single experiment shared common sensor responses to changes in EC, would suggest that something other than physical damage to the detector wires accounted for the differences between Experiments A and B.

The similarity in data collected by multiple probes during the same experiment combined with the contrasts in probe response between different experiments suggests some characteristics of the wiring and datalogging program used for each experiment could have an influence on probe response. For example, two experiments that used the same datalogger program would send an identical excitation voltage to each excitation port; if the experiments had different numbers of wires connected to the respective ports, it could potentially alter response of a sensor. Experiment A used two probes (1 and 2) excited through a single port, Experiment B used three probes (1, 2, and 3) excited through a single port, while Experiments C and D used four probes (4, 5, 6, and 7) excited through a single port. All experiments used a 2500 mV excitation at each port. Because Experiments C and D show such close agreement, while differences exist between A and B, the number of probes excited by a single port provides a systematic explanation of the differences between data recorded by each probe.

3.3.1.5 Probe calibrations for static cell with NaCl

The static cell data in Figures 3.5 and 3.6 is specific to the fixed resistor (R_f) which prevents the measurement values (X) from being directly calibrated to EC using a simple function. This is because the measurement value (X) lumps the fixed resistor (R_f) and resistance measured at the sensor (R_s) together. Calibrating dipole resistance sensor measurements to a fit with EC is desirable because it removes the influence of the fixed resistor and allows data to be reported to a real parameter, EC, rather than measurement value (X).

To produce a calibration function where EC is the dependent variable, Eq. (16) is rearranged to solve for R_s . To present the data as a parameter that correlates with EC, the Probe Conductance term introduced by Figure 2.5 can be used, where Probe Conductance is the inverse of R_s and has units of Siemens:

$$\text{Probe Conductance } (S) = \frac{1}{R_s} = \frac{1}{\frac{R_f}{X} - R_f} \quad (17)$$

Figure 3.7 shows the static cell data for Experiments A-D plotted as probe conductance vs. EC. Several different simple models were fit to the data and evaluated to determine which trend minimized the correlation coefficient, r^2 . A second order polynomial with form $y = aEC^2 + bEC + c$, where a, b, and c are constants was found to produce the best overall fit for all sets of measurements. For the fitted polynomial functions, r^2 ranged between 0.9155 and 0.9994 for all probes tested during Experiments A-D (Table 3.3). The polynomial fit is adequate for EC calibration when all measurements are within the range of calibration points. Figure 3.7 shows when the fit is extrapolated beyond the range of calibration points, it may peak and then begin to decline, which would not accurately represent sensor response. This shows a calibration may only be accurate for EC that is within the range of calibration points.

When a fit is made to a set of data, it is possible to predict solution EC for any measurement value (X). If a probe has been found to produce repeatable measurements (ie: Probes 4-7 for Experiments C and D), a single calibration could potentially be used several times. However, the exact cause of the differences between Experiments A and B is not fully understood; a user should be careful when attempting to apply a previously-determined calibration to a new dataset. The calibration fit in Figure 3.7 for Probes 1 and 2 is much different for Experiments A and B; using the wrong calibration would introduce significant error into results. The best method to minimize this potential error caused by differences in probe response from day-to-day would be to calibrate probes to several EC measurement points during each use. However, if a user does not have enough time to develop a new calibration but wishes to use a previously-determined model, a calibration check with 1-2 measurement points should be performed to verify sensor response fits the calibration model being used.

3.3.1.6 Influence of fixed resistor, R_f

The impact of the fixed resistor, R_f , used with each probe was also tested experimentally to verify the theoretical trends predicted in Figure 2.5. Figure 3.8 shows static cell Experiments E and F where Probes 4, 5, and 6 were wired with 22.0, 46.9, and 218.2 Ω fixed resistors, respectively. In comparison to Figures 3.5 and 3.6, Figure 3.8 shows the sensor measurements (X) were much lower than those recorded with the 24.9 k Ω fixed resistors for Experiments A-D.

In addition, the change in measurement value (X) for a unit change in EC is much greater in Experiments E and F compared to the previous experiments using 24.9 k Ω resistors. When analyzing the data from Figures 3.5, 3.6, and 3.8 in the context of Figure 2.5, it shows the 24.9 k Ω fixed resistor produced data that was on the horizontal asymptotic end of the sensor response curve in Figure 2.5, while the smaller fixed resistors (22.0, 46.9, and 218.2 Ω) produced data that was closer to the vertical asymptotic end of the sensor response curve. Consequently, a unit change in EC in Figures 3.5 and 3.6 produces a small change in sensor reading (X), while the same unit change in EC in Figure 3.8 produces a large change in sensor reading. In addition, for both E and F, the size of the fixed resistor (R_f) was shown to shift the measured data upwards. This is also consistent with the expected relationship from Figure 2.5, where measurement value (X) at a constant probe conductance (which would indicate constant EC) shifts upwards when the size of the fixed resistor increases.

Figure 3.8 also shows the same type of difference between Experiments E and F that was observed between Experiments A and B; curves recorded during Experiment F have lower values than what was recorded by Experiment E. Because detector response was reduced for the later experiment, it is logical to assume corrosion of detector wires caused the differences in response for Probes 4, 5, and 6. Similar to Experiments A and B, for the time between Experiments E and F, all probes were left exposed to high concentration NaCl solutions, which created a potential for corrosion or salt precipitation.

The exact same wiring configuration was used for Experiments E and F, where all four probes were connected to a single excitation port. As a result, differences in wiring configuration cannot directly explain the differences in probe response between the experiments.

To remove the influence of the fixed resistors and further analyze the differences between Experiments E and F, measurements were rearranged according to Eq. (17) and reported as probe conductance. Figure 3.9 shows Experiments E and F plotted with data for Experiments C and D. A second order polynomial, as described above, is fit to the data for E and F to provide a comparison of which Experiment is in closest agreement with C and D. Interestingly, no consistent source of error was found in the data: for Probe 5, Experiments C and D match best with the fit for F; for Probe 6, C and D match best with the fit for E; and for Probe 4, C and D fall in the middle of the fits for E and F. There appears to be no correlation between the size of

fixed resistor used and the placement of the data in comparison to C and D. This indicates the different fixed resistors did not introduce significant error into the measurements, and that the differences observed between Experiments E and F are likely caused by the same factors which caused the differences between Experiments A and B.

These results combined with the observations from section 3.3.1.4 indicates alterations to detector wires caused by corrosion or salt precipitation provides the most consistent explanation to account for changing probe response between different experiments. However, as mentioned in section 3.3.1.4, it would be unlikely that changes in detector response caused by corrosion and/or salt precipitation would affect each probe in the exact same way. This suggests the cause of differences between measurements with the same probe may be attributed to something other than what has been discussed above.

3.3.1.7 Static cell with oxidants

Static cell experiments similar to those described in section 3.3.1.4 were conducted with chemical oxidants (permanganate or persulfate) to verify that the dipole resistance sensors responded to reagents typically used for ISCO in the same manner as they did for NaCl solutions. Beaker solutions were prepared by mixing dry sodium persulfate (Sigma Aldrich, 216232-500G, 0 to 20 g/L) or potassium permanganate (Sigma Aldrich, 223468-500G, 0 to 30 g/L) with DI water. A handheld meter was not used to measure EC of the solution in each beaker to avoid damaging the meter. Consequently, oxidant test results are plotted with oxidant concentration (g/L) on the x-axis, rather than EC (mS/cm).

Results for tests with persulfate, (Experiments G and H), are shown in Figures 3.10 and 3.11, while results for a test with permanganate, Experiment I, is shown in Figure 3.12. The irregularities in curve shape for Probes 8 and 9 during Experiment G shown in Figures 3.10 and 3.11 are a result of poor rinsing when probes were moved from a beaker with high persulfate concentration to one with a lower concentration. For these curves, the first 4-5 data points show higher sensor readings than what should have been observed for the reported oxidant concentration. This expected probe response is verified in Experiment H, where the bottom panel of Figure 3.11 shows the response curves for Probes 8 and 9 fall below those of Probes 4, 5, and 7. Figure 3.10 indicates the response from each probe was consistent for Experiments G

and H. Figure 3.12 shows a static cell experiment with permanganate (Experiment I) produced results similar to the persulfate and NaCl solution experiments. One point to note is the response from Probe 7 during Experiment I was below what was expected based on the persulfate results. Figures 3.10 and 3.11 show Probe 7 produced readings similar to Probes 4 and 5. However, the readings for Probe 7 during Experiment I were well below what was observed for Probes 4 and 5. It is possible this difference is a result of damage to the probe from the persulfate used in Experiments G and H, but the difference could also be from the same source of error that caused the differences between Experiments A and B discussed above.

Static cell results indicated the dipole resistance sensors had the same response to chemical oxidant solutions as was observed for NaCl solutions. This confirms dipole resistance sensor measurements can be correlated with oxidant concentration and also verifies NaCl is a suitable surrogate for oxidants in the testing efforts in this thesis.

3.3.2 Flow cell experiments

A series of tests were performed to determine how the temperature and dipole resistance sensors respond to moving water and simulated EC breakthrough. Experiments described in this section were conducted with an open water flow cell and consisted of scenarios with either recirculating DI or with an injected pulse of NaCl solution. Controlled EC breakthrough was created by switching the feed solution from DI to an NaCl solution.

3.3.2.1 Tank construction

Plastic inlet and outlet fittings were attached to a rectangular plastic tub with dimensions 54 cm L X 39 cm W X 18 cm H and sealed with silicone (GE Model SE2184 24C). The inlet and outlet fittings were centered along the short sides of the container, at heights of 6 cm and 12 cm, respectively. Tubing was connected to both fittings. A peristaltic pump was used to control flow through the system (39 cm/hr averaged over entire water volume) and water level in the container was held constant at the height of the outlet for all tests. The outlet tube was configured to recycle water back to the inlet reservoir during tests with only DI, or to waste outlet water when salt solutions were used. Figure 3.13 shows the experimental apparatus with an example of laboratory probes positioned in the tank for a test. Although the figure shows

laboratory probes built with two inch diameter PVC, it should be noted that all of the tests discussed in this thesis were conducted with one inch diameter PVC probes.

3.3.2.2 Recirculating DI

The first series of experiments conducted with the open water tank were recirculation of DI water over an extended period of time. Temperature and resistance measurements were logged during the tests. Thermistors were attached to the outside of PVC probes and aligned adjacent to the resistance sensor as shown in Figure 3.4.

Test records for the flow cell with recirculating DI produced results similar to the static cell experiments with DI. An example of data collected during one of these experiments is shown in Figure 3.14. Two probes, similar to the one depicted on the left side of Figure 3.4, were inserted into the tank. Probe 1 was placed at the tank centerline, approximately 15 cm from the inlet, while Probe 2 was placed approximately 10 cm from the tank outlet at the tank centerline. The dipole sensors were wired with 24.9k Ω precision resistors. Velocity calculated as the flow rate through the entire cross-section of the tank was 39 cm/hr.

Similar to the observations from section 3.2, the two temperature sensors tracked temperature changes the same. The average difference between the two temperature measurements was 0.36 °C, with a range between 0.32 and 1.86 °C. Temperature differences were larger at the beginning of the test. Part of the difference was a likely a real temperature gradient between the upstream and downstream end of the tank due to the reservoir equilibrating with room temperature. The consistent difference between temperature measurements later in the test indicated a difference in calibration for each sensor. If a temperature standard were available, the calibration method described section 3.2 could shift measurements for each sensor to match true values.

Figure 3.14 shows data collected by the dipole sensors was stable; measurements did not drift significantly and only changed with a corresponding temperature change. Figure 3.14 does show a small upward trend over time, which is consistent with observations from Figure 3.2. The amount of upward drift was significantly less than what was observed for Figure 3.2, supporting the argument that most of the upward trend in Figure 3.2 was caused by increasing temperature.

A point to note is the full range of temperature fluctuation throughout the experiment shown in Figure 3.14 was 2.9 and 3.0 °C for Probes 1 and 2, respectively. These fluctuations would be abnormally large temperature changes over such a short period of time for *in situ* groundwater measurements. The relatively small effect temperature change had on the measurements in Figure 3.14 indicated *in situ* measurements may not be significantly influenced by temperature fluctuations. The influence of temperature on dipole resistance sensor measurements is investigated further in section 4.3.3.

These test results for a flow system with DI circulation confirmed the prototype design was capable of logging stable measurements in an environment with relatively high flow velocities for groundwater (>35 cm/hr).

3.3.2.3 Breakthrough experiments

Each breakthrough curve (BTC) experiment started with DI water flowing through the system while dipole resistance probes collected baseline measurements. NaCl feed solutions were mixed to various concentrations (5 – 30 g/L) in volumes of 6 L. At the beginning of each test, signified by Time 0, the feed solution at the tank inlet was switched from DI to the NaCl solution. The inlet feed was switched back to DI after the NaCl solution was pumped into the tank. Effluent from the outlet was discharged to waste.

Dipole resistance probes used during the experiments were set to take readings every 30 seconds. Data collected by the probes were compared to EC measurements recorded with a handheld meter (Thermo Orion; model 1219000 with 013010MD conductivity probe). The handheld EC measurements were collected inside the tank by placing the conductivity probe close to the dipole sensors and then recording EC at various time intervals throughout each experiment. For cases when multiple dipole probes were collecting data inside the tank, the handheld probe was used to record EC at the location of each dipole sensor. Dipole probes were generally placed in two locations; 15 cm from the upstream end of the tank and 10 cm from the downstream end. Probes were offset from the tank centerline approximately 2 cm so the wire detectors were situated directly in line with the inlet.

EC readings collected by the handheld probe were not stable due to the design of the tank. The NaCl solution tracer was injected into the tank through the inlet port with a peristaltic pump. This produced a pulsating flow effect with continually changing EC, particularly at the front of the tank. To deal with this, EC readings were recorded as a range of values over 15 to 20 seconds for each measurement, with the midpoint of this range used as the measured EC value. More variability was recorded for measurements at the upstream probe location in comparison to the downstream probe. Higher flow rate increased the range of EC values reported when monitoring at the front of the tank, although it did not appear to have a significant influence on the range of measurements observed at the back of the tank. This indicated more mixing had occurred between the tracer and the rest of the tank solution at the back end of the tank compared to the front. More details of the characteristics of handheld EC measurements are described in Table C2.

Several BTC experiments were conducted in the open water flow system. A subset of these experiments is described in Table 3.5. Results and conclusions from other BTC experiments not shown are consistent with what is observed for BTC-A – BTC-E. Sensor construction details for probes used to collect data for BTC-A – BTC-E is shown in Table 3.4. A difference from previous experiments is the probes used for BTC-A – BTC-E (Probes A and B) were constructed with two dipole resistance sensors; one larger horizontal sensor similar to those used in the static cell experiments, and one smaller vertical sensor. Figure 3.4 shows both sides of Probe A. Both sensors on each probe were set to collect data during BTC-A – BTC-E. Results from other BTC experiments where probes only used a single sensor (not shown) indicated adding the second dipole sensor to the same probe did not influence experimental results.

BTC-A is shown in Figure 3.15 where Sensor 1 (larger) and Sensor 2 (smaller) are the two dipole sensors on Probe A (see Table 3.4). All tests showed a consistent trend where the dipole sensor measurements matched fairly well with handheld EC measurements for the rising limb of the BTC, but did not correlate well with decreasing EC on the falling limb of the BTC. Although Figure 3.15 shows decreasing measurement value (X) after the EC peak, the values do not return to baseline readings at the same rate as the EC measurements. Similar results are also shown for BTC-B – BTC-E in Figure C1. Controlled parameters for the initial flow cell experiments are described in Table C1.

Several attempts were made to modify the BTC experiments to account for the divergence between dipole sensor readings (X) and EC measurements. Analyses considered potential calibration error introduced by the handheld EC meter, the influence of flow conditions created by the peristaltic pump and inlet port, corrosion of the copper wire detectors, the potential collection of ions on detector wires, and the differences between open water conditions and experiments using porous media. A discussion of these efforts is presented below, while a further investigation relating results from this thesis to data observed by other researchers is provided in Appendix C1.

3.3.2.3.1 Calibration error in handheld meter

Calibration of the handheld EC meter was investigated to determine if it could explain tailing described above. For all experiments, the handheld EC meter (Thermo Orion; model 1219000 with 013010MD conductivity probe) was only calibrated to a single 1413 $\mu\text{S}/\text{cm}$ standard, rather than a curve of multiple standards. Therefore, measurements close to 1413 $\mu\text{S}/\text{cm}$ were reliable, but it is possible error was introduced as values moved from that point. Poor probe calibration does not satisfactorily explain the tailing measurements because the handheld meter was able to provide a good match with dipole measurements on the rising limb of the BTC. Calibration of the handheld meter would not be expected to change during a BTC. Therefore, even if error in the initial handheld meter calibration, true *in situ* EC associated with an EC meter reading on the rising limb of the BTC should match true *in situ* EC at the time when the handheld meter recorded an identical reading on the falling limb of the BTC.

3.3.2.3.2 Tracer injection at inlet

Another factor of uncertainty that was investigated was the experimental set-up where the injected tracer solution was pumped directly into the tank at a single inlet point using a peristaltic pump. This experimental design created disturbed flow conditions along tank centerline that were different than those observed by the sidewalls of the tank. In addition, the use of the peristaltic pump to directly force water into the tank created a pulsating flow effect at the injection point. This design added uncertainty to the experiment because static flow conditions throughout the tank could not be assumed. Uncertainty associated with tank flow conditions made it difficult to provide strong conclusions about probe performance, but did not provide an

explanation about observed divergence between EC and dipole sensor measurements on the falling limb of BTCs. Two observations support this statement:

1. Measurements matched well on the front half of each BTC:

Pulsating flow created by the peristaltic pump would be expected to create more noise on the rising limb of a BTC when new tracer is injected into the system, compared to the falling limb of the BTC where all of the tracer is in the system and has been mixing with the background solution. The BTC experiments found strong agreement between both sensors on the rising half of breakthrough, which indicated the pulsating flow was not directly causing the tailing.

2. Differences in the amount of divergence between dipole sensor measurements and EC was not observed when comparing the upstream and downstream probe location:

Flow was more disturbed at the front of the tank than the back end. If turbulent flow conditions were influencing the tailing observed, it is expected more tailing would occur at the front end of the tank. This is supported by the handheld EC measurements that showed more variability in measurement range at the front of the tank in comparison to the back (see Table C2). The degree of tailing appeared to be consistent for measurements at both ends of the tank, which suggested the disturbed flow conditions were not a direct cause of the tailing phenomenon.

These observations indicated pulsating and disturbed flow through the tank could not directly explain tailing between EC and resistance sensor measurements. However, the non-uniform conditions in the tank made it difficult to make further conclusions about the direct source of the tailing.

3.3.2.3.3 Copper wire detectors

Corrosion of the copper wire detectors was another parameter investigated as an explanation for tailing. Potential corrosion during each BTC experiment appeared to be unlikely over such a short period. In addition, if this process were taking place, it would be expected differences in sensor response would be observed from experiment to experiment because the probe was left in damp conditions in the tank for a number of days. Differences in measurement properties of the

probe over time were not observed, indicating detector wire corrosion did not directly cause the tailing observed.

3.3.2.3.4 Collection of ions on probe detectors

A more likely explanation for tailing related to the probe detectors was the attraction of cations and anions to the detectors caused by electrical current induced by excitation voltages during each sensor measurement. A reasonable hypothesis would be electrical current caused ions in solution to attach to detectors over time while the probe was running, which lead to a change in probe response during the BTC.

The CR1000x logger was set to filter 60 Hz noise from the alternating current (AC) power source. Even if this setting were not used, this type of error would not be expected to grow over time because AC power line noise cycles in a sinusoidal relationship (Figure C3). When using a 2500 mV excitation, the 60 Hz filter uses the $\frac{1}{2}$ cycle integration shown in Figure C3 to cancel out noise (Campbell Scientific, 2011a, p.55). Because noise in this sinusoidal relationship does not grow over time, it indicates noise from the AC power source was not responsible for the tailing effect observed in BTC-A –BTC-E.

The excitation reversal, RevEx, setting on the CR1000x was used for BTC experiments, where each dipole measurement was repeated with opposite polarity; a positive voltage excitation followed by an equal magnitude negative excitation. This setting performs two separate tasks: stray voltage offsets are cancelled, and sensor polarization is avoided. Stray voltage offset is a consistent bias that could be present in a sensor. An example provided by Campbell Scientific is a sensor returns 5.003 mV after positive excitation and -4.997 mV after negative excitation. The excitation reversal setting uses an average of the positive and negative excitation measurements, giving a 5 mV reading where offset has been removed (Campbell Scientific, 2011a, p.53). Even if offset were present in experimental measurements, it would not be able to explain tailing on the falling limb of a BTC.

Sensor polarization could provide an explanation for observed tailing. If sensor excitation was consistently positive or negative, the electrical current could cause migration of cations towards one detector, and anions to another. This could potentially distort detector response to

changes in EC. The excitation reversal setting is meant to prevent this by consistently changing the direction of electrical current through the sensor. The positive and corresponding negative voltage excitations for each measurement are internally timed by the CR1000x to provide equal and opposite excitation to avoid any polarization that could occur at ionic sensors (Campbell Scientific, 2011a, p.53).

Although the reverse excitation setting was expected to avoid sensor polarization issues, an experiment was conducted to verify this assumption. A BTC (data not shown) was simulated similar to BTC-A – BTC-E, where an upstream probe was used as a control and the downstream probe was removed from the tank and rinsed several times during the experiment. The experiment tested if ions potentially gathering on the detector surfaces could be rinsed off, which would theoretically return the detectors to their measurement state before NaCl was added to the tank. No change was observed between tailing trends for the probe that was rinsed and the control. This provided evidence the reverse excitation setting was working properly and ionic polarization was not occurring.

3.3.2.3.5 Initial flow cell experiments with porous media

The tailing phenomena observed in the open water flow tank experiments necessitated more sophisticated laboratory conditions to determine whether or not the dipole sensors were capable of accurately measuring EC breakthrough *in situ*. A second flow system using porous medium was constructed and tested in an attempt to confirm if the tailing trends observed in the open was flow system was a characteristic of the dipole sensor measurement properties or experimental tank design (data not shown). Initial results suggested the tailing curves may not be present in the new flow system, although measurement noise prevented further conclusions. Preliminary results from this second flow cell experiment were a driver to undertake the laboratory experiments in Chapter 4.

3.3.2.3.6 Conclusions of BTC analysis

The troubleshooting investigations described above did not provide any conclusive evidence explaining the divergence between handheld EC measurements and dipole resistance probe measurements observed in BTC-A – BTC-E. The BTC experiments did highlight the fact that

the tank experimental designs described in section 3.3.2.1 added significant uncertainty into the interpretation of results because flow conditions throughout the system were not uniform, and handheld EC measurements showed significant variability. These results led to further laboratory testing described in Chapter 4.

3.4 CONCLUSIONS

Temperature experiments pointed to two key observations about the temperature sensors:

- a) The temperature sensor construction method provided a sensor capable of accurately measuring changes in temperature.
- b) A simple calibration can be applied to readings from a constructed sensor by adding or subtracting the average difference between constructed sensor temperature readings and those recorded by a commercial transducer such as a Schlumberger Mini-Diver.

The static cell experiments pointed to several preliminary conclusions about the dipole resistance sensors:

- a) The resistance sensors were capable of measuring aqueous solutions
- b) There is a positive correlation between the measured value (X) and solution temperature
- c) There is a positive correlation between increasing sodium chloride solution concentration and sensor reading. The relationship is nonlinear.
- d) Changes in EC on the order of 1 mS/cm influence resistance sensor measurements much more than changes in temperature on the order of 1 °C.
- e) Sensor response for static cell experiments can be calibrated to EC using a second order polynomial in the form $y = aEC^2 + bEC + c$. To produce this calibration, Eq. (16) is rearranged to solve for sensor resistance (R_s). Each data set plotted as probe conductance ($1/R_s$) vs. EC was found to fit very well with the model, with r^2 ranging from 0.92-1.00 for curves with 4-6 measurement points (Table 3.3).
- f) As indicated in Figure 2.5, increasing size of the fixed resistor, R_f , shifts curves of dipole resistance sensor measurement vs. EC upwards
- g) Dipole sensor response to sodium chloride solutions appears to be a realistic representation of the sensor response to persulfate and permanganate oxidant solutions.

- h) All hand-constructed dipole resistance sensors are unique in terms of their responses to changes in temperature and EC although sensor response and curve shape were always the same (ie: sensor value increases nonlinearly with increasing EC and temperature).
- i) Sensor response for a specific probe was not consistent for all experiments. The cause of differences in sensor response during experiments was not determined.

The flow cell experiments provided less concrete conclusions than the static cell experiments and pointed to a need for further laboratory work:

- a) Divergence between dipole resistance sensor measurements and EC measurements was observed during the open water flow cell experiments. Although multiple efforts were made to determine the cause of divergence, an explanation was not found.
- b) Observed divergence is a concern because it suggested the dipole sensor may not be capable of accurately measuring EC breakthrough. Uncertainty caused by the design of the experimental apparatus prevented a conclusive resolution.
- c) Data from flow cell experiments suggested further laboratory experiments using a more controlled flow system and porous media were required to determine if the dipole resistance sensors were capable of accurately measuring EC breakthrough. In particular, a design that did not disturb flow in the immediate vicinity of the probe during sampling was needed.

Table 3.1: Sensor construction details for static cell experiments A-I

Probe	Detector*	Orientation**	Detector Length (cm)	Detector Spacing (cm)	PVC***
1	Copper	H	2.5	2.5	1 inch
2	Copper	H	2.5	2.5	1 inch
3	Copper	H	2.5	2.5	1 inch
4	Copper	H	1.9	2.5	1 inch
5	Copper	H	1.9	2.5	1 inch
6	Copper	H	1.9	1.3	1 inch
7	Copper	H	1.9	1.3	1 inch
8	Copper	H	1.0	2.5	1 inch
9	Copper	H	1.0	2.5	1 inch

*All copper wires 18 AWG

**Orientation: H = Horizontal, V=vertical

***All PVC schedule 40

Table 3.2: Static cell experiment details

Static Cell Experiment	Beaker Solution	Date	Probes	Resistors Used
A	NaCl	2010/10/08	1, 2, 3	24.9 k Ω , 24.9 k Ω , 24.9 k Ω
B	NaCl	2010/10/19	1, 2	24.9 k Ω , 24.9 k Ω
C	NaCl	2011/02/25	4, 5, 6, 7	24.9 k Ω , 24.9 k Ω , 24.9 k Ω , 24.9 k Ω
D	NaCl	2011/03/03	4, 5, 6, 7	24.9 k Ω , 24.9 k Ω , 24.9 k Ω , 24.9 k Ω
E	NaCl	2010/10/08	4, 5, 6	22.0 Ω , 46.9 Ω , 218.2 Ω
F	NaCl	2010/10/12	4, 5, 6	22.0 Ω , 46.9 Ω , 218.2 Ω
G	Na ₂ S ₂ O ₈	2011/01/21	4, 5, 7, 8, 9	24.9 k Ω , 24.9 k Ω , 24.9 k Ω , 24.9 k Ω
H	Na ₂ S ₂ O ₈	2011/01/21	4, 5, 7, 8, 9	24.9 k Ω , 24.9 k Ω , 24.9 k Ω , 24.9 k Ω
I	KMnO ₄	2011/01/24	4, 5, 7, 8, 9	24.9 k Ω , 24.9 k Ω , 24.9 k Ω , 24.9 k Ω

Table 3.3: Second order polynomial fit to static cell probe experiments in form $y = aEC^2 + bEC + c$ where a, b, and c are constants.

Probe	r^2	a	b	c
1A	0.9947	-0.0009	0.0788	0.7541
2A	0.9965	-0.001	0.0731	0.6608
3A	0.9155	-0.0058	0.2229	0.0478
1B	0.9978	-0.0003	0.0334	0.5135
2B	0.9672	-0.0001	0.0217	0.6356
4C	0.9998	0.0004	0.2078	0.3412
5C	0.9994	-0.0011	0.2218	0.4134
6C	0.9683	-0.0167	0.3685	0.3142
7C	0.9828	-0.0156	0.3639	0.2649
4D	0.9831	-0.0237	0.4107	0.0557
5D	0.9984	-0.0118	0.3633	0.0274
6D	0.9916	-0.0128	0.3497	0.1189
7D	0.9936	0.0017	0.1736	0.4765

Table 3.4: Sensor construction details for BTC experiments BTC-A – BTC-E

Probe	Sensor Name	Detector Material*	Detector Length	Detector Spacing	Detector Orientation**	Resistor Used
A	1	Copper	2.5 cm	2.5 cm	H	2.2 k Ω ,
A	2	Copper	1.0 cm	0.3 cm	V	2.2 k Ω ,
B	3	Copper	2.5 cm	2.5 cm	H	2.2 k Ω ,
B	4	Copper	1.0 cm	0.3 cm	V	2.2 k Ω ,

*All copper wires 18 AWG

**Orientation: H = Horizontal, V=vertical

Table 3.5: Details of select open water BTC experiments

Experiment	Date	Probe A Location	Probe B Location	Tracer Volume (L)	Tracer Concentration (g/L)	Tracer EC (mS/cm)
BTC-A	2011/04/02	Front	Back	6	10	17.59
BTC-B	2011/04/03	Front	Back	6	10	17.52
BTC-C	2011/04/04	Front	Back	6	10	17.63
BTC-D	2011/04/05	Front	Back	6	10	17.59
BTC-E	2011/04/05	Front	Back	6	10	17.63

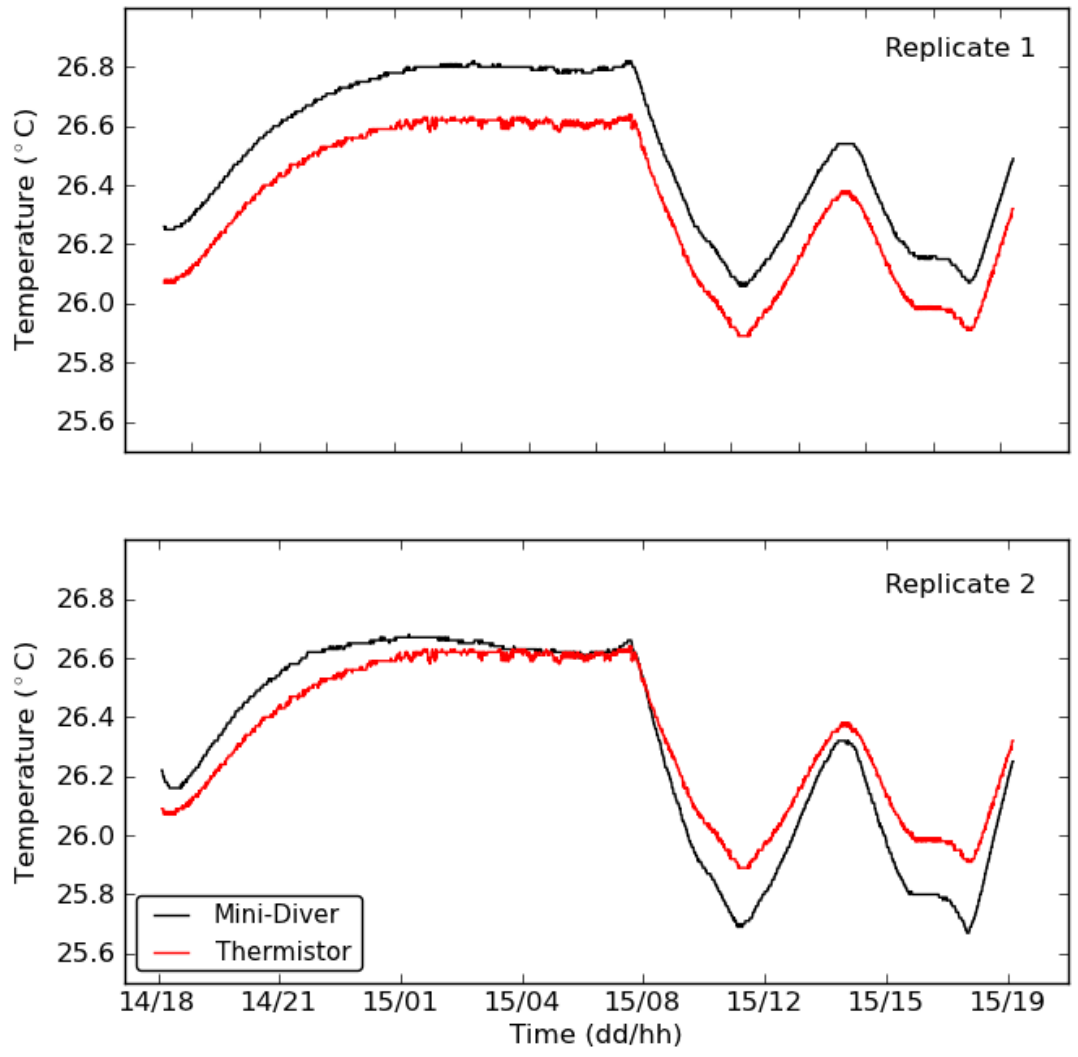


Figure 3.1: Comparison of constructed temperature sensor to Schlumberger Mini-Diver reference, sensors submerged in DI water

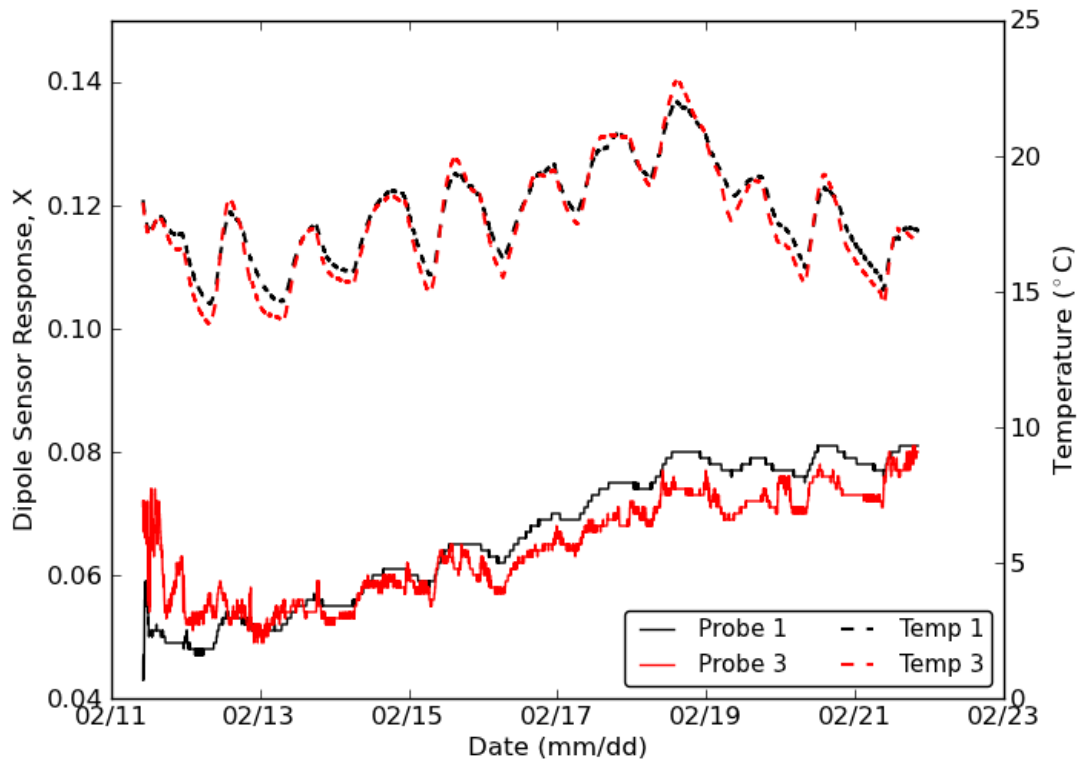


Figure 3.2: Influence of temperature on dipole resistance sensor readings in DI static cell

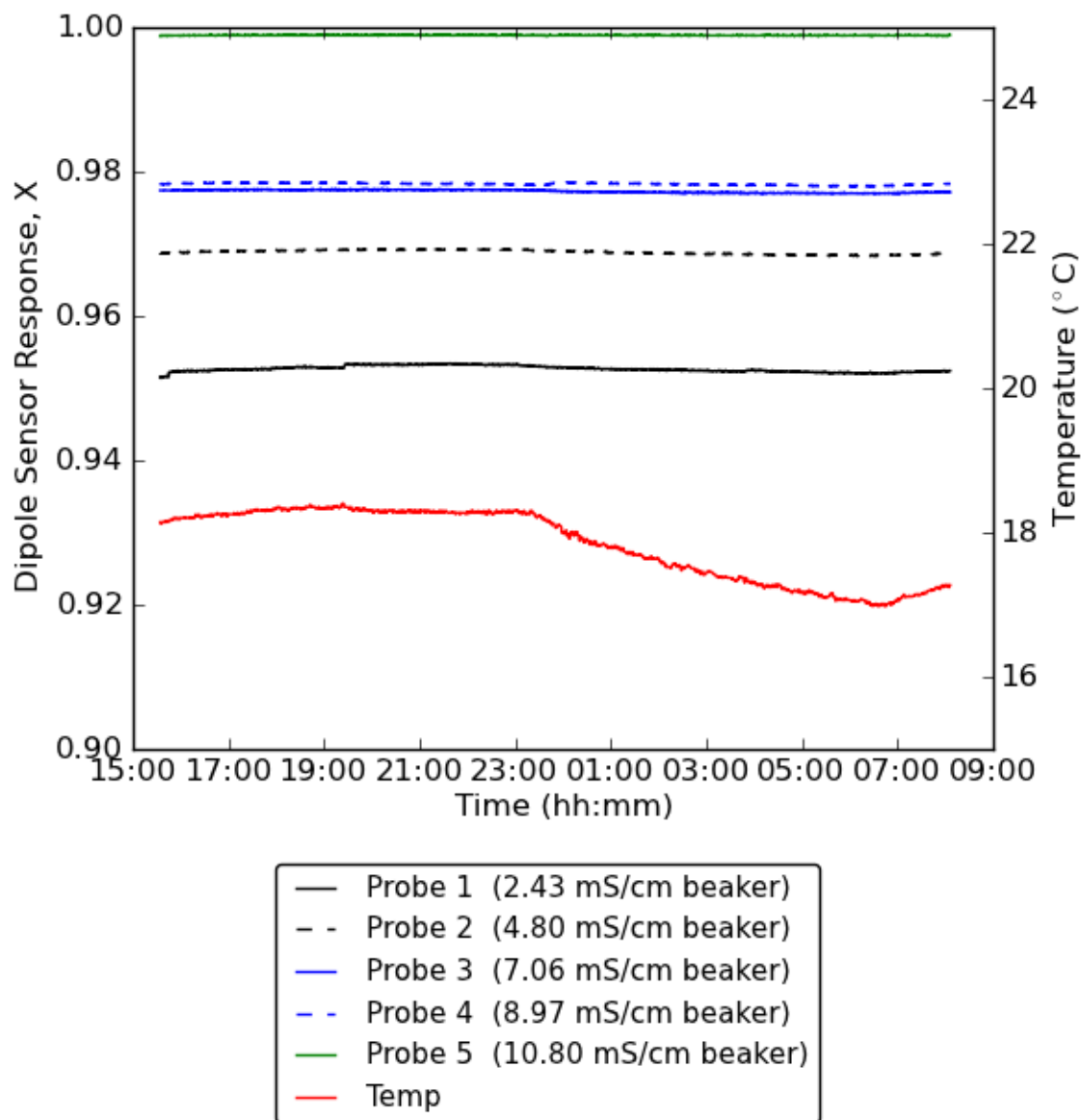


Figure 3.3: Dipole resistance sensor response to static cell EC solutions. Each 1000 mL beaker contained 400 mL solution volume. Temperature only shown for Beaker 1; temperature records for other beaker were nearly identical. Initial temperatures for Beakers 1-5 ranged between 17.3-18.1 °C.



Figure 3.4: Location of thermistors of open water tests and example of different sizes and orientations of resistance sensors

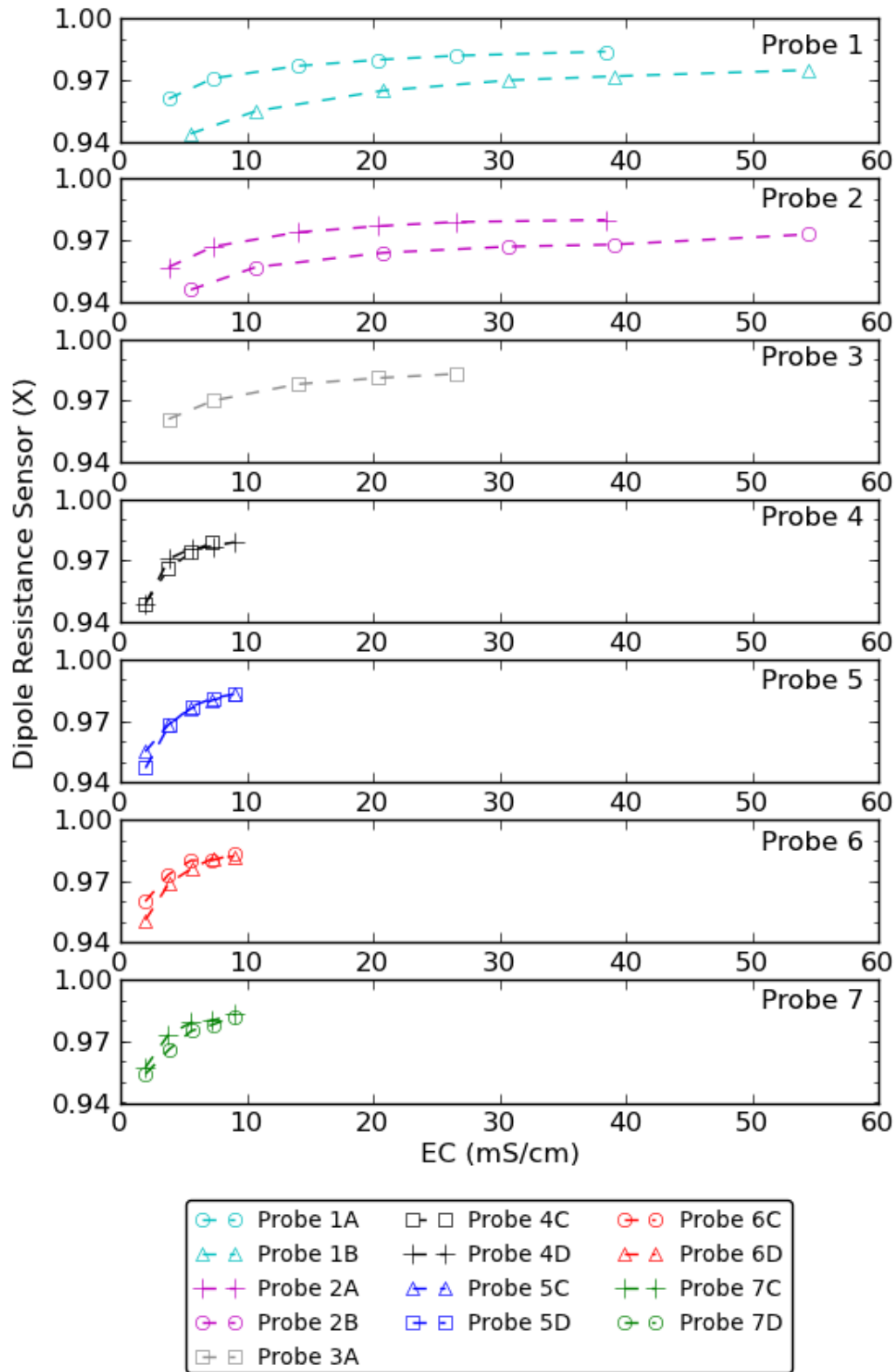


Figure 3.5: Static cell NaCl experiments with varied EC arranged by probe. Experiments A-D shown.

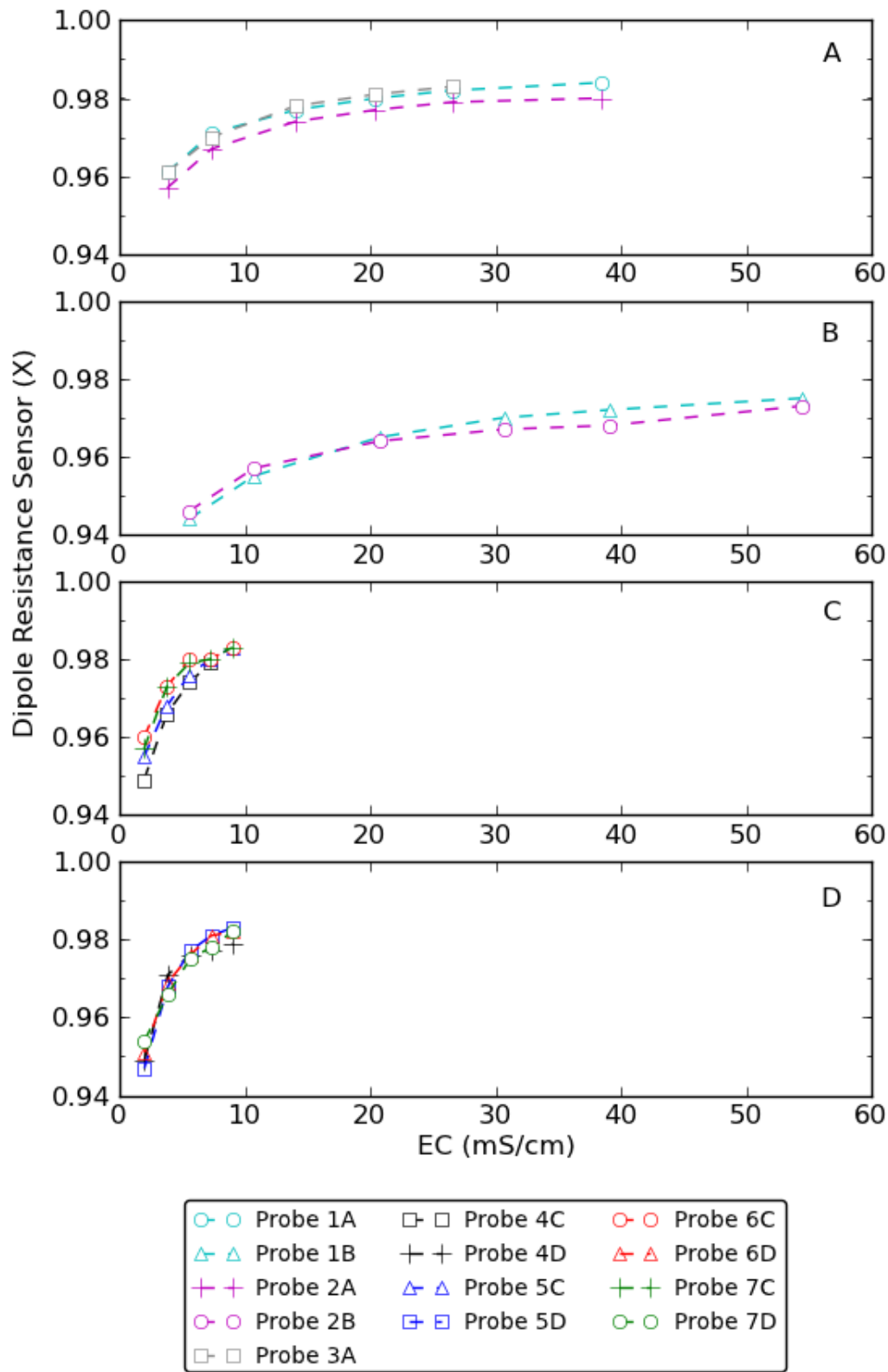


Figure 3.6: Static cell NaCl experiments with varied EC arranged by experiment. Experiments A-D shown.

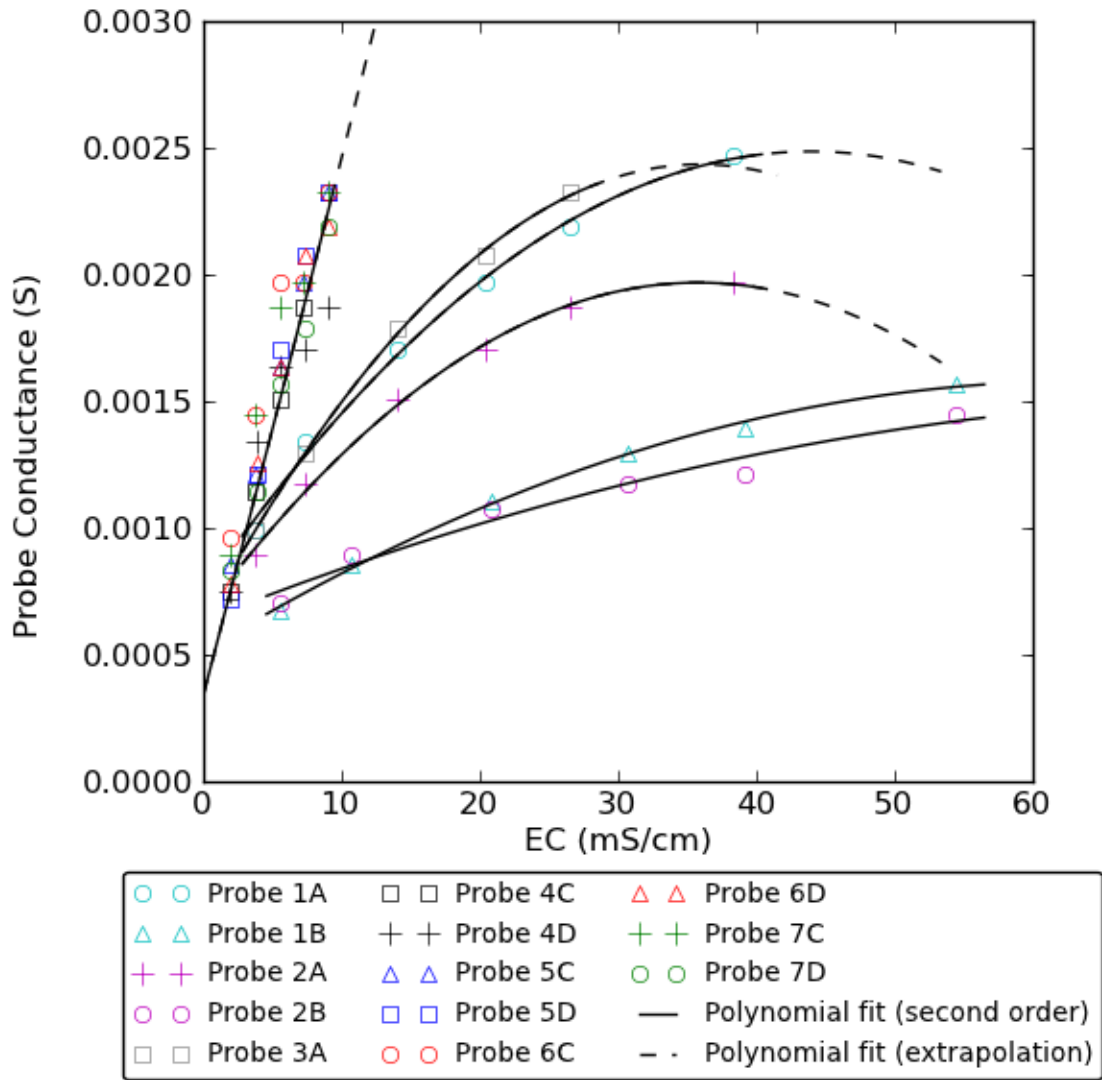


Figure 3.7: EC calibrations to static cell data where Probe Conductance is calculated as $1/R_s$. Second order polynomial fit is in form $ax^2 + bx + c$. $24.9 \text{ k}\Omega$ fixed resistor (R_f) used for all data shown. For Probes 4-7, only fit for 4C is shown.

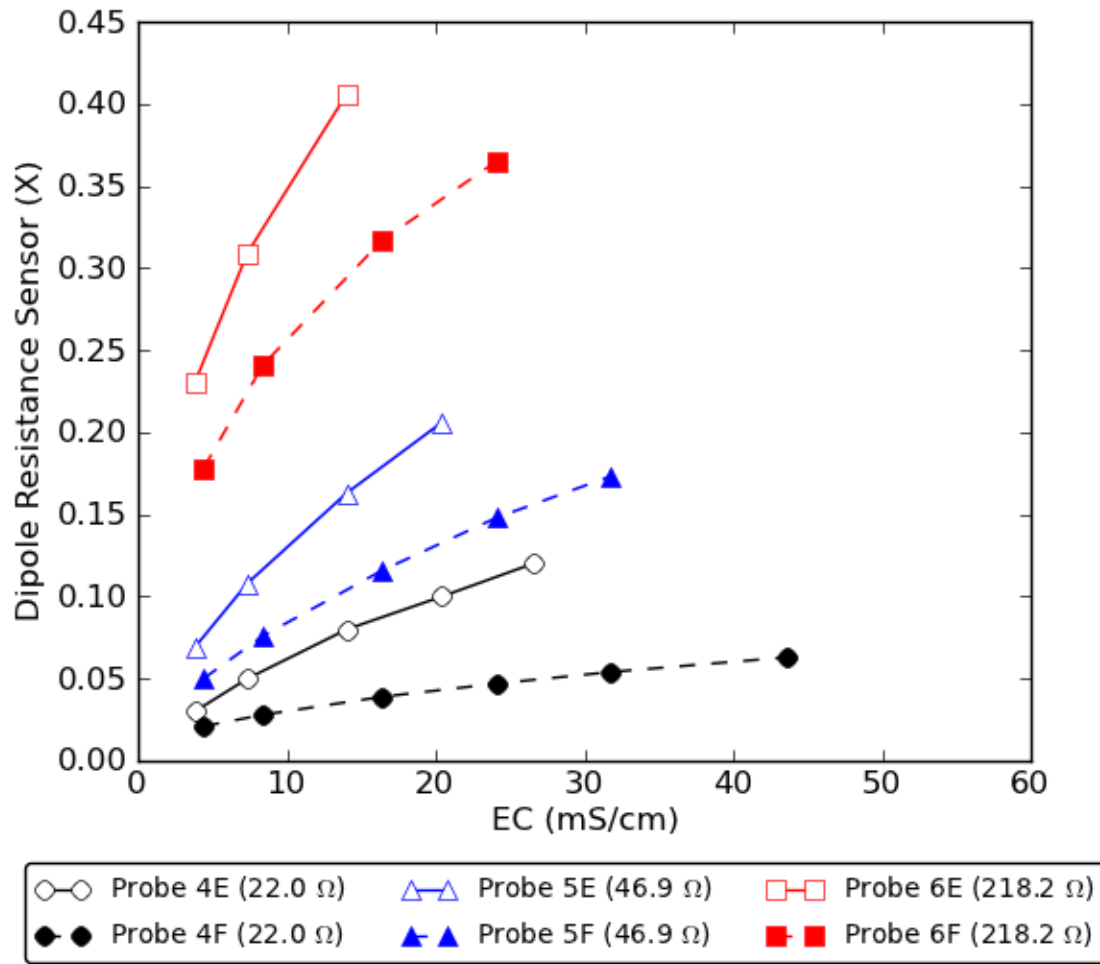


Figure 3.8: Example of influence of different resistors, NaCl beaker experiments E and F

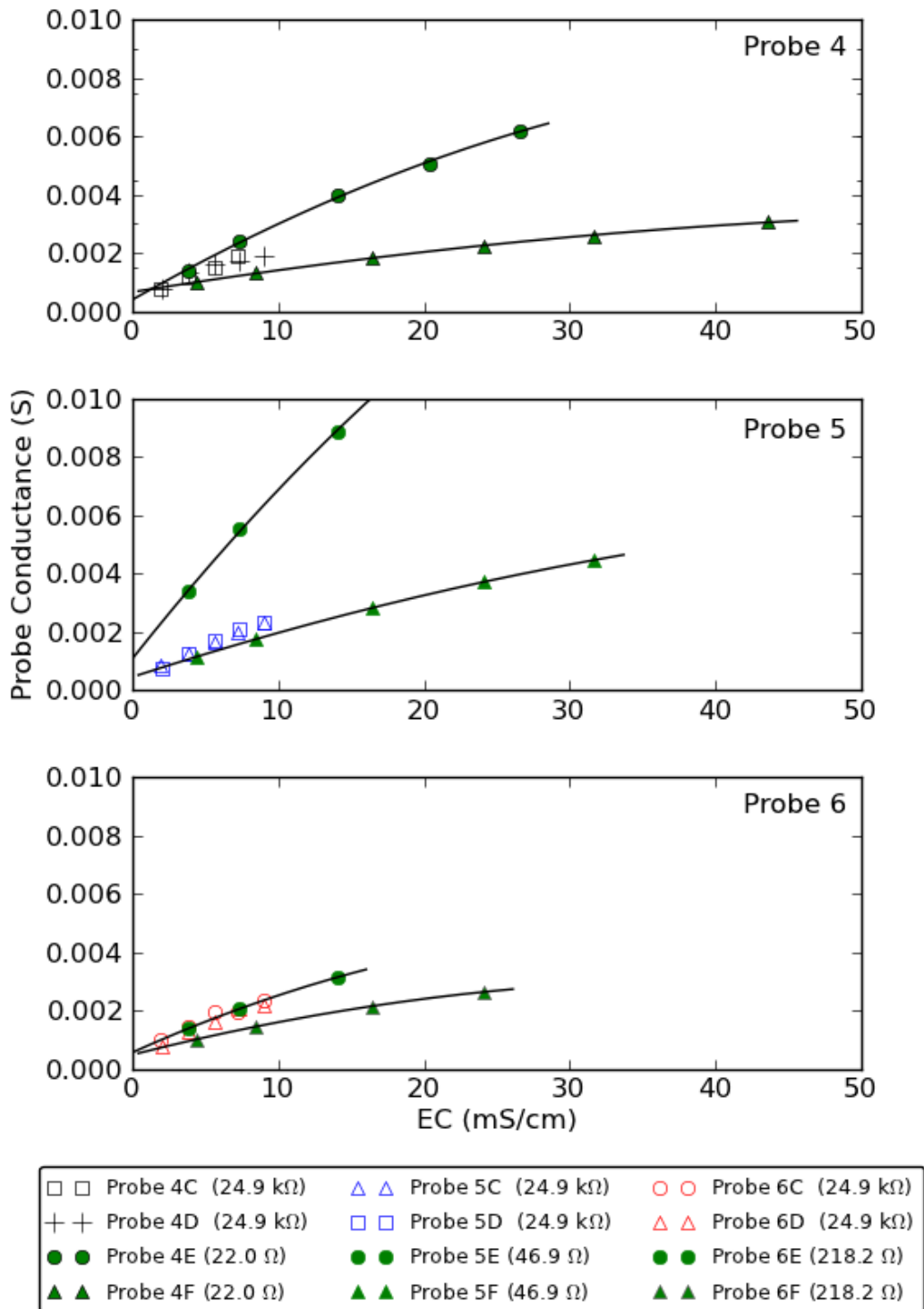


Figure 3.9: EC calibrations to static cell experiments with varied fixed resistors, R_f . Probe Conductance is calculated as $1/R_s$. Second order polynomial fit for Experiments E and F is in form $ax^2 + bx + c$.

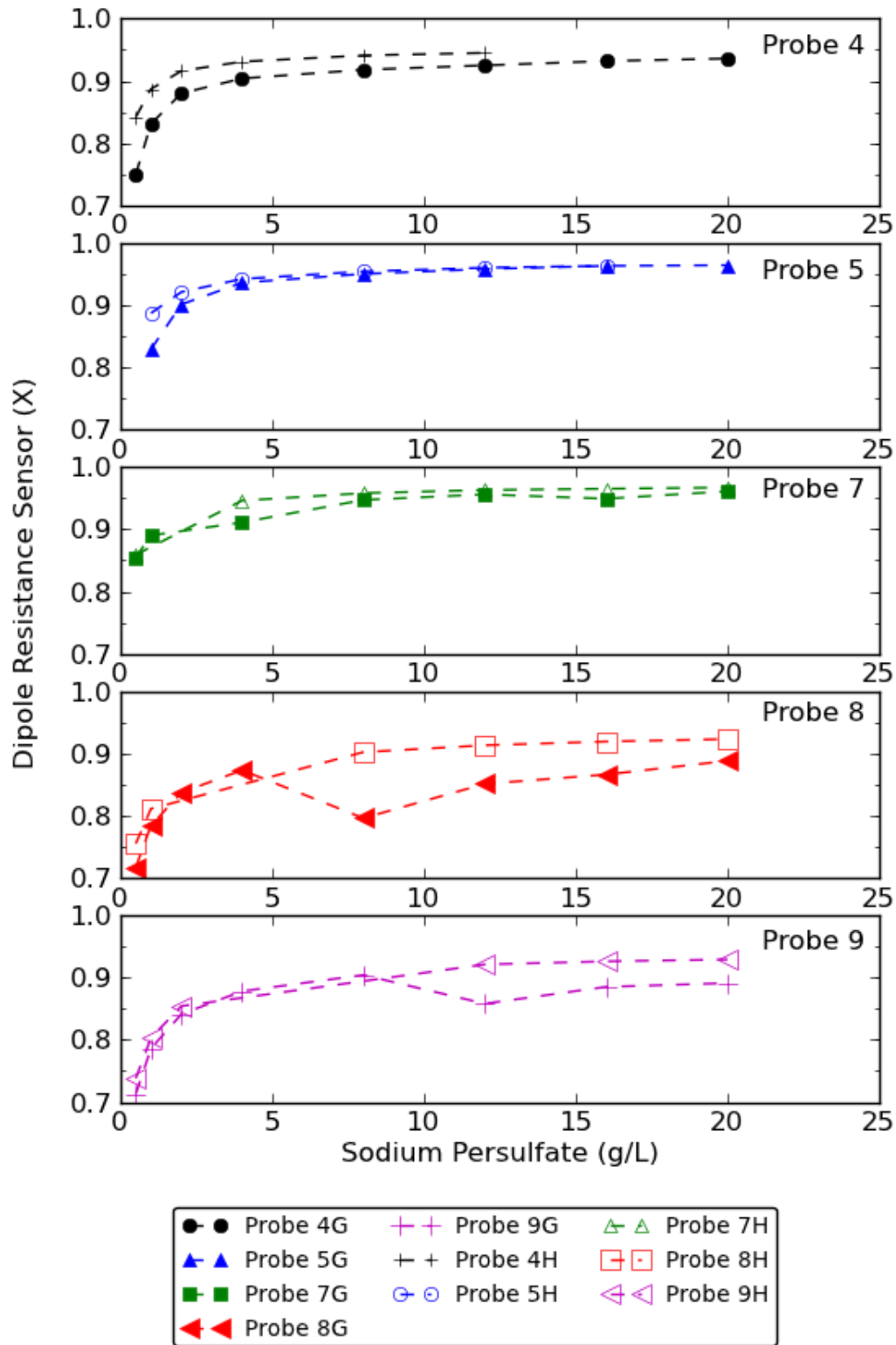


Figure 3.10: Static cell with sodium persulfate arranged by probe. Experiments G-H shown.

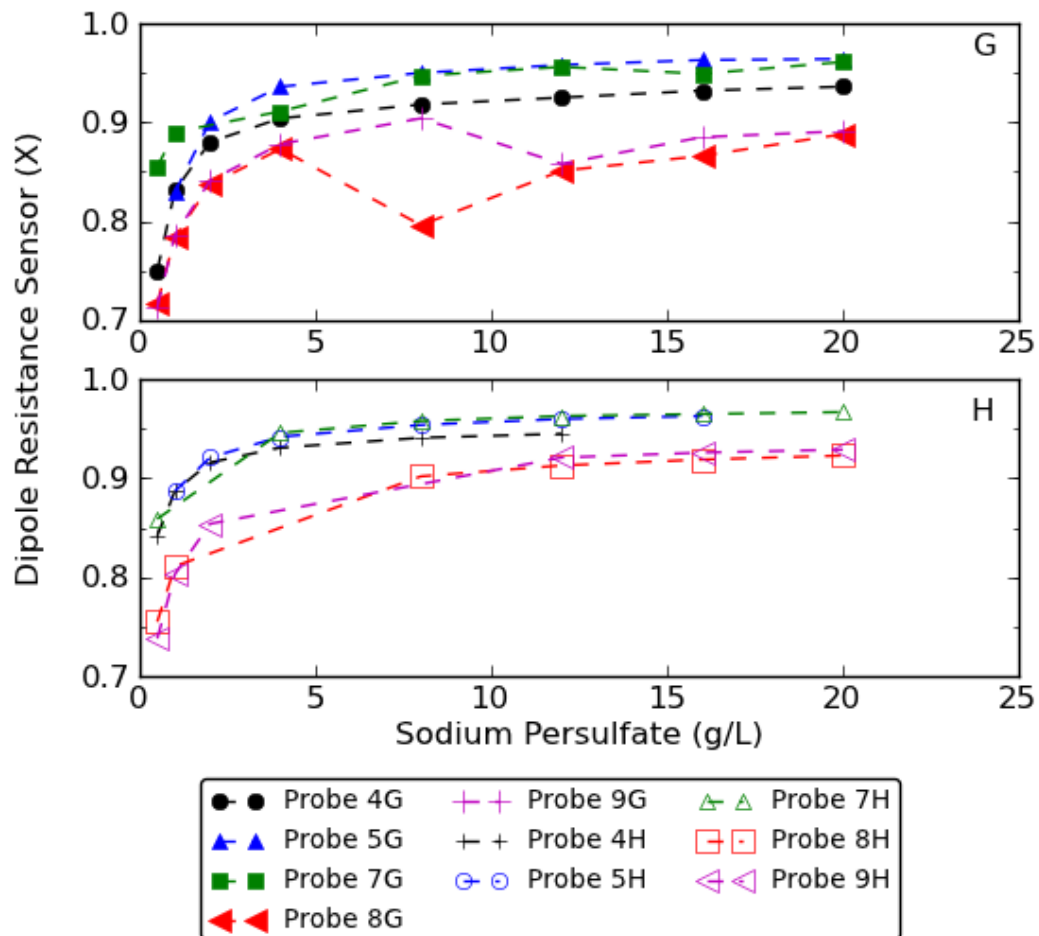


Figure 3.11: Static cell with sodium persulfate arranged by experiment. Top panel shows experiment G, bottom panel shows experiment H.

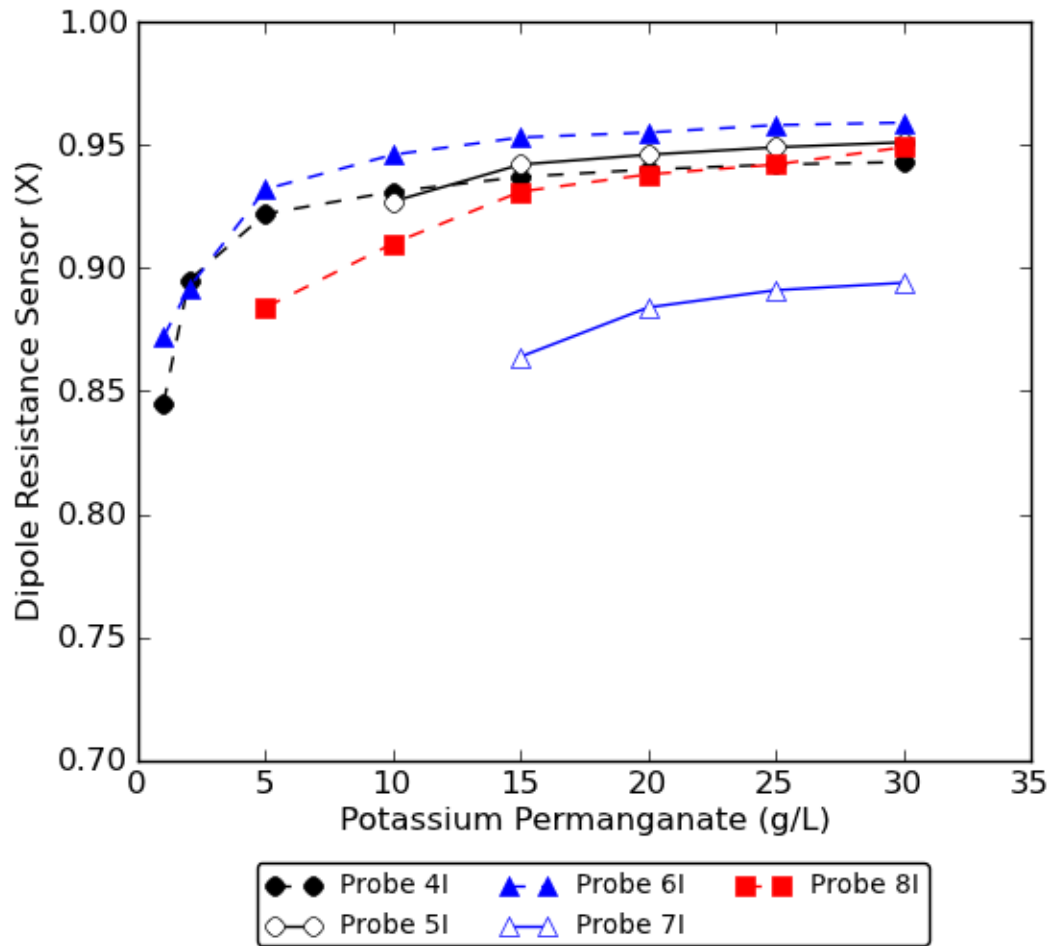


Figure 3.12: Static cell with potassium permanganate. Experiment I shown.

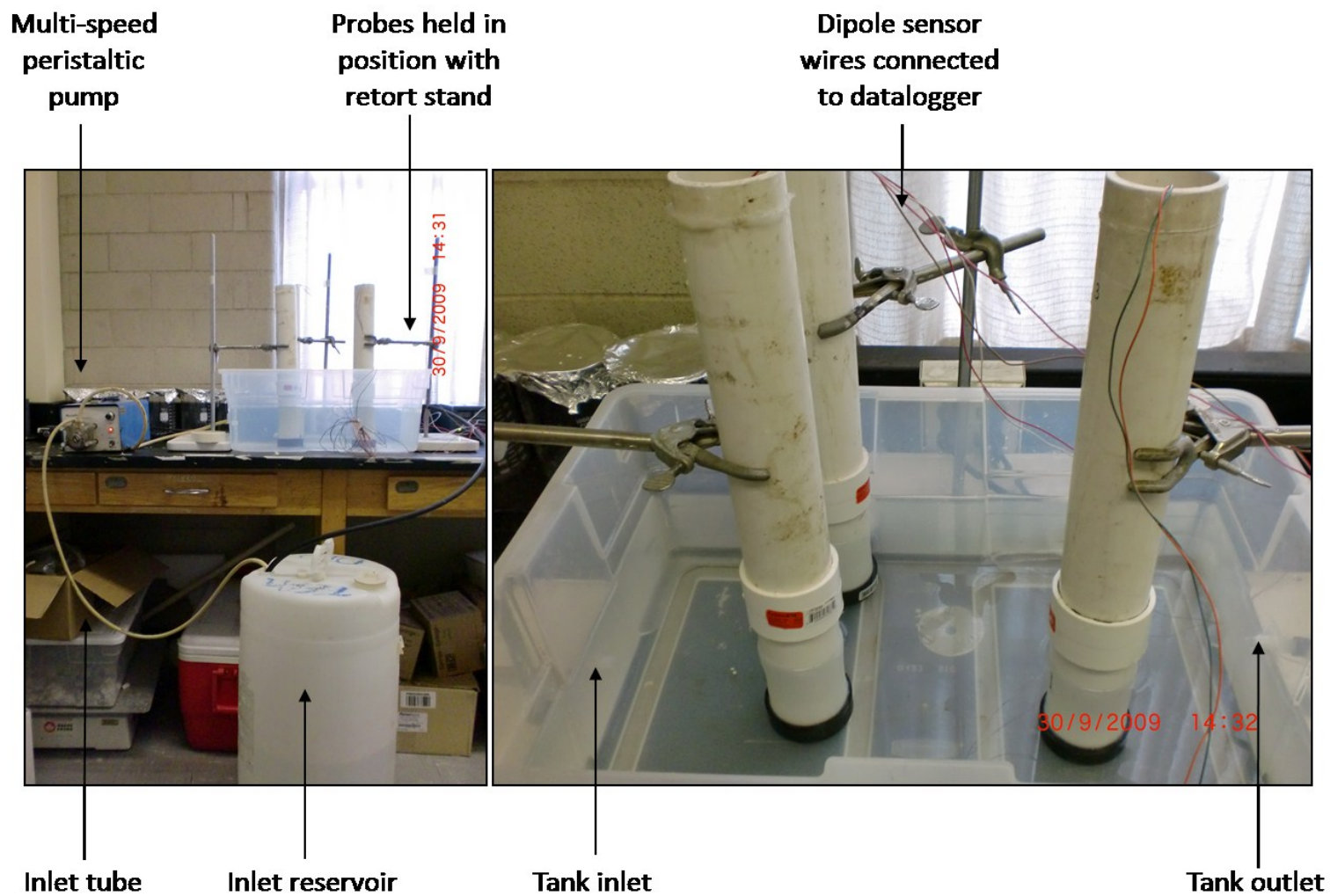


Figure 3.13: Close-up of flow system used for initial flow cell experiments

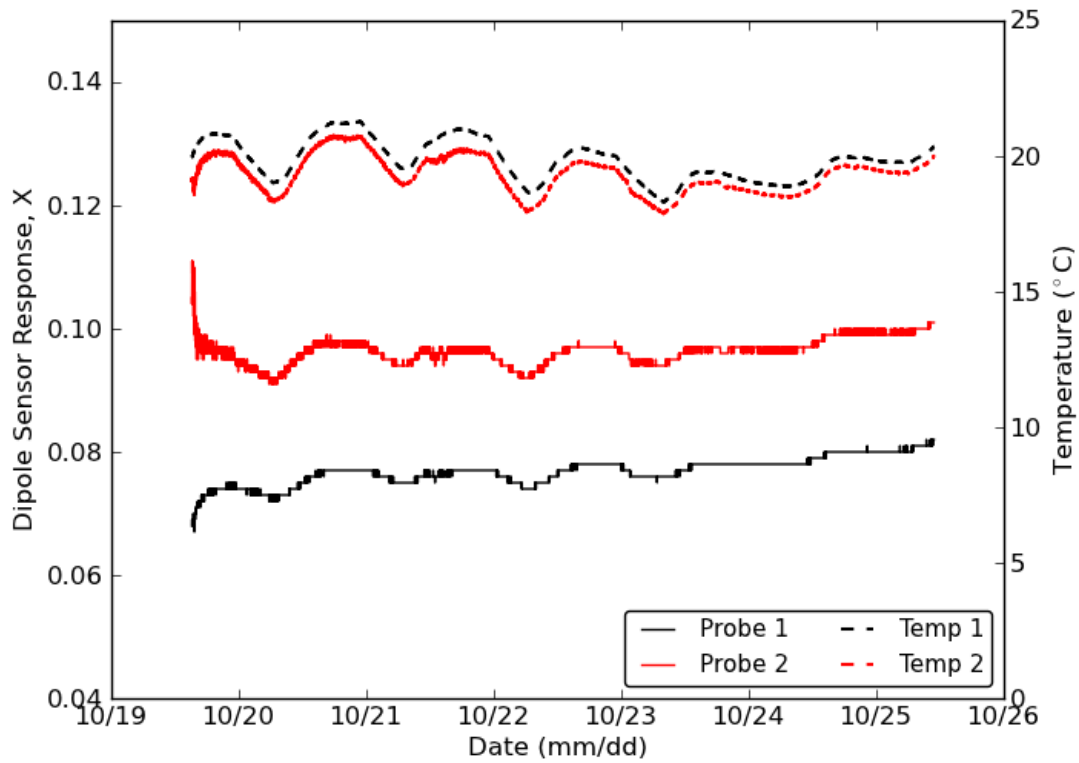


Figure 3.14: Experimental results for recirculation of DI water collected during initial flow cell experiments

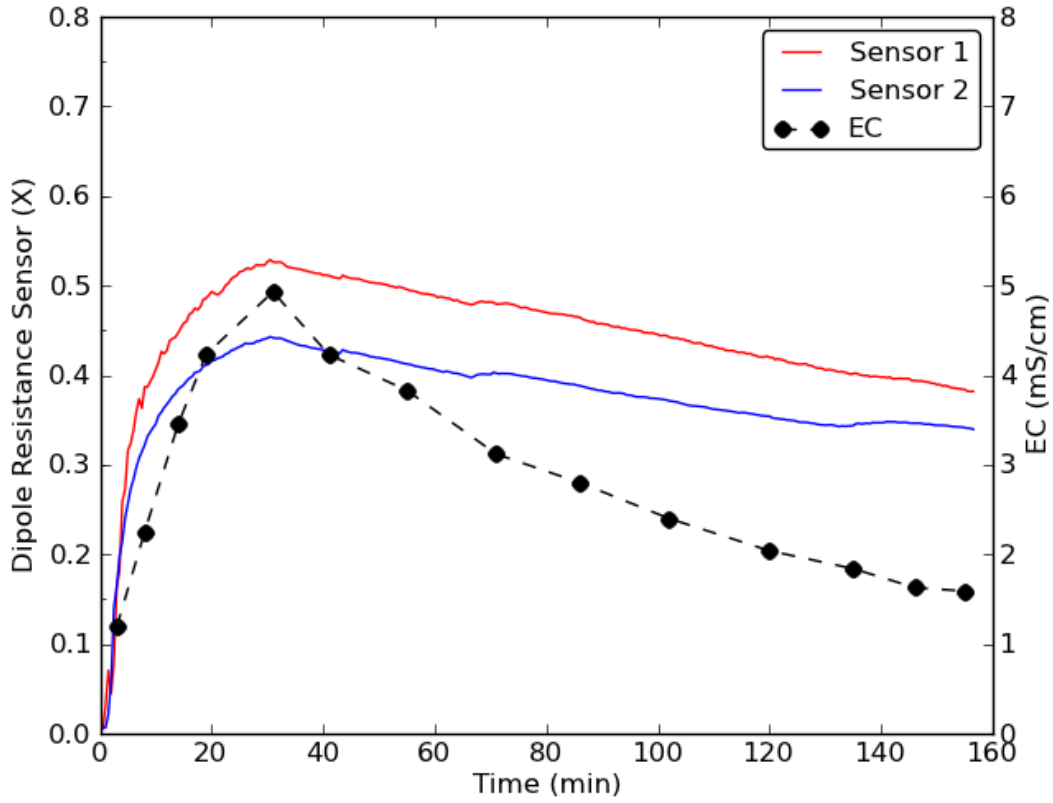


Figure 3.15: Example of BTC results from initial flow cell experiments, BTC-A shown

Chapter 4: High Resolution Laboratory Experiments

4.1 INTRODUCTION

Flow cell laboratory experiments in Chapter 3 that tested the dipole resistance sensor response to EC breakthrough were unable to provide strong conclusions on the measurement characteristics of the dipole sensor. The experiments did not observe the same correlation between EC and X on the falling limb of a BTC that was observed on the rising limb. However, the exact cause of this divergence between EC and X on the falling limb of breakthrough could not be isolated and analysis was unable to confirm whether the observed trends were a characteristic of the dipole resistance probe or the experimental flow cell design. A more sophisticated flow cell, the NeST system (Bowen et al., 2012), was constructed and tested to allow experimentation in porous media under more controlled conditions. The goals of these experiments are to analyze dipole sensor response to EC breakthrough and determine measurement capabilities of the sensor. This chapter describes BTC experiments using the NeST system for two scenarios: (1) DI water background flowing through the system during tracer injection, and (2) simulated groundwater flowing through the system during tracer injection.

4.2 MATERIALS AND METHODS

4.2.1 Probe construction

Two-wire resistance sensors were constructed using one inch diameter schedule 80 PVC pipe, 18 gauge copper lead wires, and 12 gauge stainless steel cable. The cables (1.5 cm lengths) were attached to the copper leads using electrical wire crimp connectors. After the ends of each cable was tucked into the bottom drill hole, a 1 cm length of detector cable was left exposed to the outside of the probe. Detectors were constructed from stainless steel to prevent potential corrosion during the course of laboratory experiments which was identified as a possible source of error in laboratory experiments described in Chapter 3.

A groove filed between the two holes allowed each detector wire to lay flush with the PVC surface. The two detectors were orientated vertically and parallel to each other and were spaced 0.3 cm apart. A thermistor was attached to the outside of the probe directly above the resistance

sensor to provide temperature measurements. (Note, the measurements collected by the thermistor agreed with the temperature measurement from the CTD-Diver with the same relationship shown in Figure 3.1. This data is not discussed further below.) The dipole resistance sensor was wired with a 2200 Ω resistor (1/4 W 1% MF).

4.2.2 Sandbox and monitoring equipment

EC breakthrough experiments were carried out in a sandbox tank constructed according to the Nested Storage Tank system design, NeSTs, described by Bowen et al. (2012). The size of the porous medium compartment (58.4 cm L x 41.3 cm W x 31.4 cm H) used in the NeSTs design was ideal for testing the accuracy of the dipole resistance sensors. Experiments described by Bowen et al. (2012) used a Point Velocity Probe (PVP) in a similar tank to determine groundwater velocity. Because the size of the PVP device is similar to the developed dipole resistance probe, the NeST system was an ideal choice for sandbox tests.

The NeST system is shown below in Figure 4.1. Water is added to the upstream reservoir with a peristaltic pump and enters the main compartment with porous medium through nine 1.25 cm diameter holes (Figure D1, right side). Flow leaving the reservoir through the downstream end is collected in the outlet reservoir. Figure 4.1 shows a set-up where water collected in the outlet reservoir is recycled back into the system with the peristaltic pump. Flow through the system is controlled by the hydraulic head between the upstream reservoir and the water level in the main compartment. Tank construction is described in Appendix D1 and Bowen et al. (2012).

The tank was initially damp packed in 2-3 cm layers with 57 kg (125 lb) of Barco Silica Sand provided by Opta Minerals, Waterdown, ON. The sand is highly uniform with a mean grain size (d_{50}) of 0.29 mm and a coefficient of uniformity (d_{60}/d_{10}) of 1.78 (<http://www.optaminerals.com/>, see Appendix D2). After each layer was added, the sand was tamped down to ensure an even distribution and compaction. Once a layer was tamped, the top was scraped with an abrasive brush to prevent heterogeneous layering when new sand layer was added.

The series of experimental trials using the NeST system was designed to compare EC breakthrough measured by the dipole resistance probe to breakthrough measured by a commercial sensor. A CTD-Diver model DI271, manufactured by Schlumberger Water Services

(<http://www.swstechnology.com/>), was used to provide an EC reference that could be compared to measurements recorded by the resistance probe. The CTD-Diver is a corrosion-resistant EC sensor that can also measure temperature and pressure. Specifications for the DI271 unit used in this experiment are listed in Table D2.

The conductivity detectors on the CTD-Diver and detectors of the dipole resistance sensor were installed at the same location in the tank to allow direct comparison between measurements. The CTD-Diver was fastened to the resistance probe with zip ties, with the detectors from both sensors aligned horizontally (Figure 4.2). The resulting probe bundle was installed directly in the center of the sand compartment after a 5 cm base of sand had been added and packed. The probes were positioned so the dipole resistance sensor was upstream of the CTD-Diver; the bundle was held in place with a clamp as additional sand layers were packed in the tank. Care was taken to pack sand closely around the probes to prevent heterogeneities. The cap on the bottom of the PVC probe caused the dipole resistance sensor to be located about 5 cm above the bottom of the probe, making the resistance sensor and CTD-Diver sensor sit 10 cm above the bottom of the tank.

A polyethylene tube (0.64 cm O.D.) with Nitex screen covered end was inserted into the tank 5 cm from the upstream end at tank centerline. The tube was pushed into the sand to the same depth as the resistance sensor. Disturbed sand directly surrounding the tube was repacked by hand. The tube was used with a syringe to inject NaCl solution tracer volumes into the system to produce BTCs.

The tank was packed for a second time mid-way through the experiments as discussed below in section 4.3. For the second pack, the cap of the dipole resistance probe was placed on the bottom of the tank and an additional 9 kg (20 lb) of silica sand was added to the top of the tank. Care was taken during the repacking process to replicate original packing procedures. At this time, the injection tube was reinserted at same location to the new depth of the probe sensors. The top of the tube was fastened to the upstream tank wall with duct tape to reduce movement when attaching syringes during tracer injections. The injection tube was not fastened during the first tank pack which subjected it to potential movement when attaching and removing syringes.

4.2.3 Electrical conductivity breakthrough tests

EC breakthrough tests were performed for two scenarios: (1) DI water flowing through the tank during tracer injection and (2) a simulated groundwater solution with elevated ionic concentrations flowing through the tank during tracer injection. For all tests, laboratory grade NaCl (BDH, BDH0286-500G) was used as the tracer since it is easy to use, safe, and low cost. Electrical resistivity mapping from a sand box tracer plume reported by Gheith and Schwartz (1998) suggested NaCl would be able to create controlled EC BTCs. Calcium chloride dihydrate (EM Science, CX0130-2), magnesium sulfate anhydrous (EMD, MX0075-1), and sodium bicarbonate (Sigma-Aldrich, S6014-1KG) were used to prepare the simulated groundwater solution. Constituent concentrations for the feed solution were selected based on typical ionic compositions of potable water as reported by Davis and DeWeist (1966, p.98). Ionic compositions of the two feed solutions, Solutions A and B, are listed in Table 4.1.

The resistance sensor and CTD-Diver were programmed to take simultaneous measurements at 30 sec intervals. The CTD-Diver was set for a conductivity range of 30 mS/cm and used both the specific conductivity (readings autocorrected to 25 °C) and conductivity settings (raw measurements not corrected to a reference temperature). The temperature change during a breakthrough event was generally minimal, so there was little difference when comparing general conductivity or specific conductivity measurements to the resistance measurements.

Water was pumped at a constant rate into the main storage reservoir of the tank from a larger supply reservoir. The hydraulic head difference between the upstream storage reservoir and the rest of the tank resulted in flow through the main porous medium compartment and into the outlet container. Water was removed from the outlet container by an elevated tube pumping at the same rate as the inlet tube. When tests were started, the NeST upstream reservoir was filled manually to allow saturation of the porous medium. Although the pumping rate was always constant, flow through the system varied between approximately 38 – 79 cm/hr during all tests since the water level in the upstream reservoir was slightly different for each test.

After the system was running at a constant flow rate and the monitoring probes had collected sufficient baseline data, breakthrough experiments were conducted by injecting a slug of NaCl solution into the system using a 60 mL syringe and the polyethylene tube at the upstream end of

the tank. After each tracer injection, a volume of water with the same ionic composition as the circulating water was injected to purge the injection tube. This was done because a small amount of tracer remained in the injection tube after the syringe was used to add the tracer slug; the purge volume was injected with a second syringe to ensure all remaining tracer entered the tank system. Injection rates were generally 60 mL/min +/- 10 seconds. Tracer volume (typically 30 – 60 mL), concentration (typically 20 – 40 g/L), and purge volume (typically 30 – 60 mL) were all varied during experiments to test probe responses under a range of conditions. Details of tracer injections for each BTC are described in Table 4.2.

Feed solutions were mixed in large reservoirs (20 and 60 L) by diluting concentrated solutions with deionized water. The concentrated solutions were produced by adding a mass of each constituent to a 1L volumetric measurement of water that was mixed with a magnetic stir bar.

EC measurements of tracer solutions and flow system reservoirs were recorded with a handheld Thermo Orion meter (model 1219000 with 013010MD conductivity probe) while pH was measured with an Orion 710A pH/ISE meter. The measured EC for each prepared volume of Solutions A and B ranged between 422-457 and 803-856 $\mu\text{S}/\text{cm}$, respectively (Table 4.2); pH for both solutions ranged between 7.4 and 7.6.

4.3 RESULTS AND DISCUSSION

Dipole probe measurements were analyzed by comparing plots of raw EC from the CTD-Diver with raw sensor records (X) and by comparing normalized EC to the normalized dipole resistance measurements. Normalized EC was calculated as the conductivity measurement from the CTD-Diver divided by the peak EC measured by the CTD-Diver (EC_m) during a specific BTC (EC/EC_m). Likewise, normalized dipole measurements were plotted as the measurement value divided by the peak record (X/X_m). Plotting normalized records provided a direct comparison between sensor response of the CTD-Diver and dipole resistance probe and facilitated a direct comparison of the BTC features.

Data for 38 DI water (BTC1-38) and 38 simulated groundwater (BTC39-76) trials were collected and are summarized in Table 4.2. One DI BTC (BTC38) and all of the simulated groundwater BTCs (BTC39-76) were produced with the second tank pack. The tank was

repacked after BTC37 in an attempt to improve repeatability of BTC peaks when an identical injection tracer concentration and volume was used. The first tank pack indicated some preferential pathways may have existed surrounding the monitoring probe bundle, while the second pack provided more consistency in results. Further discussion related to preferential flow paths and shifting the injection tube are included in sections 4.3.4 and 4.3.5.

4.3.1 Deionized water breakthrough tests

The BTC experiments using DI background showed the resistance sensor was capable of accurately measuring EC breakthrough to a peak, and then back to a zero baseline. Figure 4.3 shows an example of two BTCs (BTC11 and 18) recorded during the experiments. The panels on the left show normalized data, while the right panels show raw EC data collected by the CTD-Diver and raw resistance sensor measurements (X) collected by the dipole probe. Each panel of raw data shows the peak EC (EC_m) measured by the CTD-Diver and the peak dipole measurement (X_m) recorded during that particular BTC. CTD-Diver measurements are shown in blue and dipole resistance sensor measurements are shown in red. Figure 4.3 shows typical sensor response to changing EC, although the shape of BTCs varied from experiment to experiment and was not always as symmetrical as those shown.

Irregularity in BTC shape during the DI experiments is attributed to manual injection of the tracer and purge solutions with a syringe and preferential flow paths observed during the first tank pack. Preferential flow paths are discussed further in sections 4.3.4 and 4.3.5. The injection rate of both the tracer and purge solution and time needed to switch from the tracer syringe to the DI purge water syringe were subject to variability due to human error. This variability was compounded by the injection tube potentially shifting while injecting solution and changing syringes. This error likely affected the uniformity with which the tracer was added to the system, creating different tracer plumes for each BTC. The DI BTC results in Figure 4.4 and Appendix D4 show the shape of curves recorded by the CTD-Diver varied during BTC1-38. In many cases, the rising limb and falling limb of each BTC were not symmetrical and some curves were characterized by multiple peaks (see BTC1-6, 8, 10, 14, 15, 17, 19-21, 23, 24, 25, 27-29, and 37 in Appendix D4).

Irregular BTC shape during the DI experiments provided insight into the dipole sensor response during breakthrough. The data show the dipole sensor was unable to measure small changes in curve shape during breakthrough with the same resolution the CTD-Diver was able to resolve. Figure 4.4 illustrates how the resistance probe responded to these types of changes in comparison to the readings given by the CTD-Diver for BTC10 and 15. The resistance sensor was still able to accurately measure breakthrough from zero EC to a peak, and then back down to zero, but it was unable to detect fine changes throughout each curve that occurred at an elevated EC. The right panels of Figure 4.4 show the EC data collected by the CTD-Diver in blue. For both BTC10 and 15, when the rising limb of the CTD-Diver curve reached approximately 1 mS/cm, each set of measurements began to diverge from a symmetrical curve shape; BTC10 showed a period of small increases in EC before beginning a period of rapid rise again before EC_m , while BTC15 showed a sustained period of elevated EC around 1 mS/cm before reaching the falling limb. The raw measurements collected by the resistance sensor (X) on the right panels of Figure 4.4 show the dipole probe collected a very smooth and symmetrical BTC for both experiments and did not resolve the fine changes in EC recorded by the CTD-Diver.

It is possible that the fine changes in EC at elevated concentrations were masked by the resistance sensor picking up the large overall breakthrough that was occurring rather rapidly. If this were the case, the sensor may potentially be able to respond to fine changes in BTC shape if breakthrough were occurring over an extended period of time. In addition, factors such as construction methods and choice of materials could potentially contribute to a loss of resolution which impacts the sensor's ability to resolve fine changes during breakthrough.

For the two cases where EC_m was less than 0.6 mS/cm (BTC12 and 16), the resistance sensor did not show a response to changing EC. The dipole sensor did show an accurate response for EC_m of 0.618 mS/cm (BTC 26). The resistance sensor was not able to resolve peaks recorded by the CTD-Diver during BTC 12 and 15 which indicated the dipole probe had a higher detection limit than the CTD-Diver during the DI experiments.

Uncertainty related to flow conditions in the tank which likely caused the irregular-shaped BTCs influence how dipole probe response during the DI experiments can be interpreted. Response of the dipole resistance probe to small changes in curve shape at elevated EC is investigated further in section 4.3.6, where BTC results are plotted as a function of probe

conductance. Discussion related to measurement volume and minimum detection limits of the sensor is included in section 4.3.2.

4.3.2 Simulated groundwater breakthrough tests

The EC BTCs measured for the simulated groundwater experiments showed an elevated background reading (X) before and after the tracer slug passed through the system. As shown in Figure 4.5, the elevated background can be easily seen in the baseline resistance sensor measurements, where the top right panel shows a baseline of $X=0.13$ for BTC43 which was simulated with Solution A (0.424-0.457 mS/cm) and the bottom right panel shows a baseline of $X=0.2$ for BTC 49 which was simulated with Solution B (0.841 mS/cm). These elevated background measurements were not observed during the DI experiments shown in Figures 4.3, 4.4, and Appendix D4. Figure 4.5 shows the elevated background EC appeared to be more obvious in the resistance sensor measurements than the CTD-Diver measurements, which are a characteristic of the nonlinear relationship between resistance sensor readings and EC. Further processing with this data in section 4.3.6 below shows the elevated resistance sensor measurements in Figure 4.5 can be calibrated to match EC values recorded by the CTD-Diver. Time series profiles of all BTC experiments with elevated ionic background can be referenced in Appendix D5.

The supply reservoirs used to circulate flow during the BTCs were measured to have EC of approximately 0.440 and 0.830 mS/cm for Solutions A and B, respectively (Table 4.2). When these solutions were circulated through the tank to provide elevated background EC, the background measurements recorded by the CTD-Diver were much lower than EC measured for the electrolyte solutions, showing 0.012-0.013 mS/cm and 0.025-0.027 mS/cm for Solution A and B, respectively. Calibration and verification of CTD-Diver accuracy completed before the NeST experiments and after the first tank pack showed the CTD-Diver was able to accurately measure the EC of a static cell solution (see Appendix D6). The difference between EC for the simulated groundwater compared to baseline CTD-Diver measurements during BTC39-76 is likely a function of the influence the sand in the tank has on the sensors. Pure silica is an insulator; the Barco Silica sand used in the NeST system is listed as 99.7% SiO_2 (Optaminerals

Inc., 2012). Both the dipole resistance sensors and the CTD-Diver were placed in direct contact with the sand pack, so sensor response at both probes was reduced by the sand grains.

The dipole resistance probe and the CTD-Diver use a two-wire detector system as their sensors; the response between the two detectors is recorded as the measurement which is then related to EC. As described in section 1.3.3, EC is a measure of electric current transmitted by charged ions. The ions travel in solution and through surface conduction on soil grains when porous medium is present (Wildenschild et al., 2000). Because the tank was packed with sand grains in between and in direct contact with the detectors, the porous medium prevented electric current from travelling directly from one detector to another. During each measurement, ions were forced to travel through pore spaces and along grain surfaces to allow the transmission of current. As a result, the measurements collected by each probe are dampened in comparison to what would be measured by the sensor in an open electrolyte solution such as the static cell experiments in Chapter 3.

An EC measurement which lumps together the influence of a porous medium and the pore fluid electrolyte is often called bulk electrical conductivity (EC_{bulk}). The ratio of this value to the EC of the electrolyte solution ($EC_{electrolyte}$) is called the formation factor, F (Wildenschild et al., 2000):

$$F = \frac{EC_{electrolyte}}{EC_{bulk}} \quad (19)$$

EC_{bulk} needs to measure a volume of soil to be able to average the effects of soil grains and pore fluid EC. Typically, it would be measured by a four electrode system which would allow measurement penetration into the soil volume, rather than the two-wire sensors used on the dipole probe and the CTD-Diver that only provide a contact measurement.

Keeping the measurement volume of two electrode sensors in mind, calculation of formation factors still provides insight for the *in situ* measurements reported by the dipole probe and the CTD-Diver. If the baseline measurements reported by the CTD-Diver are assumed to represent EC_{bulk} , a formation factor can be calculated using the EC of Solution A and B as $EC_{electrolyte}$. For all BTC experiments with simulated groundwater, formation factors calculated from the assumed

EC_{bulk} (0.012-0.013 mS/cm Solution A, 0.025-0.027 mS/cm Solution B) and the EC of the simulated groundwater, $EC_{\text{electrolyte}}$ (0.424-0.457 mS/cm Solution A, 0.841 Solution B) ranged from 31-38. These values are much higher than a formation factor of approximately 5 for silica sand reported by Wildenschild et al. (2000). However, Wildenschild et al. (2000) used an experimental set-up designed to measure EC_{bulk} that included a four-wire electrode system for measuring EC and a sleeve to control fluid pressure. It is reasonable to assume that contact of soil grains with the dipole detectors dampened signal and response during measurements in comparison to what a four-wire electrode would report. This is because the two-wire electrodes pass a measurement signal directly between detectors, while a four electrode system passes a measurement field over a volume of soil; an obstruction caused by soil grains likely has a larger influence on a contact dipole measurement in comparison to a four-electrode measurement which samples a volume of soil. This shows that the formation factors calculated from the NeST system are expected to be larger than what was reported by Wildenschild et al. (2000) because the value assumed to be EC_{bulk} did not measure a representative volume of soil and porewater and as a result, the reported EC_{bulk} is lower than what would be measured by a four electrode sensor because soil grains are directly interfering with the measurement signal passed between detectors.

The formation factor of approximately 5 presented by Wildenschild et al. (2000) shows *in situ* EC measurements in the NeST system should be expected to be less than the EC of the simulated groundwater solutions ($EC_{\text{electrolyte}}$). Comparison of the measurement volume for two-wire and four-electrode sensors shows measurements from a two-wire sensor are influenced more by the presence of porous media; this produces a smaller value for EC_{bulk} and corresponding larger formation factor, F , than what would be reported by a four-electrode system. Thus, the formation factors of 31-38 calculated from the simulated groundwater experiments appear to agree with measurement values that would be expected for two-wire EC measurements in silica sand.

Laboratory conditions were more controlled for simulated groundwater experiments which resulted in BTCs that were more symmetrical (compare Figures D6-D18 to Figures D19-D31). Consequently, the response of the dipole sensor to small changes in BTC shape at elevated EC for the simulated groundwater experiments cannot be analyzed in detail the way they were for

the DI BTC experiments. Analysis of DI BTCs in Section 4.3.1 indicated the dipole sensor could not resolve small changes in EC when values were close to EC_m . It is anticipated a similar response would be observed for the simulated groundwater experiments if the BTCs were more irregular, although this hypothesis cannot be confirmed.

For the simulated groundwater experiments, the resistance sensor did not appear to have any measurement limitations in terms of minimum detection limits such as what was observed for the DI BTCs. During the simulated groundwater experiments, 22 BTCs had EC_m less than 0.5 mS/cm (BTC48, 55-76) where the smallest observed peak was 0.066 mS/cm during BTC66. For all cases, the resistance sensor recorded a BTC with the same shape as the CTD-Diver. It is difficult to draw definitive conclusions between the minimum detection results for the DI water and simulated groundwater BTCs due to potential irregularities caused by tank packs. The sandbox was repacked after the early DI tests (BTC1-37) where the resistance sensor response did not respond to the lowest two CTD-Diver peaks of 0.526 and 0.380 mS/cm for BTC12 and 16, respectively. Section 4.3.4 below shows the timing of EC_m and X_m indicated heterogeneities may have been present surrounding the probe bundle for the initial sand pack. It is possible that flow irregularities were responsible for the minimum detection limits observed for the DI tests. This is supported by the simulated groundwater BTCs which indicated the resistance sensor was capable of monitoring small EC peaks.

4.3.3 Influence of temperature

The CTD-Diver specific conductivity setting was used for 31 DI water BTCs (BTC1-31) where measurements are expressed as conductivity at 25 °C, while 7 DI (BTC32-38) water and all 38 simulated groundwater BTCs were measured using the conductivity setting where records were not referenced to any particular temperature.

Measurements recorded by the resistance sensor are not compensated for changing temperature, and therefore, direct comparison of measurements taken with the CTD-Diver should use the conductivity setting. Temperature change measured by the CTD-Diver during the 38 DI water breakthrough experiments averaged 0.21 °C, with a maximum change of 0.92 °C during BTC9, while temperature change during the simulated groundwater experiments averaged 0.17 °C with a maximum change of 1.53 °C during BTC 66.

The Schlumberger CTD-Diver uses the linear relationship in Eq. (5) to relate conductivity measurements to EC_{25} using a compensation factor $a = 0.0191 \text{ C}^{-1}$ (E Dijkstra, personal comm, 2012). Therefore, BTC measurements can be manually converted between raw conductivity and measurements referenced to $25 \text{ }^\circ\text{C}$ after experimental data has been collected, regardless of the CTD-Diver conductivity setting that was used.

The influence of temperature on the BTC results is minimal in the laboratory when conditions are controlled and temperature changes are minimal. Figure 4.6 shows BTC 9 where the largest temperature change during DI water BTC experiments was observed to be $0.92 \text{ }^\circ\text{C}$ and CTD-Diver conductivity was originally recorded as values referenced to $25 \text{ }^\circ\text{C}$. When specific conductivity at $25 \text{ }^\circ\text{C}$ is converted back to raw conductivity using Eq. (5), the difference between each converted value ranged between 9 to 11%. However, because this conversion is a linear correction based on temperature, the main source of this difference is the gap between measurement temperature (which averaged to be $19.6 \text{ }^\circ\text{C}$ for BTC 9) and the $25 \text{ }^\circ\text{C}$ reference.

This error is illustrated in Figure 4.7, where the solid black line represents EC breakthrough at a constant hypothetical temperature, Temp 1, and the dotted black line represents the same EC breakthrough at a higher hypothetical constant temperature, Temp 2 which can be assumed to be $25 \text{ }^\circ\text{C}$. If the Temp 1 curve converted to breakthrough at $25 \text{ }^\circ\text{C}$ using Eq. (5), they will be identical to the Temp 2 curve if the relationship in Eq. (5) was perfect and Temp 1 is between 3 and $47 \text{ }^\circ\text{C}$. Therefore, if the EC breakthrough for Temp 1 or Temp 2 were compared to another independent set of measurements, such as the resistance probe in this experiment, a comparison of curve shape would be consistent regardless of whether the comparison was made using the raw conductivity measurements, or the ones corrected to $25 \text{ }^\circ\text{C}$. A more quantitative way to say this is the difference between each measurement of the raw conductivity (Temp 1) and temperature corrected curve (Temp 2) remains the same.

Error is introduced into the comparison when measurement temperature begins to shift during a breakthrough curve. The dashed blue line in Figure 4.7 shows the example of the same EC breakthrough, where measurement temperature started at Temp 1, but then began to shift upwards. If this dashed line were corrected to $25 \text{ }^\circ\text{C}$, it will give the same curve as Temp 2, although the raw conductivity version of this curve has a different shape. In the case when temperature is shifting during the BTC, the percent difference between the raw conductivity

curve and corrected conductivity curve changes for each measurement when temperature changes.

The maximum error introduced by comparing a conductivity measurement referenced to 25 °C to raw resistance sensor measurements is the range in percent error between conductivity corrections at the minimum and maximum measurement temperatures. Therefore, for BTC 9, the 0.92 °C temperature change during the test introduced a 1.8% error into a comparison between specific conductivity and raw resistance.

Almost no difference exists between the temperature compensated and raw EC values when BTCs are plotted as relative conductivity. For BTC 9 in Figure 4.6, an average difference of 0.6% was observed between the two datasets, which is less than the CTD-Diver accuracy of 1% reported by Schlumberger (Schlumberger Water Services, 2012b, p.12). Further details of these calculations can be referenced in Appendix D7.

4.3.4 Arrival times of EC_m and X_m

The time to peak breakthrough was very consistent for the simulated groundwater experiments. All dipole resistance curve peaks (X_m) arrived before CTD-Diver peaks (EC_m), as the resistance sensor detectors were 2.1 cm upstream of the midpoint of the CTD-Diver sensor. The timing between peaks ranged between 3.0 and 5.5 minutes, which translates into a travel velocity of 22.9-42.0 cm/hr based on the 2.1 cm distance between sensor detectors. These velocities are less than the tank velocities in Table 4.2 (43.1-58.1 cm/hr, Velocity A, for the simulated groundwater BTCs calculated as distance from the injection point to the CTD-Diver divided by the time from injection start to EC_m ; or 47.1-63.2 cm/hr, Velocity B, calculated as distance from the injection point to the dipole sensor divided by the time from injection start to X_m).

$$Velocity A = \frac{\text{Time from start of tracer injection to } EC_m}{\text{Distance from injection tube to CTD - Diver}} \quad (20)$$

$$Velocity B = \frac{\text{Time from start of tracer injection to } X_m}{\text{Distance from injection tube to dipole resistance sensor}} \quad (21)$$

The differences between the calculated velocities could indicate a difference in response time for the dipole resistance sensor in comparison to the CTD-Diver. The lower velocities calculated from the time between EC_m and X_m (22.9-42.0 cm/hr) suggests the dipole resistance sensor responded faster to EC than the CTD-Diver. A faster response from start of breakthrough to X_m at the dipole sensor would increase the time gap between X_m and EC_m ; consequently, velocity calculated as the time gap between X_m and EC_m divided by the 2.1 cm distance between sensors produces a lower velocity than Velocity A in Table 4.2. This is further supported by Velocity B in Table 4.2. Velocity B is slightly higher than Velocity A; if sensor response was faster at the dipole probe, the shorter time from injection start to X_m results in a higher velocity than the time from injection start to EC_m . A source of uncertainty in these calculations is the exact location of the bottom of the injection tube in the sandbox is unknown; if the actual distance to the sensor bundle was slightly shorter than the distance measured at the top of the sandbox, it could account for some of the differences between the velocities in Table 4.2 and the range calculated from the time between X_m and EC_m (22.9-42.0 cm/hr). The response time of the dipole resistance sensor can only be compared to the CTD-Diver response time; little can be said to compare timing of peak NaCl solution concentration with X_m and EC_m .

In addition to uncertainty related to the exact location of the injection tube, analysis of the dipole resistance sensor response time is affected by uncertainty due to measurement interval. The measurement interval of 30 seconds allows for up to 30 seconds in uncertainty in the exact arrival time of measurement peak at each probe. Peak time used for calculation of Velocity A and B could potentially have 30 seconds of uncertainty, while a comparison of X_m and EC_m to calculate a velocity (22.9-42.0 cm/hr) could have up to 60 seconds of measurement uncertainty. The velocity calculations indicate the dipole resistance sensor may have had a slightly faster response time than the CTD-Diver, although uncertainty related to the exact position of the end of the injection tube and the measurement interval likely accounts for some of the calculated differences.

Timing between peaks for the DI water BTCs showed less separation and was less predictable; BTCs showed an average of 1.7 minutes between each peak, although resistance sensor peaks did not consistently arrive before CTD-Diver peaks. The variability in arrival time of the BTC peaks for the DI experiments suggests preferential flow pathways may have existed

surrounding the monitoring probe bundle during the first tank pack which was used for all of the DI BTC experiments. Certain preferential paths may have allowed the tracer to reach the CTD-Diver before the dipole sensor, explaining why EC_m could arrive first when it was positioned 2.1 cm downstream from the resistance probe (see BTCs 6, 7, 9, 11, 13-15, 18, 26, 37 in Table 4.2). The amount of variability was likely caused by human error during the manual tracer injection process: the injection tube was not fastened to a solid object during the first tank pack and the process of attaching a syringe, injecting tracer, and removing the syringe likely caused the tube to shift which influenced the location of the tracer injection in the sandbox. The amount of variability in CTD-Diver peaks (EC_m) for the DI BTCs from the first tank pack compared to the simulated groundwater experiments supports this idea. For tracer injections of the same volume and comparable EC, the standard deviation of for EC_m was 2.9-8.7 times greater for the DI experiments compared to the simulated groundwater BTCs (Table 4.3). Cases where EC_m arrived before X_m indicates that preferential pathways existed around the monitoring probe bundle during the first tank pack, while the variability in arrival time of EC_m compared to X_m indicates movement of the injection tube during each syringe application shifted the location where the tracer was injected in the sandbox, allowing the tracer to reach different preferential paths.

The variability in peak timing for the DI BTC experiments did not appear to be a characteristic of the dipole probe response because of the consistency in peak arrival time observed during the simulated groundwater BTCs and was attributed to preferential pathways in the first sand pack. Consequently, BTCs using the first sand pack cannot be used to analyze sensor response time the same way they were for the simulated groundwater experiments.

4.3.5 Repeatability of measurements

Table 4.2 shows measured EC peaks were often different, even when tracer volume and EC was similar. These differences are mainly attributed to human error during the manual tracer injection process such as moving the injection tube during the injection and altering the rate of injection. During the simulated groundwater experiments, the injection tube was held in place against the tank using duct tape which was found to improve the consistency of recording similar EC peaks. Although more robust laboratory methodology could likely reduce these errors, the

inconsistency did not interfere with the overall study goals of showing the resistance sensor was capable of measuring EC breakthrough. For the simulated groundwater experiments in particular, the results showed consistency between sensor responses when similar BTCs were measured by the CTD-Diver; when multiple BTCs showed similar EC peak and shape, the corresponding resistance sensor curves were also comparable.

4.3.6 Probe calibrations for NeST experiments

As mentioned in section 4.3.2, the response of both the dipole probe and the CTD-Diver *in situ* in the NeST system is dampened in comparison to how the probes would respond in a static cell with the same solution from the tank. As a result, a calibration of probe response to EC during a static cell experiment such as those in section 3.3.1.5 cannot be applied to the dipole sensor from the NeST breakthrough experiments. However, a calibration of *in situ* dipole probe measurements to *in situ* EC was needed to further analyze observed characteristics from sections 4.3.1 and 4.3.2 that indicated the dipole resistance sensor did not respond well to small changes in EC during breakthrough and also indicated the sensor recorded an elevated background reading well above what was recorded by the CTD-Diver during the simulated groundwater experiments.

Results from the NeST experiments were calibrated to EC by two methods: (1) a direct comparison of CTD-Diver peak, EC_m , with dipole resistance probe peak, X_m and (2) a comparison of all BTC data plotted as dipole sensor response against CTD-Diver readings after the datasets had been shifted to account for travel time between the two probes. Figure 4.8 shows the calibration produced by the first method where only probe peaks were used. The red 'x' markers show the peaks collected during the DI experiments while the blue '+' markers show peaks collected from the simulated groundwater experiments. The top panel from Figure 4.8 is included to illustrate the relationship between the raw peaks, EC_m and X_m before any processing was done with the data. The bottom panel shows the same data after the X_m measurements were rearranged according to Eq. (17) and reported as probe conductance. The bottom panel indicates the relationship between probe peaks was much tighter for the simulated groundwater experiments in comparison to the DI experiments. The second order polynomial fit to the simulated groundwater experiments agrees well with the data ($r^2 = 0.91$) and continually

increases over the range of CTD-Diver readings. The fit for the DI experiments peaks around $X_m = 9$ mS/cm and begins to decline by the time it reaches the end of the data series. This is likely caused by a bias to the lower peak values (14 of 35 values for $X_m < 1.5$ mS/cm) and shows that this fit may not provide an ideal representation of sensor response (X) to CTD-Diver measurements.

The second method of calibration was produced using all measurements during the breakthrough experiments. To directly compare CTD-Diver measurements to dipole sensor measurements, the BTC data had to be shifted to account for tracer travel time between probes; if measurements at the same time are compared, each probe is measuring a different part of the tracer plume. Each dipole resistance sensor BTC was shifted to account for the time lag between the two peaks. This shift was not required for the first calibration method where peaks were compared because the assumption could be made that the EC_m and X_m corresponded to the same tracer concentration. The second calibration is shown in Figure 4.9. The top panel shows large variability between dipole sensor response and CTD-Diver reading, while the bottom panel indicates very little fluctuation of dipole sensor response in comparison to the CTD-Diver. Polynomial fits to all data points in Figure 4.9 (not shown) were found to provide a poor representation of sensor response due to measurement bias caused by the large number of low EC measurements. Trend lines were fit by manually selecting 14 points for each dataset that were considered to represent expected sensor response and then fitting a polynomial to that subset of data.

Analysis of Figures 4.8 and 4.9 shows variability in dipole probe response was much higher for the DI BTC experiments and that any calibration applied to this data includes significant error. This error can be explained by the discussions in sections 4.3.4 and 4.3.5 which highlight flow irregularities caused by preferential flow paths and shifting of the injection tube. The peak in the fit in Figure 4.8 for the DI experiments indicated the first calibration method was biased to values of low EC. The second calibration method shown in Figure 4.9 is considered to provide a better representation of probe response.

The calibration from Figure 4.9 was applied to the BTC data analyzed above. The data in Figure 4.9 was plotted so the dipole measurements were shown on the x-axis. The polynomial fit of the calibration data points was multiplied by probe conductance for each dipole measurement

to provide a calibrated dipole measurement in mS/cm. Figure 4.10 shows BTC11 and 18, which are examples of symmetrical BTCs collected during the DI experiments. The left panels show the raw data collected by the CTD-Diver and the dipole resistance probe, while the right panels show the raw data collected by the CTD-Diver and the calibrated dipole probe measurements. The calibration is quite poor, but curve shape does not appear to be significantly altered when comparing the raw dipole measurements to the calibration. Figure 4.11 shows the same calibration applied to BTC10 and 15, which are examples of irregularly shaped BTCs. The calibration is much better compared to BTC 11 and 18, with differences between EC_m and dipole sensor peak of 0.2-0.6 mS/cm. The error in the calibrations of BTC10, 11, 15, and 18 is expected based on the variability shown in the top panel of Figure 4.9.

An important observation from Figure 4.11 is the calibration did not improve measurement resolution. The calibrated dipole sensor data does not show a response to the small changes in BTC shape at elevated EC which were recorded by the CTD-Diver. The only difference between curve shape for raw dipole measurements (X) and the calibrated measurements is the calibrated measurements show higher kurtosis (sharper peak). A more rounded peak is shown for the raw dipole measurements because the magnitude of sensor response (X) to changes in EC declines as EC increases. This was illustrated in the static cell experiments in Chapter 3.

Figure 4.11 confirms observations from section 4.3.1 where the dipole probe was shown to have less measurement resolution during breakthrough than the CTD-Diver. Flow irregularities caused by the first sand pack and potential movement of the injection tube add uncertainty as to whether both probes measured the same profile of NaCl tracer, which could account for some differences in curve shape. However, the dipole probe recorded smooth BTC shapes for all DI tests, while many of the CTD-Diver BTCs showed unsymmetrical shapes. These results show that calibrating the dipole probe to EC does not improve measurement resolution and confirms that the dipole resistance probe was not able to capture the fine changes in curve shape measured by the CTD-Diver at elevated EC during the DI experiments.

Figure 4.12 shows BTC43 and 49 from the simulated groundwater experiments with the calibration from the bottom panel of Figure 4.9 applied. The calibrated dipole probe data show excellent agreement with the CTD-Diver measurements, with differences between EC_m and the calibrated dipole peak less than 0.05 mS/cm. The elevated background measurements for the

dipole sensor on the left side of Figure 4.12 are removed during calibration and match with the CTD-Diver measurements on the right side of the figure. The homogeneous conditions for the second sand pack which produced the tight relationship between responses at both probes (bottom panel Figure 4.9) produced a very accurate calibration of dipole probe response to CTD-Diver measurements.

4.3.7 Considerations when scaling technology to field setting

4.3.7.1 Ionic concentration

Extremely high ionic concentrations can produce ionic mobility effects that cause a divergence between EC and expected reagent concentration. At low ionic concentrations, the relationship between solute concentration and EC for salt solutions is positive and can be approximated by the empirical relationship in Eq. (8). As discussed by Klein and Santamarina (2003), the EC of a salt solution eventually peaks and then begins to decline with increasing ionic concentration (eg: peak at 350 g/L for NaCl) due to reductions in ionic mobility (Figure 4.13). These effects are most significant for higher ionic concentrations than those observed for typical ISCO injections at field sites. However, potential ionic mobility effects on EC measurements should be considered when working in environments with very high TDS electrolyte solutions such as brines. If TDS were very high, the relationship between EC and salt concentration may no longer be linear and calibrations applied to a dipole probe at lower EC may no longer be valid. When installing dipole resistance probes in the subsurface, a user should have an understanding of TDS at the site to determine if ionic mobility effects could potentially distort EC measurements.

4.3.7.2 Soil characteristics

In addition to EC of the pore fluid and temperature, soil properties influence *in situ* EC measurements; porosity, water content, soil structure, particle shape and orientation, particle-size distribution, cation exchange capacity, and wettability all contribute to EC measured in contact with porous medium (Friedman, 2005).

If a dipole resistance probe is installed in direct contact with porous medium, the combination of factors that influence EC are too complicated for a user to isolate and quantify the contribution from each property to the overall measurement value. The most straightforward approach for determining the presence of an injected reagent in the field is to look for changes from baseline measurements. If monitoring probes are left undisturbed during an injection event, only water saturation and ionic conductivity of the pore fluid are expected to change over time. This type of approach was found to be successful by Cavé et al. (2007) in correlating changes in resistance and ORP measurements with the presence of permanganate.

Looking for changes from baseline values is susceptible to errors due to changes in fluid saturation and mobilization of ionic species which can potentially occur at a monitoring point. Although ambient groundwater and chemical oxidants typically have contrasting EC, changing the degree of saturation at a measurement point can potentially yield an even larger contrast in EC. For cases where the initial water saturation at a probe measurement point is less than 100% or is unknown before an ISCO event, it may be difficult to determine whether changes in resistance sensor measurements are caused by changes in groundwater saturation or by the injected reagent. In addition, an injected oxidant slug can potentially displace stagnant groundwater which has a higher ionic conductivity than what is observed at a monitoring point, or it can potentially mobilize metal ions *in situ* (Suthersan and Horst, 2008). Both of these situations could create a change from baseline measurements that is not caused by the presence of an injected reagent.

Dipole measurements could also be distorted if sensors are in direct contact with highly conductive soil material. Direct sensor contact with soils that have high clay and/or metal content may result in a very high background resistance sensor reading (X). It is unknown whether the dipole resistance sensor would be able to pick up small changes in pore fluid EC relative to a high baseline from the soil (ie: small formation factor). Surface conduction of a soil has been shown to significantly contribute to EC measurements for soils with high specific surface area, S_a , when the pore fluid has low ionic conductivity. The contribution to EC measurements due to specific surface area increases as soil porosity decreases (Klein and Santamarina, 2003). Therefore, it is reasonable to assume that field scenarios may be encountered where the resistance sensor may not be able to respond to small changes in pore

fluid EC when in contact with high specific surface soils. This should be considered when taking *in situ* EC measurements in clay stratigraphy, particularly in situations when pore fluid EC is relatively low.

4.4 CONCLUSIONS

This experiment illustrated that two-wire resistance sensors are capable of monitoring high-resolution changes in EC in a controlled laboratory environment. BTC shape recorded by the resistance probe was very consistent with data recorded by a refined commercial EC datalogger and showed distinct beginning, peak, and end of tracer breakthrough. Tailing observed in the BTC experiments from Chapter 3 was not observed during the NeST experiments. The data indicated the resistance sensor was not capable of responding to fine changes in EC during breakthrough. The experimental results also illustrated that a temperature change of up to 1 °C had little impact on the EC measurements which were typically below 1.5 mS/cm.

Much of the variability in experimental results during the DI tests appeared to be related to flow through the sandbox, rather than precision of probe measurements. Differences between exact timing between the Schlumberger logger and dipole resistance sensor, as well as variability in expected conductivity peak appeared to be related to changes to physical flow properties of the sandbox system. The simulated groundwater experiments had much more controlled flow conditions. Analysis of the simulated groundwater experiments indicated the dipole sensor may have a slightly faster response time than the CTD-Diver, although uncertainty related to measurement interval and tracer travel distances suggest this difference is likely not significant. Figure 4.9 shows the relationship between data recorded by the Schlumberger logger and resistance sensor was very similar for the simulated groundwater tests.

The silica sand dampened *in situ* measurements by both the CTD-Diver and dipole resistance probe in comparison to data collected during static cell experiments in Chapter 3. Analysis of formation factors indicated the amount of interference caused by the silica sand is likely larger for a two-wire dipole sensor in comparison to a four-electrode probe. This suggests a four-electrode system may be a better design for direct push field applications.

The *in situ* dipole probe measurements were calibrated to the *in situ* CTD-Diver measurements for all recorded BTCs. The calibration produced for *in situ* measurements differs from what would be produced during static cell tests because of contact with the porous medium. The DI experiments did not show an accurate calibration, which was a result of the large variability in flow conditions during the DI tests. However, a very accurate calibration was produced for the simulated groundwater experiments, which indicated it was possible to calibrate the dipole probe to real EC values *in situ*. The probe calibrations did not increase measurement resolution.

Factors to consider when applying this type of technology to reagent injections in the field are potential fluid saturation changes at a monitoring point, mobilization of ionic species, and the influence of sensor contact with high specific surface soils. These laboratory results confirm that the resistance sensor design used in this experiment has promise for use in a field setting to monitor EC changes during reagent injections.

Table 4.1: Simulated groundwater ionic concentrations in comparison to other potable water. Solution Type A was used for BTC39-44, Solution Type B used for BTC45-76

Constituent	Solution Type A mg/L (~ 450 μS/cm)	Solution Type B mg/L (~ 825 μS/cm)	50th Percentile Concentration for Potable Water (mg/L) *
Ca ²⁺	22	44	~35
Cl ⁻	39	77	~20
SO ₄ ²⁻	32	64	~30
Mg ²⁺	10	20	~10
Na ⁺	68	137	~30
HCO ₃ ⁻	182	363	~300
TDS	352	705	~400

*Interpreted from Davis and DeWeist, 1966, Fig 4.1, p.98

Table 4.2: Summary of data collected during NeST BTC experiments

BTC	Background Solution EC (mS/cm)	Tracer Solution EC (mS/cm)	Tracer Volume (Injection, Purge) (mL)	CTD-Diver Peak (EC_m)	Resistance Peak (X_m)	Velocity A (cm/hr)	Velocity B (cm/hr)	Time Between Peaks (min)*
1	DI	61.3	120, 0	2.758	0.5964652	61.88	58.91	1.0
2	DI	61.2	120, 0	10.172	0.8524547	41.25	39.88	2.0
3	DI	61.4	300, 0	4.777	0.7707832	49.94	49.85	2.5
4	DI	~62 (42g/L)	300, 0	10.358	0.8462716	44.48	43.20	2.0
5	DI	~62 (42g/L)	60, 0	3.804	0.7777137	38.46	38.12	3.0
6	DI	~62 (42g/L)	60, 0	1.211	0.3650756	66.20	50.82	-4.0
7	DI	62	60, 0	1.066	0.1390182	61.88	54.00	-1.0
8	DI	62	60, 0	2.238	0.7287244	60.56	58.91	1.5
9	DI	61.9	60, 0	1.166	0.0946492	60.56	51.84	-1.5
10	DI	61.8	60, 0	2.099	0.7035843	52.71	51.84	2.0
11	DI	61.8	60, 60	1.176	0.1259725	69.42	60.28	-1.0
12	DI	61.8	60, 60	0.526	N/A	79.07	N/A	18.0
13	DI	61.3	60, 60	1.001	0.2151181	74.91	66.46	-0.5
14	DI	61.3	60, 60	0.996	0.4201801	72.98	63.22	-1.0
15	DI	61.2	60, 30	1.202	0.5861730	71.16	60.28	-1.5
16	DI	61.2	60, 30	0.380	N/A	74.91	N/A	19.0
17	DI	61.7	60, 30	3.935	0.8075422	61.88	61.71	2.0
18	DI	61.7	60, 30	1.082	0.2038390	72.98	64.80	-0.5
19	DI	61.7	60, 30	1.502	0.6372007	61.88	61.71	2.0
20	DI	61.7	60, 30	1.808	0.6711739	66.20	66.46	2.0
21	DI	61.7	60, 30	4.407	0.8197728	67.77	68.21	2.0
22	DI	61.7	60, 30	2.544	0.7442642	66.20	66.46	2.0
23	DI	61.7	60, 30	2.846	0.7502634	67.77	70.05	2.5
24	DI	61.7	60, 30	4.006	0.8114831	64.69	64.80	2.0
25	DI	33.2	60, 30	2.491	0.7663667	63.25	63.22	2.0

*Time between peaks = (Time to EC_m – Time to X_m, where positive values indicate X_m arrived before EC_m)

BTC	Background Solution EC (mS/cm)	Tracer Solution EC (mS/cm)	Tracer Volume (Injection, Purge) (mL)	CTD- Diver Peak (EC_m)	Resistance Peak (X_m)	Flow rate (cm/hr)	Velocity B (cm/hr)	Time Between Peaks (min)*
26	DI	33.2	60, 30	0.618	0.3272295	76.93	68.21	-0.5
27	DI	33.2	60, 30	2.110	0.7461866	61.88	63.22	2.5
28	DI	33.2	60, 30	2.494	0.7660949	64.69	64.80	2.0
29	DI	33.2	60, 30	2.704	0.7723460	66.20	66.46	2.0
30	DI	62.1	60, 30	3.386	0.7071175	54.74	52.90	1.5
31	DI	62.1	60, 30	2.242	0.5519280	63.25	60.28	1.0
32	DI	61.8	60, 30	0.857	0.0158315	58.09	56.35	1.5
33	DI	61.5	60, 30	0.914	0.0256158	54.74	54.00	2.0
34	DI	61.5	60, 30	1.183	0.0286757	59.30	55.15	0.5
35	DI	61.5	60, 30	1.180	0.0381308	55.81	54.00	1.5
36	DI	61.5	180, 30	1.461	0.0038055	60.56	61.71	2.5
37	DI	30.6	1100, 250	7.315	0.8140675	56.93	50.82	-0.5
38	DI	62.1	60, 30	1.624	0.7666498	74.91	78.55	2.5
39	0.422-0.457 (A)	62.1	60, 30	1.420	0.7678725	53.71	56.35	3.5
40	0.422-0.457 (A)	62.1	60, 30	1.507	0.7797590	52.71	54.00	3.0
41	0.422-0.457 (A)	62.1	60, 30	1.499	0.7859401	50.83	52.90	3.5
42	0.422-0.457 (A)	62.1	60, 30	1.461	0.7854649	49.94	51.84	3.5
43	0.422-0.457 (A)	62.1	60, 30	1.515	0.7899503	49.08	51.84	4.0
44	0.422-0.457 (A)	62.1	60, 30	1.452	0.7874344	47.44	49.85	4.0
45	0.841 (B)	62.1	60, 30	1.513	0.7675071	46.66	48.00	3.5
46	0.841 (B)	62.1	60, 30	1.179	0.7388412	47.44	48.91	3.5
47	0.841 (B)	62.1	60, 30	0.988	0.7226906	51.75	54.00	3.5
48	0.841 (B)	62.1	60, 30	0.494	0.6269844	54.74	58.91	4.0
49	0.841 (B)	62.1	60, 30	1.782	0.8031257	55.81	57.60	3.0
50	0.856 (B)	62.1	60, 30	1.488	0.7832865	53.71	56.35	3.5

*Time between peaks = (Time to EC_m – Time to X_m, where positive values indicate X_m arrived before EC_m)

BTC	Background Solution EC (mS/cm)	Tracer Solution EC (mS/cm)	Tracer Volume (Injection, Purge) (mL)	CTD-Diver Peak (EC_m)	Resistance Peak (X_m)	Flow rate (cm/hr)	Velocity B (cm/hr)	Time Between Peaks (min)*
51	0.856 (B)	62.1	60, 30	1.272	0.7641382	51.75	54.00	3.5
52	0.856 (B)	33.3	60, 30	0.658	0.6962177	54.74	57.60	3.5
53	0.856 (B)	33.3	60, 30	0.590	0.6799936	51.75	55.15	4.0
54	0.856 (B)	33.3	60, 30	0.639	0.7172883	56.93	60.28	3.5
55	0.856 (B)	33.3	60, 30	0.403	0.6851823	58.09	63.22	4.0
56	0.803 (B)	33.3	60, 30	0.392	0.6849268	52.71	56.35	4.0
57	0.803 (B)	33.3	60, 30	0.382	0.6814396	49.94	54.00	4.5
58	0.803 (B)	33.3	60, 30	0.397	0.6870610	49.08	52.90	4.5
59	0.803 (B)	33.3	60, 30	0.383	0.6826044	49.08	52.90	4.5
60	0.803 (B)	33.3	60, 30	0.387	0.6871369	48.24	51.84	4.5
61	0.803 (B)	33.3	60, 30	0.360	0.6803873	48.24	51.84	4.5
62	0.803 (B)	33.3	60, 30	0.365	0.6804552	47.44	51.84	5.0
63	0.803 (B)	33.3	60, 30	0.392	0.6865683	47.44	50.82	4.5
64	0.803 (B)	33.3	60, 30	0.400	0.6890135	47.44	50.82	4.5
65	0.803 (B)	33.3	60, 30	0.392	0.6868400	46.66	50.82	5.0
66	0.803 (B)	33.4	60, 30	0.457	0.7167656	53.71	57.60	4.0
67	0.803 (B)	33.4	60, 30	0.412	0.7046711	47.44	51.84	5.0
68	0.803 (B)	33.4	60, 30	0.357	0.6630880	49.08	54.00	5.0
69	0.803 (B)	17.74	60, 30	0.173	0.5547816	47.44	52.90	5.5
70	0.803 (B)	17.74	60, 30	0.189	0.6047218	43.79	47.13	5.0
71	0.803 (B)	17.74	60, 30	0.202	0.5825706	49.08	54.00	5.0
72	0.803 (B)	9.34	60, 30	0.066	0.3385567	45.91	50.82	5.5
73	0.803 (B)	9.34	60, 30	0.073	0.3700840	48.24	54.00	5.5
74	0.803 (B)	9.34	60, 30	0.110	0.5100767	46.66	50.82	5.0
75	0.803 (B)	9.34	60, 30	0.108	0.5138506	43.13	47.13	5.5
76	0.803 (B)	9.34	60, 30	0.106	0.5062376	45.91	49.85	5.0

*Time between peaks = (Time to EC_m – Time to X_m, where positive values indicate X_m arrived before EC_m)

Table 4.3: Summary statistics comparing variability in CTD-Diver peaks, EC_m

	Tracer : 60 mL, ~60 mS/cm		Tracer : 60 mL ~30 mS/cm	
	DI	Sim GW	DI	Sim GW
BTC	10-24, 30-36	45-51	25-29	52-68
average (mS/cm)	1.870	1.245	2.083	0.433
max (mS/cm)	4.407	1.782	2.704	0.658
min (mS/cm)	0.380	0.494	0.618	0.357
stdev (mS/cm)	1.210	0.419	0.847	0.097

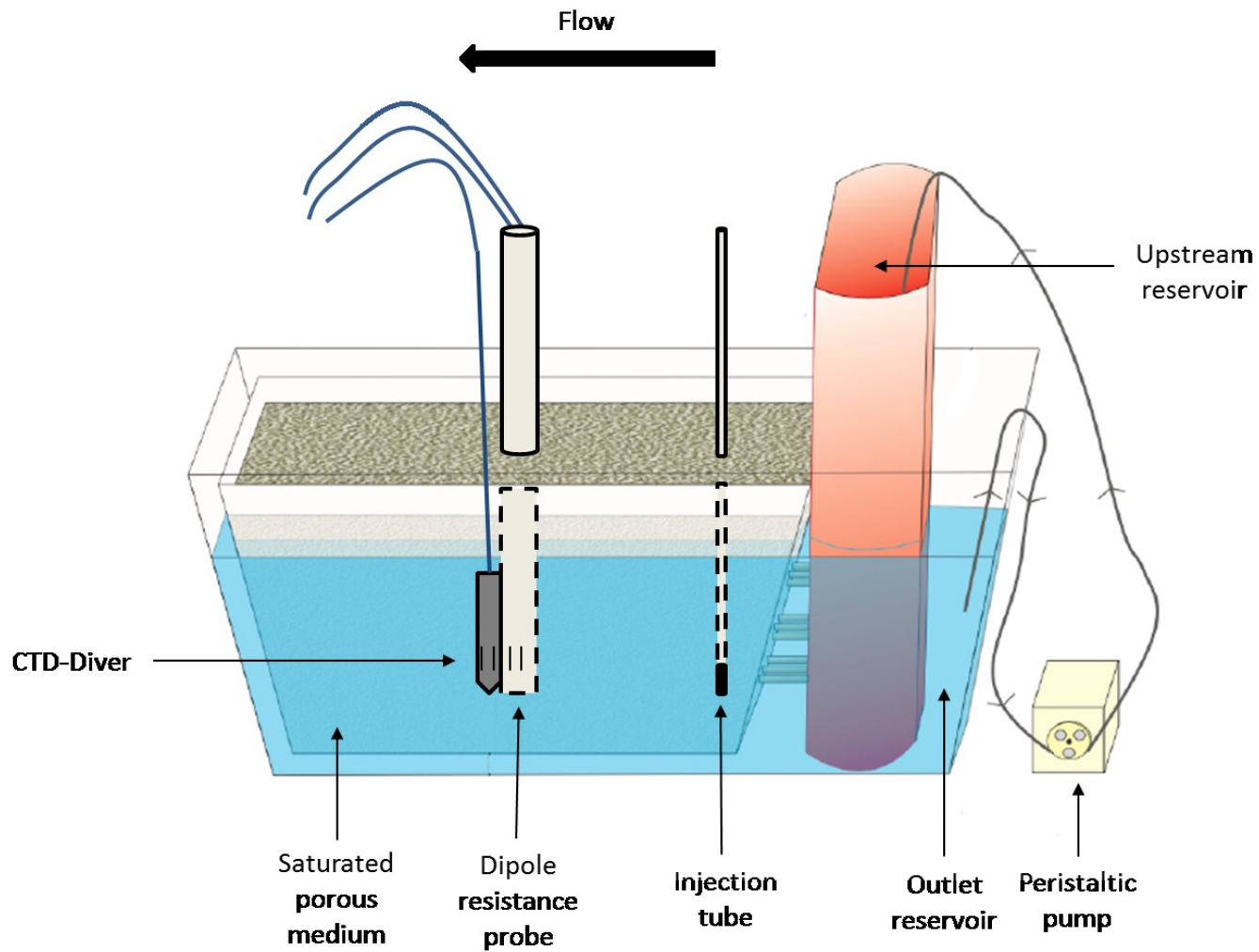


Figure 4.1: Schematic of flow through NeST system driven by peristaltic pump. Diagram shows case for water recirculated from outlet reservoir back to upstream reservoir. BTC experiments pumped water from outlet reservoir to waste. Adapted from (Bowen, 2010, p.18).

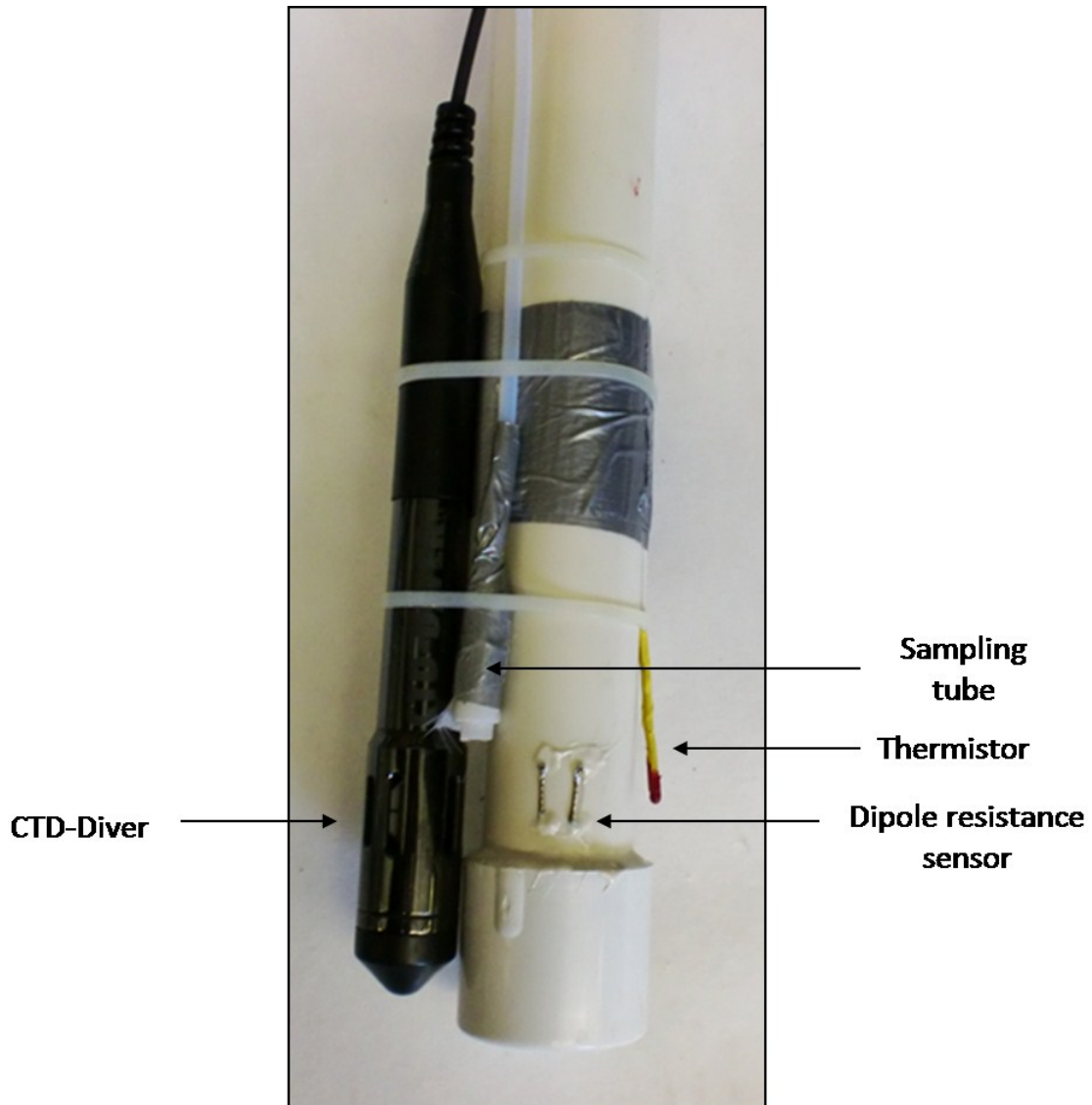


Figure 4.2: CTD-Diver bundled with dipole resistance sensor and thermistor for NeST breakthrough experiments. Sampling tube was not used during BTC experiments.

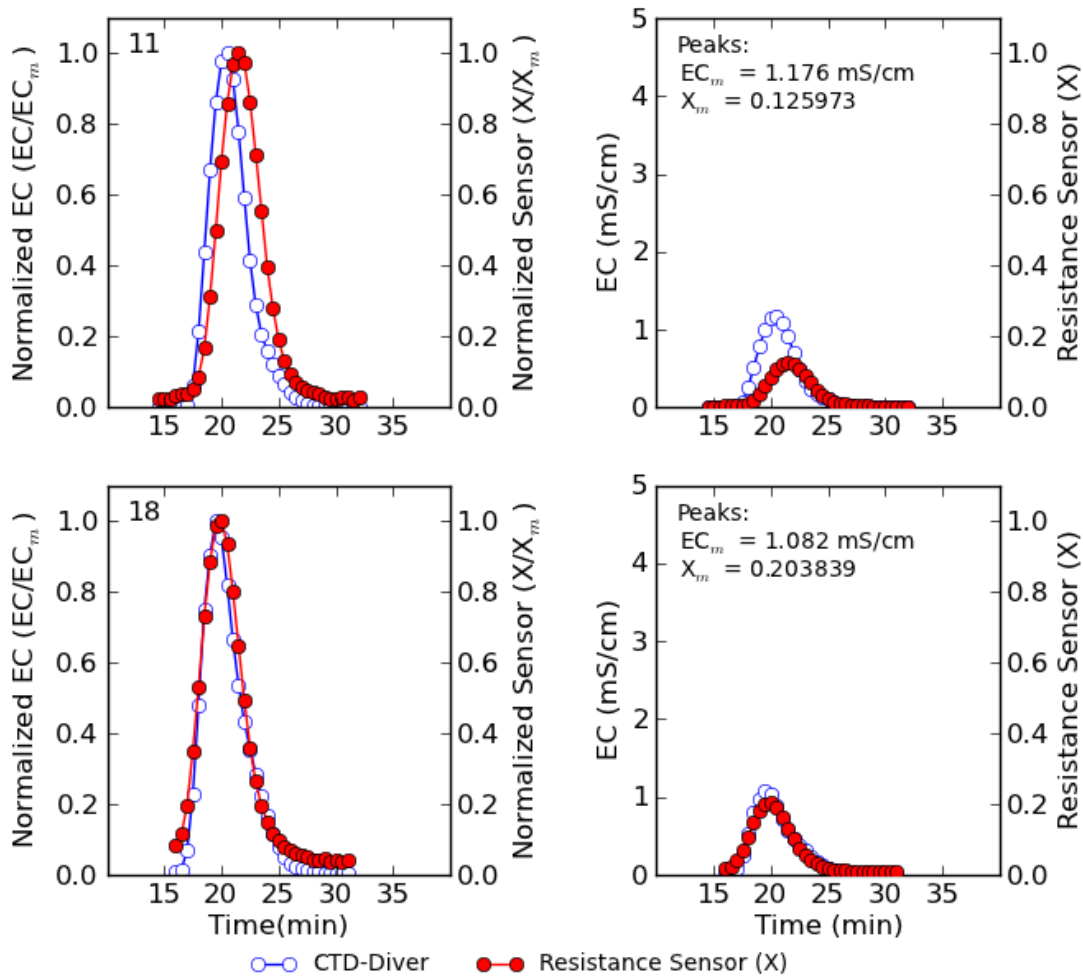


Figure 4.3: Example of BTCs measured during DI BTC experiments. BTC11 shown in top panels, BTC18 shown in bottom panels. Hollow blue points indicate records collected by the CTD-Diver, solid red shows data collected by the dipole resistance sensor. The panels on the right show the raw CTD-Diver (mS/cm) and dipole sensor (X) data. Panels on the left show data normalized to the peak value measured by each probe.

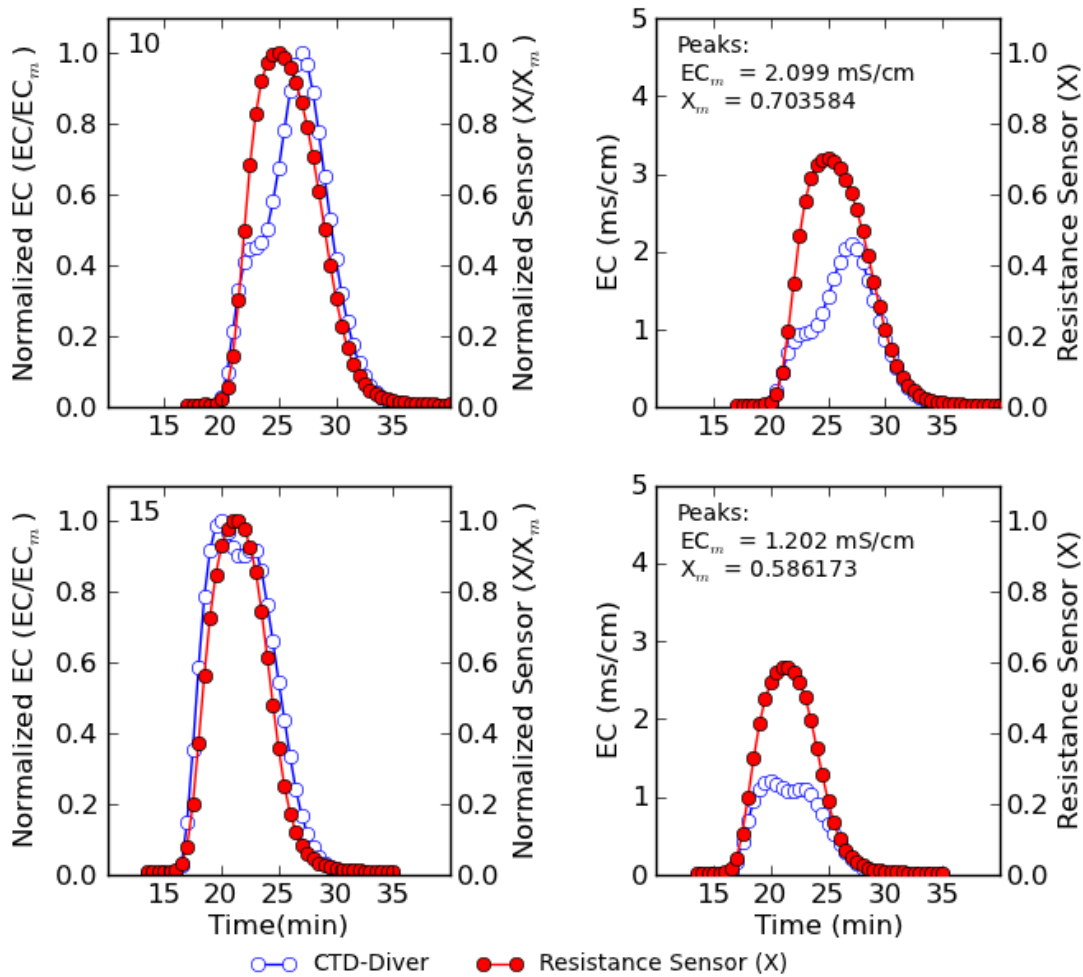


Figure 4.4: Example of dipole resistance sensor response to BTCs with irregular shapes. BTC10 shown in top panels, BTC15 shown in bottom panels. Hollow blue points indicate records collected by the CTD-Diver, solid red shows data collected by the dipole resistance sensor. The panels on the right show the raw CTD-Diver (mS/cm) and dipole sensor (X) data. Panels on the left show data normalized to the peak value measured by each probe. The raw CTD-Diver data shows examples where EC breakthrough did not follow a symmetrical curve.

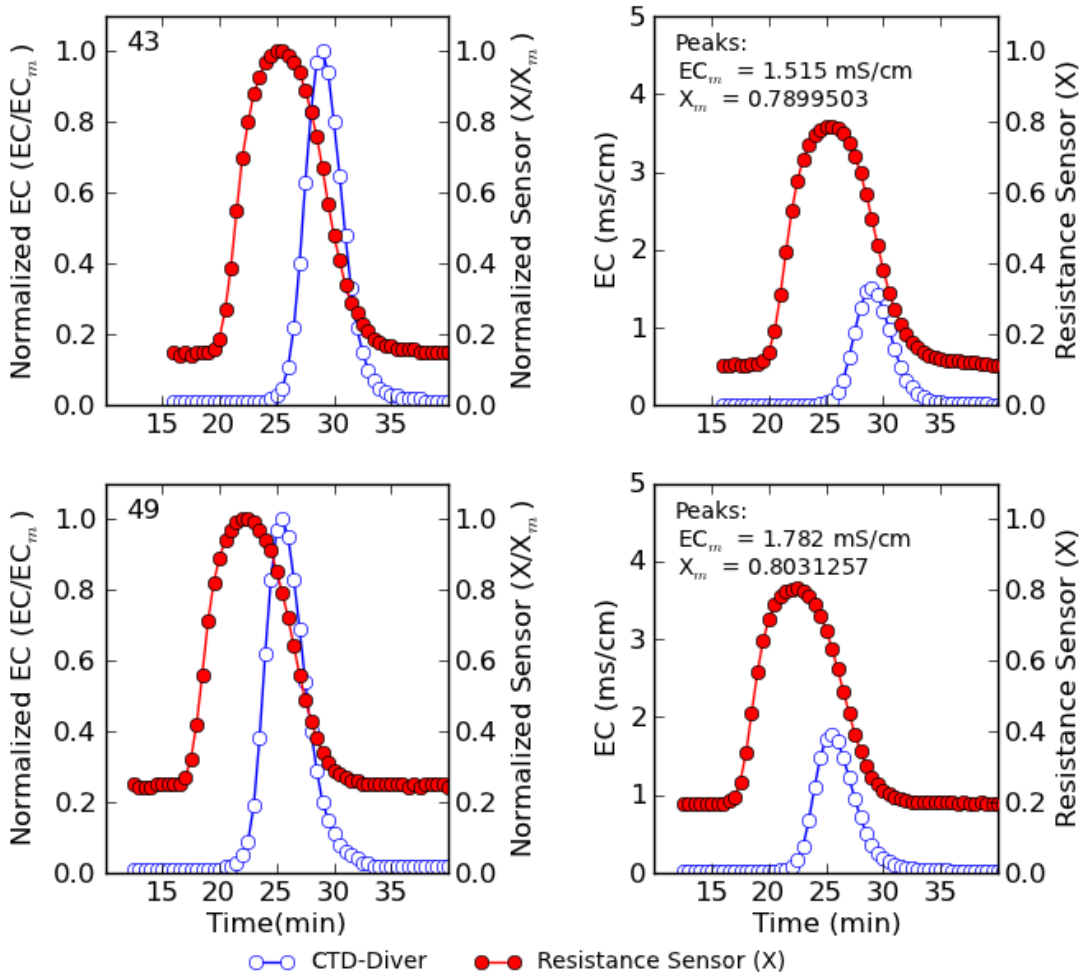


Figure 4.5: Example of BTCs measured during simulated groundwater experiments. BTC43 shown in top panels, BTC49 shown in bottom panels. Hollow blue points indicate records collected by the CTD-Diver, solid red shows data collected by the dipole resistance sensor. The panels on the right show the raw CTD-Diver (mS/cm) and dipole sensor (X) data. Panels on the left show data normalized to the peak value measured by each probe.

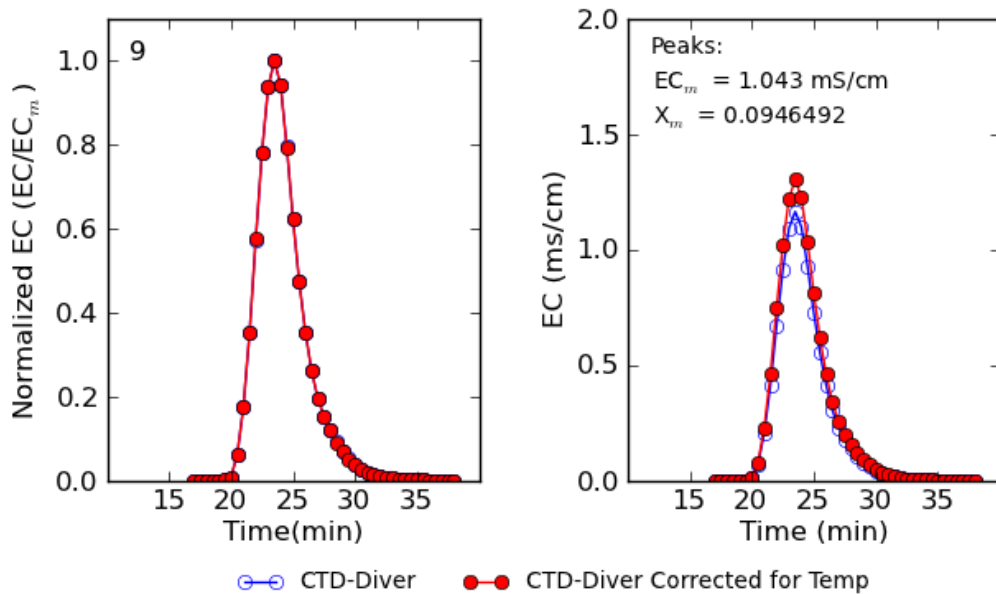


Figure 4.6: Influence of temperature correction on CTD-Diver measurements for BTC 9. The hollow blue points show the raw CTD-Diver measurements, which were collected using as values referenced to 25 °C. The solid red points show the CTD-Diver data referenced to the *in situ* measurement temperature.

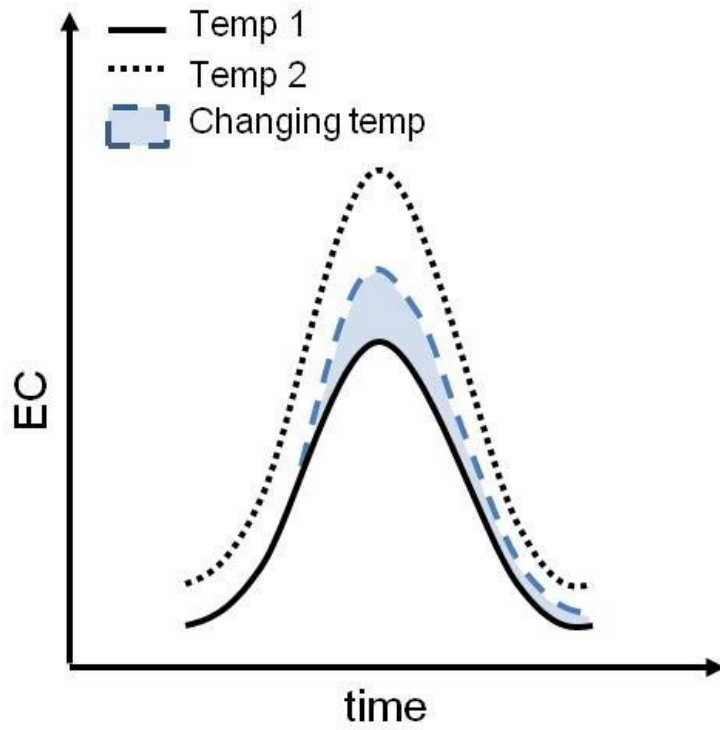


Figure 4.7: Example of error introduced by changing temperature during breakthrough

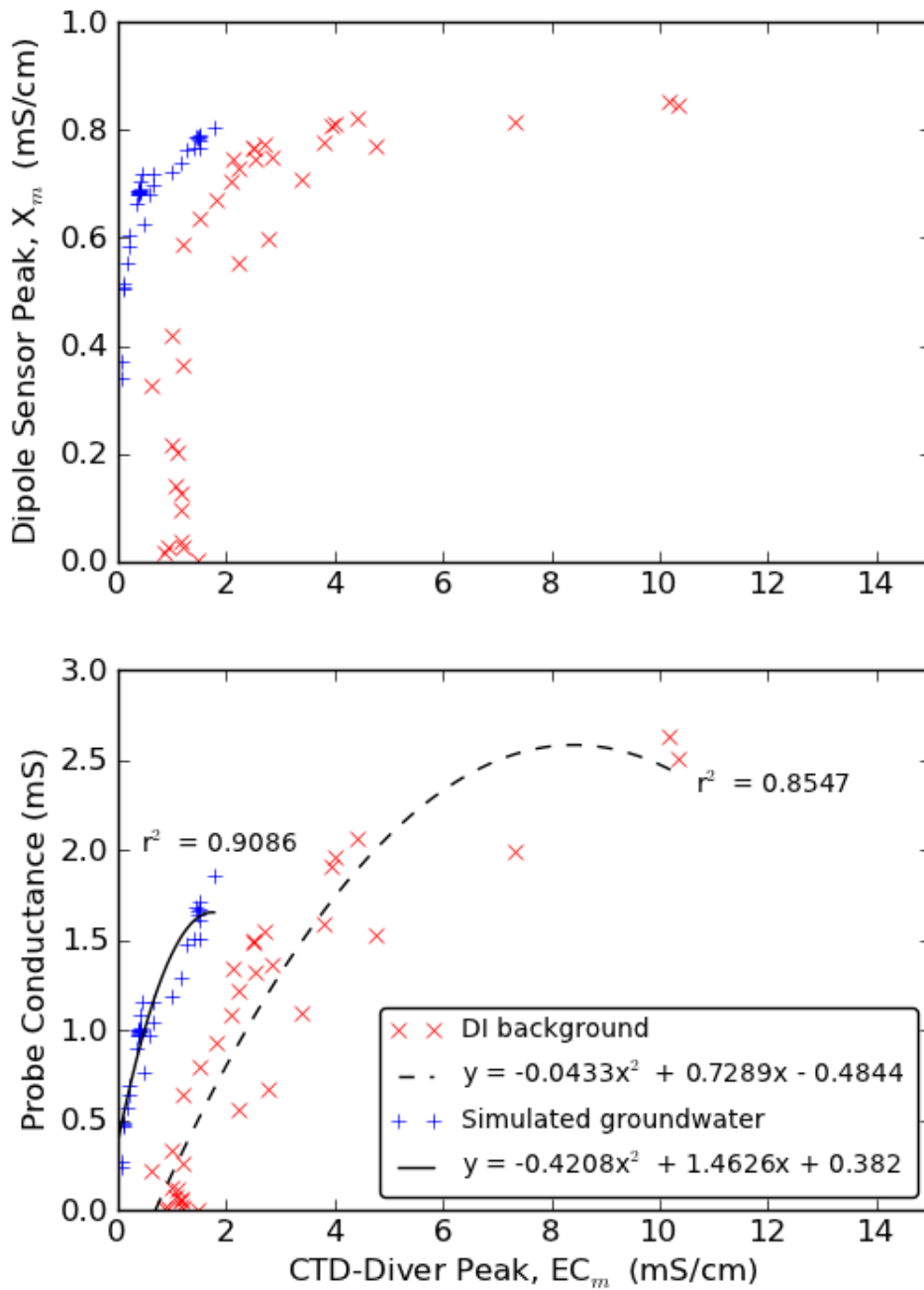


Figure 4.8: Calibrated NeST data. Top panel shows dipole sensor peak, X_m , against CTD-Diver peak, EC_m . Probe conductance is calculated as inverse of sensor resistance (R_s). Second order polynomial fit is in form $ax^2 + bx + c$, where $x = EC_m$ and $y =$ probe conductance.

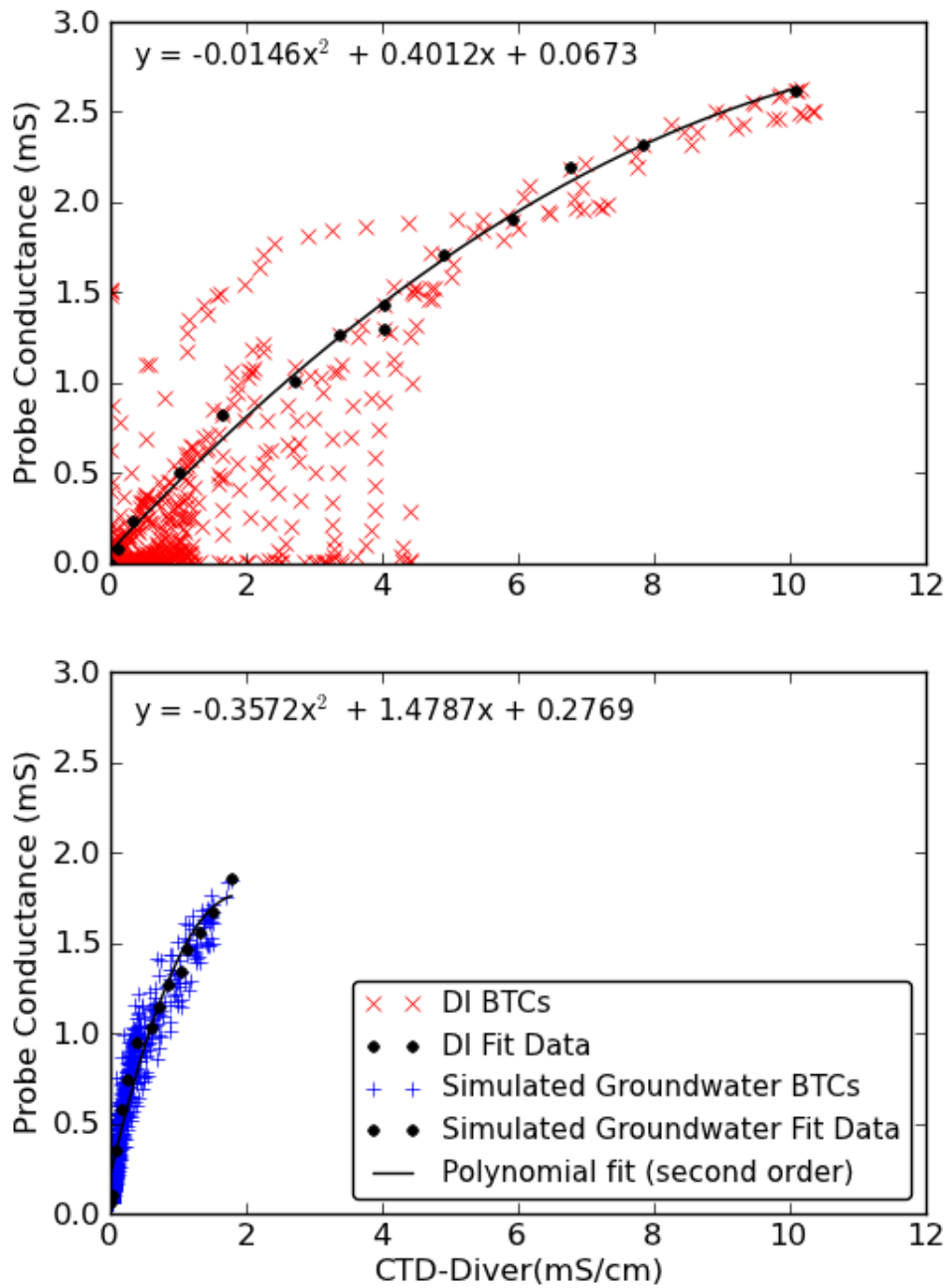


Figure 4.9: All NeST BTC data shifted according to gap between each peak. Probe conductance is calculated as inverse of sensor resistance (R_s). Second order polynomial fit is in form $ax^2 + bx + c$, where x = CTD-Diver readings and y = probe conductance. Each fit was produced by manually selecting 14 points from each data series that represented average sensor response.

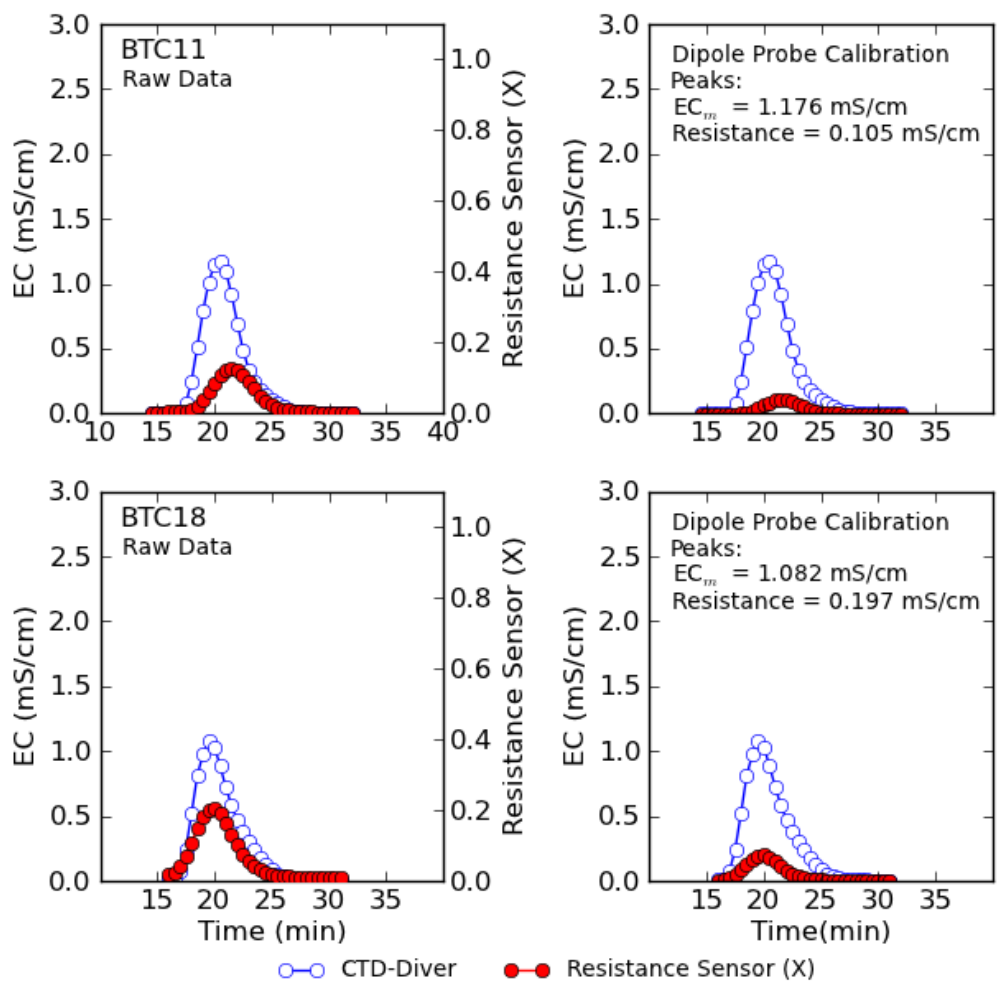


Figure 4.10: Example of BTCs measured during DI experiments. BTC11 shown in top panels, BTC18 shown in bottom panels. Hollow blue points indicate records collected by the CTD-Diver, solid red shows data collected by the dipole resistance sensor. The panels on the left show the raw CTD-Diver (mS/cm) and dipole sensor (X) data. Panels on the right show the data calibrated to the fit from Figure 4.9.

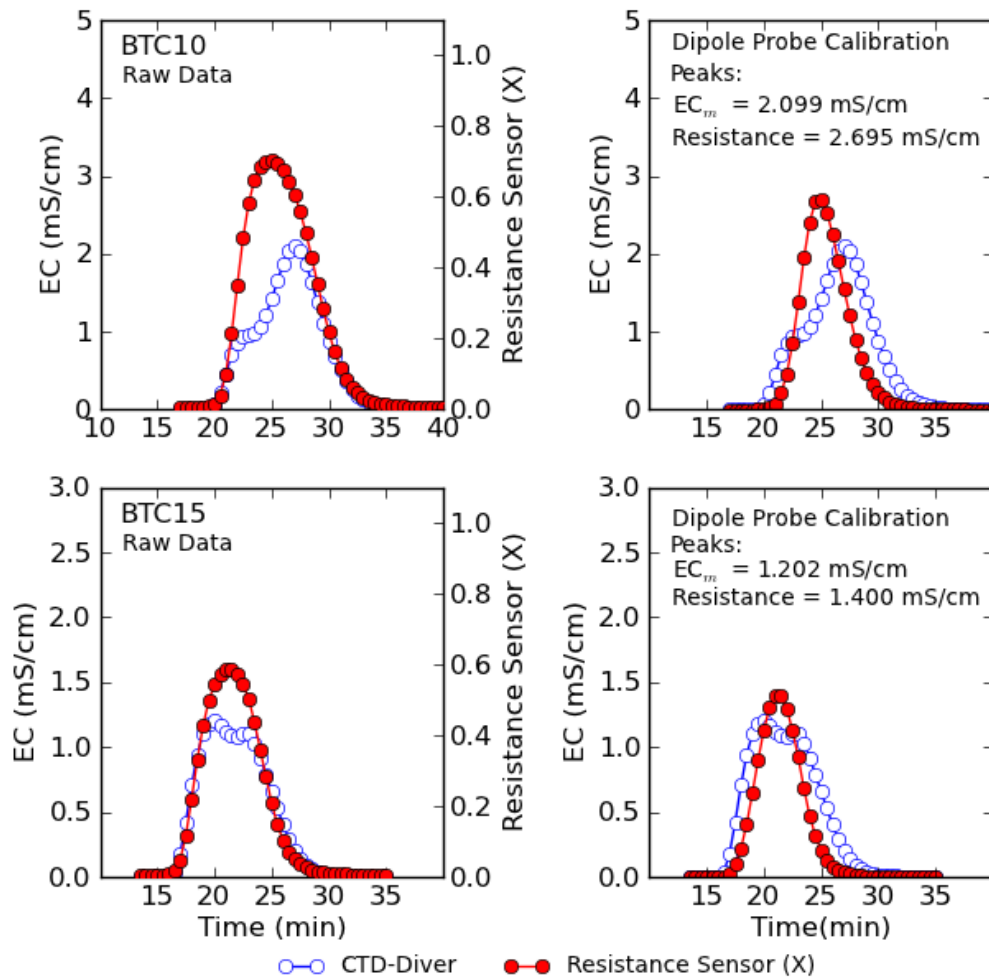


Figure 4.11: Example of irregularly shaped BTCs measured during DI experiments. BTC10 shown in top panels, BTC15 shown in bottom panels. Hollow blue points indicate records collected by the CTD-Diver, solid red shows data collected by the dipole resistance sensor. The panels on the left show the raw CTD-Diver (mS/cm) and dipole sensor (X) data. Panels on the right show the data calibrated to the fit from Figure 4.9.

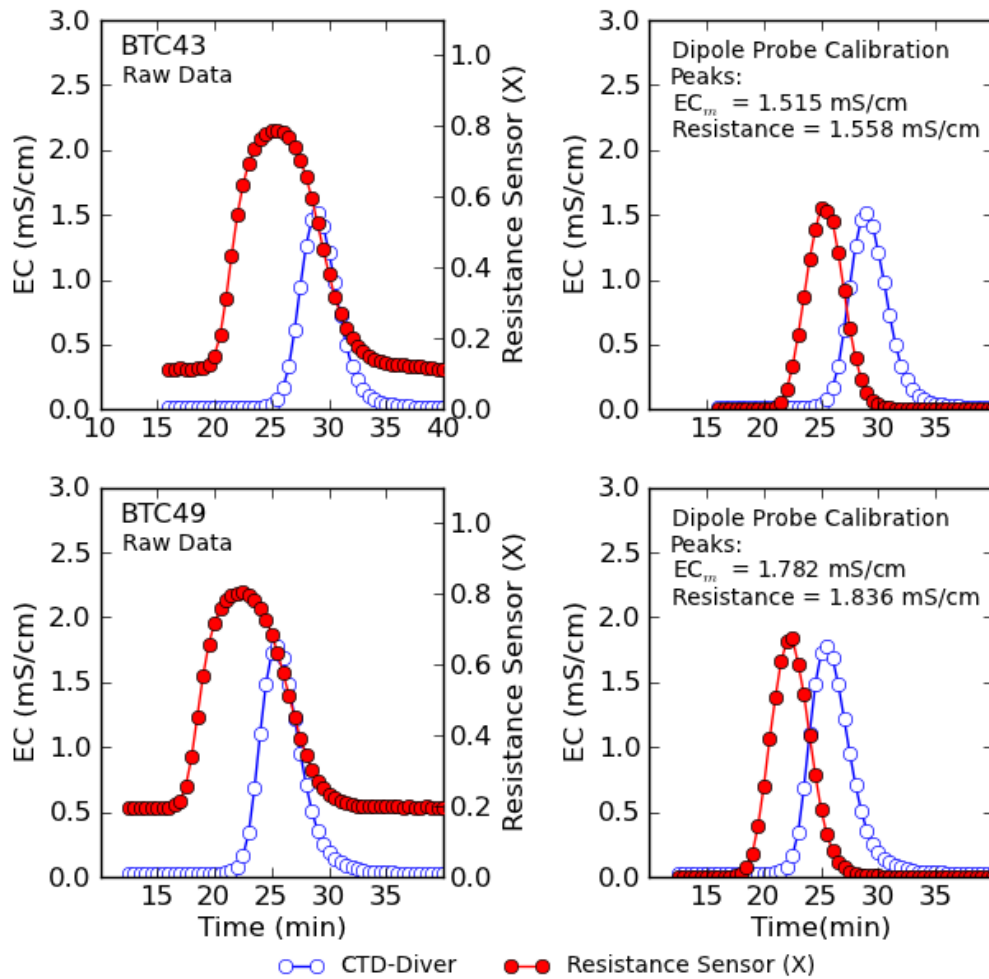


Figure 4.12: Example of BTCs measured during simulated groundwater experiments. BTC43 shown in top panels, BTC49 shown in bottom panels. Hollow blue points indicate records collected by the CTD-Diver, solid red shows data collected by the dipole resistance sensor. The panels on the left show the raw CTD-Diver (mS/cm) and dipole sensor (X) data. Panels on the right show the data calibrated to the fit from Figure 4.9.

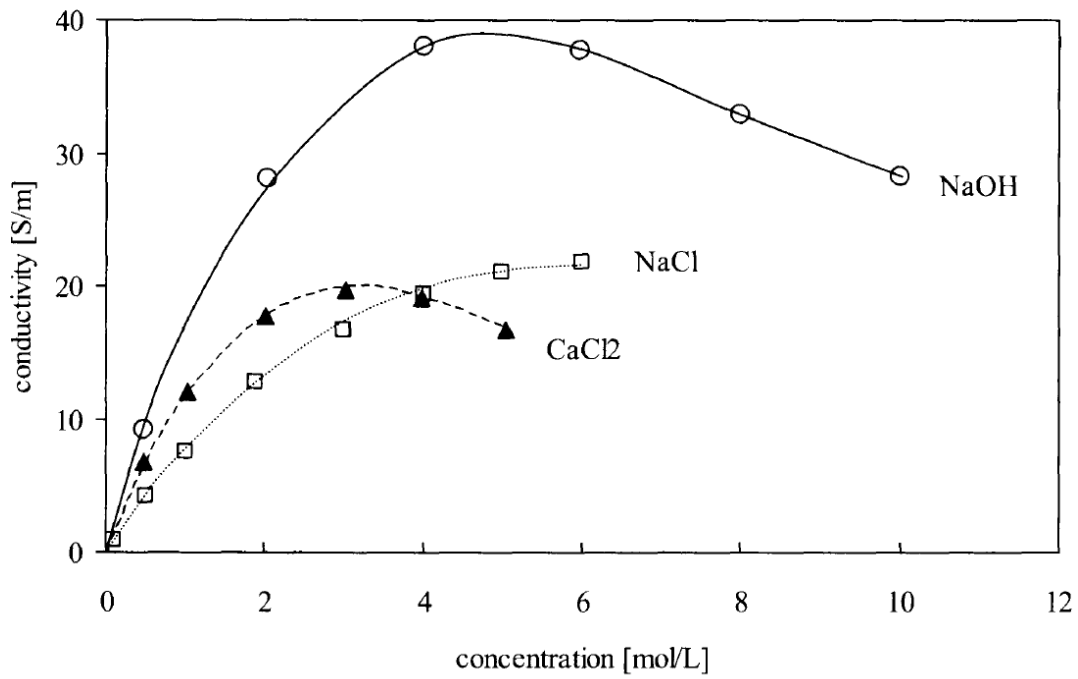


Figure 4.13: Effect of ionic concentration on EC, taken from (Klein and Santamarina, 2003). EC peaks correspond to concentrations of ~6 mol/L (350 g/L) NaCl, 3 mol/L CaCl₂ (333 g/L), 4.5 mol/L NaOH (180 g/L).

Chapter 5: Field Trials

5.1 OVERVIEW

Two field trials were carried out to test the prototype probe designs. Both trials were conducted during ISCO events using sodium persulfate at former gasoline stations. The first trial took place at a fractured bedrock site early in the probe design stage, while the second field site consisted of unconsolidated porous media and took place later in the design stage after some changes to initial prototypes had been undertaken. For both trials, probes were constructed with 1-inch PVC pipe. Probes were installed in existing pumping and monitoring wells on site and were left to record data before, during, and after the ISCO injection events. Data collected by the probes were compared to water samples analyzed for EC and temperature in the field, and persulfate concentration at the University of Waterloo. The focus in this effort was observed correlations between oxidant concentration, EC, and dipole sensor measurements rather than treatment performance.

5.2 FIELD TRIAL 1: FERGUS, ONTARIO

The Fergus field site is a fractured limestone aquifer that is contaminated by residual hydrocarbons. The trial consisted of a pilot-scale 2% sodium persulfate (20 g/L $\text{Na}_2\text{S}_2\text{O}_8$) injection at a single point, RW 16, on November 10-11, 2010. Packers were used to isolate an injection interval 4-5.5 mbgs. Volumes of 6000 L and 10000 L were pumped into RW16 on November 10th and 11th, respectively, for a total injection volume of 16000 L. Monitoring and recovery wells were sampled from November 10-16.

Figure 5.1 shows the Fergus site and location of injection well RW16. Local groundwater flow at the site is from top to bottom of Figure 5.1 (Greer, 2009, p.12). Three monitoring probes, each with a single dipole sensor, were installed 18 m downgradient of the injection point in recovery wells RW8, RW9, and RW10. Details of probe construction and wiring characteristics are provided in Table 5.1. Water samples were collected and analyzed for EC, temperature, and pH in the field using a handheld meter (Thermo Orion; model 1219000 with 013010MD conductivity probe), and were subsequently sent to the University of Waterloo for analysis of persulfate concentration.

Figure 5.2 shows persulfate breakthrough during the monitoring period. Note that persulfate was not observed in samples from RW10 for the duration of the monitoring period. For all sampling points, EC correlated well with persulfate concentration, as shown in Figure 5.3. Figure 5.4 indicates there was no correlation between persulfate concentration and pH. Data collected by the field probes and correlations with EC and persulfate concentration is shown in Figure 5.5. The top two panels show the relationship between persulfate concentration and EC at two of the monitoring wells, RW8 and RW9, which indicated changes in EC at these wells was likely a result of changes in dissolved $\text{Na}_2\text{S}_2\text{O}_8$ species.

Figure 5.5 shows the data collected by the dipole sensors has little correlation with the changes in EC and persulfate concentration. In particular, dipole sensor measurements show a period of large increase in measurement values, from 0.8 to 0.96, at the beginning of the measurement interval. After this period, there was limited sensor response to changes in EC, although these changes did not correlate particularly well.

There were two major factors which could have potentially caused the poor correlations observed: (1) the presence of particulate material collecting on the detector wires, and (2) the size of the detectors. After the dipole resistance probes were removed from the monitoring wells, it was observed that significant particulate material had gathered on the detector wires (Figure 5.6). This rust-coloured particulate material was also observed in water samples, and can likely be attributed to the heavy residual hydrocarbon contamination at the site. It is reasonable to assume that detector response during monitoring was distorted by this material. Another potential factor, interrelated with the presence of particulate material, was the size of the dipole resistance detector. With detector wire lengths of 1.5 cm and spacing of 2.8 cm, the field probes had the largest detectors tested in this research. It is possible that larger-sized detectors reduce the responsiveness of the sensor, which could potentially be compounded by the presence of particulate material gathering on the detector surfaces. This was observed later during experiments in the laboratory that tested the field probes from the Fergus site; although the probes generally appeared to respond similarly to the other laboratory probes, there were two instances when the same type of behavior from the Fergus field test was observed (data not shown). The exact cause of these poor responses could not be determined.

5.3 FIELD TRIAL 2: SOUTHERN ONTARIO

The second field trial took place in southern Ontario, June 7-8, 2011 at a former gasoline station contaminated with petroleum hydrocarbons. Four dipole resistance probes were hung in 2-inch existing monitoring wells before an injection on June 7. Construction and wiring details for all four probes installed at the site are provided in Table 5.1. Figure 5.7 shows the site and the location of injection wells and monitoring probes. Groundwater flow at the site was from East to West. Injection well MW-1 was approximately 11 m upgradient from MW-4. (Holtze, 2011, p.5). A polyethylene sampling tube with Nitex mesh covered end was attached to each probe near each resistance sensor as shown in Figure 5.8.

A 20% sodium persulfate solution (200 g/L $\text{Na}_2\text{S}_2\text{O}_8$) was used throughout the injection. A total of 1500 L was gravity-fed into each injection well each day over 2 days (total injection volume of 9000 L). Monitoring probes were left to collect data for two weeks after the injection. Water samples were collected at various intervals during monitoring. Samples were analyzed in the field for EC and temperature using a handheld Thermo Orion meter (model 1219000 with 013010MD conductivity probe) and were also collected and brought back to the University of Waterloo for analysis of persulfate concentration. Samples were approximately 100 mL, and were collected after a purge volume of 100 mL.

Laboratory analysis showed no persulfate present in the samples collected from the monitoring wells where dipole probes were installed. This was supported by relatively stable EC records at these locations. This was not completely unexpected, as previous work at this site indicated high persulfate concentration, similar to what was used during this injection, caused the reagent to sink due to density effects (Katanchi, 2011, p.32). The downgradient wells where the dipole probes were installed were the only locations on site with 2-inch diameter or larger openings that would accommodate the size of the probes, necessitating installation at these locations.

Figure 5.9 shows data collected by the monitoring probes and corresponding handheld EC measurements. Data was not collected at MW-106 due to a loose wire on the monitoring probe. Dipole sensor measurements appear to agree fairly well with the EC measurements throughout the field trial. The high frequency of sampling on June 6 and 7 resulted in EC spikes on the

order of 100 $\mu\text{S}/\text{cm}$ at MW-202. This was likely caused by solutes drawn into the monitoring well. Dipole resistance sensor measurements in Figure 5.9 for MW-202 appear to respond fairly well to these changes. Spikes in EC caused by sampling were less obvious for MW-4 and MW-107. A significant spike in dipole resistance sensor readings around June 11 was present at each of the three monitoring locations. Although water samples at this were not available to verify a change in EC, the timing of the spike appeared to correspond with a heavy rainfall event at the site. It is possible that infiltration from this event caused a change in the ionic composition of water inside the monitoring wells. Although this field trial was not able to correlate sensor response with the presence of the injected reagents, the probes were able to collect stable measurements that appeared to reflect the *in situ* EC in the monitoring wells.

5.4 CONCLUSIONS

The initial field trial in Fergus was useful for learning and improving methods for field installations, but did not provide any data which supported laboratory results described in Chapters 3 and 4. Because this test took place early in the prototype design process, and had sources of uncertainty related to particulate material and sensor size, conclusions about the effectiveness of the probe design cannot be made.

The second field trial provided encouraging results that the dipole resistance probes could effectively monitor changes in EC in the field even though the injected reagent was not observed at the dipole probe monitoring wells. The stability of the sensor measurements, which correlated well with EC data, indicated the system is capable of logging accurate data in the field.

Table 5.1: Probe construction details for field trials

Probe Characteristic	Field Trial 1	Field Trial 2
Material	Schedule 40, 1-inch PVC	Schedule 80, 1-inch PVC
Length	1.7 – 1.9 m	3.5 – 4 m
End cover	PVC cap	PVC cap
Water seal	PVC cement and marine epoxy	PVC cement and marine epoxy
Detector material	Galvanized wire	Stainless steel cable
Detector orientation	Horizontal	Vertical
Detector dimensions	1.5 cm long, 2.8 cm spacing	1 cm long, 0.3 cm spacing
Sampling tube	Yes, Nitex covered end	Yes, Nitex covered end
Fixed resistor	24.9 k Ω	2.2 k Ω
Data collection interval	2 min	3 min

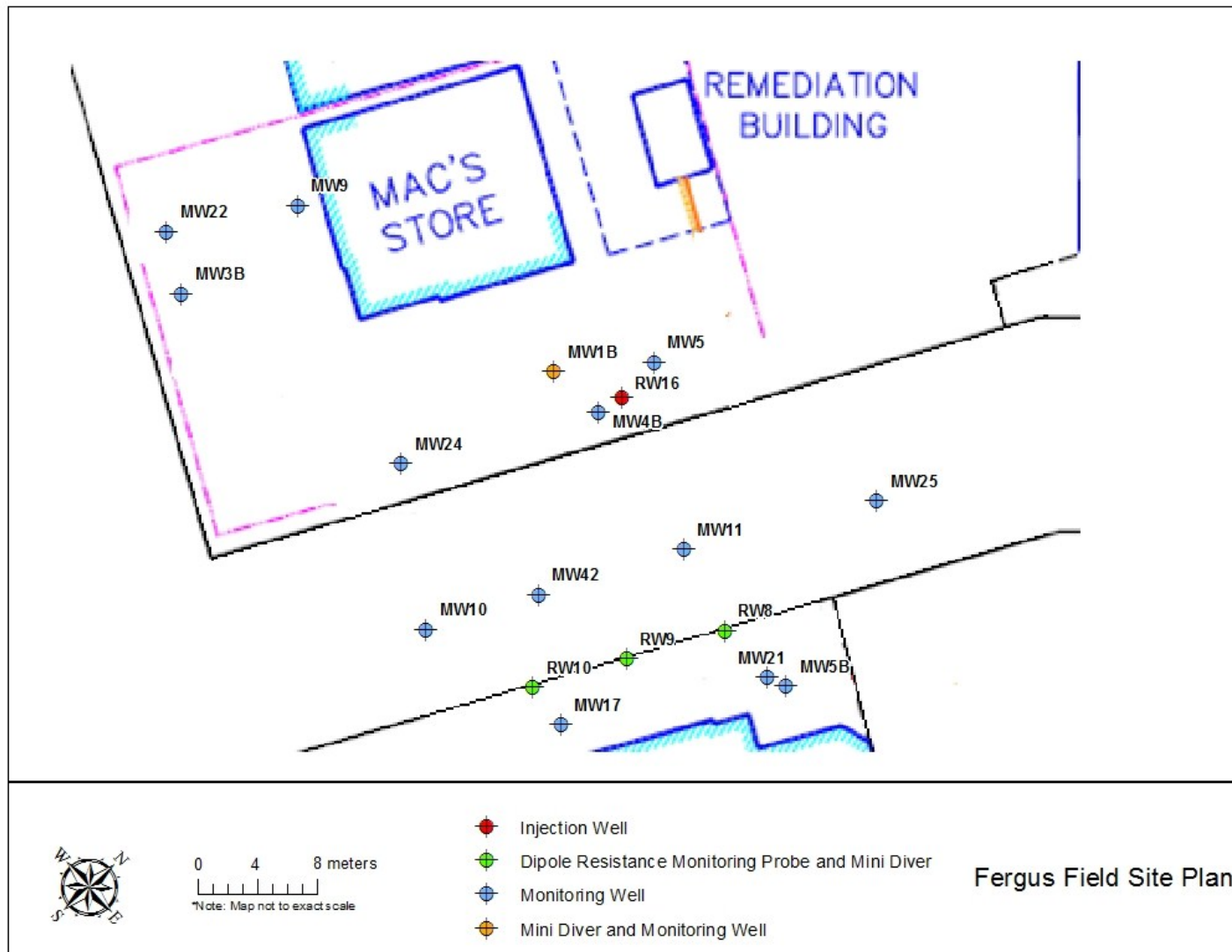


Figure 5.1: Field Trial 1, Fergus, ON, Site Plan

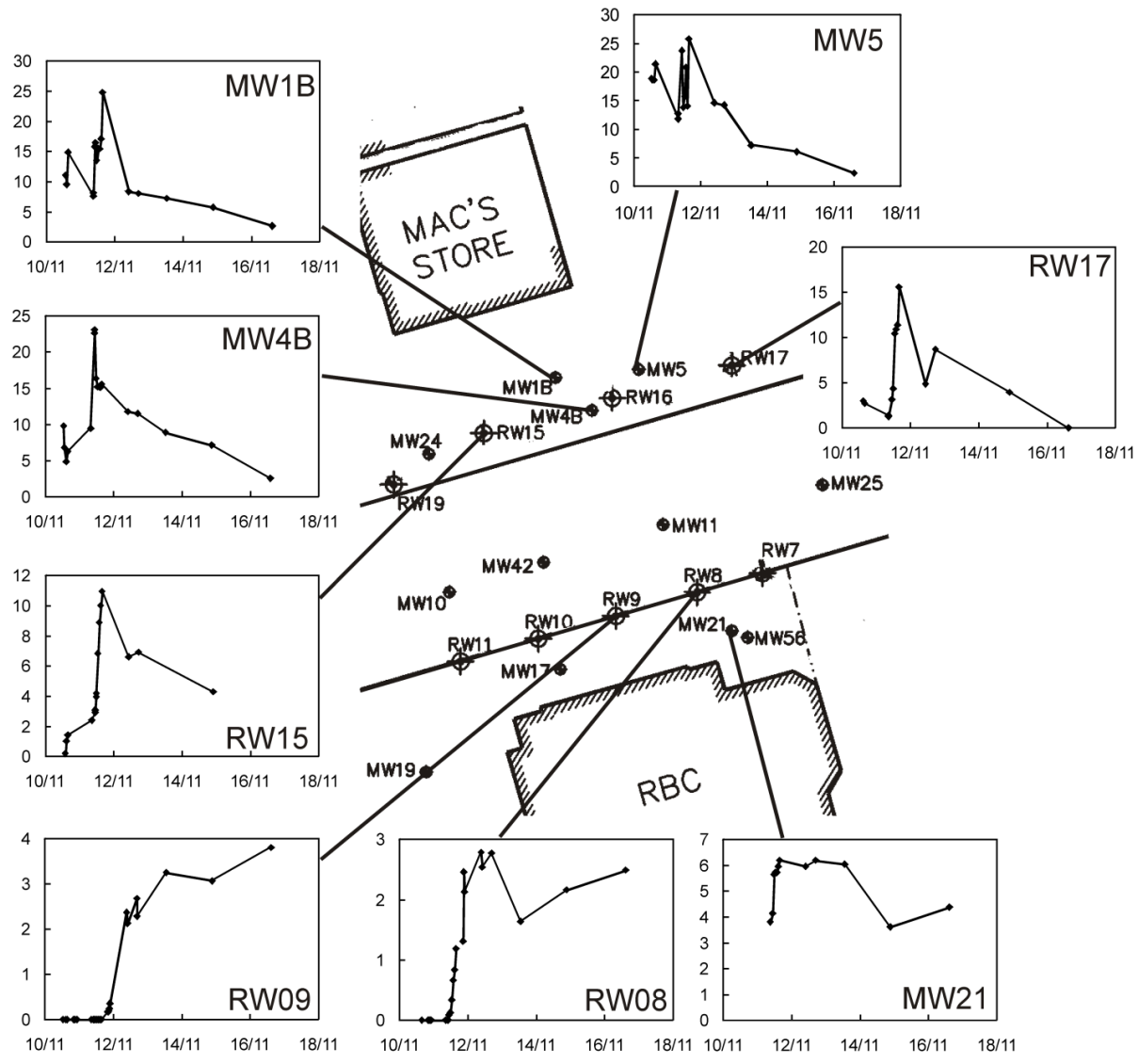


Figure 5.2: Persulfate BTCs from Field Trial 1, taken from Greer et al.,(2011). The y-axis of each plot shows persulfate concentration in g/L.

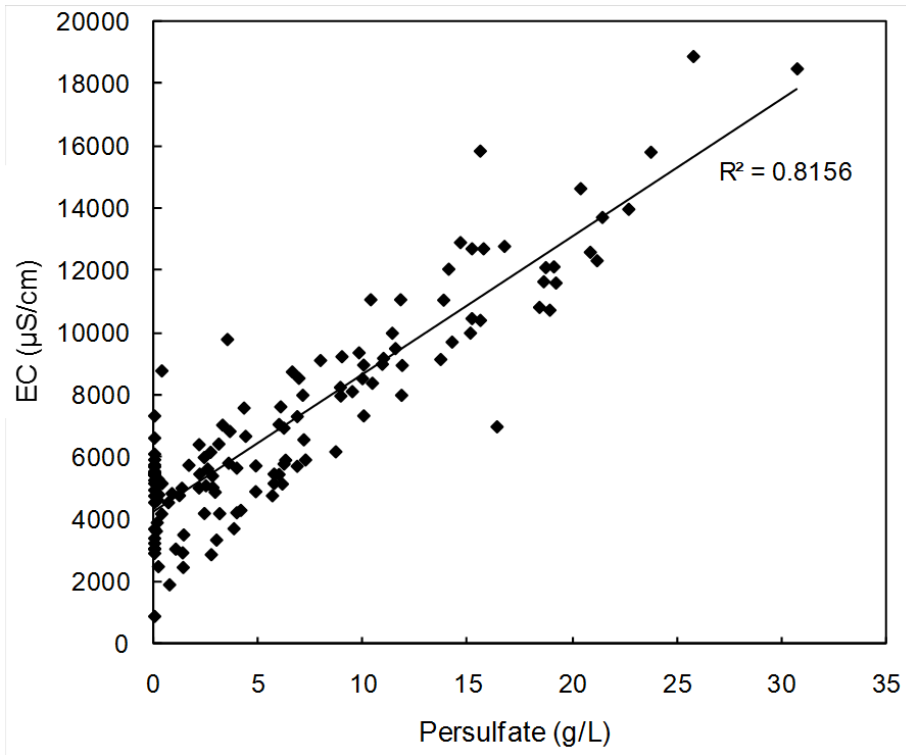


Figure 5.3: Persulfate vs. EC for all Fergus samples (Greer et al., 2011)

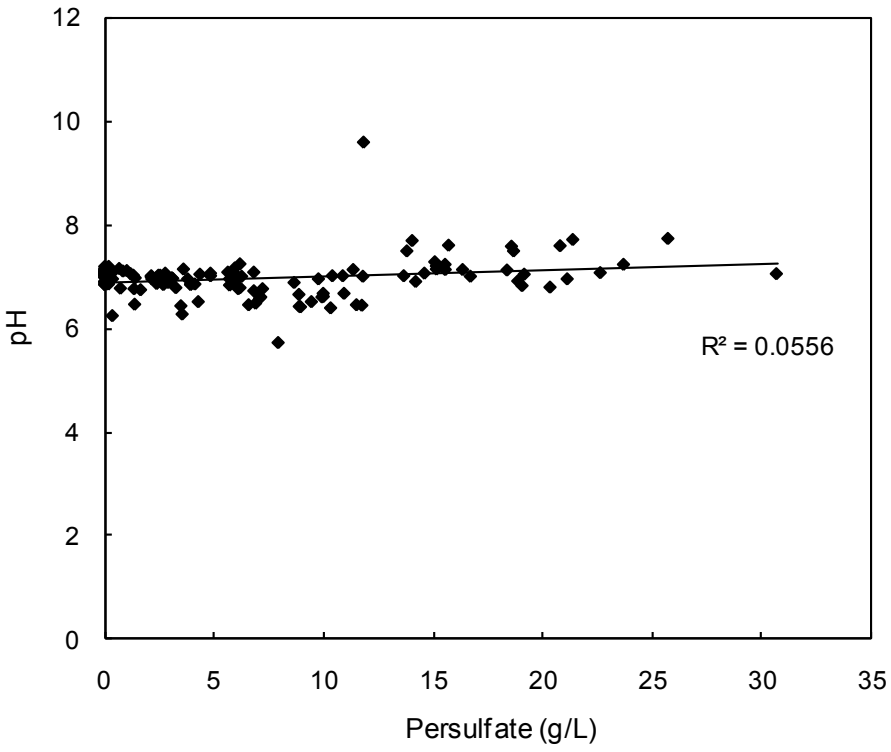


Figure 5.4: Persulfate vs. pH for all Fergus samples (Greer et al., 2011)

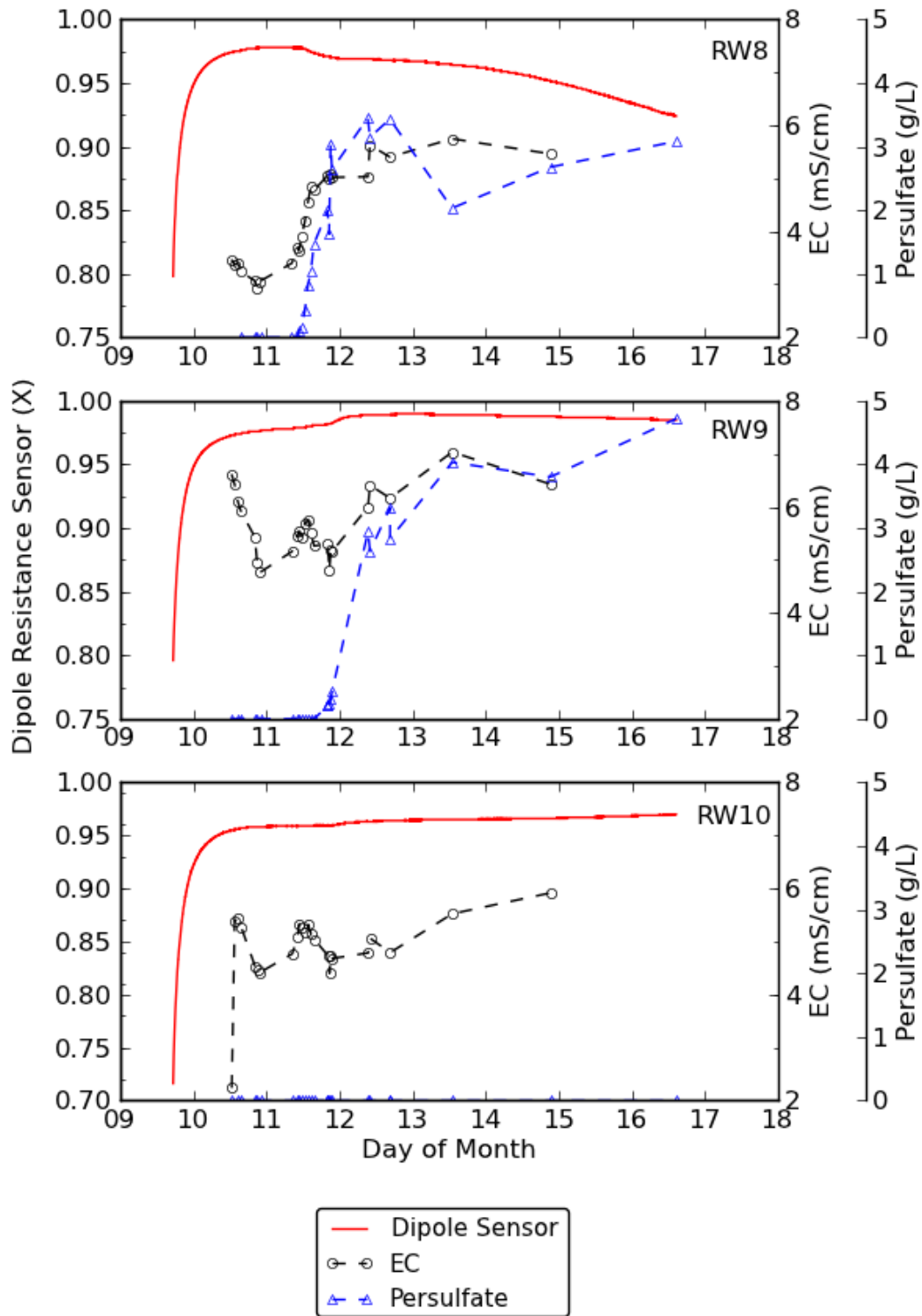


Figure 5.5: Correlation of Persulfate with EC, RW8



Figure 5.6: Particulate material collected on detector surfaces

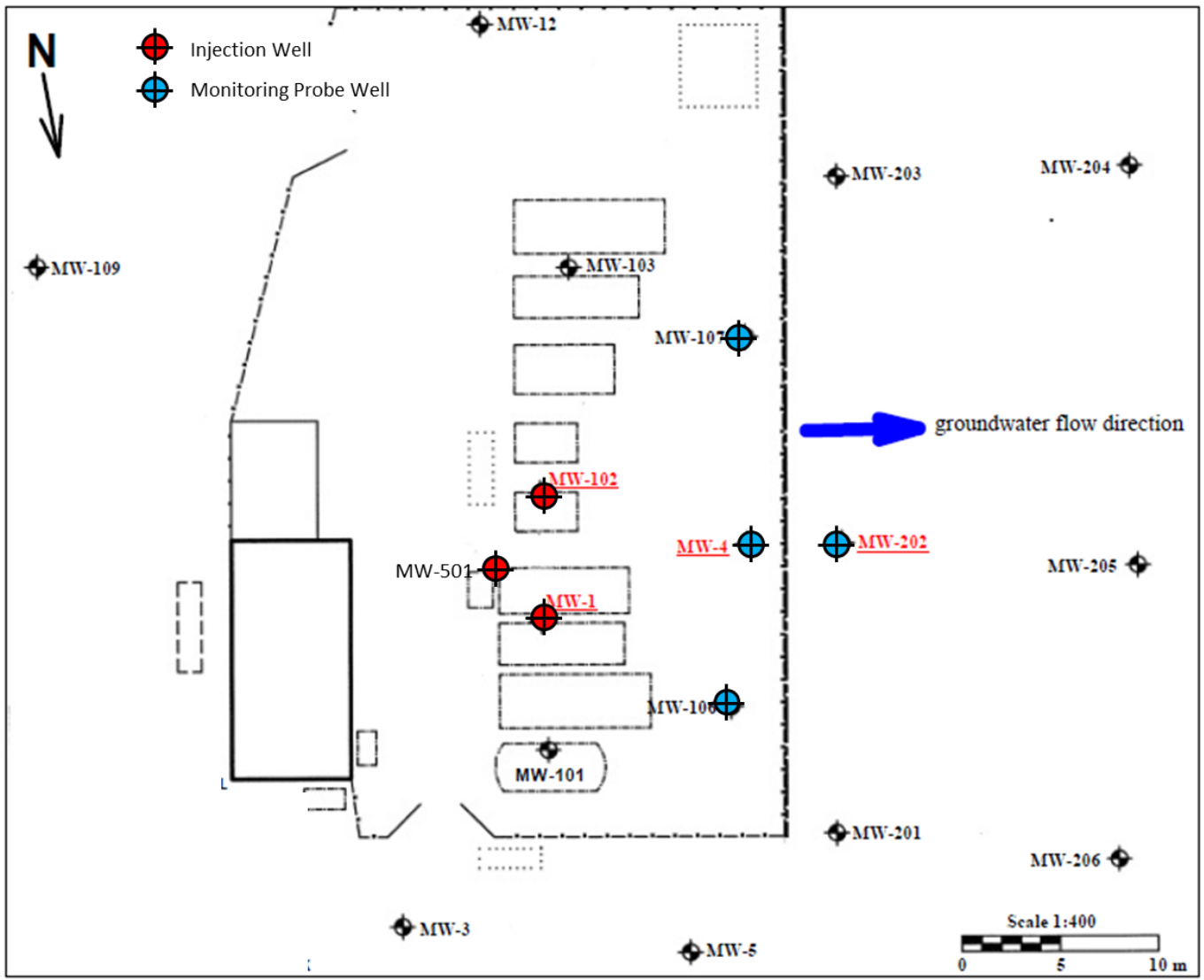


Figure 5.7: Field trial 2 site plan (adapted from Holtze, 2011)

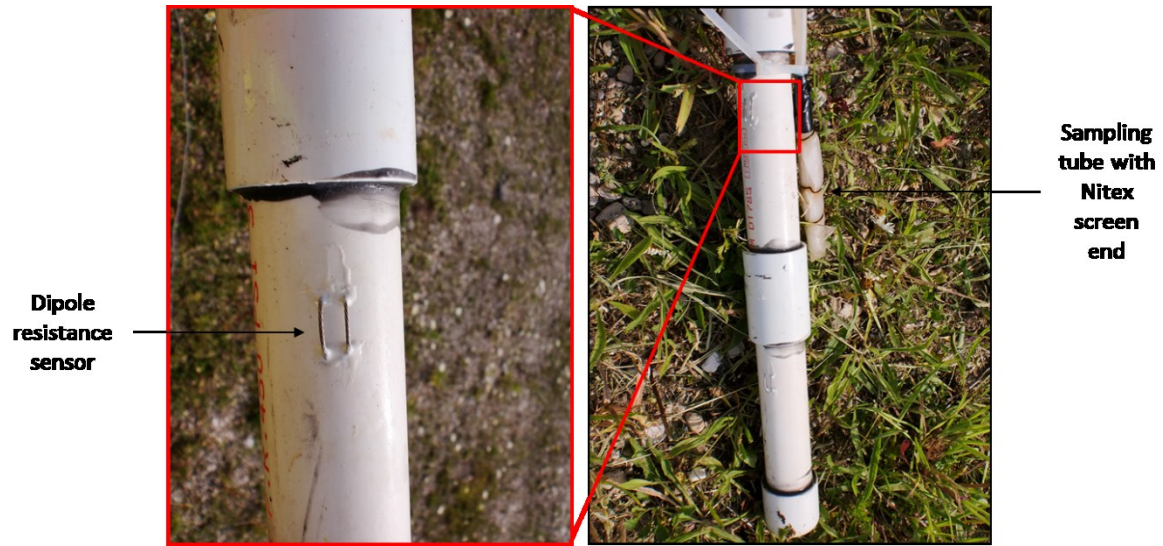


Figure 5.8: Schematic of probe installed at Field Site 2

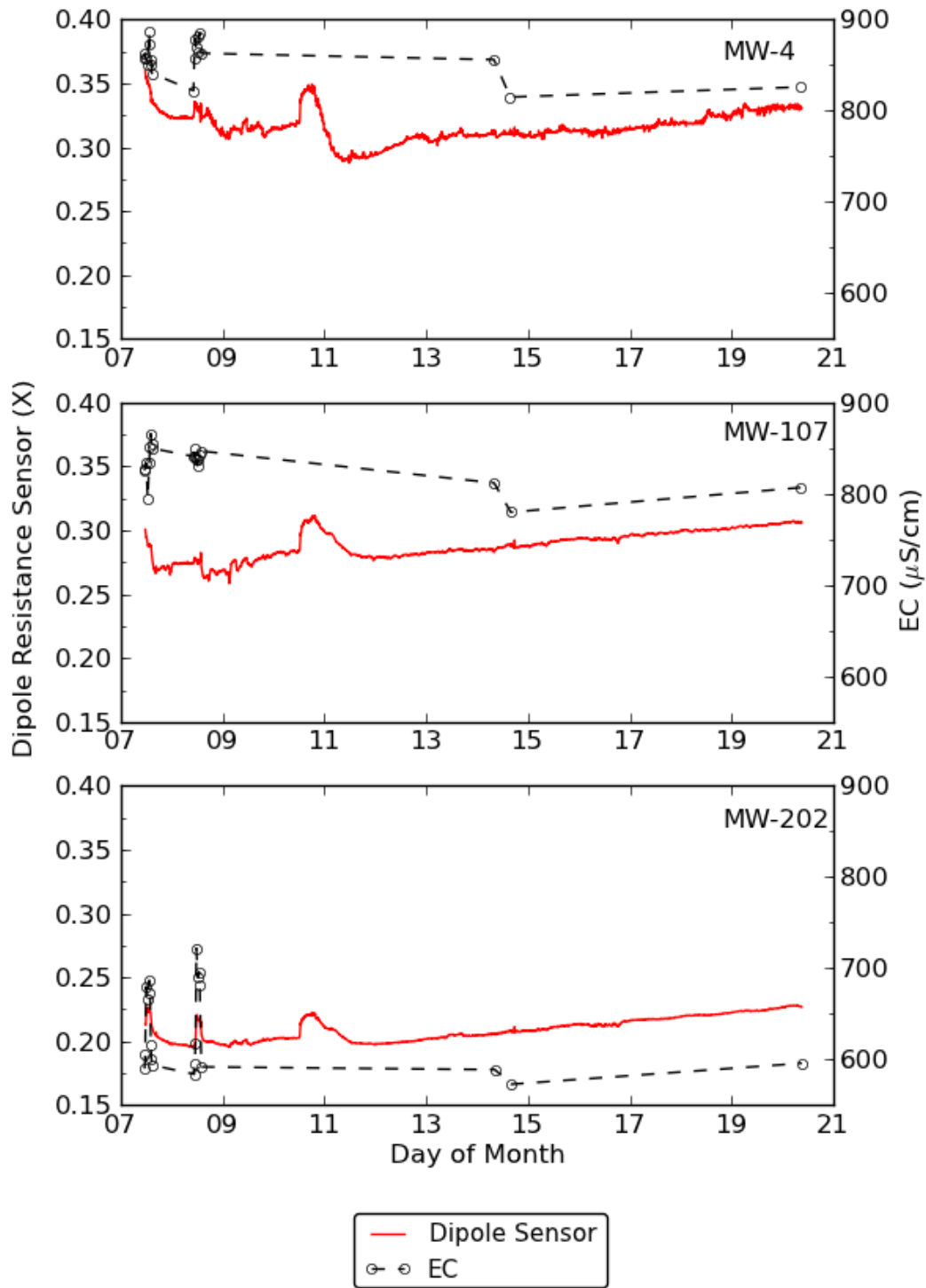


Figure 5.9: Field trial 2, probes installed at MW-4, MW-107, and MW-202

Chapter 6: Conclusions

6.1 REVIEW OF RESEARCH GOALS

This research was focused on the design and testing of a prototype probe for *in situ* monitoring of injected reagents, specifically chemical oxidants. Prototypes were built with sensors attached to PVC conduits and focused on systems which could feasibly be adapted for direct-push implementation. Design constraints were to produce a low-cost and robust system which could be used to vertically discretize reagent distribution over large areas. Based on these criteria and constraints, the prototype included simple temperature sensors and two-wire dipole resistance sensors to measure the electrical conductivity signature associated with chemical oxidants. Research focused on detailed laboratory experimentation supplemented by field trials to determine how the temperature and dipole resistance sensors responded under varied conditions. Research goals for laboratory tests were to:

1. Determine if temperature fluctuations could be monitored
2. Determine capabilities of dipole resistance sensors
 - a. Quantify how measurements respond to changes in temperature
 - b. Determine if EC can be considered to be a relevant representation of reagent concentration, specifically oxidant concentration
 - c. Quantify how measurements respond to changes in EC

6.2 TEMPERATURE SENSOR PERFORMANCE

Testing of the constructed temperature sensors answered research question 1. Figure 3.1 showed that the constructed temperature sensors responded to temperature changes similarly to a commercial transducer (Schlumberger Mini-Diver, model DI501). In addition, the data showed the temperature difference between the commercial transducer and the constructed temperature sensor was mostly constant. This showed a constructed temperature sensor could be calibrated to a commercial probe by removing the constant bias in measurements of the constructed temperature sensor.

6.3 DIPOLE RESISTANCE SENSOR PERFORMANCE

Testing of the dipole resistance sensors addressed research question 2. Chapter 3 showed the sensor responded to changes in temperature and illustrated that changes in EC on the order of 5-10 mS/cm had a much larger effect on dipole resistance sensor measurements (X) than changes in temperature on the order of 0-5 °C. Section 4.3.3 and Eq. (5) were used to analyze how temperature changes influenced the BTCs recorded in Chapter 4.

Chapters 3 and 4 showed the tested prototype probe responded accurately to changes in EC. The static cell experiments in Chapter 3 also showed that probe response to sodium persulfate and potassium permanganate solutions was similar to observed results for NaCl solutions. This addressed research question 2b, confirming that EC can be used as an indicator of oxidant concentration.

The calibrations of sensor response to EC for the static cell experiments in Chapter 3 and the BTC experiments in Chapter 4 addressed research question 2c. The results showed that an accurate calibration could be applied for a single set of measurements, although the static cell experiments indicated the calibration for a single probe may differ between usages. Laboratory testing for both the temperature sensors and dipole resistance sensor showed the prototype probes meet the research goals of this thesis to produce a system that can indicate the presence of an injected reagent.

6.4 LIMITATIONS OF DESIGNED SYSTEM

The NeST experiments with DI in Chapter 4 showed the constructed two-wire dipole sensor was not capable of responding to fine changes in EC during a BTC with the same resolution of a commercial logger. Applying a calibration to the raw dipole resistance sensor measurements (X) did not increase measurement resolution. The designed system was capable of accurately responding to changes in EC from a background value, to a peak, and then back to background. Users should take care when drawing more detailed conclusions about sensor response.

Chapter 4 also highlighted the effects of a porous medium on two-wire resistance measurements. The two-wire design provides a direct-contact measurement that is more susceptible to interference from the soil matrix in comparison to a four-electrode system. The

experimental results show the system responded accurately to changes in EC when in contact with silica sand. However, it is possible that *in situ* contact with porous medium in the field could cause more interference with a two-wire dipole sensor than what was observed in the lab.

6.5 CONTRIBUTIONS

This work has provided a theoretical representation of two-wire dipole resistance sensor response to EC and has verified expected results through high-resolution laboratory experiments. Experiments have shown that simple dipole resistance sensors constructed by hand can be calibrated to measurements from a commercial EC probe and have illustrated the impact of temperature and the choice of fixed resistor on measurements. This research has extensively tested sensor response to EC during static cell and BTC experiments, and has displayed the prototype probe is capable of indicating of the presence of injected reagents that have an EC signature. These results support preliminary findings by Cavé et al. (2007), which indicated dipole resistance sensors can respond to the presence of chemical oxidants. Results in this thesis add to work by Cavé et al. (2007) by providing a mathematical representation of sensor response of a half bridge measurement on a CR1000x datalogger and describing a calibration method based on this relationship, both of which are not currently available in the environmental monitoring literature. Sensor construction techniques, calibration methods, and expected sensor responses discussed in this thesis are applicable for applications that employ dipole resistance sensors to measure EC. In particular, this work provides insight for *in situ* EC monitoring when low-cost materials are required.

6.6 FUTURE WORK

6.6.1 Pilot scale field testing

Chapter 5 showed the prototype system appeared to be capable of recording accurate measurements in the field similar to what was observed during the laboratory experiments in Chapter 4. The first field trial took place early in the design and testing phase. Probe response during this trial was not consistent with laboratory results which indicated the first field trial did not accurately represent sensor capabilities. The second field trial produced results that were

consistent with observations from laboratory tests; sensor response provided an accurate representation of EC in the monitoring wells where field probes were installed. However, the second field trial was not fully successful because the injected persulfate did not reach the installed field probes so sensor response to the presence of the injected reagent could not be verified.

Further field testing of the probe system where prototypes similar to those tested in Chapter 5 are installed in existing monitoring wells would provide verification that laboratory observations can be repeated in the field. In particular, field trials where the injected reagent reaches the monitoring probes are required to correlate probe response with the presence of the injected reagent. Ideal pilot scale tests would include only a single injection point at a site where reagents have not been injected before. A single point of injection is desirable because it leaves no uncertainty when determining the location where an injected reagent comes from. Further to this, a site where the reagent of interest has not previously been injected is also ideal.

6.6.2 Direct-push design

A key issue related to direct-push design and implementation is the cost associated with this type of monitoring program. Based on findings of the laboratory results in this thesis, it is realistic a direct-push design capable of indicating the presence of an injected reagent could be developed using sensors similar to those tested on the PVC prototypes. However, simply being able to develop a direct-push system does not mean it would be widely adopted by industry.

Reagent injections form a niche market of the total scope of work carried out at contaminated sites. In contrast to standard practices of geologic characterization, source zone identification, and water sampling methods widely applied at contaminated sites, reagent injections consist of one of the many tools available to a remediation engineer that may be desirable to use under the right site conditions and treatment goals. Furthermore, a direct-push system would likely be most useful under a subset of sites where reagent injections are applied:

1. Sites where a Geoprobe© or comparable vibrating hammer device is already being used for the injection. For cases where an injection takes place in existing wells, bringing a direct-push device to a site adds significant costs that may outweigh benefits from the

monitoring probe. Cost-savings could also be realized through the use of a jackhammer rather than a direct-push drill rig.

2. Large sites where injections take place over multiple days. The cost of the monitoring program needs to be manageable in comparison to the total budget of the remediation design. When the scope of work at a site is large, installation of direct-push monitoring probes are more viable because the monitoring cost can represent a smaller portion of the total budget. Strategically installing monitoring probes at an injection site should provide useful information while minimizing total costs.
3. Sites where pilot-scale and push-pull testing takes place. These types of tests always include significant sampling and are often accompanied by the installation of new monitoring wells. If a direct-push system could reduce the required sampling frequency or negate the need for monitoring well installations, the probe system could potentially provide cost savings and improved monitoring data. In addition, these types of tests often take place at sites where the scope of work is significant, which supports the previous statement that a direct-push system is more viable when monitoring costs represent a small portion of the total budget.

References

APHA, AWWA, and WEF. 2012. Standard Methods for the Examination of Water and Wastewater. 22nd ed. American Public Health Association, American Water Works Association, and Water Environment Federation. Method 2510: Conductivity. Baltimore, Maryland, USA. pp. 2-52 – 2-55.

Bowen, I.R. 2010. Characterization of a dipole flow system using point velocity probes. MSc. Thesis, Department of Geology, University of Kansas. p.18. <http://hdl.handle.net/1808/7827>.

Bowen, I.R., Devlin, J.F., and P.C. Schillig. 2012. Design and Testing of a Convenient Sandbox for Controlled Flow Experiments. *Groundwater Monitoring and Remediation*. 32: 87–91. doi: 10.1111/j.1745-6592.2012.01400.x

Campbell Scientific. 2011a. CR1000 Measurement and Control System Operator's Manual, Revision 7/11. Campbell Scientific Canada Corp.

Campbell Scientific, 2011b. Model 109 Temperature Probe Instruction Manual, Revision 11/11. Campbell Scientific Canada Corp.

Cavé, L., Hartog, N., Al, T., Parker, B., Mayer, K.U., and S. Cogswell. 2007. Electrical monitoring of *in situ* chemical oxidation by permanganate. *Ground Water Monitoring & Remediation* 27, no.2, Spring 2007, pp.77-84.

CGPM, 1972. 14th Conférence Générale des Poids et Mesures Conférence Générale des Poids et Mesures, 78 pp.

Christy, C.D., Christy, T.M., and V. Wittig. 1994. A percussion probing tool for the direct sensing of soil conductivity. Direct Image, Geoprobe Systems Technical paper No.94-100, March, 1994.

Davis, E.L. 1997. How heat can enhance in-situ soil and aquifer remediation: Important chemical properties and guidance on choosing the appropriate technique. United States Environmental Protection Agency, Office of Research and Development, Office of Solid Waste and Emergency Response. EPA/540/S-97/502 April 1997.
<www.epa.gov/tio/tsp/download/heatenh.pdf>

Davis and DeWeist. 1966. Hydrogeology. John Wiley & Sons, Inc. New York.

Devlin, J.F., Tsoflias, G., McGlashan, M., Schillig, P. 2009. An inexpensive multilevel array of sensors for direct ground water velocity measurement. *Ground Water Monitoring and Remediation*, v. 29, no. 2, 73-77.

Devlin, J.F., Schillig, P.C., Bowen, I., Critchley, C.E., Rudolph, D.L., Thomson, N.R., Tsoflias, G.P., and J.A. Roberts. 2012. Applications and implications of direct groundwater velocity measurement at the centimetre scale. *Journal of Contaminant Hydrology* 127. pp. 3-14.

Dijkstra, E. 2012. Personal communication June 1 2012, Schlumberger Water Services.

Einarson, M. 2006. Multi-Level Ground Water Monitoring. Final Manuscript submitted to *Practical Handbook of Groundwater Monitoring*, D. Neilson (ed), Chapter 11, CRC Press, pp. 1-51.

Freeze, R.A. and J.A. Cherry. 1979. *Groundwater*. Prentice-Hall, New Jersey.

Friedman, S.P. Soil properties influencing apparent electrical conductivity: a review. *Computers and electronics in agriculture* 46, 2005, pp.45-70.

Gawande, N.A., Reinhart, D.R., Thomas, P.A., McCreanor, P.T., and T.G. Townsend. 2003. Municipal solid waste in situ moisture content measurement using an electrical resistance sensor. *Waste Management* 23, pp.667-674.

Geoprobe Systems. 2012. Geoprobe Systems: Direct Image Products. Internet <<http://geoprobe.com/geoprobe-systems-direct-image-products>>. Retrieved October 2012.

Gheith, H.5., and F.W. Schwartz. 1998. Electrical and visual monitoring of small scale three-dimensional experiments. *Journal of Contaminant Hydrology* 34 (1998) pp.191-205.

Greer, K.D. 2009. Evaluation of an oxygen injection technology for in-situ hydrocarbon bioremediation in a fractured bedrock environment. MSc Thesis, Department of Earth Science, University of Waterloo, Waterloo, ON, Canada.

Greer, K.D, Freitas, J.G, Stevenson, D.R., Molson, J., Thomson, N.R., and J.F. Barker. 2011. An in-situ chemical oxidation pilot scale test for treatment of petroleum hydrocarbons in fractured bedrock. Presented at GeoHydro, August 28-31, 2011, Quebec, QC, Canada. http://www.geohydro2011.ca/gh2011_user/cle_usb/pdf/doc-2218.pdf

Halihan, T., Albano, J., Comfort, S.D., and V.A. Zlotnik. 2011. Electrical resistivity imaging of a permanganate injection during *in situ* treatment of RDX-contaminated groundwater. *Ground Water Monitoring & Remediaton*, Vol. 32, No.1, Winter 2012, pp.43-52.

Halihan, T., McDonald, S.W., Patey, P., and 5. Stonecipher. 2012. ERI evaluation of injectates used at a dry-cleaning site. *Remediation*, Summer 2012, pp.79-91. Published online, wileyonlinelibrary.com DOI. 10.1002/re5.21322.

Harte, P.T., Smith, T.E., Williams, J.H., and J.R. Degnan. 2012. Time series geophysical monitoring of permanganate injections and *in situ* chemical oxidation of PCE, OU1 area, Savaga Superfund Site, Milford, NH, USA. *Journal of Contaminant Hydrology* 132 (2012), pp.58-74.

- Hayashi, S. 2004. Temperature-electrical conductivity relation of water for environmental monitoring and geophysical data inversion. *Environmental monitoring and Assessment* 96, 119-128.
- Hem, J.D. 1970. Study and interpretation of the chemical characteristics of natural water. USGS water-supply paper 2254, 3rd ed.
- Holtze, D. 2011. Demonstration of nitrate-enhanced in situ bioremediation at a petroleum hydrocarbon contaminated site. MSc Thesis, Department of Earth Science, University of Waterloo, Waterloo, ON, Canada.
- Katanchi, B. 2011. In situ chemical oxidation using unactivated sodium persulphate at a former fuel storage facility. MSc Thesis, Department of Earth Science, University of Waterloo, Waterloo, ON, Canada.
- Klein, K.A. and J.C. Santamarina. 2003. Electrical conductivity in soils: underlying phenomena. *Journal of Environmental Engineering and Geophysics*. December 2003, Vol.8 (4), pp.263-273.
- Krembs, F.J., Siegrist, R.L., Crimi, M.L., Furrer, R.F., and B.G. Petri. 2010. ISCO for groundwater remediation: analysis of field applications and performance. *Ground Water Monitoring & Remediation* 30, No.4, pp.42-53.
- Labaky, W. 2004. Theory and testing of a device for measuring point-scale groundwater velocities. Ph.D. thesis, Department of Earth Science, University of Waterloo, Waterloo, ON, Canada.
- Labaky, W., Devlin, J.F., Gillham, R.W. 2007. A probe for measuring groundwater velocity at the centimetre scale. *Environmental Science and Technology*, v. 41, no. 24, 8453-8458.
- Labaky, W., Devlin, J.F., and R.W. Gillham. 2009. Field comparison of the point velocity probe with other groundwater velocity measurement methods. *Water Resources Research*. Vol. 45. W00D30, doi:10.1029/2008WR007066.
- Langelier, W.F. The analytical control of anti-corrosion water treatment. *J. American Water Works Association*. 28: 1500 (1936).
- Lind, C.J., 1970. Specific conductance as a means of estimating ionic strength: U.S. Geological Survey Professional Paper 700-D: D272-D280.
- Lewis, G.N. and M. Randall. 1921. The activity coefficient of strong electrolytes. *Journal of the American Chemical Society*. Vol. 43, No.5. pp. 1112-1154.
- Ma, R., McBratney, A., Whelan, B., Minasny, B., and S. Short. Comparing temperature correction models for soil electrical conductivity measurement. *Precision Agric*, 2011, 12 :55-66. DOI 10.1007/s11119-009-9156-7.

Mackay, D.M. and J.A. Cherry. 1989. Groundwater contamination: pump-and-treat remediation. *Environmental Science and Technology*, Vol.23, No.6.

Mastrocicco, M., Prommer, H., Pasti, L., Palpacelli, S., and N. Colombani. Evaluation of saline tracer performance during electrical conductivity groundwater monitoring. *Journal of Contaminant Hydrology*. Vol 123, pp.157-166.

Miller, R.L., Bradford, W.L., and N.E. Peters. 1988. Specific conductance: theoretical considerations and application to analytical quality control. USGS water-supply paper 2311.

Millero, F.J. 2001. *The Physical Chemistry of Natural Waters*. Wiley-Interscience, New York.

McCleskey, R.B. 2010. *Electrical conductivity: Theory and applications for natural waters*. Ph.D. thesis, Department of Civil, Environmental, and Architectural Engineering, University of Colorado: USA.

Nyquist, J.E., Carr, B.J., and R.K. Davis. 1999. DC resistivity monitoring of potassium permanganate injected to oxidize TCE *in situ*. *Journal of Environmental Engineering and Geophysics* Vol.4, 3, pp.135-147.

Opta Minerals Inc. 2012. Internet. <<http://www.optaminerals.com/Construction/Barco-Silica-Sand.html>>. Retrieved August 2012.

Palaia, T., Smith, B., and R.W. Lewis. 2011. ISCO performance monitoring. In situ chemical oxidation for groundwater remediation, 2011, Siegrist, R.L., Palaia, T., Clayton, W., and R.W. Lewis. (eds), chapter 12, Springer Science and Business Media, pp.481-510.

Robinson, R.A., and R.H. Stokes. 1965. *Electrolyte Solutions: The measurement and interpretation of conductance, chemical potential and diffusion in solutions of simple electrolytes*. Second ed. Butterworths, London Publications Limited, 571 pp.

Schlumberger Water Services. 2012a. Product Manual: Mini-Diver, Micro-Diver, Cera-Diver, Baro-Diver, CTD-Diver. Internet. <http://www.swstechnology.com/pdfs/equipment/Diver_manuals/Diver_Product_Manual_en.pdf> . Retrieved June 2012.

Schlumberger Water Services. 2012b. Groundwater dataloggers: CTD-Diver. Internet. <<http://www.swstechnology.com/groundwater-monitoring/groundwater-dataloggers/ctd-diver/>> Retrieved June 1, 2012.

Sellwood, S.M., Healey, J.M., Birk, S., and J.J. Butler Jr. 2005. Direct-push hydrostratigraphic profiling: coupling electrical conductivity logging and slug tests. *Ground Water*. Vol. 43, No. 1. pp. 19-29.

Siegrist, R.L., Crimini, M., and R.A. Brown. 2011. In situ chemical oxidation: technology description and status. In situ chemical oxidation for groundwater remediation, 2011, Siegrist,

R.L., Palaia, T., Clayton, W., and R.W. Lewis. (eds), chapter 1, Springer Science and Business Media, pp.1-32.

Snoeyink, V.L. and D. Jenkins. 1980. Water Quality. John Wiley & Sons Inc. Toronto, Ontario.

Sorensen, J.A. and Glass, G.E. 1987. Ion and temperature dependence of electrical conductance for natural waters. *Analytical Chemistry* 59, 1594-1597.

Suthersan, S., and J. Horst. 2008. Aquifer minerals and *in situ* remediation: the importance of geochemistry. *Ground Water Monitoring & Remediation* 28, no.3, summer 2008, pp.153-160.

Suthersan, S., Horst, J., Nelson, D., and S. Schnobrich. 2011. Insights from years of performance that are shaping injection-based remediation systems. *Remediation*, Spring 2011, pp.9-25. Published online, wileyonlinelibrary.com DOI. 10.1002/re5.20279.

Tchobanoglous, G. and E.D. Schroeder. 1987. Water Quality. Addison, Wesley, Longman Publishing. Don Mills, Ontario.

Wildenschild, D., Roberts, J.J., and E.D. Carlberg. 2000. On the relationship between microstructure and electrical and hydraulic properties of sand-clay mixtures. *Geophysical Research Letters*, Vol. 27, No.19., October 1, 2000, pp. 3085-3088.

Appendix A: Supplementary Information for Chapter 1

A1: SUMMARY OF PROS AND CONS RELATED TO POTENTIAL MEASUREMENT PARAMETERS

pH

With the exception of hydrogen peroxide, reagent injections are not typically associated with a change in pH, which vastly limits the usefulness the measurement can provide. In addition, the use of pH sensors in prototype designs was impractical due to sensor size and cost. Inexpensive pH sensors use reference electrode designs that make installation on a direct push drill rod difficult, while corrosion resistant sensors made for *in situ* applications are generally expensive and too large for installation on a drill rod.

Oxidation Reduction Potential

Cavé et al. described simple low-cost ORP sensors that can be constructed by hand (2007). Field tests indicated a good correlation between sensor response and the presence of permanganate. The main obstacle to installing this type of sensor on a direct push apparatus is the reference electrode needed for the sensor. If a method were created for easy installation of the reference electrode, this type of sensor could be a viable addition to a direct push design. One point to note is Cavé et al. found two-wire dipole EC sensors, similar to the ones used in this project, provided the same indication of permanganate presence that the ORP sensor did, although the EC sensor was correlated with concentration, making it a more useful measurement (2007). These results indicated when ORP sensors are used in combination with a two-wire EC sensor, the ORP measurements can confirm the EC sensor is correctly measuring a reagent, but EC measurements are able to provide the most detailed information.

Pressure

Pressure sensors were initially selected for inclusion in the prototype design although two major obstacles prevented them from being included in later stages. Sensor cost was prohibitive, while inclusion of a pressure sensor on a direct push design was anticipated to be difficult. A pressure sensor capable of measuring water level measurement changes with resolution relevant to reagent injections, such as the centimeter scale, was unlikely to be able to withstand the driving forces associated with a percussion hammer drill rig. In addition, sensor size was also an issue.

Ion Selective Electrodes

Similar to issues with pH and ORP electrodes, barriers to using ion selective electrodes (ISE) *in situ* are related to appropriate use of a reference solution. Similar to most pH and ORP electrodes, an ISE requires calibration and use of a reference solution for measurements, which is a barrier for designs using direct push drill rods.

Appendix B: Supplementary Information for Chapter 2

B1: MATERIAL DEGRADATION WITH PERSULFATE

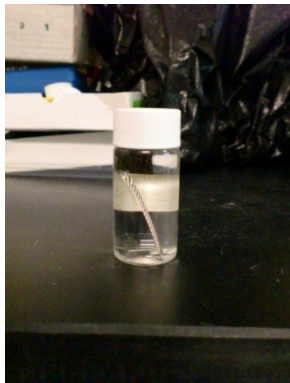
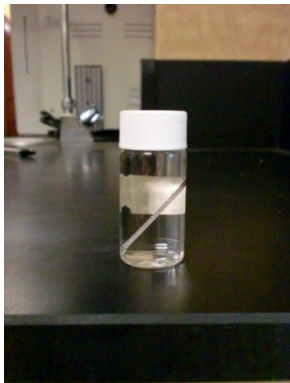










Sample	2010/08/27	2010/08/30	2010/09/17
1H			
1L			
2H			
2L			

Figure B1: Material tests with persulfate, visual results for samples 1 and 2




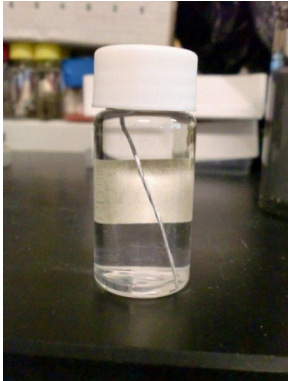


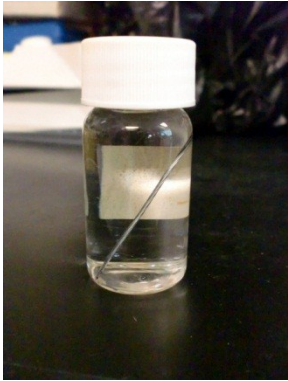


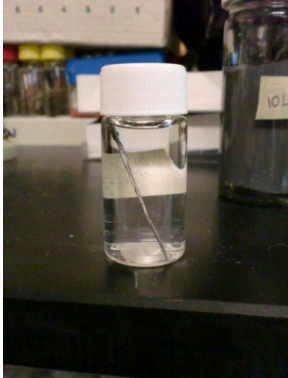


Sample	2010/08/27	2010/08/30	2010/09/17
3H			
3L			
4H			
4L			

Figure B2: Material tests with persulfate, visual results for samples 3 and 4


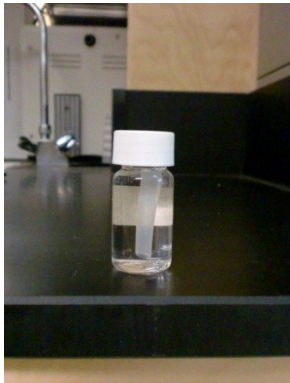

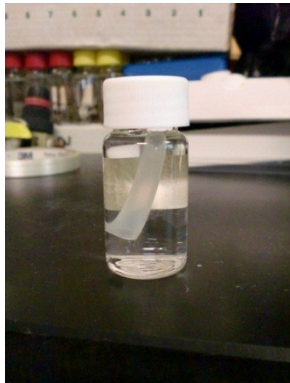


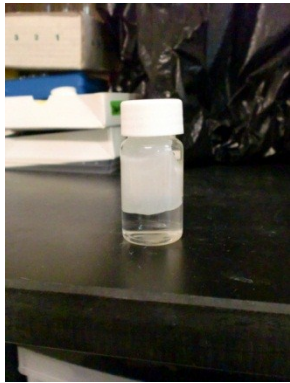





Sample	2010/08/27	2010/08/30	2010/09/17
5H			
5L			
6H			
6L			

Figure B3: Material tests with persulfate, visual results for samples 5 and 6













Sample	2010/08/27	2010/08/30	2010/09/17
7H			
7L			
8H			
8L			

Figure B4: Material tests with persulfate, visual results for samples 7 and 8

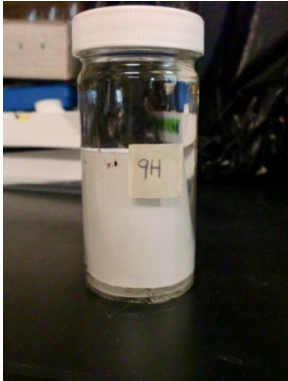


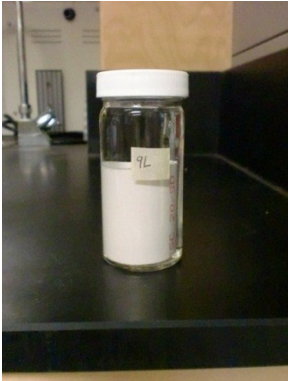
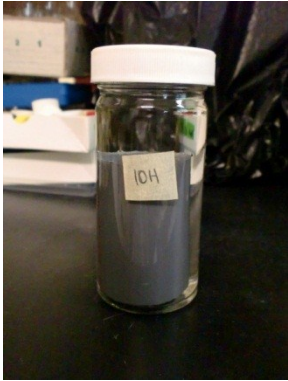



Sample	2010/08/27	2010/08/30	2010/09/17
9H			
9L			
10H			
10L			

Figure B5: Material tests with persulfate, visual results for samples 9 and 10

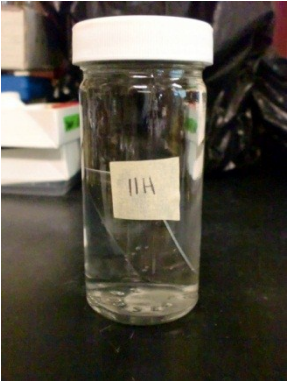





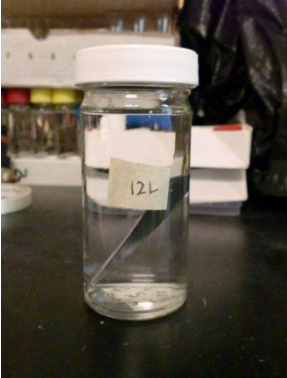

Sample	2010/08/27	2010/08/30	2010/09/17
11H			
11L			
12H			
12L			

Figure B6: Material tests with persulfate, visual results for samples 11 and 12






Sample	2010/08/27	2010/08/30	2010/09/17
13H			
13L			

Figure B7: Material tests with persulfate, visual results for sample 13

Appendix C: Supplementary Information for Chapter 3

C1: INITIAL FLOW CELL EXPERIMENTS

Tailing on the falling limb of the BTC has been previously observed when dipole resistance sensors have been used to measure a salt tracer. Labaky tested PVPs that use a NaCl solution injection to create a BTC that can be used in the calculation of groundwater velocity (2004, p.118). Figure C2 below shows an example of BTCs collected by Labaky (2004, p.118), which show significant tailing at the end of breakthrough when a high tracer injection rate was used. This data only shows the dipole resistance sensor response to EC breakthrough and does not have a EC reference for comparison, but the tailing observed where the end of breakthrough does not return to baseline values is similar to what has been reported in Chapter 3 and this appendix. This may indicate, under certain conditions such as high tracer injection rate or fast breakthrough, the resistance sensor is not capable of accurately measuring the second half of a BTC.

Tailing was also observed during EC BTCs in a column experiment by Mastrocicco et al. where multiple tracers were evaluated with different types of porous media (2011). EC BTCs of the different tracers were collected using two commercial dataloggers and were compared to sampling data analyzed by ion chromatography (IC). IC analysis in this experiment evaluated conservative species Br^- and Cl^- , which showed less tailing than EC curves derived from dataloggers. The authors explained this tailing as a result of cation exchange processes and noted tailing increased with higher flow velocities. Increased tailing with flow velocity described by Mastrocicco et al. agrees with increased tailing with tracer velocity observed by Labaky, although a contrast in experimental data is BTCs collected by Labaky (2004) do not return to baseline values for the high tracer injection rate in Figure C2 while Mastrocicco et al. (2011) shows BTCs that do return to baseline. Hence, the tailing observed by Labaky may not be a result of cation exchange processes and rather is an artifact of some part of Labaky's experimental design or a property of the dipole resistance sensor itself. This is supported by comments provided by Mastrocicco et al. (2011) which describe a BTC will have a sharper rise on the front end of breakthrough and will tail more on the back end when the number of sites available for cation exchange are exceeded. Because the tailing observed by Labaky is

significant, if cation exchange processes were responsible for the tailing on the back end of breakthrough, the front end of breakthrough should show a sharp peak. In contrast to data presented by Mastrocicco et al. (2011), Labaky's BTCs (2004) in Figure C2 show a slightly more gradual increase on the front end of breakthrough, but more significant tailing on the back half, indicating cation exchange processes may not be responsible for the tailing after the peak.

Cation exchange processes are not present in the experimental data in Figure C1 because these BTCs were simulated in open water with no porous media. This indicates, with support from the discussion above, that the cause for tailing BTCs observed by Labaky (2004) and in this thesis may be the same.

Table C1: Controlled variables in open water BTC experiments

Experiment	Measurement Parameter Details
A	Order of sensors were EC1, 2, 3, 4 Probes slightly offset from middle so all sensors aligned along the middle of tank
B	Same as A
C	Same as A and B, slightly higher pumping rate
D	Different probe orientation: Probes in same location, rotated 90 degrees so sensors were facing flow direction
E	Same as D, except settling time programmed for sensor to be 5000 μ s

Table C2: Variability in handheld conductivity measurements during open water BTC experiments

BTC	Pumping Rate (L/min)	Average Variability (mS/cm)		Maximum Variability (mS/cm)	
		Point A	Point B	Point A	Point B
A	0.20	0.09	0.03	0.30	0.15
B	0.21	0.18	0.05	0.47	0.15
C	0.32	0.20	0.08	0.50	0.38
D	0.32	0.17	0.05	0.49	0.22
E	0.32	0.26	0.04	0.74	0.17
Average		0.18	0.05	0.74	0.38

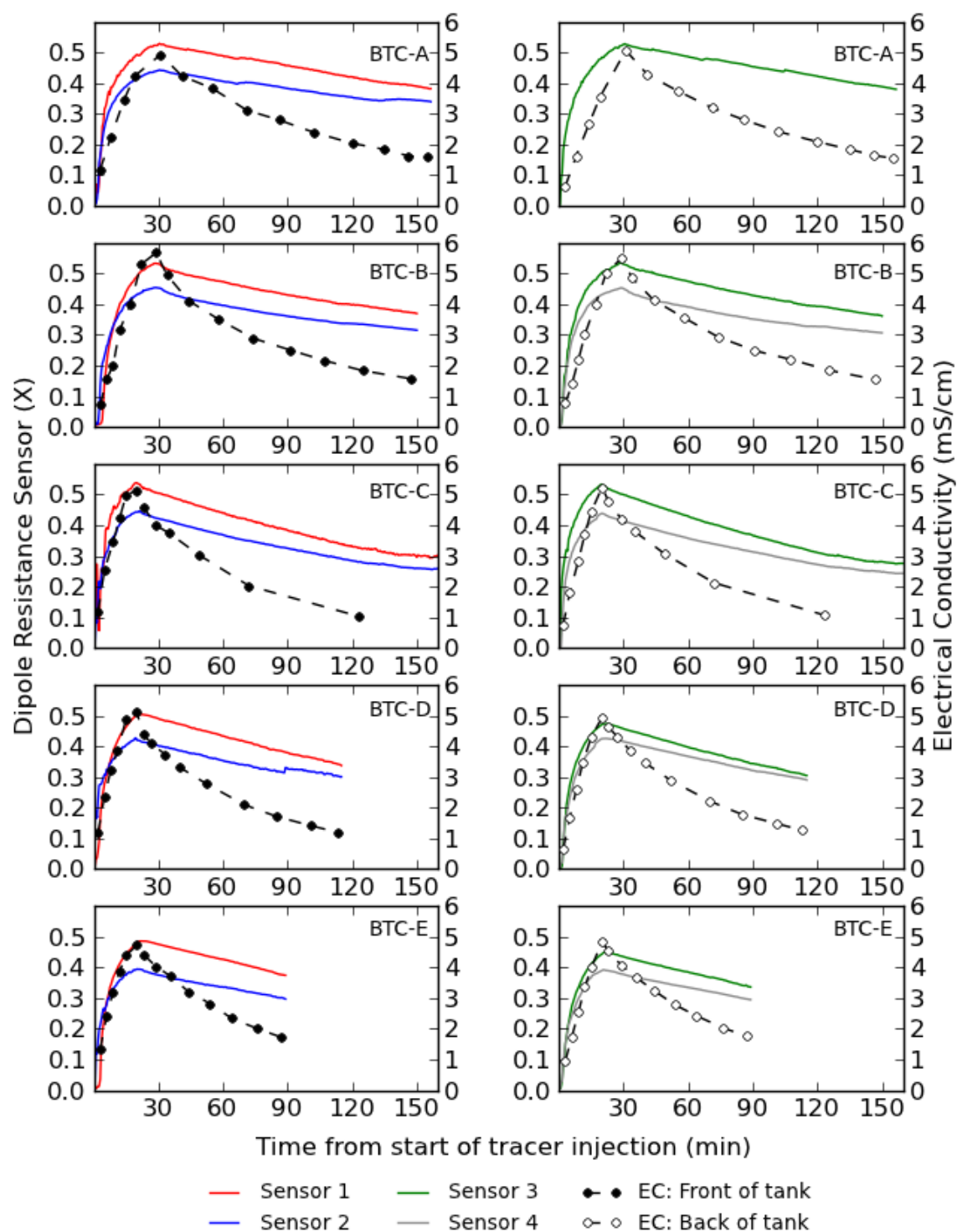


Figure C1: BTC-A to BTC-E collected during initial flow cell experiments. Dipole resistance measurements shown on left axis of left and right panels. EC measurements corresponding to the same tank location as dipole measurements shown on right axis of left and right panels. Start of injection defined as time when feed solution at inlet tube switched to NaCl.

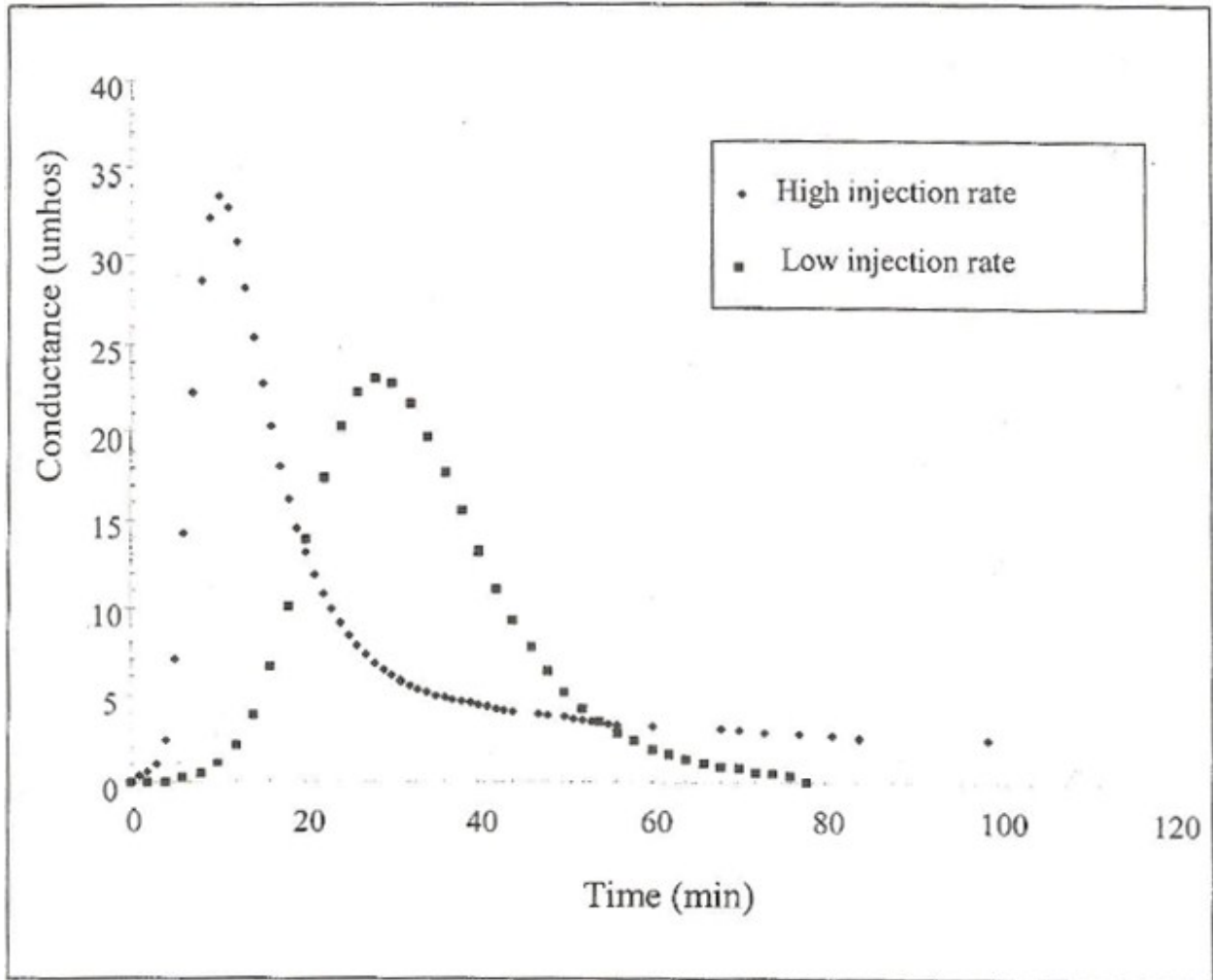


Figure C2: Example of tailing BTC (Labaky, 2004, p.118)

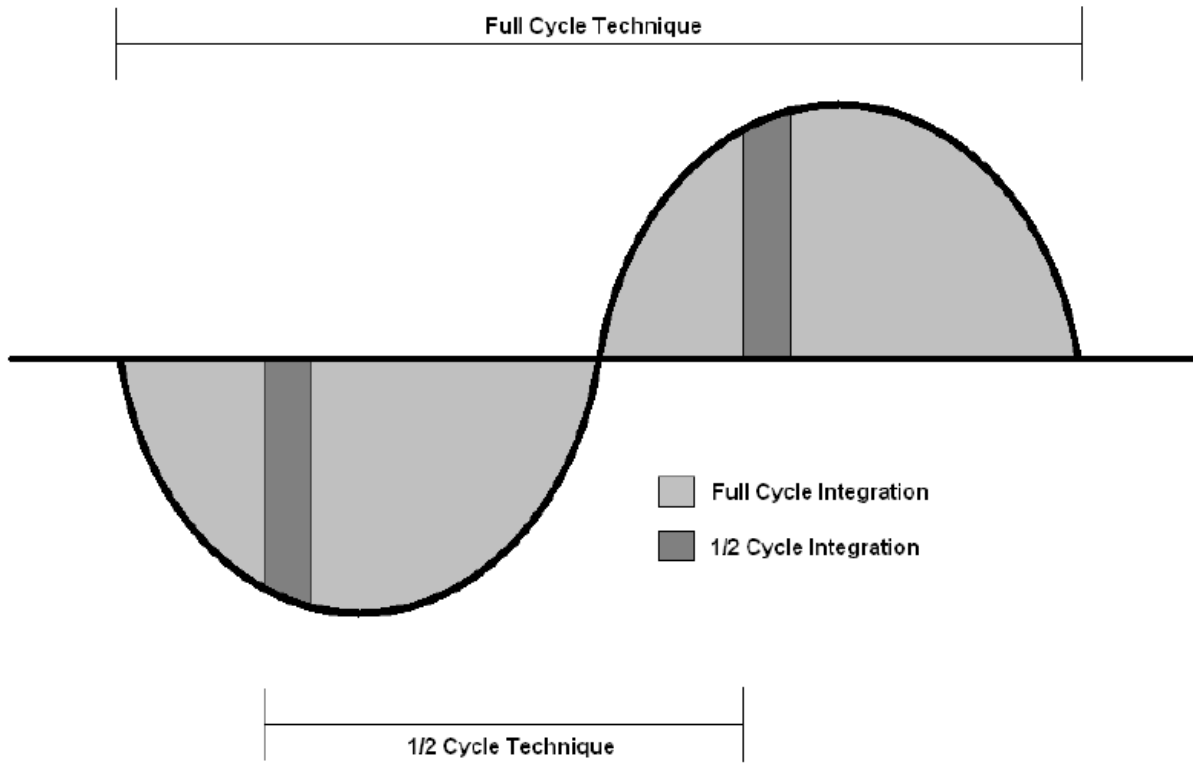


Figure C3: Removal of noise caused by alternating current power source (Campbell Scientific, 2011a, p.55)

Appendix D: Supplementary Information for Chapter 4

D1: NeSTs CONSTRUCTION

The NeST system is introduced and described by Bowen et al. (2012). The tank built and tested in this thesis was constructed according to these guidelines which are summarized below.

Construction Materials

- 1 58.4 cm L x 41.3 cm W x 31.4 cm H, plastic storage container for main compartment (Rubbermaid® 53 L)
- 1 40.6 cm L x 30.5 cm W x 83.8 cm H plastic storage container for upstream reservoir (Rubbermaid® 47 L wastebasket)
- 1 73.7 cm L x 44.9 cm W x 16.6 cm H plastic plastic storage container for holding main compartment and upstream reservoir (Rubbermaid® 39 L)
- 1 larger container for holding entire NeST system to prevent spills or overflow (189 L)
- 9 plumbing fittings (Waterline® Push N Turn©)
- Nitex® screen
- 18 rubber gaskets
- Silicone
- 2 bar clamps (Jobmate® 24-inch Quick Ratcheting Clamps)

Construction Procedure

1. Trim lip off upstream end of main tank to allow easy connection with upstream reservoir (Figure D1, right)
2. Drill 9 1.25 cm (0.5 in) diameter holes in upstream end of main tank (Figure D1)
3. Drill 9 1.25 cm (0.5 in) diameter holes in upstream storage reservoir to match those in main tank
4. Drill approximately 400 0.16 cm (1/16 in) diameter holes in downstream end of main reservoir (Figure D2)
5. Attach storage reservoir and main tank using plumbing fittings. Tighten fittings with one gasket for each hole.
6. Seal connection between plumbing fittings and reservoir with silicone
7. Cover plumbing fittings with Nitex® screen using rubber gaskets (Figure D3, left)
8. Place main tank with reservoir inside outlet reservoir (39 L) tank
9. Place all three containers inside larger tank to prevent spills
10. Attach bar clamps to main tank to prevent tank deformation when porous media added
11. Add monitoring instrumentation to main tank and pack with porous media (Figure D4)



Figure D1: 9 holes (1.25 cm diameter) drilled in upstream end of main reservoir



Figure D2: Approximately 400 1/16 inch holes drilled in downstream end of main reservoir

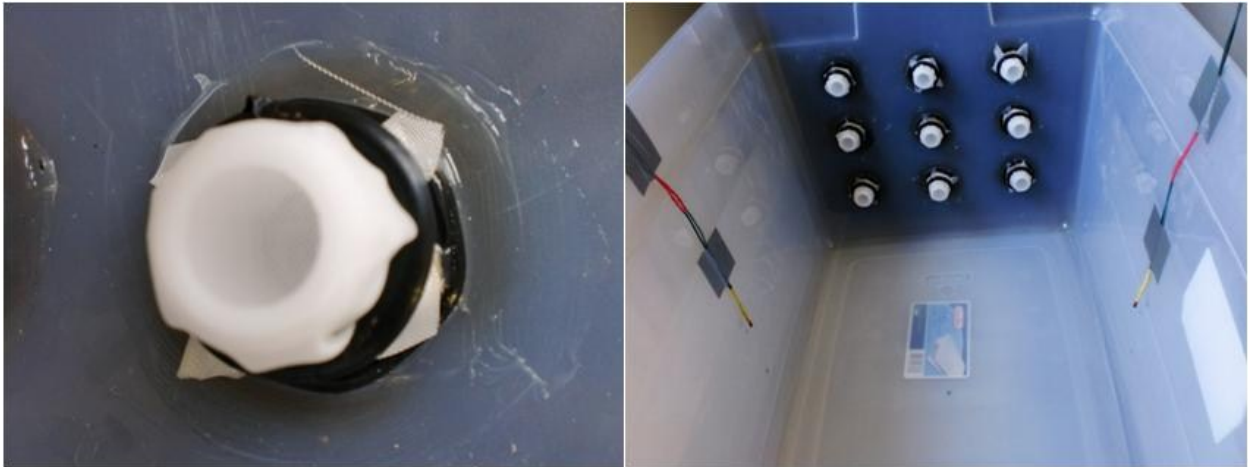


Figure D3: Nitex® screen

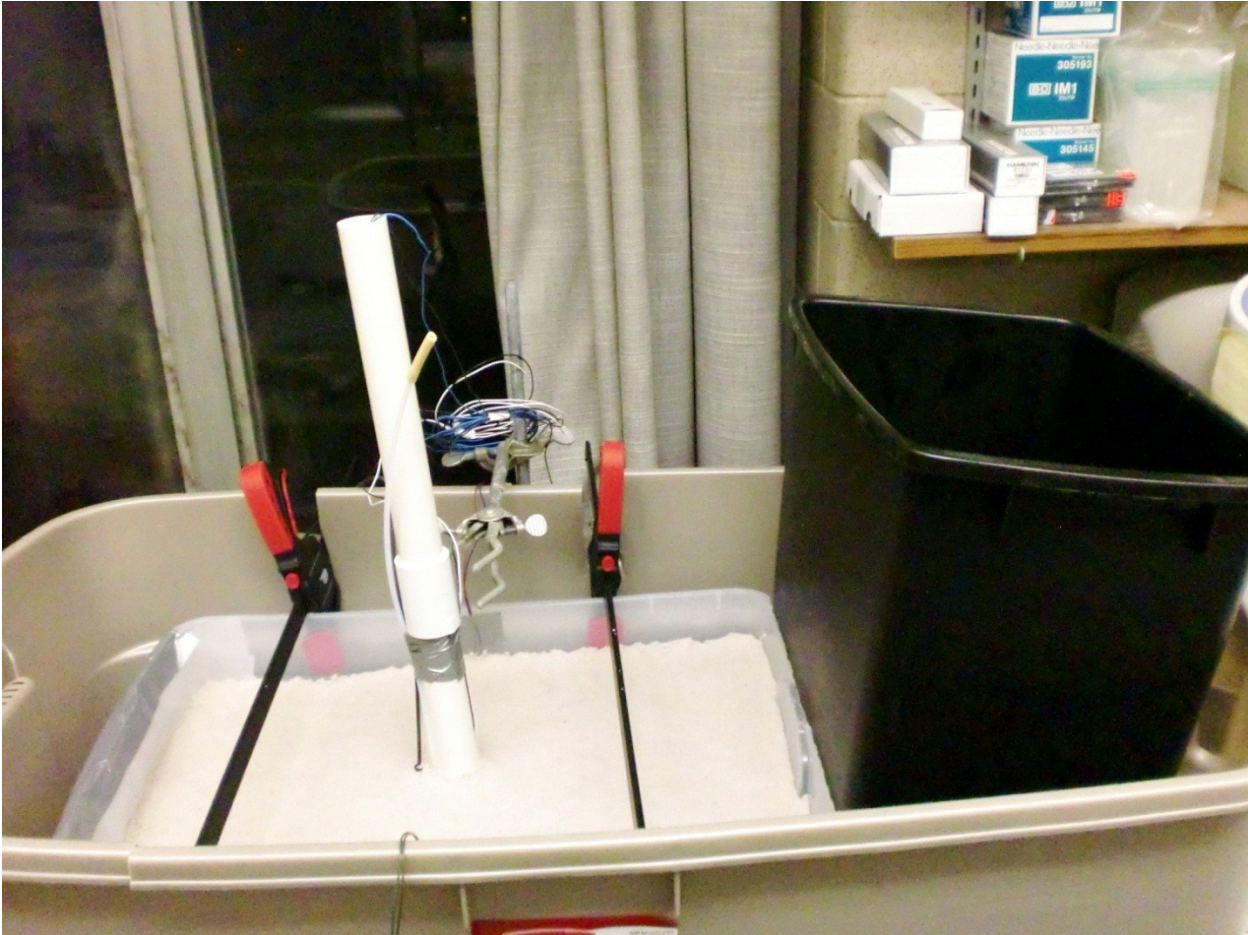


Figure D4: Completed NeST system used for BTC experiments described in Chapter 4

D2: SILICA SAND SPECIFICATIONS

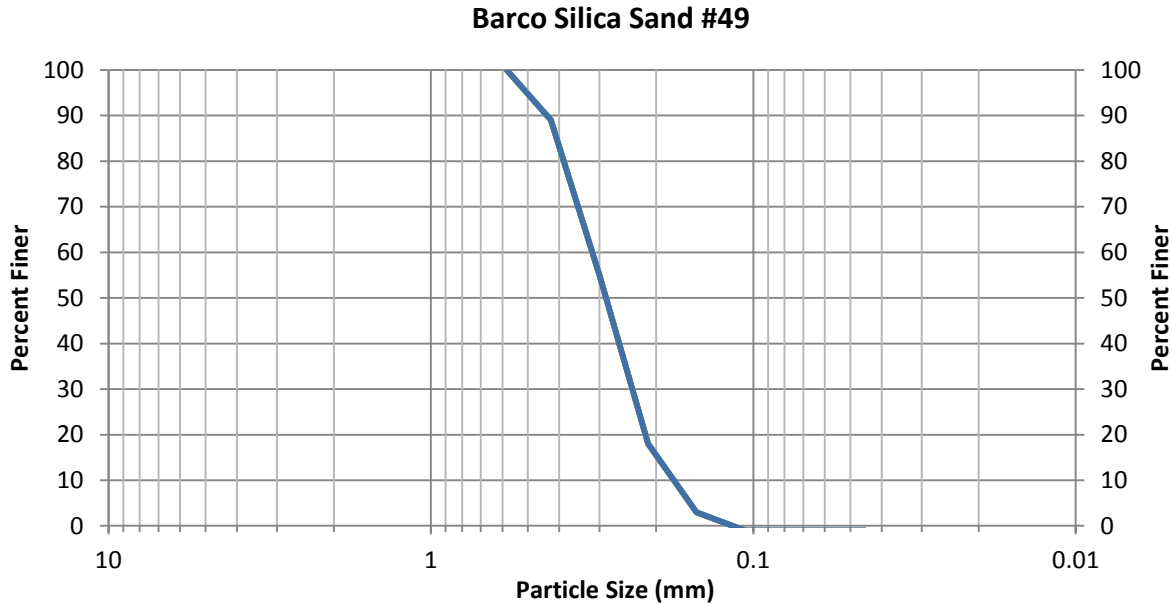


Figure D5: Grain size analysis for Barco Silica Sand #49*
 *(<http://www.optaminerals.com/Construction/Barco-Silica-Sand.html>)

Calculation of Coefficient of Uniformity, C_u :

Grain size of 60% finer: $d_{60} = 0.32 \text{ mm}$

Grain size of 10% finer: $d_{10} = 0.18 \text{ mm}$

$$C_u = \frac{d_{60}}{d_{10}} = 1.78$$

Table D1: Properties of silica sand in NeST*

Other Parameters	
Mineral	Quartz (99.7% SiO ₂)
Solubility	Insoluble
Specific gravity	2.65
Bulk density (aerated)	1586 kg/m ³
Grain shape	Sub-angular
Hardness	7 Mohs

*(<http://www.optaminerals.com/Construction/Barco-Silica-Sand.html>)

D3: CTD-DIVER SPECIFICATIONS

Table D2: Product specifications for CTD-Diver (Schlumberger Water Services, 2010, p.12)

Parameter	Range	Accuracy	Resolution
Pressure	10 (meters)	+/- 0.5(cm H ₂ O)	0.2 (cm H ₂ O)
Temperature (°C)	-20 to +80	+/- 0.1	+/- 0.01
Conductivity (mS/cm)	set to 30 or 120	+/- 1% of reading	+/- 1% of reading

D4: DEIONIZED WATER BTCs

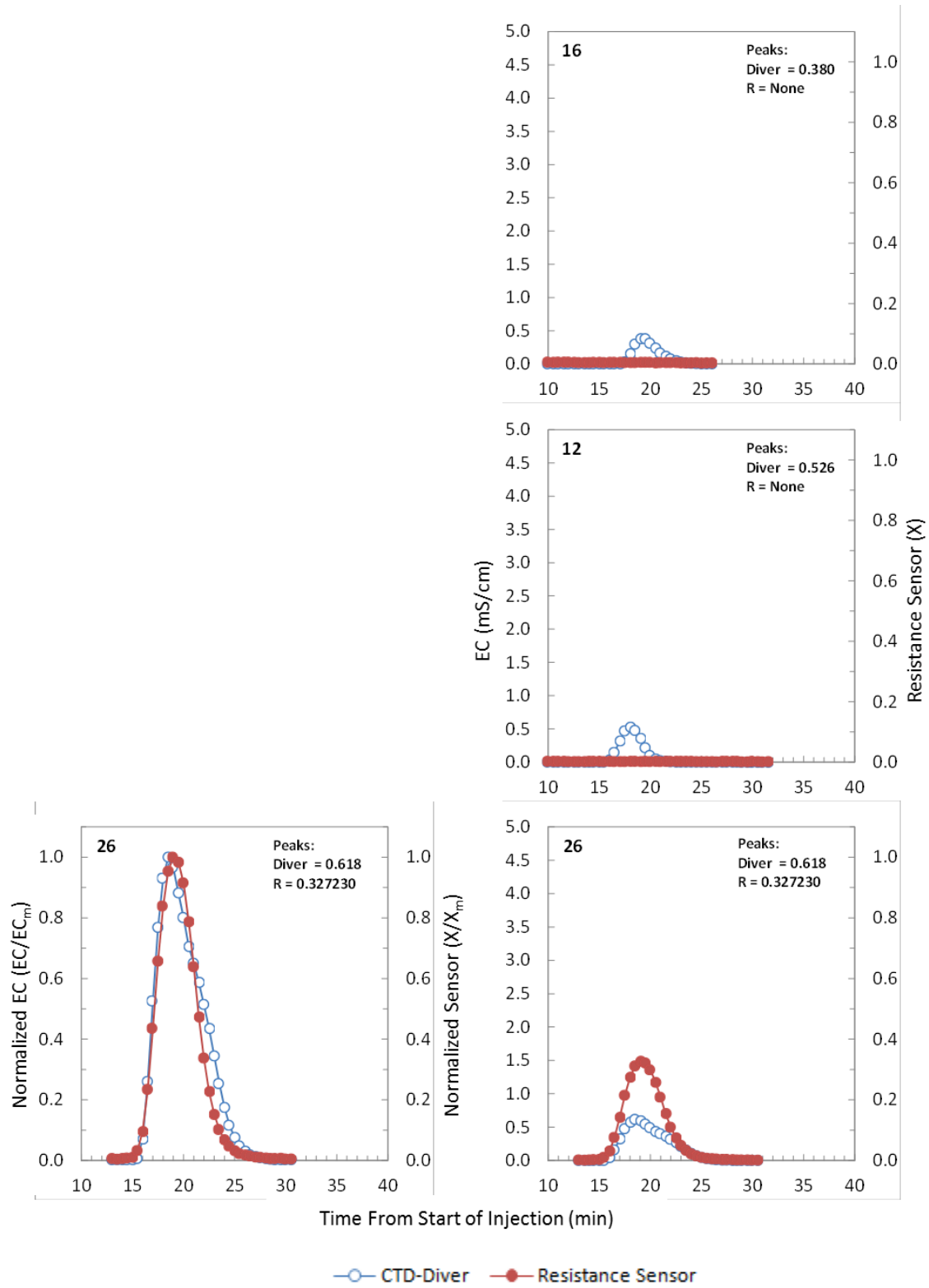


Figure D6: BTC 16, 12, and 26

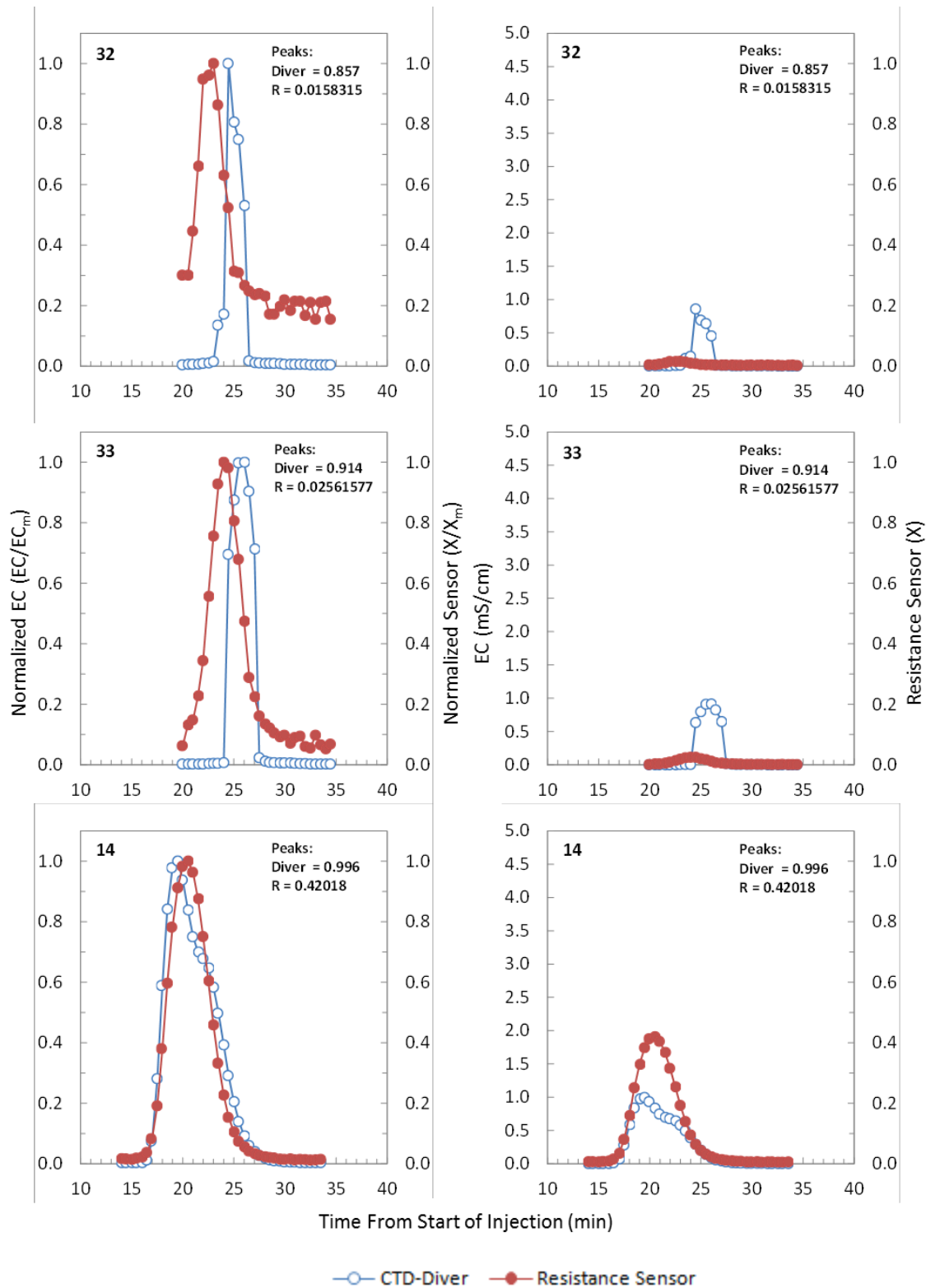


Figure D7: BTC 32, 33, and 14

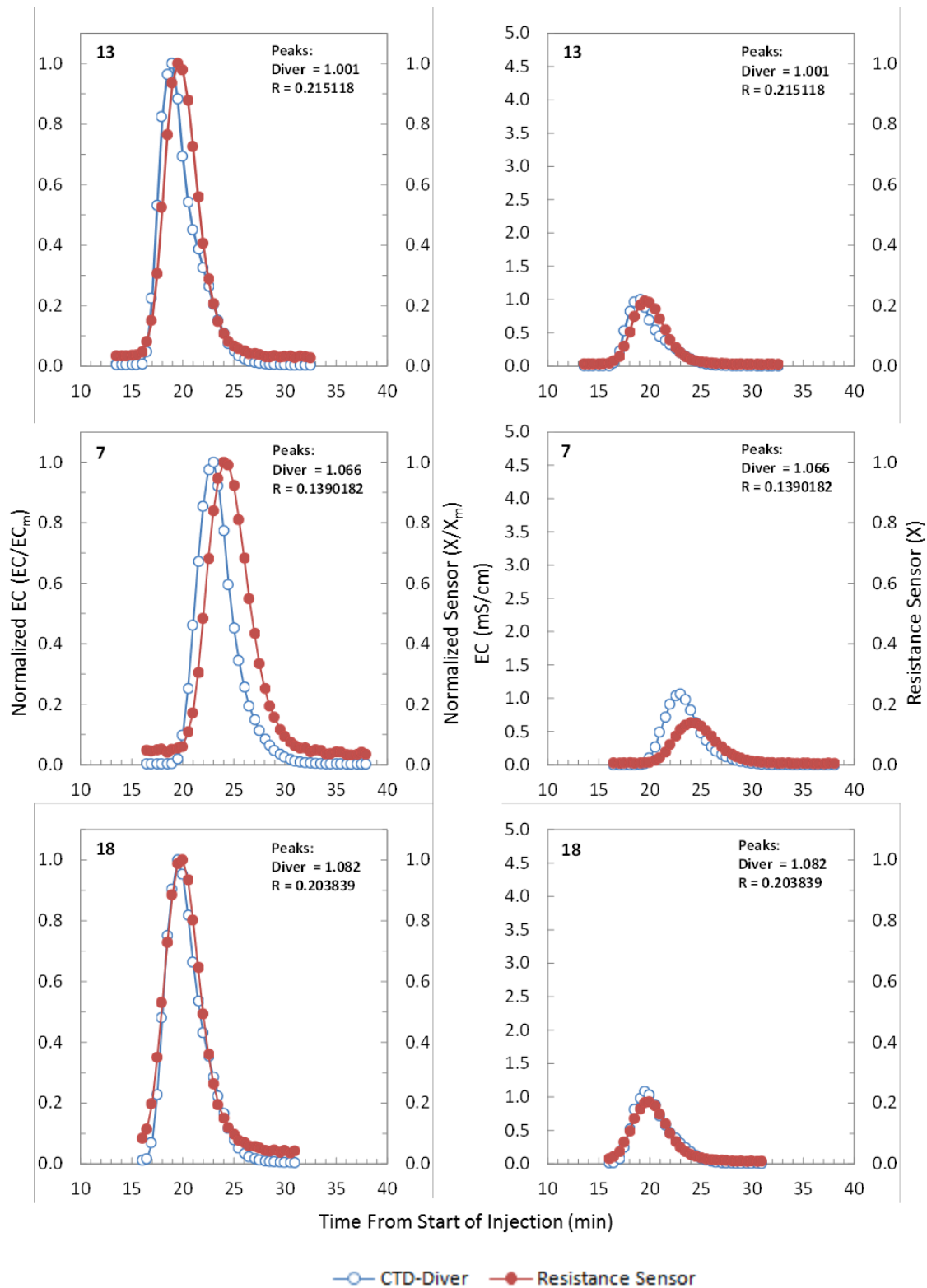


Figure D8: BTC 13, 7, and 18

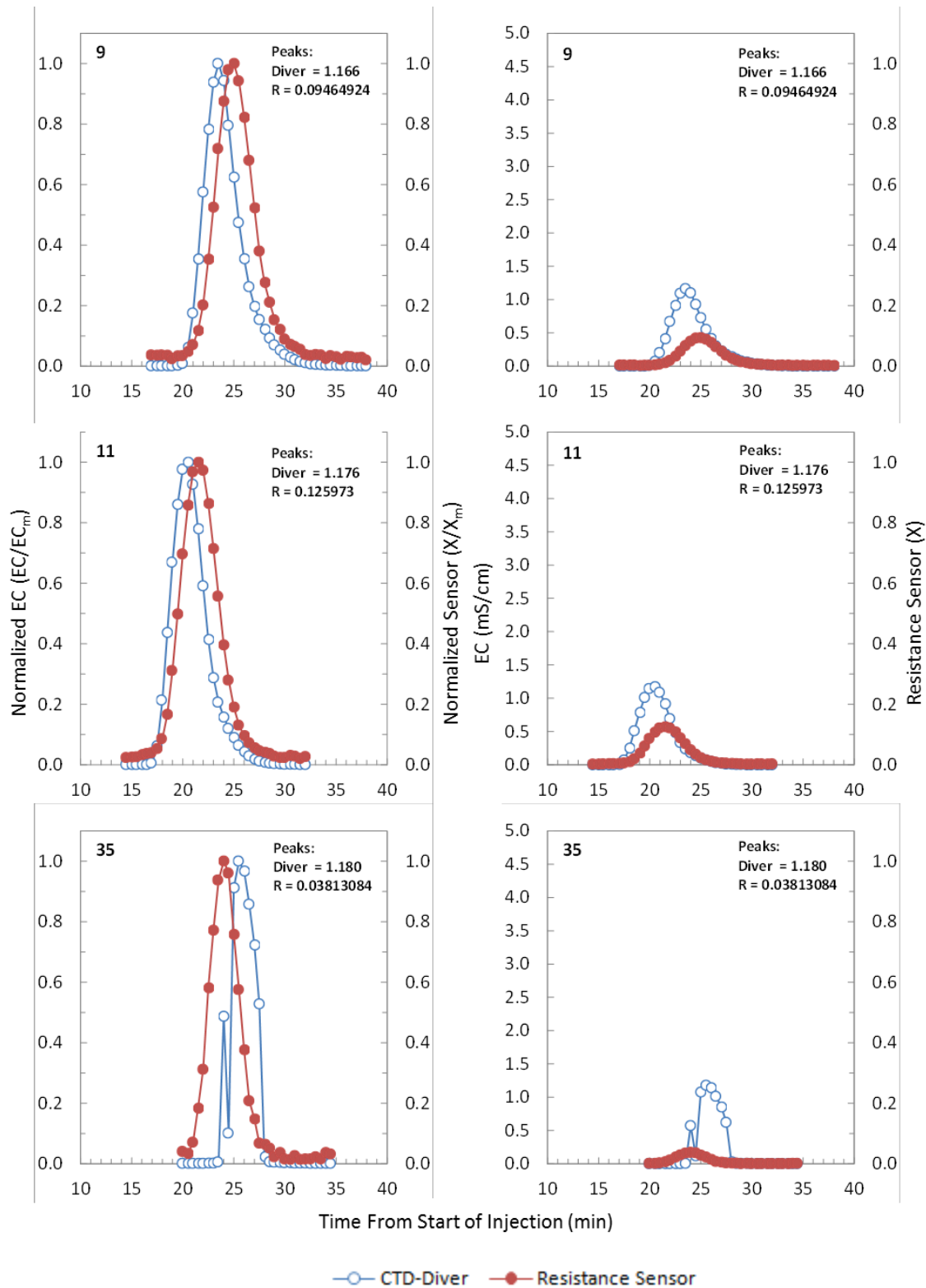


Figure D9: BTC 9, 11, and 35

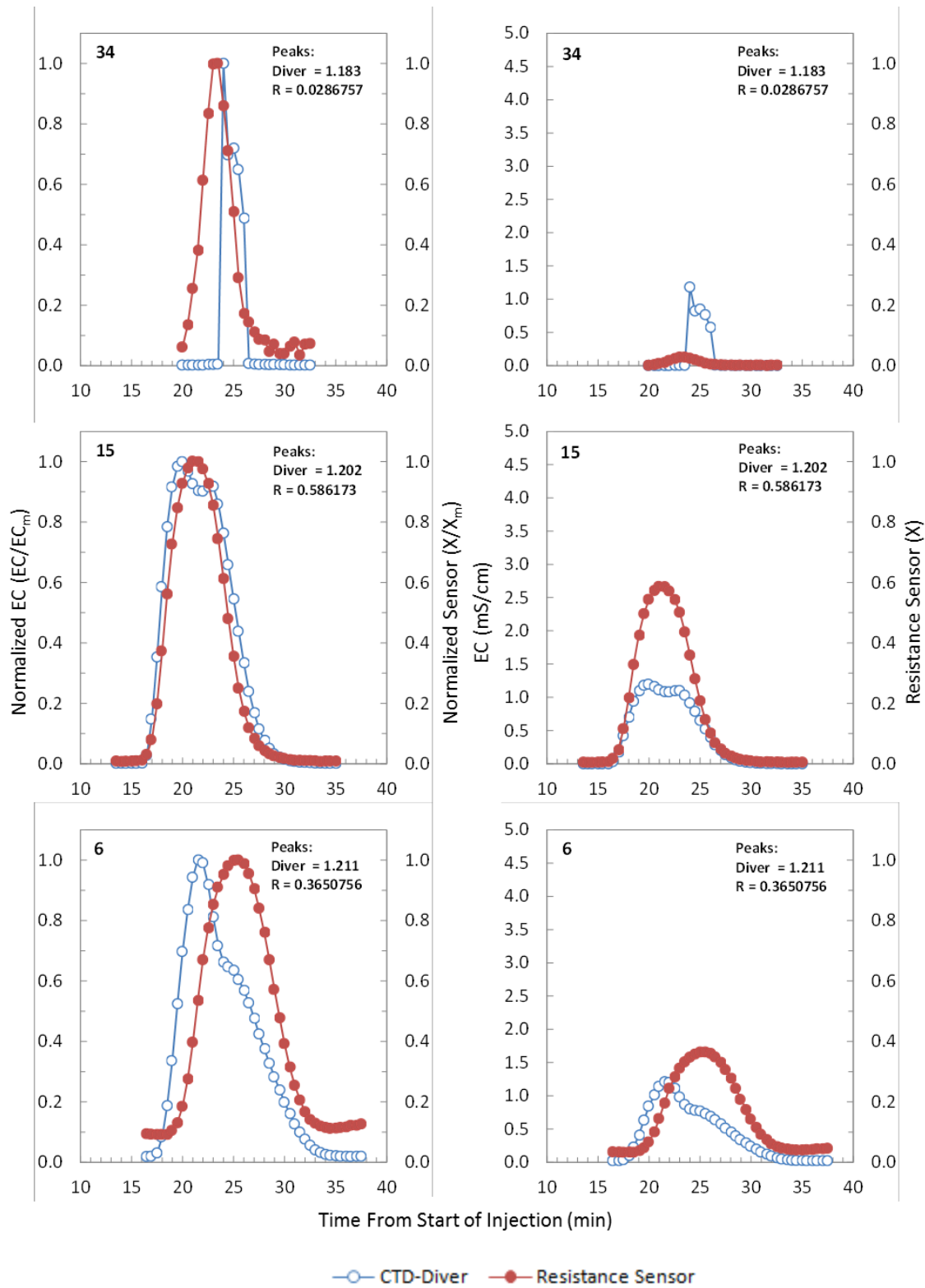


Figure D10: BTC 34, 15, and 6

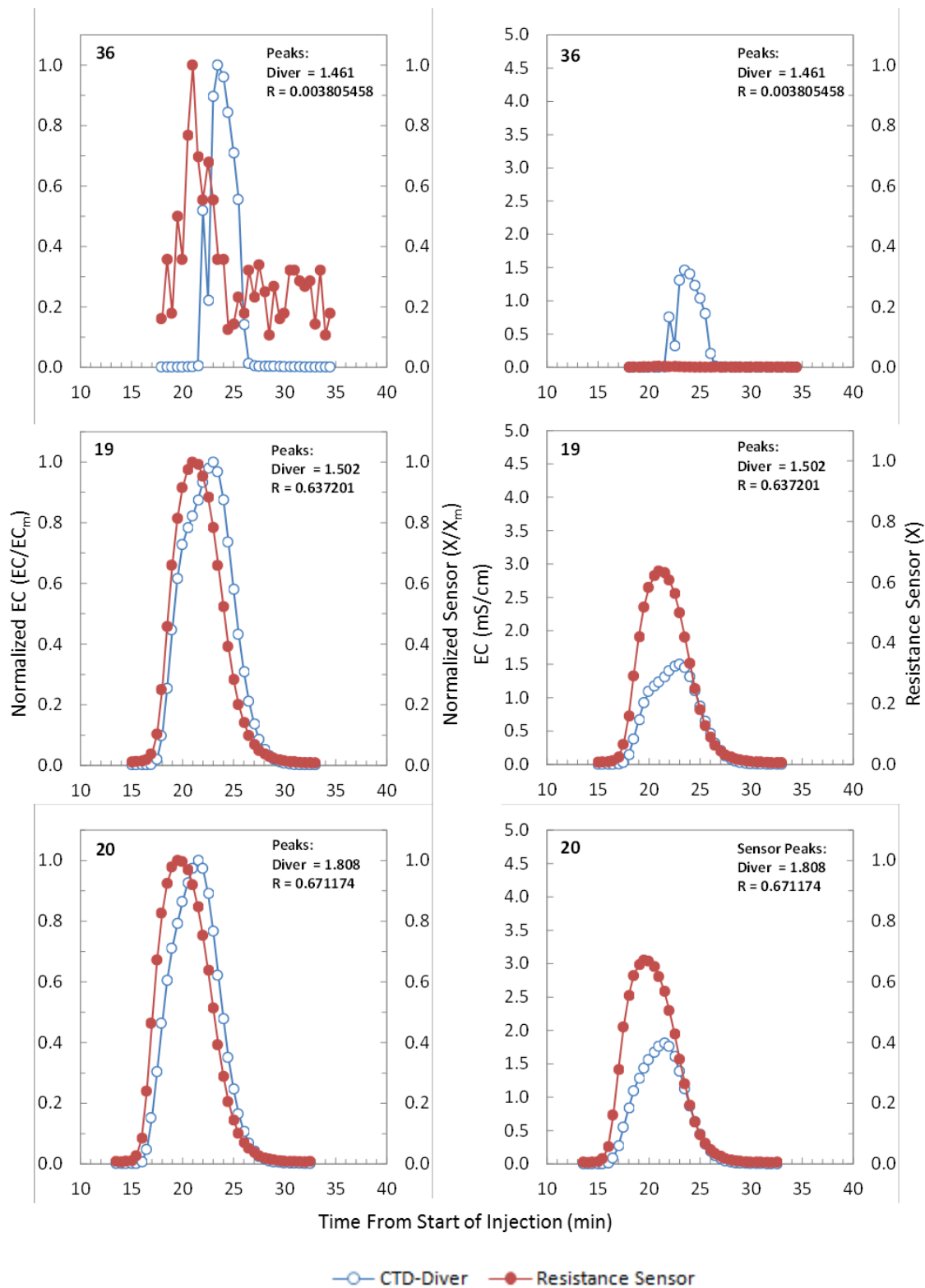


Figure D11: BTC 36, 19, and 20

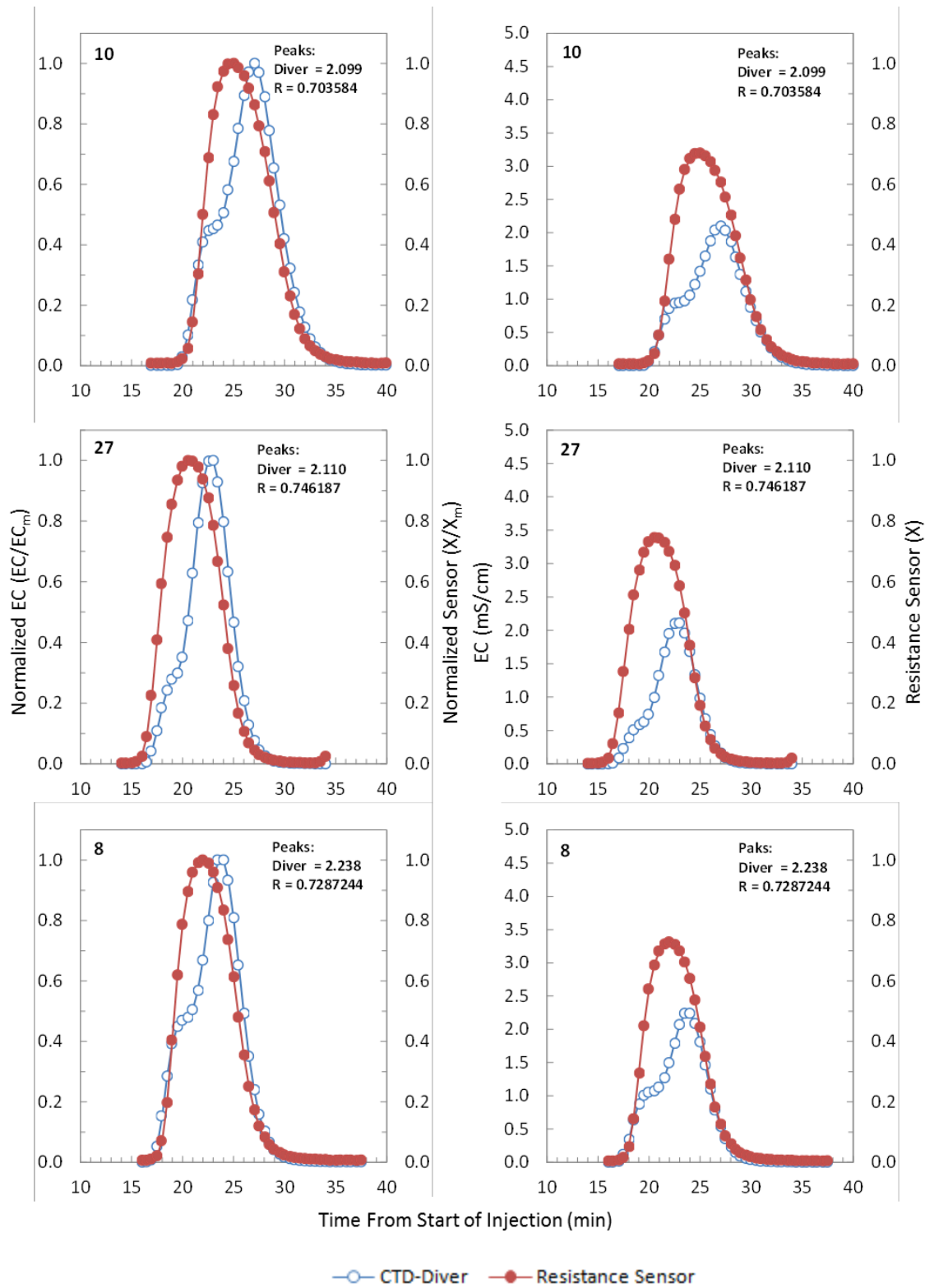


Figure D12: BTC 10, 27, and 8

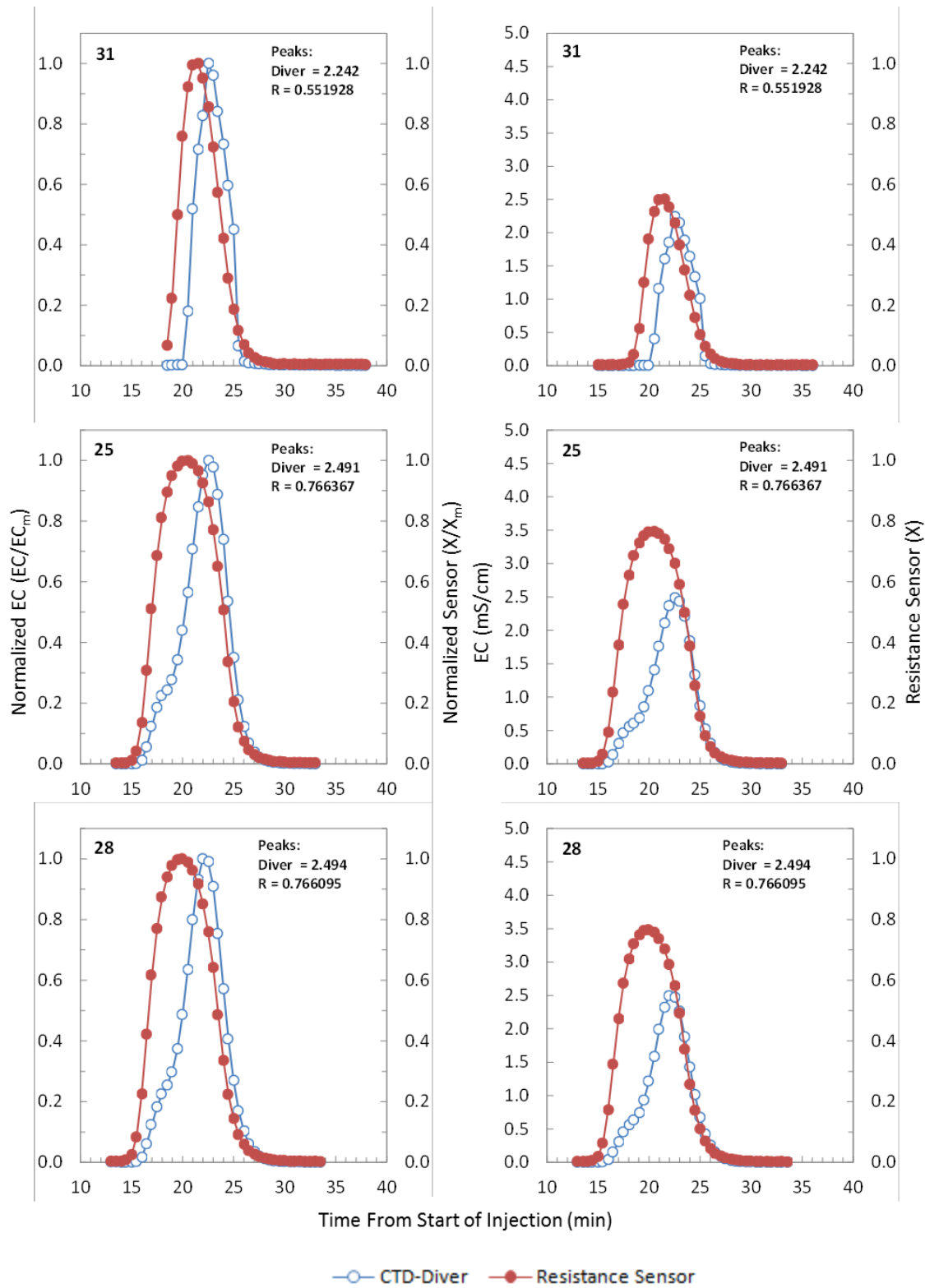


Figure D13: BTC 31, 25, and 28

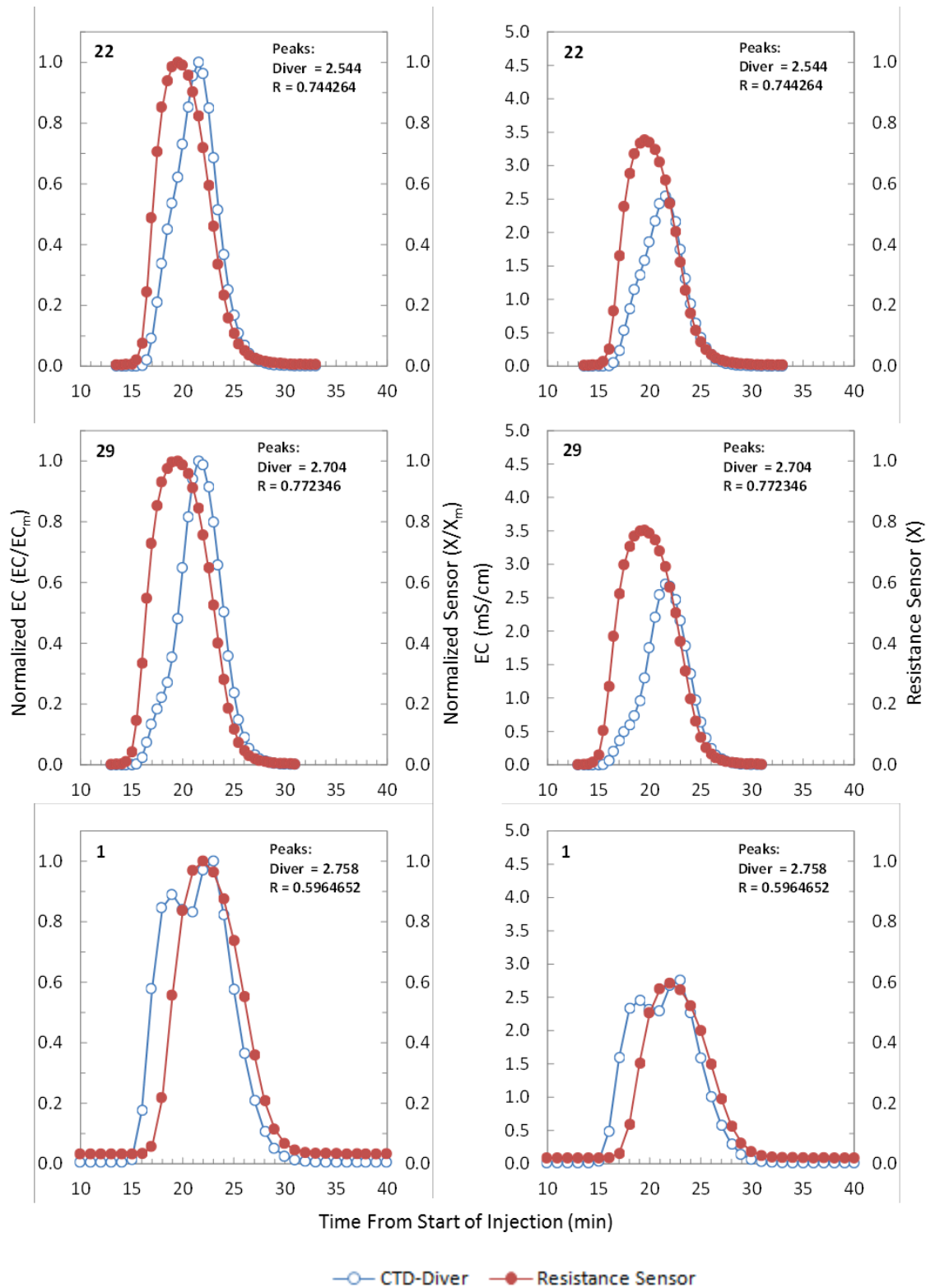


Figure D14: BTC 22, 29, and 1

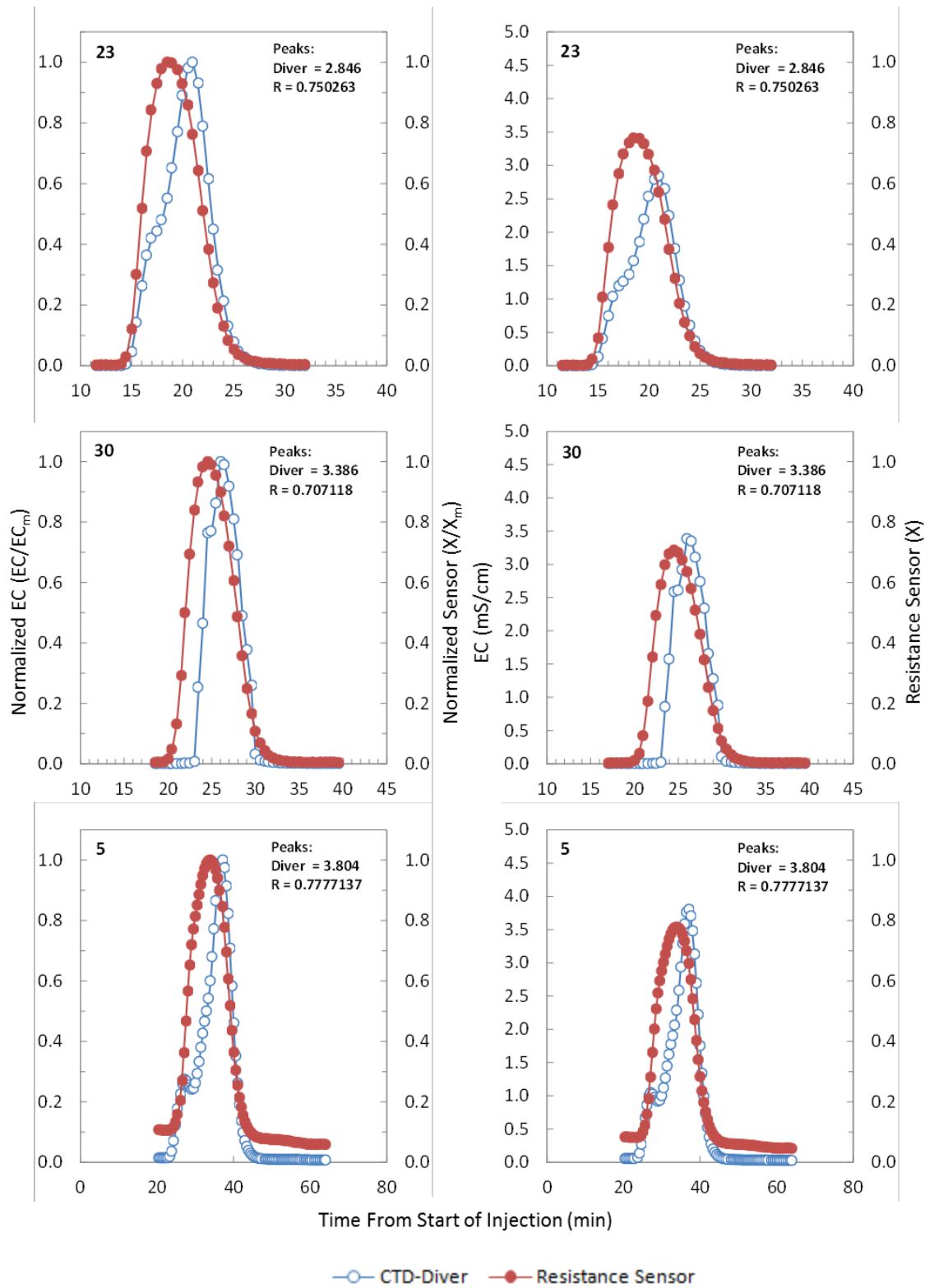


Figure D15: BTC 23, 30, and 5

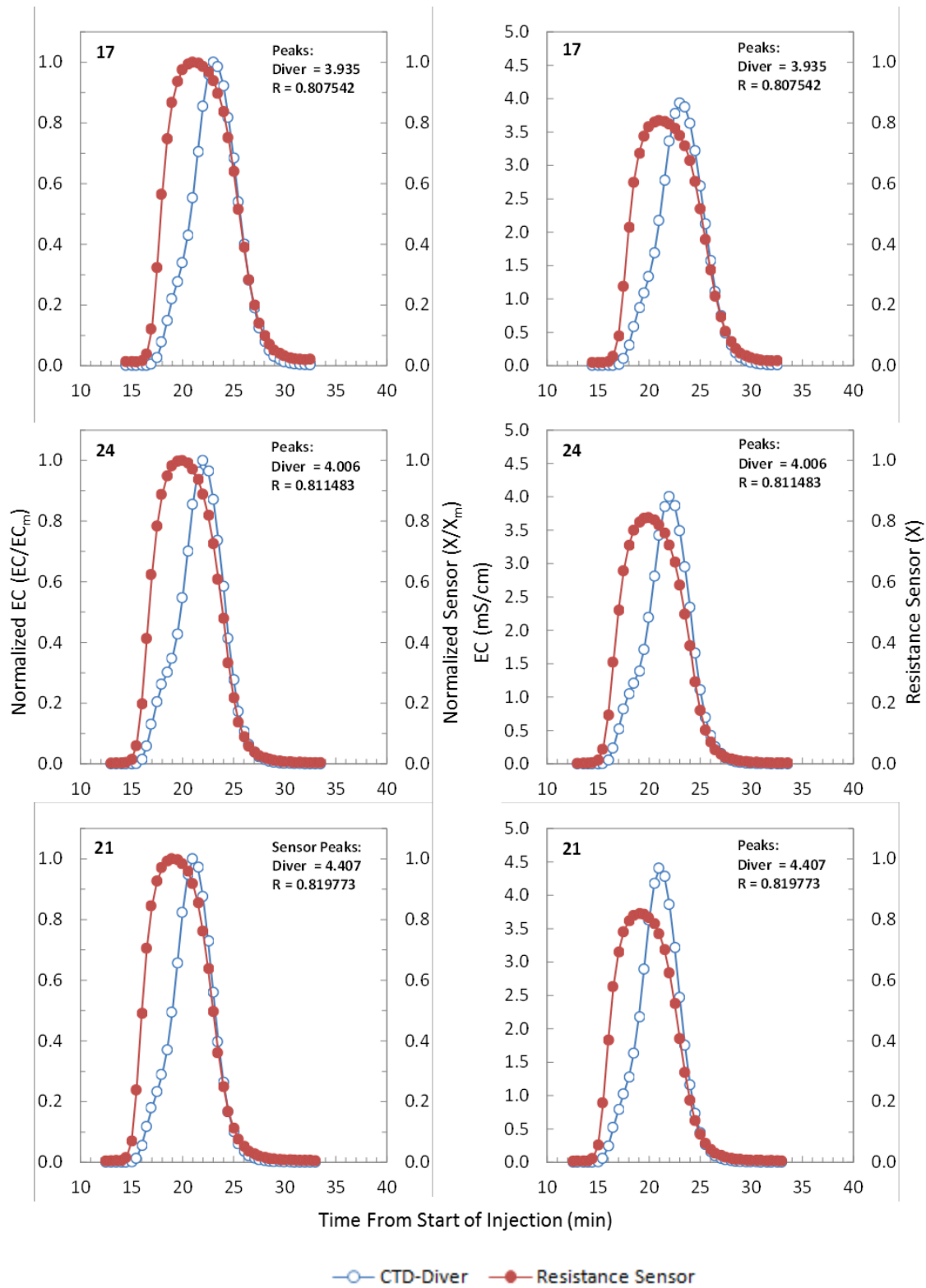


Figure D16: BTC 17, 24, and 21

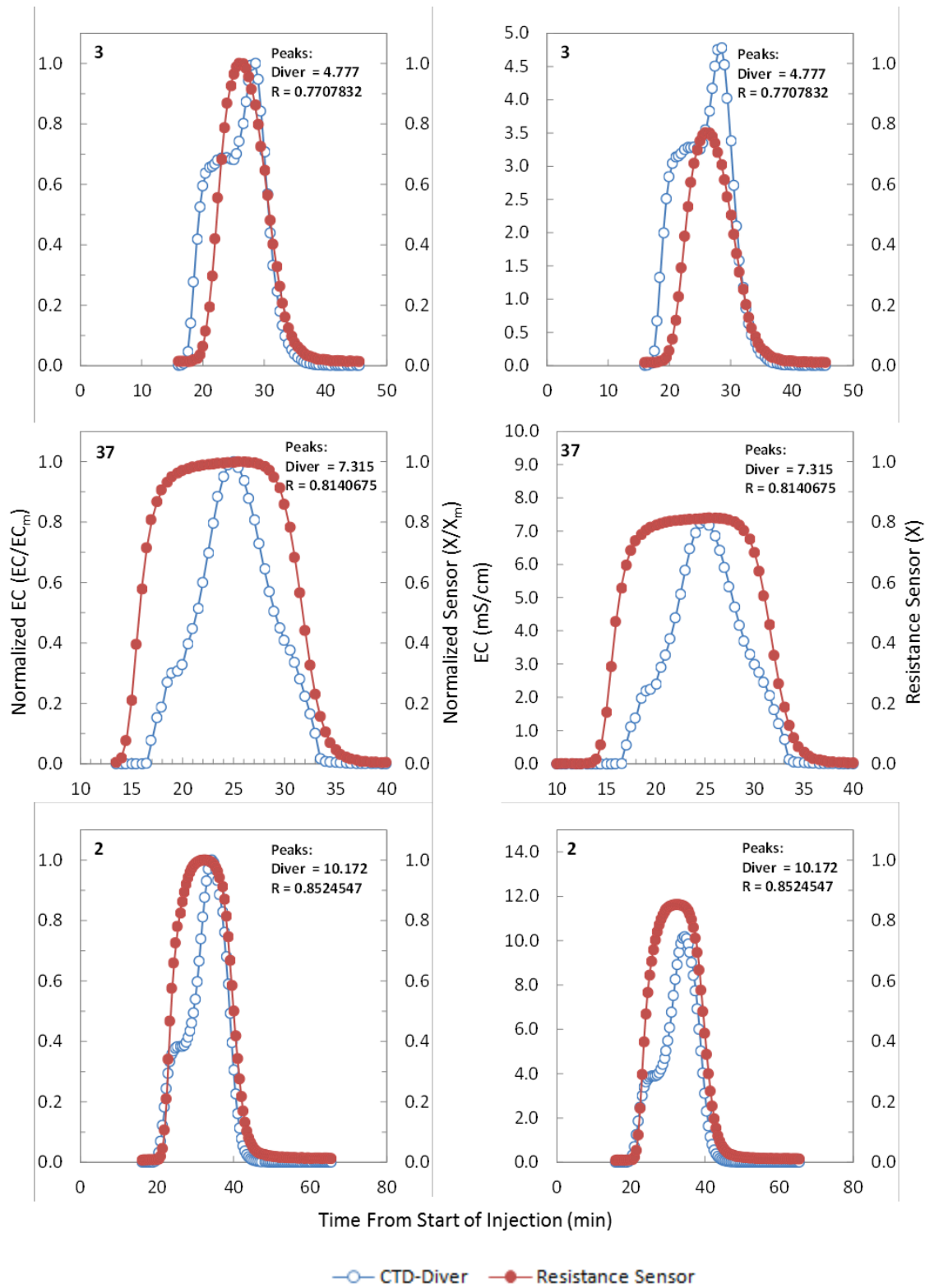


Figure D17: BTC 3, 37, and 2

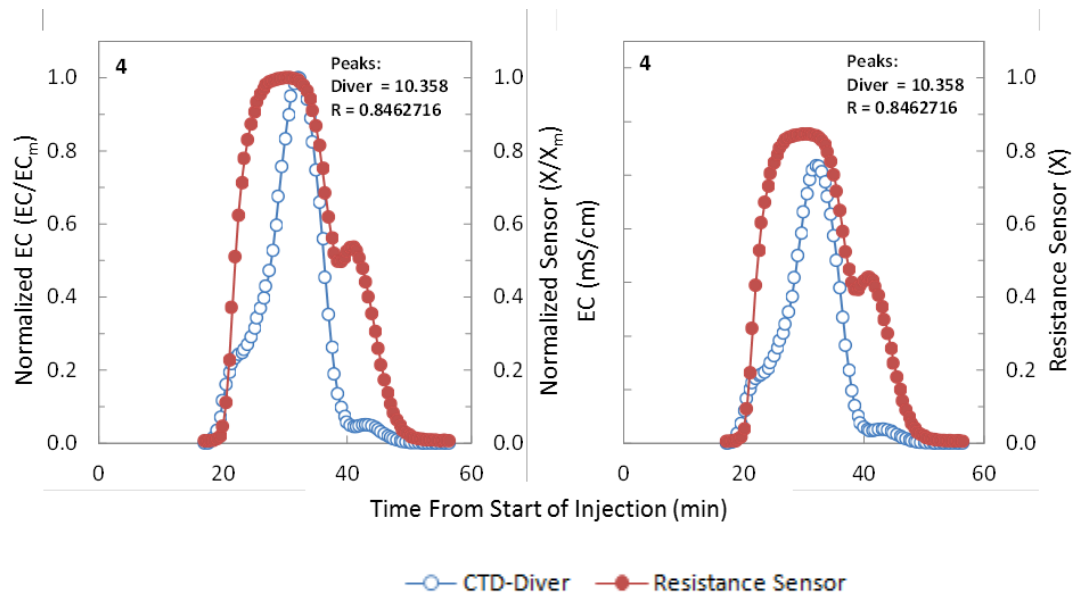


Figure D18: BTC 4

D5: SIMULATED GROUNDWATER BTCs

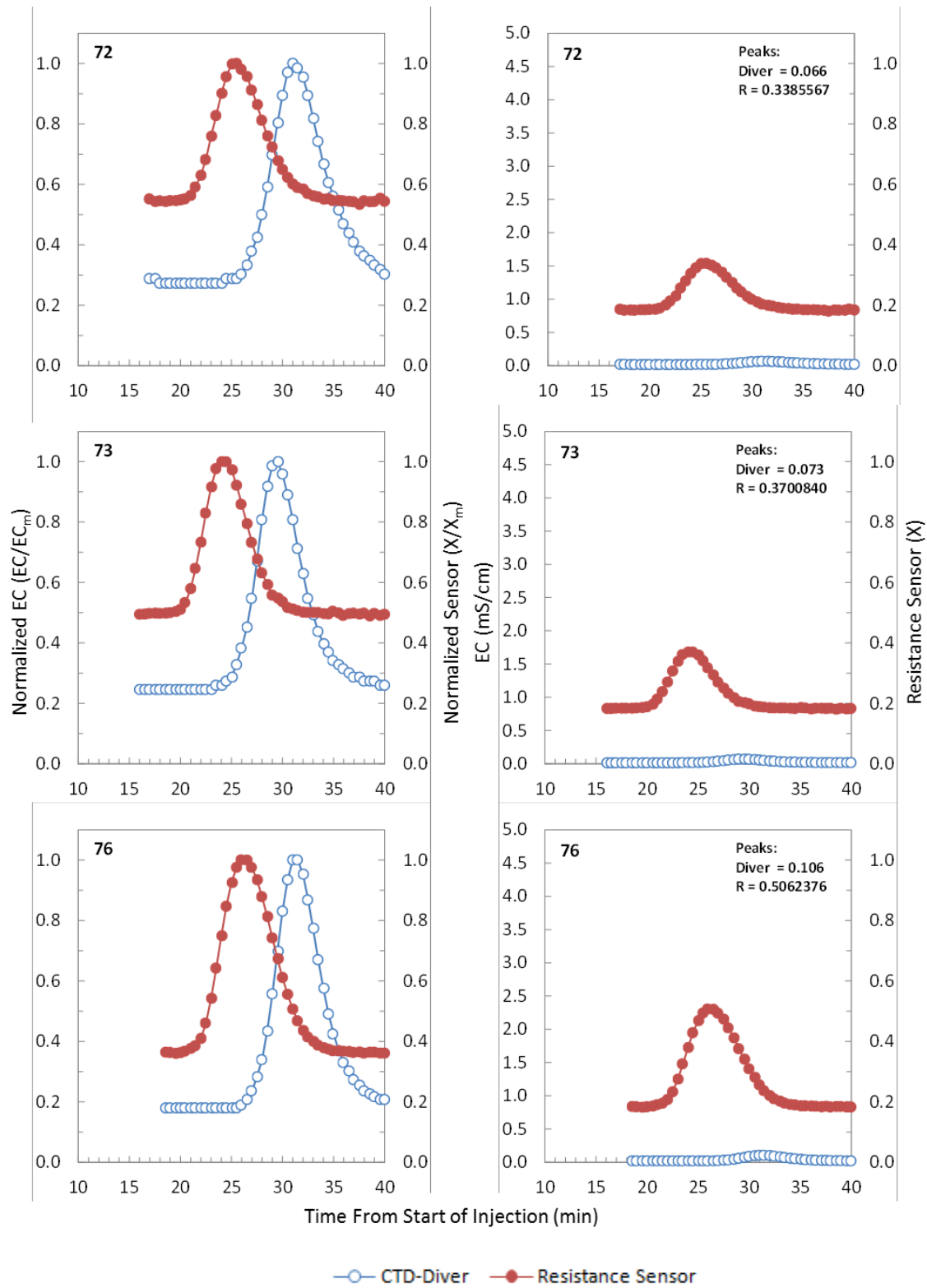


Figure D19: BTC 72, 73, and 76

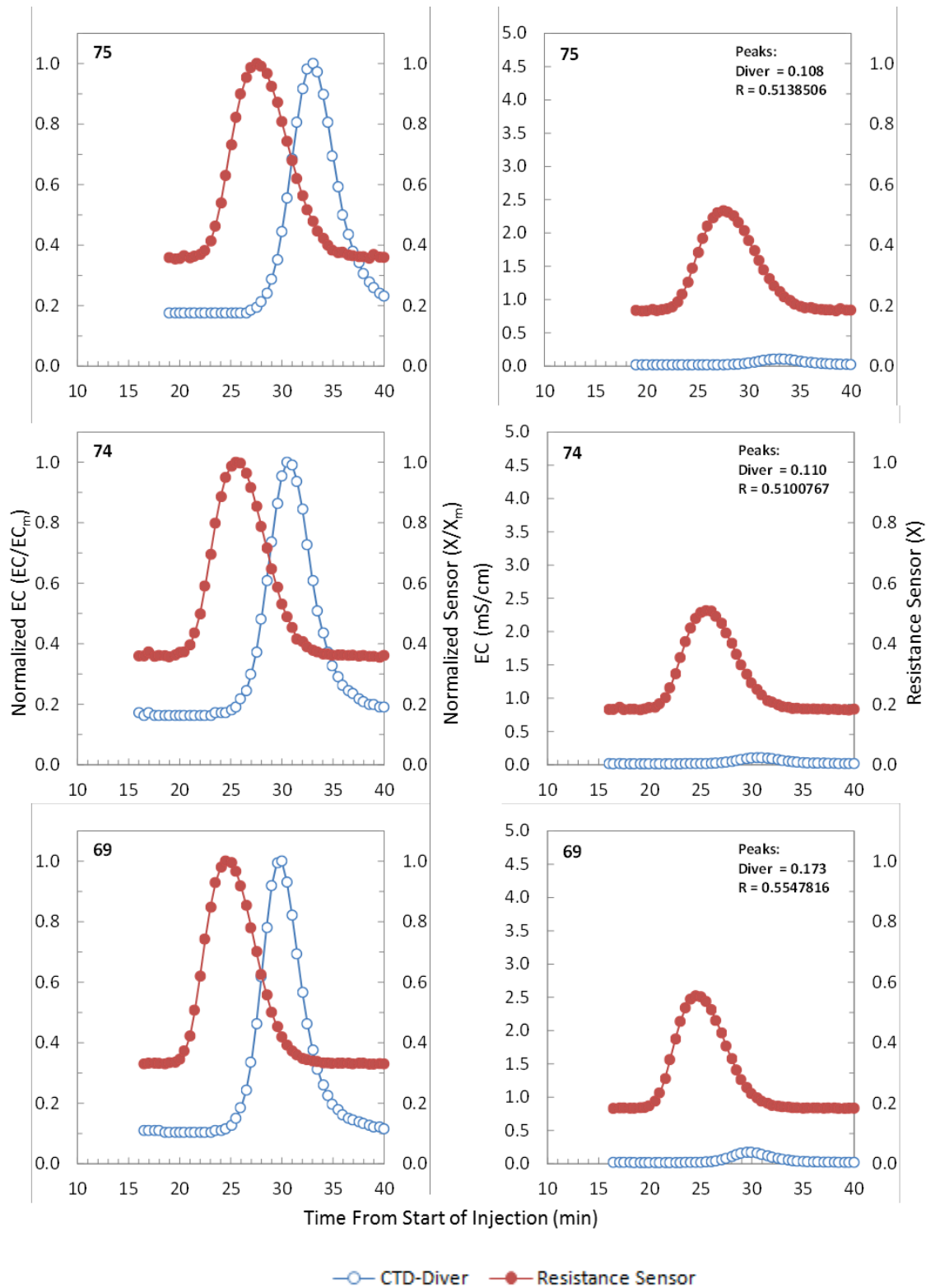


Figure D20: BTC 75, 74, and 69

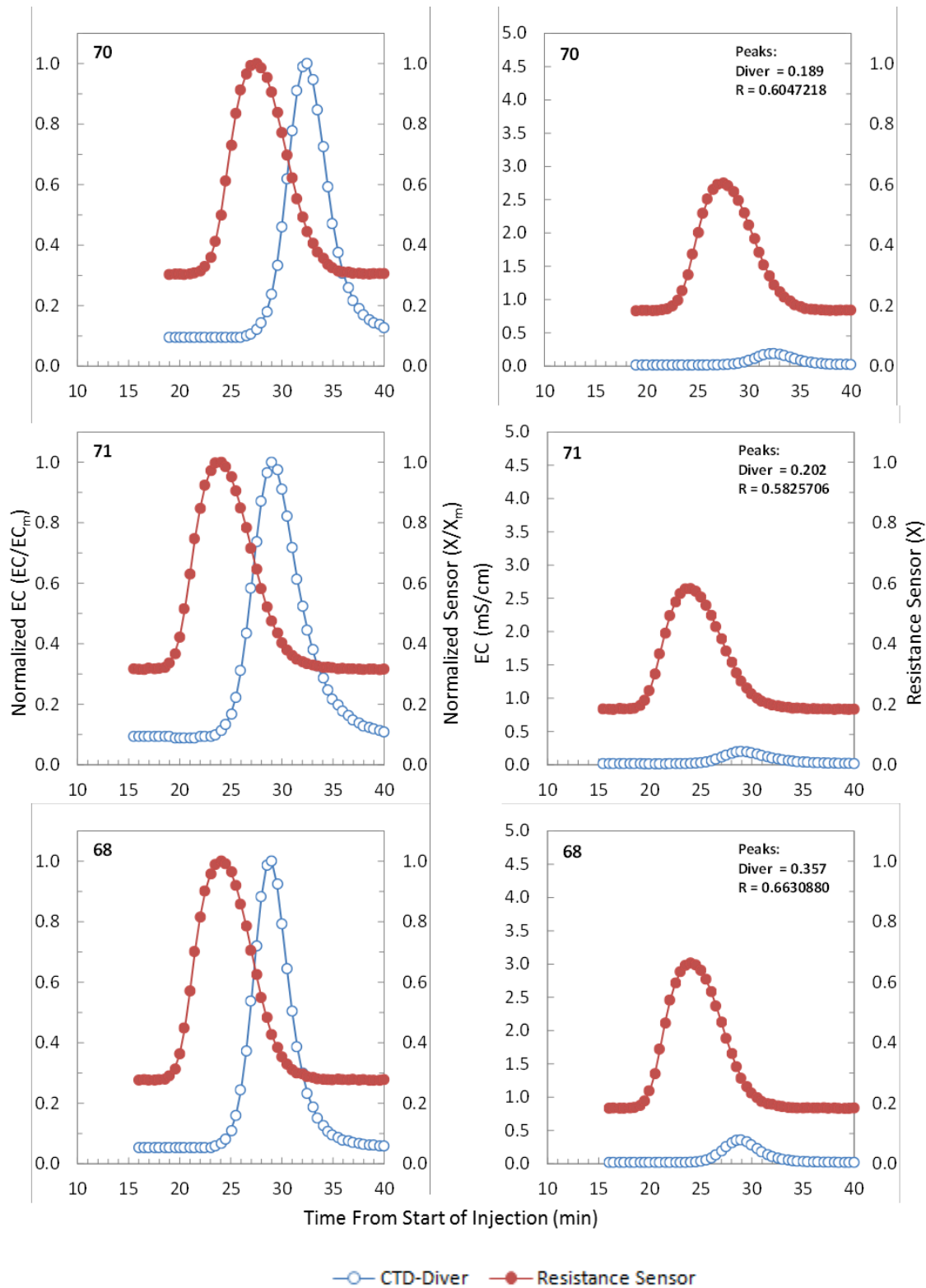


Figure D21: BTC 70, 71, and 68

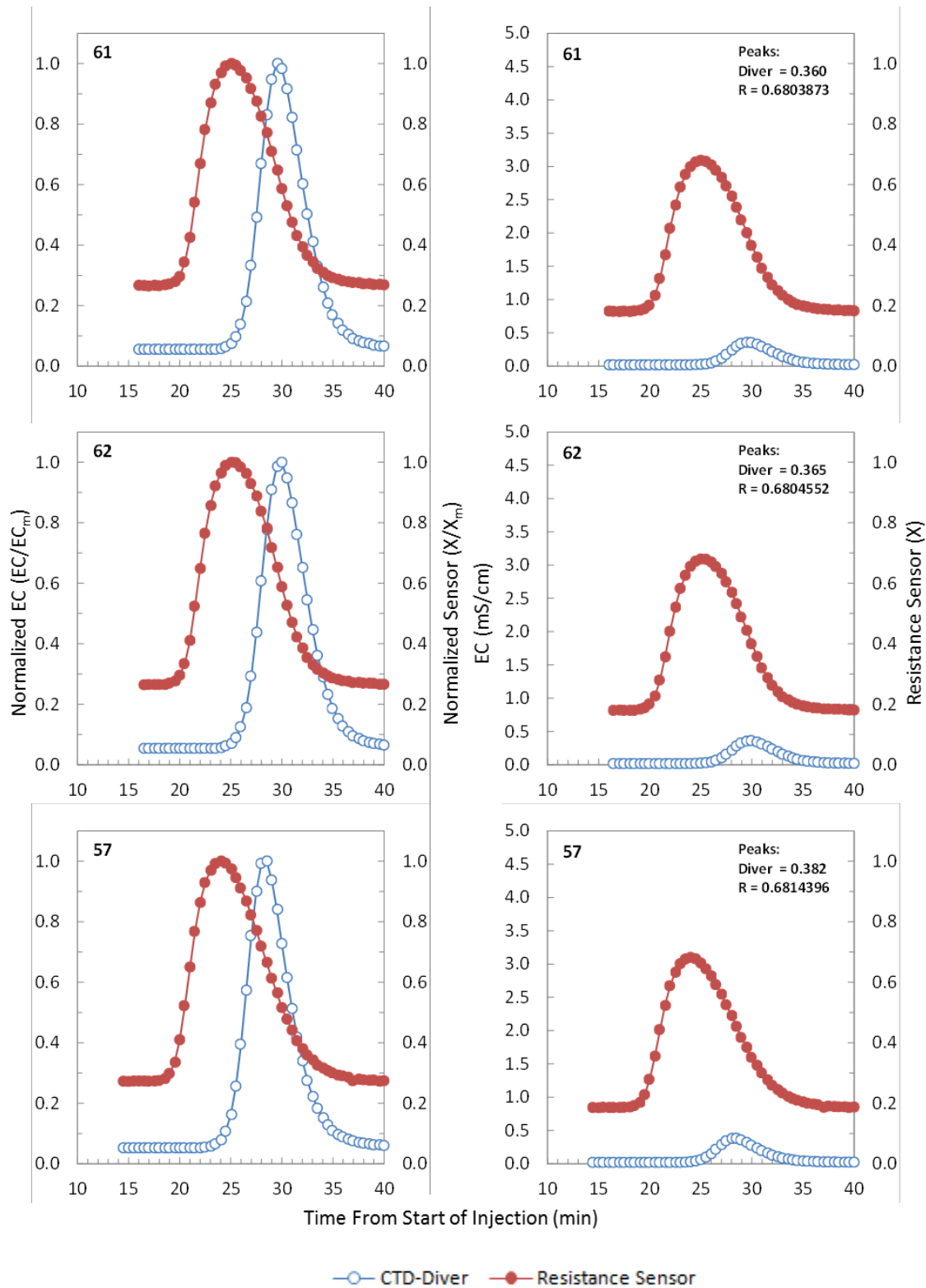


Figure D22: BTC 61, 62, and 57

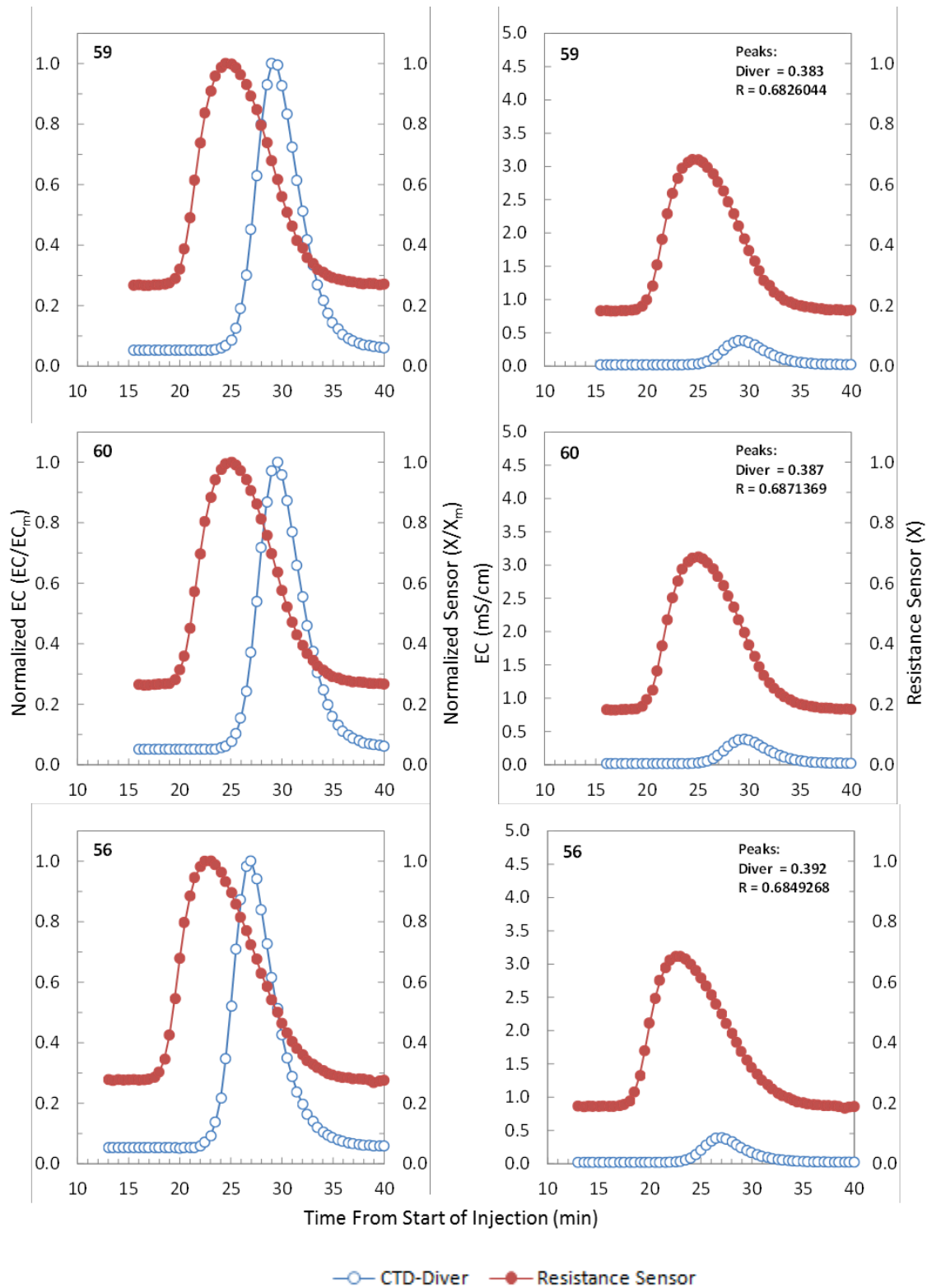


Figure D23: BTC 59, 60, and 56

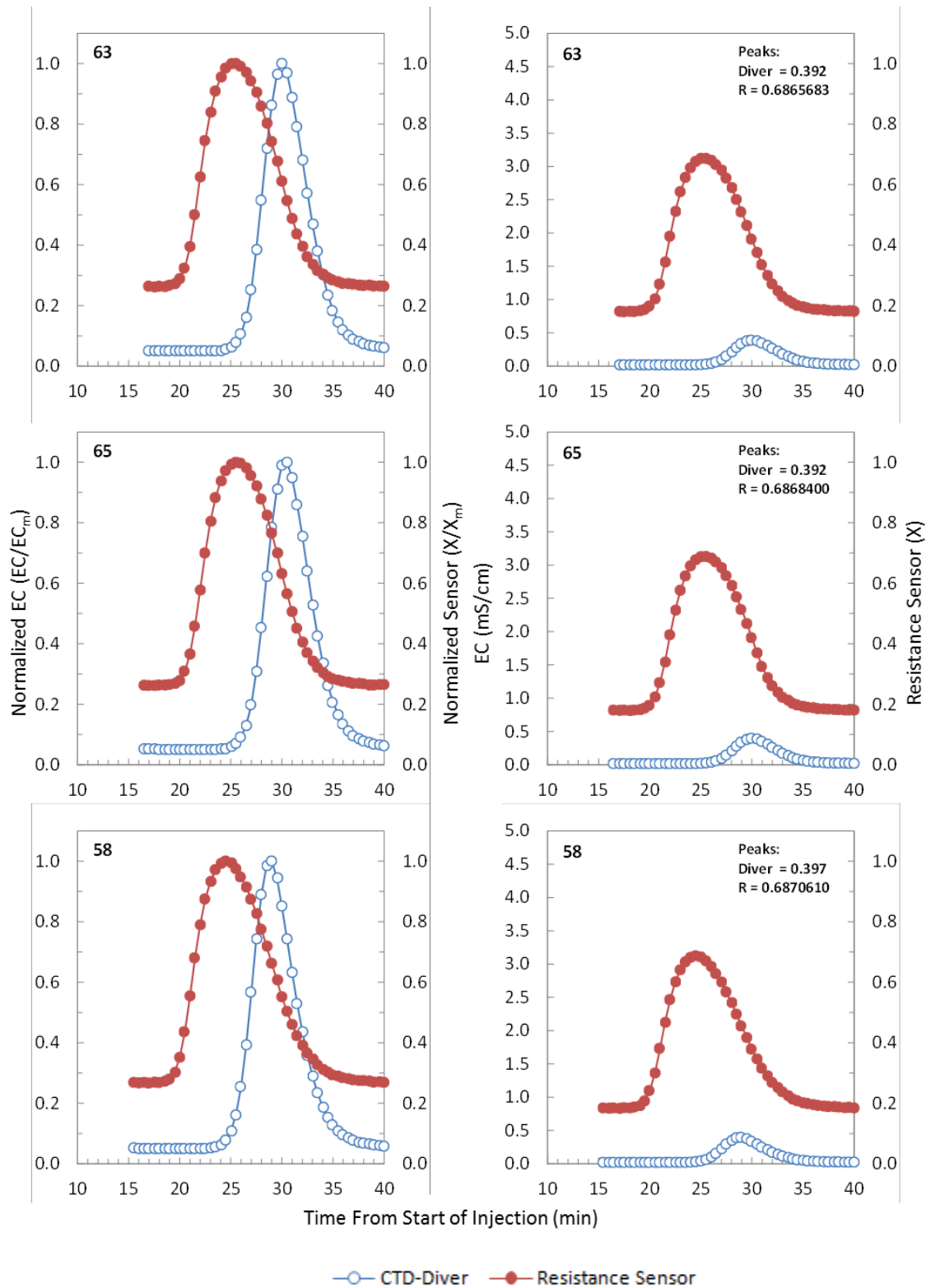


Figure D24: BTC 63, 65, and 58

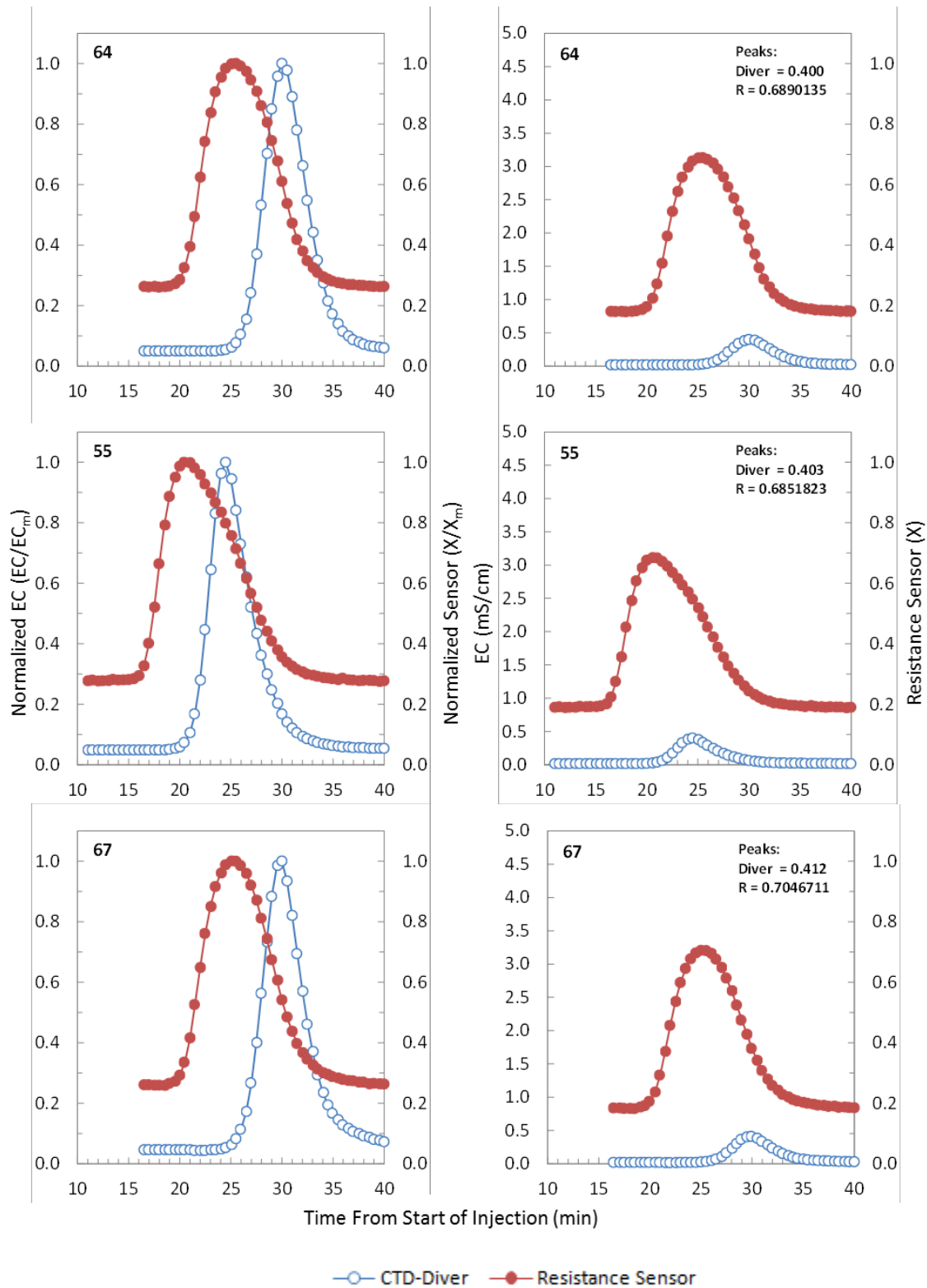


Figure D25: BTC 64, 55, and 67

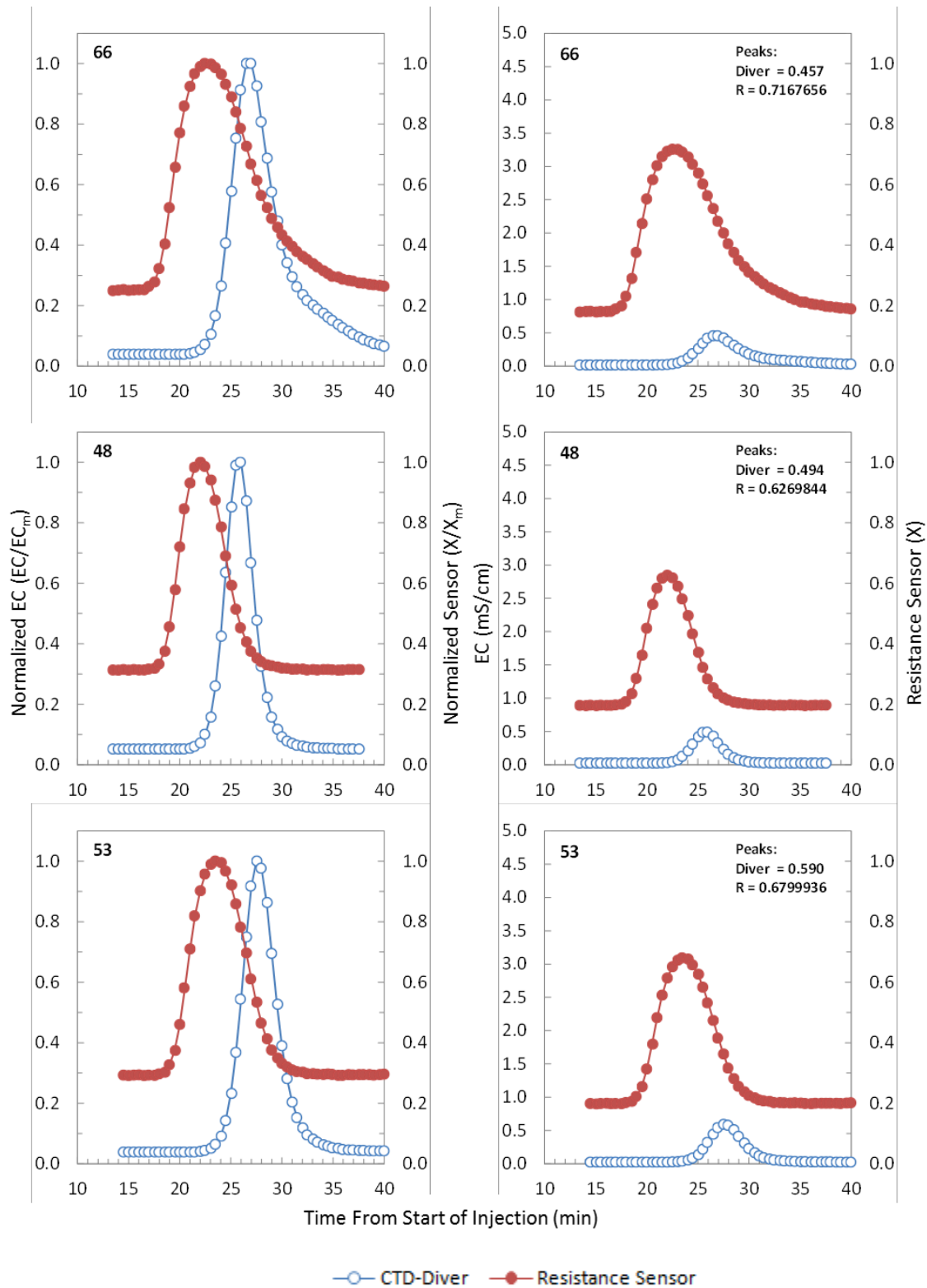


Figure D26: BTC 66, 48, and 53

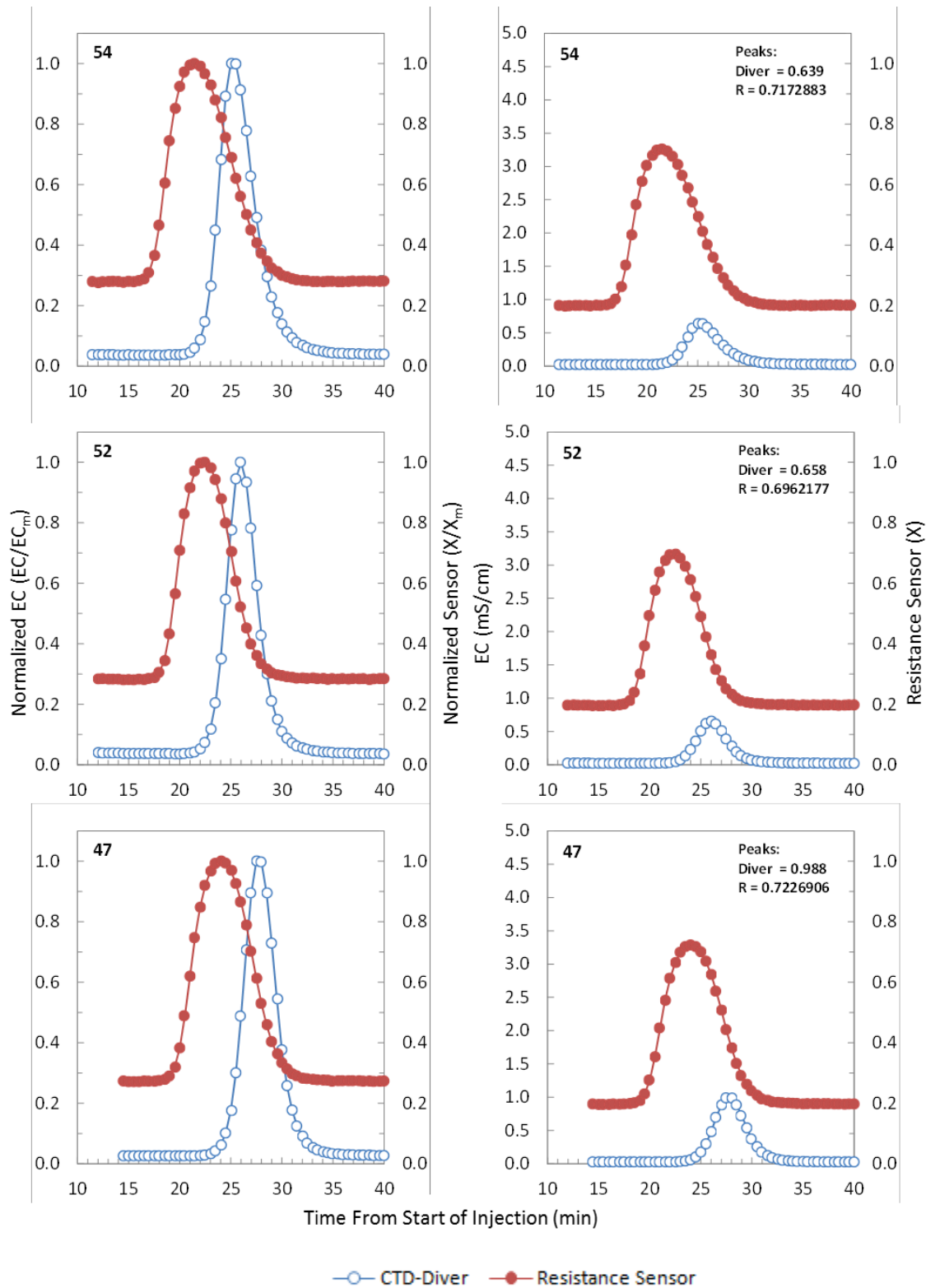


Figure D27: BTC 54, 52, and 47

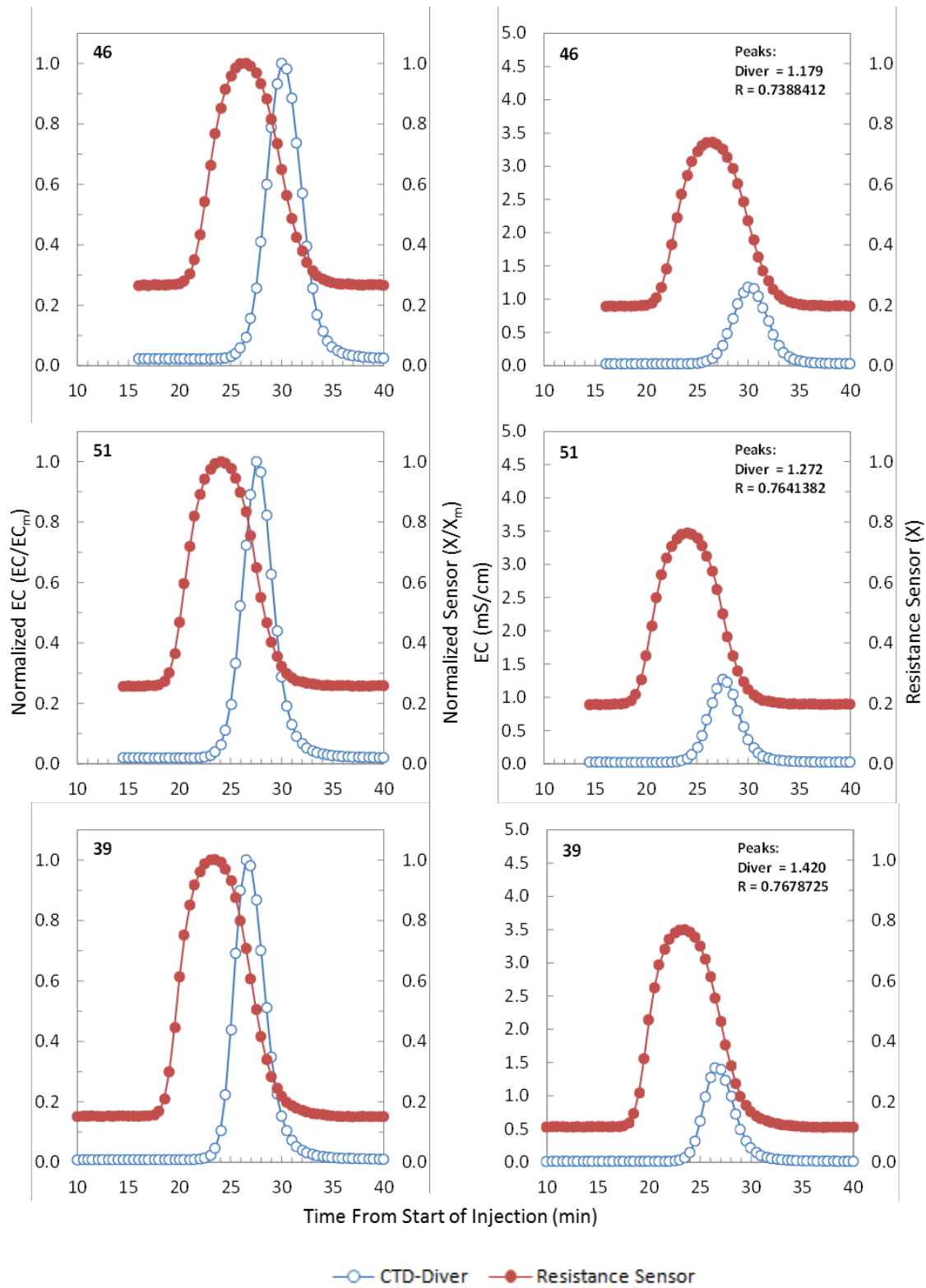


Figure D28: BTC 46, 51, and 39

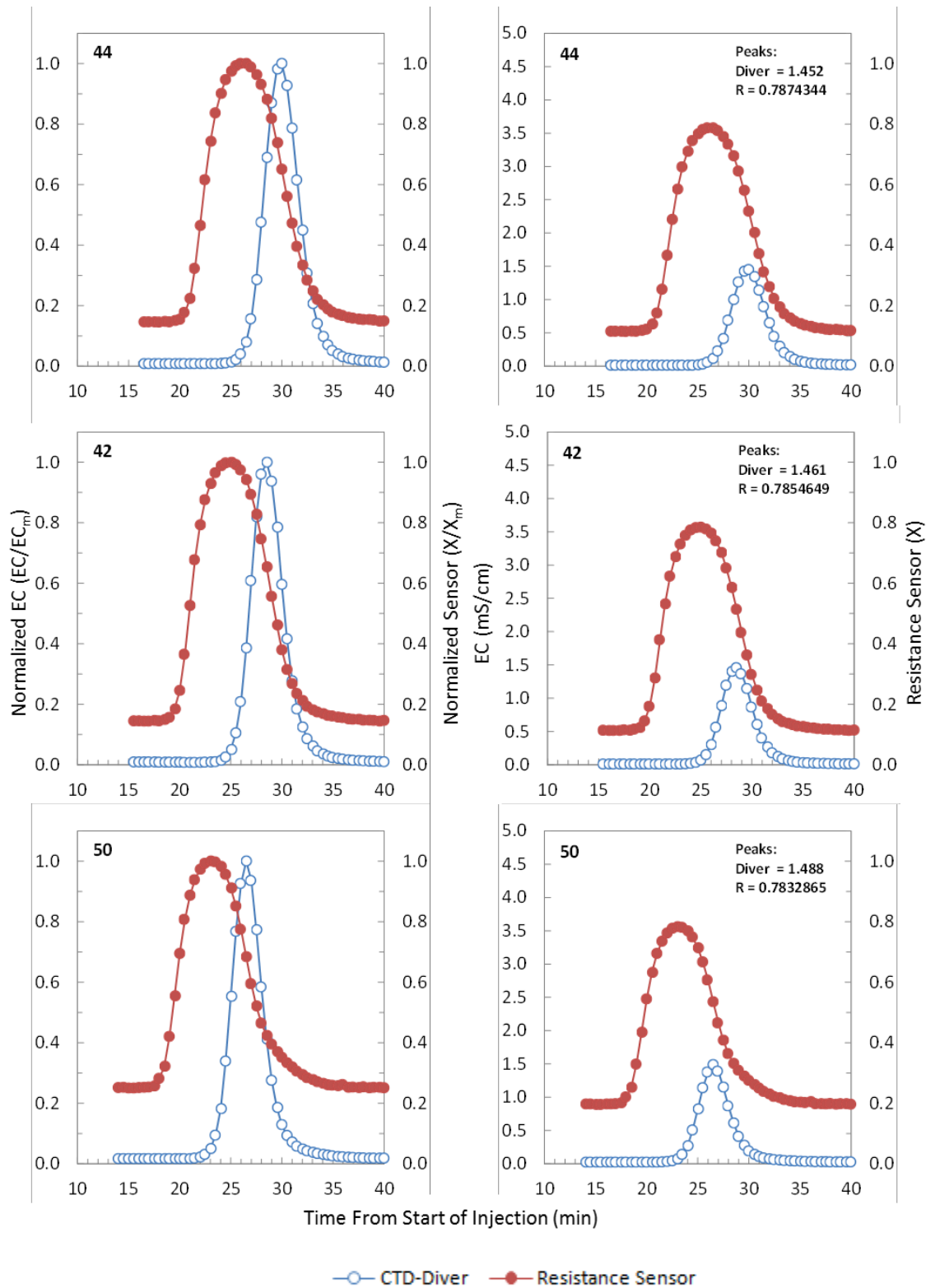


Figure D29: BTC 44, 42, and 50

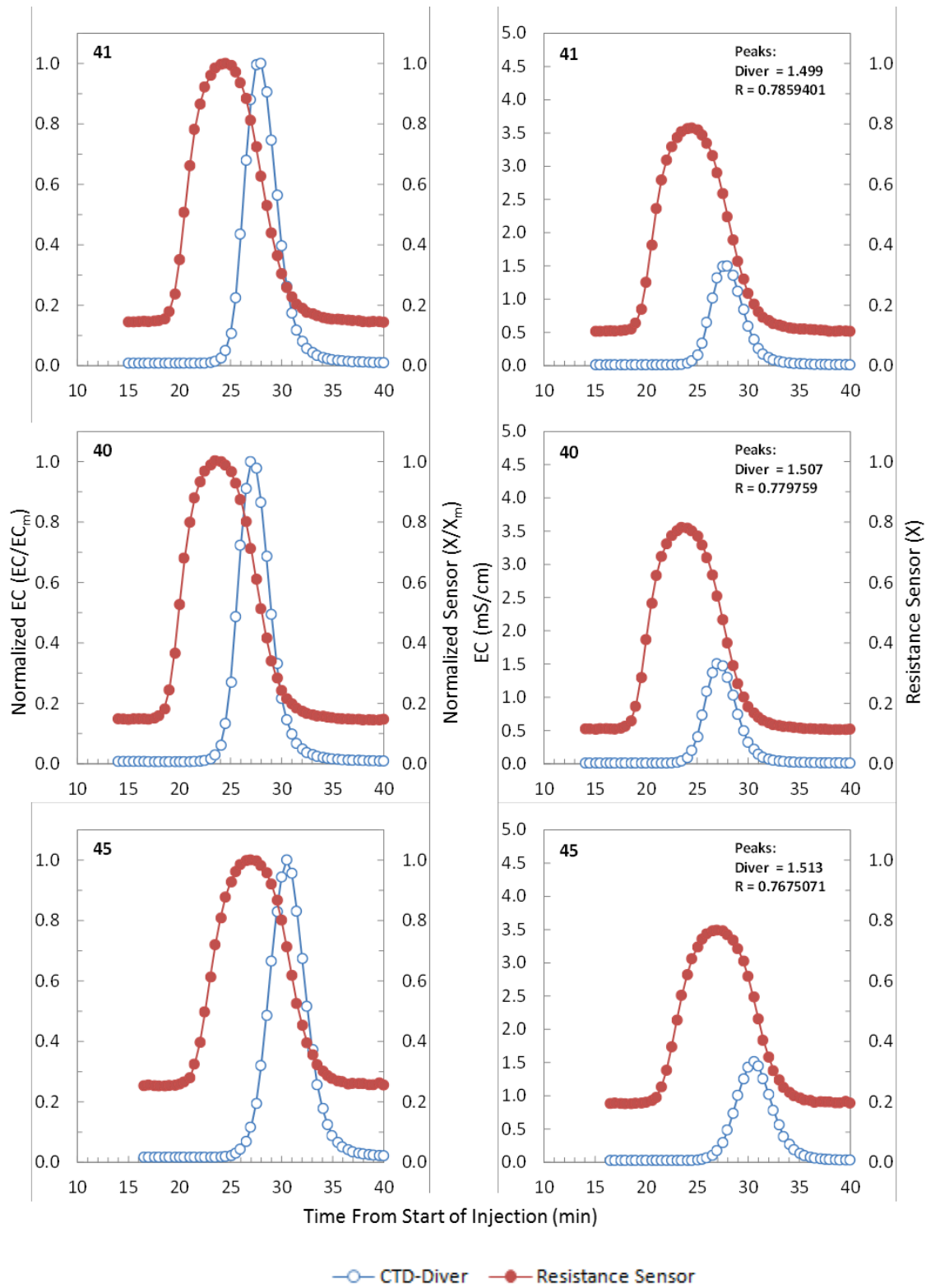


Figure D30: BTC 41, 40, and 45

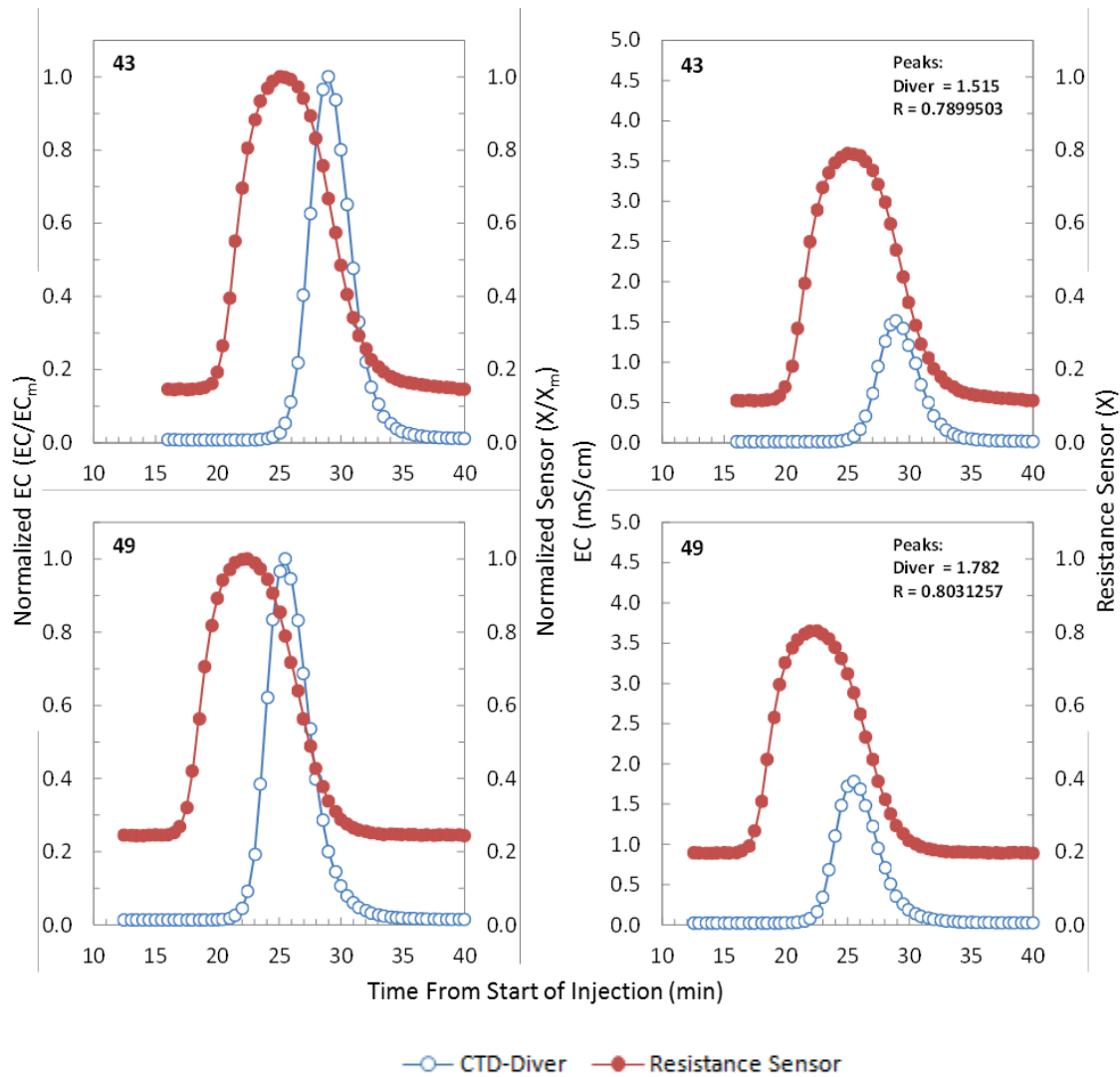


Figure D31: BTC 43, and 49

D6: PROBE CALIBRATION FOR HANDHELD METER AND CTD-DIVER

The handheld Thermo probe and the CTD-Diver were only calibrated to a single 1413 $\mu\text{S}/\text{cm}$ standard during experiments, rather than a curve of multiple standards. Therefore, these probes were accurate for measurements close to 1.4 mS/cm , but potentially introduced error into measurements with different conductivity than the calibration standard. The risk of calibration error is greater for the handheld Thermo Orion probe compared to the Schlumberger CTD-Diver.

A factory calibration is completed for the Schlumberger CTD-Diver when it is first constructed. CTD-Divers are calibrated to six standards; 150, 1000, 3000, 12500, 38000, and 89500 $\mu\text{S}/\text{cm}$. This factory calibration is always stored in the memory of the CTD-Diver, regardless of the number and type of field calibrations that are done by the user (Schlumberger Water Services, 2010, p.24). Therefore, although the CTD-Diver was only calibrated to a single 1413 $\mu\text{S}/\text{cm}$ standard, the factory calibration still applies to values significantly different than the field calibration standard. Furthermore, the CTD-Diver has only four field calibration standards; 1413, 5000, 12880, and 80000 $\mu\text{S}/\text{cm}$. Schlumberger states that field calibrations can be done with only 1 or 2 calibration standards and that the datalogger will be accurate for the range of values between those standards (Schlumberger Water Services, 2010, p.25). However, the 1413 $\mu\text{S}/\text{cm}$ standard is the lowest EC value available, so it is reasonable to assume that the datalogger is relatively accurate for all readings between 0-1413 $\mu\text{S}/\text{cm}$.

Most of the measurements which were conducted by the CTD-Diver during BTC experiments were less than the 1413 $\mu\text{S}/\text{cm}$ standard, and very few were significantly higher than this range. All of the simulated groundwater BTCs had CTD-Diver peaks less than 1800 $\mu\text{S}/\text{cm}$. For the clean water BTCs, 20 of the 38 curves had peaks above 1800 $\mu\text{S}/\text{cm}$. However, a much smaller number of total measurements that comprise each BTC were above 1800 $\mu\text{S}/\text{cm}$. Considering the total number of measurements that were outside of the 1413 $\mu\text{S}/\text{cm}$ range along with the validity of the factory and field calibrations which were completed on the probe, it is unlikely that measurement error due to poor calibration significantly affected the data collected by CTD-Diver.

The Schlumberger probe was tested for accuracy on November 13, 2011, when the flow tank was repacked. The probe was removed from the original sand pack, cleaned with DI, and then

placed in a clean beaker containing a 1413 $\mu\text{S}/\text{cm}$ standard. The probe was set to collect data three different times, twice using the specific conductivity setting where values are referenced to 25 °C, and once with the uncompensated conductivity setting. The results in Table D3 show the logger was reading within 67-71 $\mu\text{S}/\text{cm}$ of the standard, assuming the standard was exactly 1413 $\mu\text{S}/\text{cm}$. Exposure to the air, and ionic contamination on the beaker and/or CTD-Diver may have caused slight alterations to the conductivity standard. These results indicated that the Schlumberger CTD-Diver measurements were accurate within 5% of the 1413 $\mu\text{S}/\text{cm}$ measurement point. This maximum error was considered acceptable and the probe was not recalibrated before it was placed back in the tank for use during the simulated groundwater BTC experiments.

Table D3: Summary of CTD-Diver accuracy. Tests A and C used the specific conductivity setting where measurements are referenced to 25°C while Test B used the conductivity setting where measurement are not corrected. Summary statistics for Test B were calculated after the EC values were converted to EC_{25} using Eq.(5).

Test	(Average EC - 1.413 mS/cm Standard)	Standard Deviation	Number of Measurements*	Average Temperature (°C)
A	0.071	0.0008	13	21.27
B	0.067	0.0011	19	21.19
C	0.076	0.0009	8	21.18

*Measurement interval was 30 seconds.

D7 EC TEMPERATURE CORRECTIONS

The following is an example of temperature conversion from EC₂₅ (specific conductivity setting on the CTD-Diver) to EC (conductivity setting on CTD-Diver, not referenced to a specific temperature) and subsequent calculation of percent differences between the converted values. Summary statistics are shown for BTC9.

Corrected CTD-Diver:

EC₂₅ (EC_{ref}) converted to EC (EC_T) using Eq.(5) and a factor of 0.0191 °C⁻¹ for *a*

Normalized Corrected CTD-Diver:

Normalized CTD-Diver conductivity measurement (EC/EC_m) calculated from “Corrected CTD-Diver” values

Difference A:

$$Diff A = (CTD_Diver) - (Corrected CTD_Diver)$$

Difference B:

$$Diff B = (Normalized CTD_Diver) - (Normalized Corrected CTD_Diver)$$

Raw data compared to raw data corrected for temperature (% Difference):

$$\% Difference = \left[\frac{Diff A}{Corrected CTD_Diver} \right] \times 100$$

Normalized compared to normalized corrected for temperature (% Difference):

$$\% Difference = \left[\left| \frac{Diff B}{Relative Corrected CTD_Diver} \right| \right] \times 100$$

Table D4: Example of percent difference calculation for BTC9. Summary statistics were calculated using each measurement for BTC9 and subsequent spreadsheet calculations described in Appendix D7.

	Percent Difference			
	Diff A	Diff B	Raw data compared to raw data corrected for temperature	Normalized data compared to normalized data corrected for temperature
Maximum during BTC9	-2.08E-04	1.00E-03	11.19	1.26
Minimum during BTC9	-1.38E-01	-9.32E-04	9.44	0.00
Average for BTC9	-2.61E-02	-1.10E-04	10.24	0.59